



HAL
open science

Unbiased Spectral Survey towards the intermediate-mass Class 0 protostar Cep E-mm

Susana Pacheco-Vazquez

► **To cite this version:**

Susana Pacheco-Vazquez. Unbiased Spectral Survey towards the intermediate-mass Class 0 protostar Cep E-mm. Astrophysics [astro-ph]. Université de Grenoble, 2012. English. NNT : 2012GRENY066 . tel-01561004

HAL Id: tel-01561004

<https://theses.hal.science/tel-01561004>

Submitted on 12 Jul 2017

HAL is a multi-disciplinary open access archive for the deposit and dissemination of scientific research documents, whether they are published or not. The documents may come from teaching and research institutions in France or abroad, or from public or private research centers.

L'archive ouverte pluridisciplinaire **HAL**, est destinée au dépôt et à la diffusion de documents scientifiques de niveau recherche, publiés ou non, émanant des établissements d'enseignement et de recherche français ou étrangers, des laboratoires publics ou privés.

THÈSE
PRESENTÉE PAR

Susana Pacheco Vázquez

POUR OBTENIR LE TITRE DE DOCTEUR
DE L'UNIVERSITÉ JOSEPH FOURIER - GRENOBLE 1

SPÉCIALITÉ ASTROPHYSIQUE

**UNBIASED SPECTRAL
SURVEY TOWARDS THE
INTERMEDIATE-MASS CLASS
0 PROTOSTAR CEP E-MM**

DATE DE SOUTENANCE: 11/12/2012

COMPOSITION DU JURY:

	Président
Claudio CODELLA	Rapporteur
Serena VITI	Rapporteur
Valentine WAKELAM	Examineur
Claudine KAHANE	Examineur
Cecilia CECCARELLI	Directeur de thèse
Bertrand LEFLOCH	Co-directeur de thèse

THÈSE PRÉPARÉE AU SEIN DE L'INSTITU DE
PLANÉTOLOGIE ET ASTROPHYSIQUE DE GRENOBLE

Observatoire de Grenoble, UJF/CNRS, BP 53? F-38041 Grenoble CEDEX 9

Contents

Contents	iii
List of Figures	vii
List of Tables	xix
Introduction	xxi
1 Star formation and ejection phenomena	5
1.1 Molecular clouds	6
1.1.1 Giant molecular clouds	6
1.1.2 Dark clouds	7
1.1.3 Turbulence and the evidence for magnetic field in molecular clouds	7
1.2 The overall picture of low-mass star formation	8
1.2.1 Fragmentation and pre-collapse phase	10
1.2.2 First phase of the collapse	13
1.2.3 Accretion phase	15
1.2.4 YSOs classification	16
1.2.5 Outflow phase	18
1.3 The overall picture of the intermediate and high-mass star formation	19
1.3.1 Global properties	19
1.3.2 Formation schemes	20
1.3.3 Chemical properties	21
1.4 Observations of outflows	22

1.4.1	The importance of the outflow phenomenon	24
1.4.2	H ₂ emission	24
1.4.3	Radio continuum	25
1.4.4	Outflow chemistry	26
1.4.5	Herbig-Haro objects	29
1.5	Theory of the outflow phenomenon	31
1.5.1	Origin and structure of the outflows	31
1.5.2	Outflow Models	33
1.5.3	J versus C shocks: structure and chemistry	36
2	Radio observations	41
2.1	The first steps of Radioastronomy	41
2.2	Some basic concepts	44
2.2.1	The radiative transfer	45
2.2.2	Antenna and brightness temperature	46
2.2.3	The beam	47
2.2.4	The signal and the receiver	49
2.3	Observing below the atmosphere	51
2.3.1	Atmopheric transmission	51
2.3.2	Calibration procedure	54
2.3.3	Spectral line Observations	56
2.3.4	Single-dish IRAM-30m telescope	58
2.3.4.1	Receivers and backends	61
2.3.4.2	Software	63
2.4	Observing above the atmosphere	63
3	The source: Cep E-mm	67
3.1	The Cep E molecular cloud	67
3.2	The Cepheus E-mm source	69
3.2.1	The dusty envelope	69
3.2.2	Single or binary protostar	72
3.2.3	Chemical properties	73
3.3	Cepheus E bipolar outflow	74

3.4	HH 377	80
3.5	Shock models of Cep E	82
4	The spectral survey of Cep E	87
4.1	Introduction	87
4.2	Kinematics and morphology of the outflow	89
4.3	Observations	89
4.3.1	Data calibration	93
4.3.1.1	Atmospheric calibration	93
4.3.1.2	Spurious features	95
4.3.2	Errors	96
4.4	Results	98
4.5	Line identification	100
4.6	Rotational diagrams	105
4.7	Overview of the chemical structure of the envelope	105
4.8	Molecular deuteration	108
5	The jet of Cep E	177
5.1	The jet molecular tracers	177
5.2	Derivation of the column density	183
5.2.1	Rotational diagrams	183
5.2.2	Non-LTE LVG analysis	187
5.2.3	North-MV component	188
5.2.4	North-HV component	189
5.2.5	South-EHV component	190
5.3	Discussion	192
5.3.1	Comparison with other outflow sources	192
	Summary and conclusions	195
	A Population Diagram	199
	B LVG or Sobolev approximation	203
	References	207

List of Figures

1.1	Before the 80's, the collapse was treated in the spherical symmetry approximation (<i>left panel</i>). With the discovery of the outflow phenomena and circumstellar disks, it was clear that the spherical approximation was not valid and a new paradigm (<i>right panel</i>) emerged.	8
1.2	Stages of the low-mass star formation process. Taken from Hogerheijde 1998 after Shu et al 1987.	10
1.3	Fragmentation is a multi-scale process from spiral arms of a galaxy down to protostars whose characteristic lengths spanning from 10 kpc to 100 AU. Taken from [Schulz, 2005]	11
1.4	Column density map of Aquila derived from SPIRE/PACS data from the Gould Belt Survey carried out by Herschel Space Observatory. The candidate Class 0 protostars and bound prestellar cores identified in Aquila by [Bontemps et al., 2010] and [Könyves et al., 2010] are shown as green stars and blue triangles, respectively. Note the good correspondence between the spatial distribution of the cores and protostars and the regions where the filaments are unstable to gravitational collapse. For more details see [André et al., 2010].	12
1.5	Evolutionary sequence and spectral energy distributions of low-mass YSOs as proposed by André (1994). The four classes 0, I, II, and III correspond to successive stages of evolution. Adapted from [Feigelson and Montmerle, 1999].	17

- 1.6 *(top)* Interferometer map of the molecular jet in the HH211 outflow. The CO J=2–1 line (white lines) [Gueth and Guilloteau, 1999] is overlaid on a false color image of H₂ [McCaughrean et al., 1994]. The red lines delineate the 230 GHz continuum emission from dust concentration around the protostar. *(bottom)* In color scale we see the near infrared H₂ emission, in contours blue and red there are the blue- and red-shifted emission of SiO (8–7), the green contours mark the dust emission at 870 micron surrounding the protostar. [Lee et al., 2007] 23
- 1.7 Gray scale of the 2.12 μm S(1) line emission from molecular hydrogen. The cross marks the position of the IRAS 23011+6126 central source. Taken from [Ladd and Hodapp, 1997]. 25
- 1.8 Overabundance factors with respect to dense core values for a number of molecules towards the outflows from L1448-mm and IRAS 04166+2706. Data from Tafalla et al. (2010). Taken from [Tafalla and Bachiller, 2011] 26
- 1.9 *left:* CO 2→1 emission from the L1157 outflow. *right:* Maps of integrated intensity for different molecular species towards the blue (southern) lobe of the L1157 outflow. Note the different extension and peak position of each species. Taken from [Bachiller and Perez Gutierrez, 1997]. 28
- 1.10 HH 1/2. These are among the brightest HH objects in the sky, they form bow shocks in a highly collimated bipolar outflow with dimension of 2.5 arsec (0.34 pc), symmetrically opposite from a young star which is ejecting material along its polar axis. 30

1.11	Several types of outflows are observed in low-mass YSOs. High velocity and very collimated jets are mainly observed in Class 0 sources. The figure indicates the trend that outflow collimation decreases with the age. Similarly the flow velocity (several hundreds km s^{-1}) decreases from the jet to the outer edges of a disk wind ($\approx 5 \text{ km s}^{-1}$). The process that originates the outflows is still not fully understood, but it seems that magnetic fields and rotation trigger the jet launching mechanism. Taken from [Schulz, 2005]	32
1.12	Observable molecular outflow properties predicted by the four leading broad classes of models: 1) turbulent jet [Canto and Raga, 1991]; 2) jet bow shock [Raga and Cabrit, 1993]; 3) wide-angle wind [Shu et al., 1991]; and 4) circulation models [Fiege and Henriksen, 1996b]. Taken from [Arce et al., 2007].	35
1.13	The postshock temperature structure of a fast shock. Taken from [Hollenbach and McKee, 1989]	36
1.14	The structure of J shocks.	37
1.15	The structure of C shocks.	38
2.1	In 1931 Karl Jansky built the first radiotelescope. This 14.6 meter rotatable, directional antenna system was designed, to investigate interference problems on long distance communication circuits. Using this antenna, Jansky was able to make the first positive identification of radio waves of extra-terrestrial origin.	43
2.2	Schematic diagram which shows how the specific intensity is defined.	45
2.3	Schema of an antenna pattern.	49
2.4	Typical radio telescope, a large parabolic antenna collects incoming radio waves and focuses them onto a smaller antenna called the feed horn. The signal is then carried to the radio receiver.	50

2.5	Top Atmospheric transmission of the Earth’s atmosphere for electromagnetic radiation. Bottom Radiation transmitted by the atmosphere between 0.2 and 70 μm . The pannel shows the absorption bands in the Earth’s atmosphere and above the individual absorption spectrum for major greenhouse gases plus Rayleigh scattering.	53
2.6	IRAM30–m antenna at Pico Veleta in Spain.	58
2.7	Gain elevatin dependence.	60
2.8	Overview of EMIR bands. Possible band combinations: E090, E150, E230, E330, E090&E150, E090&E230 and E150&E330. . .	62
2.9	Atmospheric transmission for 2mm and 4mm of precipitable water vapors at IRAM 30m. The EMIR and HERA bands are marked together with the frequencies of a few important molecular transitions.	62
2.10	Herschel space observatory.	64
3.1	The Cepheus OB3 active star formation region overlaid on the map of visual extinction, obtained from 2MASS [Lombardi and Alves, 2001]. Large circles denote the clouds associated with young stars. The meaning of the different symbols are as follows: Filled triangles are T Tauri stars, filled squares are Herbig Ae/Be stars, filled circles are weak-line T Tauri stars, open squares are photometric candidate and possible PMS members, X are H_α emission stars, crosses are T Tauri candidates. For details see [Kun et al., 2008]. . .	68
3.2	Cep OB3b region. In the image the molecular clouds Cep A to Cep F, the dark cloud Lynds 1211, as well as the most prominent associated young stars are labeled. In contours the distribution of the visual extinction [Dobashi et al., 2005]. The lowest contour of the extinction is at $A_V = 1$ mag, and the increment is 0.7 mag. For details see [Kun et al., 2008].	68
3.3	Spectral energy distribution of Cep E-mm (IRAS 23011+6126) source observed and modeled. Taken from [Crimier et al., 2010]. . .	70

-
- 3.4 Cep E-mm dust temperature (*left panel*) and H₂ density (*right panel*) profiles from the best-fit model. For details see [Crimier et al., 2010]. 70
- 3.5 (*left*) HiRes (Spitzer) maps of the inner 10'' region around the Cep E protostar. The crosses represent the positions of the mm double source from [Moro-Martín et al., 2001]. Taken from [Velusamy et al., 2011]. (*right*) Superposition of the H₂ 1-0 S(1) 2.12 μm emission (gray scale) on the ¹³CO and 222 GHz continuum in contours. The dashed contours toward the north correspond to the redshifted lobe ($v_{LSR} = -9.5$ to -2.5 km s⁻¹), while the solid contours to the south correspond to the blueshifted lobe ($v_{LSR} = -20.5$ to -13.5 km s⁻¹). Note that the 222 GHz continuum trace a double component. Adapted from [Moro-Martín et al., 2001]. 73
- 3.6 (*top*) Model 1: In the first panel shows the standard chemical model for Cep E assuming a binding energy of 1100 K. The C¹⁸O abundance is shown in black, N₂H⁺ in red, and N₂D⁺ in blue. In the center; comparison between the predicted C¹⁸O 1 → 0 line intensities (continuous line) and the observed values (filled squares). At the right: the same for N₂H⁺ 1 → 0. (*middle top*) Model 2. (*middel bottom*) Model 3 (*bottom*) Model 4. Taken from [Alonso-Albi et al., 2010]. 75
- 3.7 K' band image of the Cep E region in a ~ 8' × 3' field. In the center of the image we see the double lobe morphology of the Cep E outflow. Taken from [Hodapp, 1994]. 76
- 3.8 Contour plot of Cep E in H₂ 1-0 S(1) emission line. The solid line trace the precession model plotted over the 1-0 S(1) line contours of Cep E that can explain the wiggle structure in the southern lobe and the regular sideways positional offsets of the bows of the northern lobe. Taken from [Eisloffel et al., 1996]. 77

- 3.9 $^{12}\text{CO}(2-1)$ emission at three different positions respect to the reference position of the IRAS 23011+6126 source. The *top* panel shows line emission comes from north lobe, a first component is centered at the ambient velocity ($\approx -11 \text{ km s}^{-1}$) and it extends to red velocities up to reach a second component that peak at about 50 km s^{-1} . The *middle* panel shows emission comes from the central source, the spectrum display a main component centered at ambient velocity and weak emission comes from the blue-shifted velocities. The *bottom* panel exhibit the spectrum comes from the south lobe. It shows again a bright component at ambient velocity and a second component that peak around -125 km s^{-1} . These second components at high velocities are interpreted as evidence of the presence of jets. [Lefloch et al., 1996]. 78
- 3.10 (*left*) $\text{H}_2 1 - 0 \text{ S}(1)$ contour map shows the bipolar structure of Cep E. There are also two H_2 knots at the west of the IRAS source region labeled as W1 and W2. [Eisloffel et al., 1996] interpret these knots as a second independent outflow and, therefore, the presence of a second outflow source can be inferred. (*right*) Cep E could be a double or multiple system. In gray scale, the $2.12 \mu\text{m}$ $\text{S}(1)$ emission from H_2 overlaid to contours of redshifted [-6 to 0 km s^{-1}] (dotted) and blueshifted [-14 to -20 km s^{-1}] (solid) ^{12}CO $\text{J}= 2-1$ emission. Both maps are centered on the IRAS source. For details see [Ladd and Hodapp, 1997]. 79
- 3.11 The figure shows the 450 , 850 and $1300 \mu\text{m}$ images of the IRAS 23011+6126 region. The dust emission trace the quadrupolar outflow observed by [Ladd and Hodapp, 1997] (See text). Taken from [Chini et al., 2001]. 80

- 3.12 Panel (a) shows a H₂ 1-0 S(1) contour map overlaid with gray-scale representations of the H α image. In panel (b) again the H₂ 1-0 S(1) contour map overlaid with the [S II] $\lambda\lambda$ 6717, 6731 image. Panels (c) and (d) are closed-ups to the bowshock region. They show the H α and [S II] 6717, 6731 images (respectively) as dark contour maps, over the H₂ light contours. Taken from [Ayala et al., 2000]. 81
- 3.13 The upper panels displays the H₂ data. The lower panels displays the CO rotational fluxes. Taken from [Smith et al., 2003]. *(left)* **Planar shock models for Cep E south.** *(a)* A hot C-shock component with 32 km s⁻¹ provides a fit to the vibrationally excited columns but does not contribute to the CO rotational lines. *(b)* A cool C-shock with speed 11 km s⁻¹ provides a fit to the rotationally excited H₂ and CO but does not contribute to the vibrational lines. *(right)* **C-type bow shock model for Cep E South 1** with speed 120 km s⁻¹. In all the cases the density is 10⁵ cm⁻³. The H₂ models values are displayed for the ground (*solid line*), first (*dashed line*) and second (*dot-dashed line*) vibrational levels. 84
- 3.14 The upper panels displays the H₂ data. The lower panels displays the CO rotational fluxes. Taken from [Smith et al., 2003]. *(left)* **C-type bow shock model for Cep E North (Nd)**. The model bow speed is 120 km s⁻¹. *(right)* **J-type bow shock model for Cep E North (Nd)** with shape parameter s=1.5 and a speed of 60 km s⁻¹. 85
- 4.1 CO (2-1) velocity maps taken with PdB toward Cep E region. *(top)* The cross mark the position of the central source. The gas emission comes from two main components, the cavity between 30 and 45 km s⁻¹ and the jet between 50 and 80 km s⁻¹. *(bottom)* Cep E south jet, the emission comes mainly from the gas between -100 and -130 km s⁻¹. 90

4.2	SiO (2-1) velocity maps taken with PdB toward Cep E region. Clearly the emission at positive velocities comes from two components, the first one around 25 and 45 km s^{-1} and the second one between 50 and 70 km s^{-1} . At negative velocities, the emission similarly is mainly from one component between -25 and -50 km s^{-1} and a second component from -50 to -90 km s^{-1} . In this transition the EHV emission is not observed.	91
4.3	The high-velocity jet emission from CepE CO (2-1) emission map at 1" resolution obtained with the PdBI (Lefloch et al. 2011). Central position is placed at 23h03m13.0s +61°42'21" (J2000). The red circle represents the IRAM beam at 3mm, the green one at 1.3mm and the blue one at 0.8mm.	92
4.4	(left) A spectra with fluctuations in the continuum baseline, it is different to zero along the spectra. (right) The same spectra of the left but corrected, it has been removed a baseline in order to obtain a continuum close to zero.	94
4.5	Examples of spikes present in the spectra. Note that the intensity of these spikes are 4 times brighter than the emission from the lines.	95
4.6	Example of a ghost line: CS (5-4) spectra (black line) with a contamination in the wing by CO (2-1). For comparison we overplot the CS (6-5) spectra in blue.	96
4.7	Cep E CO (2-1) spectra. This image illustrates the addition of errors of each channel along the velocity interval from v_1 to v_2	97
4.8	Upper level energy distribution in the Cep E unbiased spectral survey.	98
4.9	Three kinematical components were found: the ambient gas at $\sim -10.9 \text{ km s}^{-1}$, the entrained gas between $-90 \rightarrow -12$ and $-9 \rightarrow +30$ and the jet, detected at -125 km s^{-1} (south jet) and at around $+50 \text{ km s}^{-1}$ (north jet).	99

4.10	Overview of all the detected lines in the 3 mm band from 80-116 GHz. At the <i>bottom</i> the (0,0) position and at the <i>top</i> the (-12, -18) position. The temperature axis is zoomed to appreciate the line richness in both position. Signals are in antenna temperature (K).	101
4.11	Overview of all the detected lines in the 2 mm band from 164-170 GHz. At the <i>bottom</i> the (0,0) position and at the <i>top</i> the (-12, -18) position. The temperature axis is zoomed to appreciate the line richness in both position. Signals are in antenna temperature (K).	102
4.12	Overview of all the detected lines in the 1.3 mm band from 207-260 GHz. At the <i>bottom</i> the (0,0) position and at the <i>top</i> the (-12, -18) position. The temperature axis is zoomed to appreciate the line richness in both position. Signals are in antenna temperature (K).	103
4.13	Overview of all the detected lines in the 0.9 mm band from 260-350 GHz. At the <i>top</i> the (0,0) position and at the <i>bottom</i> the (-12, -18) position. The temperature axis is zoomed to appreciate the line richness in both position. Signals are in antenna temperature (K).	104
4.14	Rotational diagrams of CO, SiO and SO. The <i>squares</i> are the data and the red line are the fit. In some cases the error bar is smaller than the symbol. The resulting column density and rotational temperature are listed in table 4.4.	106
4.15	Rotational diagrams of HCO ⁺ , HCN, CH ₃ OH and H ₂ CO. The <i>squares</i> are the data and the red line are the fit. In some cases the error bar is smaller than the symbol. The resulting column density and rotational temperature are listed in table 4.4. In the CH ₃ OH rotational diagram are grey lines that indicate that there are transitions at different E _{up} for a same frequency.	107
4.16	Some brightest ion spectra at both positions. At the <i>top</i> we show the N ₂ H ⁺ lines at the <i>middle</i> the HCO ⁺ lines and at the <i>bottom</i> the DCO ⁺ spectra. Vertical dotted line indicates the systemic velocity.	109

4.17	Assembly of the line profiles of deuterated molecules observed towards Cep E (Offset 0,0). The dash line indicates the systemic velocity.	111
4.18	Rotational diagrams of CH ₂ DOH, DCN, N ₂ D ⁺ , HDCO and D ₂ CO. The <i>squares</i> are the data and the red line are the fit. The resulting column density and rotational temperature are listed in table 4.9.	112
4.19	3 mm band taken toward Cep E region. Each line is labeled with the molecular specie (See Table 4.11). Features appearing as absorption spikes were removed because they are artifacts. Signals are in antenna temperature (K).	121
4.20	2 mm band from 164-170 GHz. Each line is labeled with the molecular specie (See Table 4.11). Features appearing as absorption spikes were removed because they are artifacts. Signals are in antenna temperature (K).	125
4.21	1.3 mm band from 207-260 GHz. Each line is labeled with the molecular specie (See Table 4.11). Features appearing as absorption spikes were removed because they are artifacts. Signals are in antenna temperature (K).	126
4.22	0.9 mm band from 260-305 GHz. Signals are in antenna temperature (K).	130
4.23	3 mm band from 80-116 GHz. Signals are in antenna temperature (K).	136
4.24	2 mm band from 164-170 GHz. Signals are in antenna temperature (K).	140
4.25	1.3 mm band from 207-260 GHz. Signals are in antenna temperature (K).	141
4.26	0.9 mm band from 260-350 GHz. Signals are in antenna temperature (K).	145
4.27	146

5.1	Spectra of the CO emission lines observed toward both positions. At the <i>left</i> (0,0) position, and at the <i>right</i> the (-12,-18) position. In both pannels the spectra of lowest transition were observed with IRAM-30m telescope and transition CO (4-3) were observed with CSO for the (0,0) offset and with JCMT for the offset (-12,-18). Intensities are in units of antenna temperature (K). A vertical offset is added to each emission line to help the comparison. The vertical <i>dotted lines</i> show the velocity range where appear the EHV component associated with the jet. (See the text).	179
5.2	SiO jet emission from both; the source and bowshock positions. A vertical offset is added to each emission line to help the comparison. The vertical <i>dotted lines</i> show the velocity range components. . .	180
5.3	HCO ⁺ jet emission from both; the source and bowshock positions. A vertical offset is added to each emission line to help the comparison. The vertical <i>dotted lines</i> show the velocity range components.	181
5.4	HCN jet emission from both; the source and bowshock positions. A vertical offset is added to each emission line to help the comparison. The vertical <i>dotted lines</i> show the velocity range components. . .	181
5.5	SO jet emission from both; the source and bowshock positions. A vertical offset is added to each emission line to help the comparison. The vertical <i>dotted lines</i> show the velocity range components. . .	183
5.6	(<i>left</i>) CO, SiO, HCN, HCO ⁺ and SO spectra at (0,0) offset with detected jet emission at high velocities. <i>Vertical dash line</i> marks the ambient cloud velocity ($\sim -10.9 \text{ km s}^{-1}$), and <i>vertical dotted lines</i> mark the velocities at 30, 50 and 80 km s^{-1} . In the range 30 to 45 km s^{-1} we have the moderate velocity component of the north jet (North-MV), and between 50 to 80 km s^{-1} we have the high velocity component (North-HV). (<i>right</i>) The same molecular transitions at (-12,-18) offset. Unlike the spectra on the left, only CO and HCO ⁺ spectra show clearly detected jet emission at South-EHV. <i>Vertical dotted lines</i> mark the velocity limits between -100 and -150 km s^{-1}	184

5.7	Rotational diagrams of CO and SiO molecules. The <i>squares</i> are the data and the red line are the fit. In some cases the error bar is smaller than the symbol. The resulting column density and rotational temperature are listed in table 5.3.	185
5.8	Rotational diagrams of SO, HCO ⁺ and HCN molecules. The <i>squares</i> are the data and the red line are the fit. In some cases the error bar is smaller than the symbol. The resulting column density and rotational temperature are listed in table 5.3.	186
5.9	Observed (red points) and best fit model predictions (green line) of the SiO lines in the North-MV (<i>left</i>) and North-HV (<i>right</i>) components (Tab. 5.1). The blue lines show the warm and dense components (marked as Component II in Tab. 5.4) while the magenta lines at the left bottom corners show the less dense and colder components (marked as Component I in Tab. 5.4.	190
5.10	Observed (red points) and best fit model predictions (green line) of the SiO lines in the South-EHV component observed towards the south lobe (Tab. 5.1). The magenta line shows the warm and dense component (marked as Component II in Tab. 5.4) while the blue line shows the less dense and colder component (marked as Component I in Tab. 5.4.	191
5.11	Comparison between the normalized CO abundances found by [Tafalla et al., 2010] (<i>red diamonds</i>) towards L1448 and our values from the LVG analysis (<i>stars</i>) for the HV I (<i>top</i>) and MV I regime (<i>bottom</i>).	193
5.12	Comparison between the normalized SiO abundances found by [Tafalla et al., 2010] (<i>red diamonds</i>) towards L1448 and our values from the LVG analysis (<i>stars</i>) for the HV I (<i>top</i>) and MV I regime (<i>bottom</i>).	194

List of Tables

2.1	The largest radio-mm-submm telescopes and interferometers to observe in radio to submm wavelengths.	52
2.2	IRAM 30m telescope parameters	59
2.3	List of some satellites that work(ed) from near-infrared to radio wavelengths.	65
3.1	Cep E protostar parameters.	69
3.2	Cep E envelope parameters calculated from different models.	71
3.3	Summary of the dust radiative transfer analysis for Cep E protostar. Adapted from [Crimier et al., 2010].	72
3.4	Summary of the Cep E outflow properties.	83
4.1	Observational parameters.	93
4.2	Frequency ranges and interpolation functions used for derive the Beff for each line frequency in the Cep E survey. The Beff values were taken from IRAM's website.	95
4.3	Component velocity limits. The jet component present two components, MV (moderate velocity) and the HV (high velocity) gas.	100
4.4	Molecular column densities and rotational temperatures derived towards Cep E for ambient velocity component (See Figs 4.14 and 4.15). The abundances are expressed respect to H ₂ and CO-normalized, i.e, $X^{\text{CO}}_4 = N/N_{\text{CO}} \times 10^4$	106

4.5	Summary of the molecules detected. The first and second columns number indicate the number of lines detected toward the central and the south position respectively. Between brackets the total number of transitions in the case of multiplets are indicated. In the third column are the reference numbers from Tables 4.11 and 4.12.	113
4.6	Summary of ions detected. Between brackets the total number of transitions in the case of multiplets are indicated. In the third column are the reference numbers from Tables 4.11 and 4.12. . . .	115
4.7	Summary of deuterated molecules detected. Between brackets the total number of transitions in the case of multiplets are indicated. In the third column are the reference numbers from Tables 4.11 and 4.12.	116
4.8	Summary of complex organic molecules detected. Between brackets the total number of transitions in the case of multiplets are indicated. In the third column are the reference numbers from Tables 4.11 and 4.12.	116
4.9	Column densities and T_{rot} derived using a rotation diagram analysis. These values are used to compute the deuterated fraction (see Table 4.10). The abundances are expressed respect to H_2 and CO-normalized, i.e, $X^{\text{CO}}_4 = N/N_{\text{CO}} \times 10^4$	118
4.10	Ratios between some of the deuterated molecules and its corresponding non-deuterated molecule. In the first column there are the values obtained in our survey towards (0,0) position. The values listed here correspond to the ambient gas component (envelope) towards offset (0, 0). See the text. The other columns show the same ratios towards Class 0 low-mass protostars, pre-stellar cores, L1157-B1 and IM protostars in order to compare our results.	118
4.11	Overview of the Cep E spectral survey, 0,0 offset	152
4.12	Overview of the Cep E spectral survey, -12, -18 offset	164
5.1	Velocity components.	178

5.2	Integrated flux intensities between 30 to 45 km s ⁻¹ (MV component) and 50 to 80 km s ⁻¹ (HV component) towards the central position, and between -100 to -150 km s ⁻¹ towards the south out-flow lobe (EHV component).	182
5.3	Molecular column densities and rotational temperatures derived by interpreting the emission between 30 to 80 km s ⁻¹ (MV and HV components together). The abundances are expressed with respect to H ₂ and CO-normalized, i.e, X ^{CO} ₄ =N/N _{CO} ×10 ⁴ . The beam dilution correction was performed considering a source size of 3" ×3".	184
5.4	Temperature, density and sizes of the velocity components of Tab. 5.1.	187
5.5	Column densities and abundances. Note: the abundances are computed assuming a CO abundance with respect to the H ₂ of 10 ⁻⁴ .	188
5.6	List of the abundance with respect to CO of the species present in L1157-B1, CepE, L1448, I04166. The abundances are expressed with respect to H ₂ and CO-normalized, i.e, X ^{CO} ₄ =N/N _{CO} ×10 ⁴ . .	192

Introduction

Intermediate-mass (IM) protostars ($2 \leq M_* \leq 8 M_\odot$) are the link between low and the high mass stars as they cover also an intermediate range of luminosities, densities and temperatures [Fuente et al., 2012]. When they are on the pre-main-sequence they are known as Herbig Ae/Be stars.

These young stellar objects (YSOs) are located in *less complex regions* than high mass star forming regions and they are in larger number *closer to the Sun* (< 1 kpc). At least in some cases, it is possible to study the physical and chemical structures at similar spatial scales as those achievable in low mass protostars. Once on the main sequence, the IM stars are among the sources that *dominate the FUV interstellar radiation field* that regulate the different phases of interstellar medium and therefore the overall Galaxy star formation process [Habing, 1968]; [Gondhalekar and Wilson, 1975]. In addition, the study of IM-YSOs is fundamental to establish the initial conditions of the *planet-formation process* around Herbig Ae/Be stars, the precursor of Vega-type debris disks [Schütz et al., 2005].

Even though the IM-YSOs are important in the study of star formation, very *little is known* about the formation and first evolutionary stages of *IM protostars*.

Unbiased spectral surveys are a powerful tool to characterize the *chemical composition* of an astrophysical object, and the only way to obtain a complete census of the chemical species. A spectral survey provides also *multiple lines* from the same molecule, giving the possibility of a multi-frequency analysis and modeling. Besides, different lines from transitions with different excitation conditions (upper level energies and Einstein coefficients) are excited at different

temperatures and densities. Therefore, they probe different physical regions in the line of sight.

Finally, through line profiles, we can obtain *kinematic information*, and identify structures along the line of sight, as *multiple sources, outflows, jets or cavities*, e.g. [Caux et al., 2011].

Several *unbiased spectral surveys*, carried out in the millimeter and sub-millimeter bands accessible from the ground, were obtained mainly toward *high-mass protostars* e.g. Orion KL [Margulès et al., 2009], [Tercero et al., 2011] and [Tercero et al., 2012], AFGL 2591, IRAS 20126+4104 [Plume et al., 2007], IRAS 23385+6053 [Thompson and Macdonald, 2003], NGC 6334 I, I(N) [Thorwirth et al., 2007] and compact HII regions as W3 IRS5, IRS4 [Kim et al., 2006], G34.3+0.15 [Kim et al., 2000], G5.89-0.39 [Thompson and MacDonald, 1999]. These targets are mainly chosen because they have bright molecular lines and a rich chemistry. On the contrary, only two *solar-type* protostars have been studied in the mm/submillimeter window: IRAS 16293-2422 ([Blake et al., 1994];[van Dishoeck et al., 1995];[Caux et al., 2011] and L1527 [Sakai et al., 2008]. A complete list of these surveys can be found in the review by [Herbst and van Dishoeck, 2009].

The *outflow phenomena* (jets, winds and bipolar molecular outflows), are an *inherent phase in the process of star formation* observed in YSOs of all range of masses at millimeter wavelengths. In the last years, *biased observational studies* were carried out towards *young protostellar outflows*, e.g. [Bachiller, 1996], [Bachiller et al., 2001], [Jiménez-Serra et al., 2004]. The latest works present unbiased surveys towards L1157-B1 with Herschel satellite as part of the key program CHESS [Lefloch et al., 2012], [Codella et al., 2012], the most studied outflow to date.

Recently, the 500-2000 GHz range was covered by the Herschel satellite as part of the key programs CHESS [Ceccarelli and CHESS Consortium, 2010] and HEXOS [Bergin et al., 2010] towards low- to high- mass star forming regions.

Up to date only few *individual IM protostars* have been studied in detail ([Hogerheijde et al., 1999]; [Neri et al., 2007]; [Schreyer et al., 2002]; [Fuente et al., 2007]; [Crimier et al., 2010]; [Lefloch et al., 2011]). However, *there are*

not systematic studies in IM range as in the case of low- and high-mass protostars.

Given the lack of a systematic study of the mm/submm spectrum of IM protostars, during my thesis I carried out an unbiased spectral survey towards Cep E and its molecular outflow.

This source was chosen because it is a nearby (distance 730 pc) young, Class 0 candidate, whose age is estimated to be in the range of $20 - 400 \times 10^3$ years [Froeblich, 2005]. It has a remarkably bright outflow ($10 L_{\odot}$) and a bolometric luminosity of $\sim 100 L_{\odot}$ [Lefloch et al., 2011].

This thesis manuscript is composed of six chapters. In *chapter 1*, I give an introduction of the process of star formation of low-, intermediate- and high-mass regimes and a general review on outflows, observationally and theoretically. In *chapter 2*, I present some fundamental concepts of radioastronomy. In *chapter 3*, I present a detailed description of the source Cep E and the studies carried out to date. In *chapter 4*, I present the spectral survey overview, together with the line catalogue. In *chapter 5*, I present the results of the jet component analysis. In *chapter 6* I will conclude the thesis.

Chapter 1

Star formation and ejection phenomena

The star formation is not a process that only occurred in the past, but it is an active process that takes place nowadays in our Galaxy even, in regions close enough, that the birth of stars can be examined in detail.

The molecular clouds are the sites where the star formation occurs. Gas in these regions is so cold (~ 10 K) that the bulk of radiation is emitted at radio and mm wavelengths. Protostars are also relatively cold ($T \leq 1000$ K) and emit in the mm to IR wavelengths.

The radio/mm astronomers use single dishes telescopes to map extended areas of the sky covered by these clouds. For a detailed study of individual regions they use interferometers, especially for observe the distribution of matter around newly formed stars.

After the 80's instrumental advances in IR and FIR detections provided the first high-sensitivity maps at infrared wavelengths. The launch of IRAS (*Infrared Astronomical Satellite*) in 1983 allowed to scan more than 96 percent of the sky at mid- and far-infrared wavelengths and provided the first census ever of protostars. Years later in 1995, ISO (*Infrared Space Observatory*), allowed to carry out higher sensitivity, and higher spectral resolution observations on a larger wavelength range than IRAS. More detailed studies have been possible thanks to the launching of Spitzer Space telescope in 2003 and recently in 2009 with Herschel

Space Observatory.

1.1 Molecular clouds

Molecular clouds get their name from the fact that they are made mainly of molecular hydrogen (H_2). Although molecular hydrogen is their main constituent, molecular clouds are detected and mapped using the second most abundant molecule, carbon monoxide (CO) because the upper energy level of the first rotational level ($J = 1$) of the molecule is only 5.5 K and then readily excited at cloud temperatures. On the contrary, the H_2 first rotational transition lies at about 500 K, making impossible to detect it at the ~ 10 K molecular cloud temperature. Thus, large-scale molecular cloud maps are usually carried out with the $J=1 - 0$ rotational transition line of the CO molecule, at a wavelength of 2.6 millimeters. The 2.6 mm transition is most readily excited by gas with number density around 10^3 cm^{-3} . However, other tracers are available to explore denser regions, for example the 3.1 mm line of CS or the 1.3 cm of NH_3 are transitions excited near to 10^4 cm^{-3} . This is because of their larger critical density.

Molecular clouds come in all sizes. In the following we briefly review the main classes of molecular clouds.

1.1.1 Giant molecular clouds

Large clouds, called, Giant Molecular Clouds (GMC), have masses in the range of $10^5 - 10^6 M_\odot$, sizes of tens of pc, temperatures about 10 - 30 K, and number densities in the order of $10^3 - 10^5 \text{ cm}^{-3}$. The 80 percent of the molecular hydrogen in our Galaxy resides in GMCs. A well-known example is the Orion molecular cloud at 450 pc of distance. Massive stars ($M_* > 9M_\odot$) are formed in this type of clouds. Recent studies suggest that Infrared Dark Clouds (IRDCs) are the cold condensations inside which massive stars form e.g., [Beuther and Steinacker, 2007], [Kauffmann and Pillai, 2010].

1.1.2 Dark clouds

Dark clouds¹ have masses and radii in the range of $10^3 - 10^4 M_\odot$ and 2 - 5 pc, respectively and they do not show high mass star formation. This kind of clouds form exclusively low and intermediate mass stars ($M_* \leq 8M_\odot$). The Taurus cloud at a distance of 140 pc, is a good example of this type of cloud.

Molecular transitions sensitive to higher densities like NH_3 ($n_{\text{crit}} \simeq 10^4 \text{ cm}^{-3}$) [Myers, 1985] have been used to examine the denser regions now called *dense cores*. These dense cores may or may not contain infrared sources in their center.

These cold ($\leq 10 \text{ K}$) and dense ($\geq 10^5 \text{ cm}^{-3}$) condensations are believed to be the first step towards the formation of low-mass stars and are called *prestellar cores* (e.g. [di Francesco et al., 2007], [Caselli, 2011]).

1.1.3 Turbulence and the evidence for magnetic field in molecular clouds

The observation of supersonic motions in molecular clouds (e.g., [Zuckerman and Palmer, 1974]) raised the question of how these motions could be supported. Supersonic motions are expected to dissipate their energy quickly in highly radiative shocks because of the very short cooling time of molecular gas or metal-rich atomic gas ([Goldreich and Kwan, 1974]).

Closely related was the issue of the support of molecular clouds (MCs) against gravitational collapse, since it was soon realized that the observed motions could not be understood as a gravitational collapse ([Zuckerman and Palmer, 1974]), although MCs contain many Jeans masses.

Theoreticians therefore formulated the hypothesis that MCs were primarily magnetically supported ([Mouschovias, 1976], [McKee and Zweibel, 1995]) i.e., $E_{\text{Gravitational}} \sim E_{\text{Kinetic}} \sim E_{\text{Magnetic}} \gg E_{\text{Thermal}}$ ([Shu, 1977]). They interpreted the observed motions as long-wavelength hydromagnetic waves ([Falgarone and Puget, 1986]). In this scenario star formation is controlled by *ambipolar diffusion*:

¹Mixed with the gas, molecular clouds contain interstellar dust grains. These particles absorb light with wavelengths smaller than their diameters ($\sim 0.1 \mu\text{m}$) and reradiate this energy in infrared wavelengths. Regions where the dust prevents the passage of visible light from background stars are traditionally known as *dark clouds*, because they trace regions of strong obscuration in optical photographs.

while the electrons and ions remain linked to the field lines, the neutral particles (mostly molecular hydrogen) do not feel the magnetic field and pass through, allowing collapse.

It was also shown that the properties of the observed "turbulence" (e.g. [Larson, 1981]) could be understood if the motions were sub-Alfvénic ([Mouschovias and Psaltis, 1995], [Xie, 1997]).

Studies based on the Zeeman effect in lines of molecules such as OH and CN, which probe regions of dense gas, resulted in measures of the magnetic field of a few to a few tens of μG for regions with densities of $\sim 10^4 \text{ cm}^{-3}$ ([Troland and Crutcher, 2008]) and lower, $\sim 0.5 \mu\text{G}$, in dense regions (e.g. [Falgarone et al., 2008]; [Crutcher et al., 2010]).

The next section will describe, in a general way, the process that leads to low-mass and high-mass star formation.

1.2 The overall picture of low-mass star formation

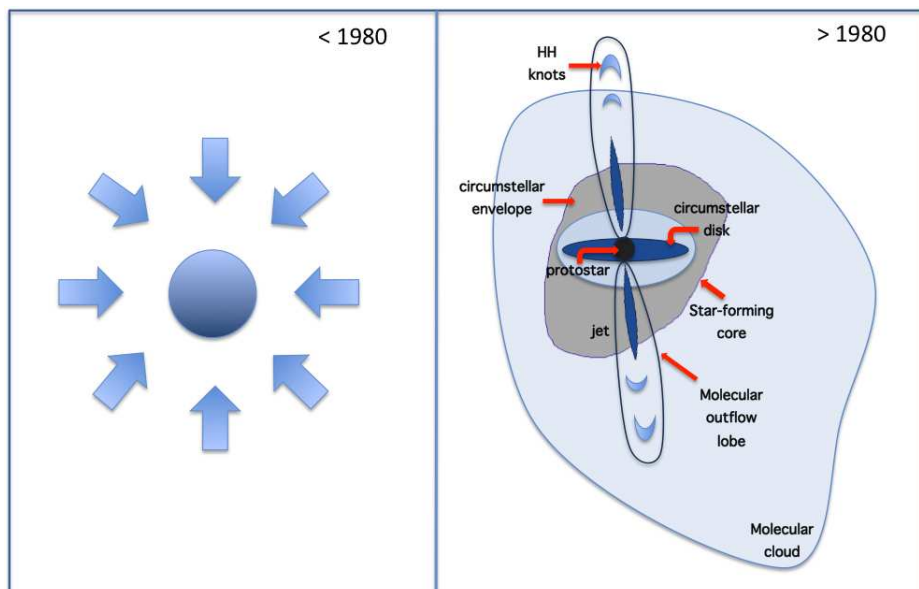


Figure 1.1: Before the 80's, the collapse was treated in the spherical symmetry approximation (*left panel*). With the discovery of the outflow phenomena and circumstellar disks, it was clear that the spherical approximation was not valid and a new paradigm (*right panel*) emerged.

The multiple observational studies towards region of star formation demonstrate that a variety of stars of different masses from 0.1 to $<100 M_{\odot}$ continuously form. But what is the sequence of events that brings a molecular cloud condensing into a star? and what are the right conditions to trigger the star formation process?

A breakthrough in terms of theoretical modeling of the stellar formation process was the work by Larson in 1969. Using numerical models, Larson was able to simulate, for the first time, all the evolution process, from a fragment of interstellar cloud of gas to a pre-main-sequence object. Larson simplified the problem and modeled the evolution of a molecular cloud fragment with spherical symmetry without rotation or magnetic field and initially homogeneous and isothermal, for different values of its mass. The initial conditions for the models were determined in a way that the initial molecular spheres were just at the point to become unstable, according to the criterion of Jeans.

A second major milestone was achieved by Shu (1977), who developed a "self-similar collapse" theory. Shu found a semi-analytical solution for a sphere in isothermal collapse. He described the collapse like non-homologous, i.e., in his model the central parts of the sphere collapse earlier than the outer parts introducing pressure gradients. In practice, the inner parts collapse first and the outer parts remain in hydrostatic equilibrium until they are reached by the outward propagating expansion wave that moves at the speed of sound. This type of collapse is known like *inside-out collapse*.

However, in the 1980s, it was soon realized that this simplistic view had fundamental problems and was not in agreement with the new observed phenomena like circumstellar disks, outflows, and multiple star formation. The spherical symmetry was then abandoned (Fig.1.1). The mass ejection phenomenon was first discovered through detection of the Doppler shift in the CO line towards the Orion Nebula in the BN-KL region [Kwan and Scoville, 1976], where, high-velocity gas is streaming away from the infrared star. In the vicinity there is also copious near-infrared emission from H_2 , resulting from collisional excitation of the molecule in shock fronts, and interstellar masers, small regions of strongly beamed radiation from molecules such as H_2O .

Several stages have been proposed (e.g., [Andre et al., 1993], [Lada and Wilk-

ing, 1984]) to describe the process of the birth of a star, but any classification scheme necessarily has a degree of arbitrariness. The following sections present the main stages involved in the low-mass star formation process (Fig.1.2).

1.2.1 Fragmentation and pre-collapse phase

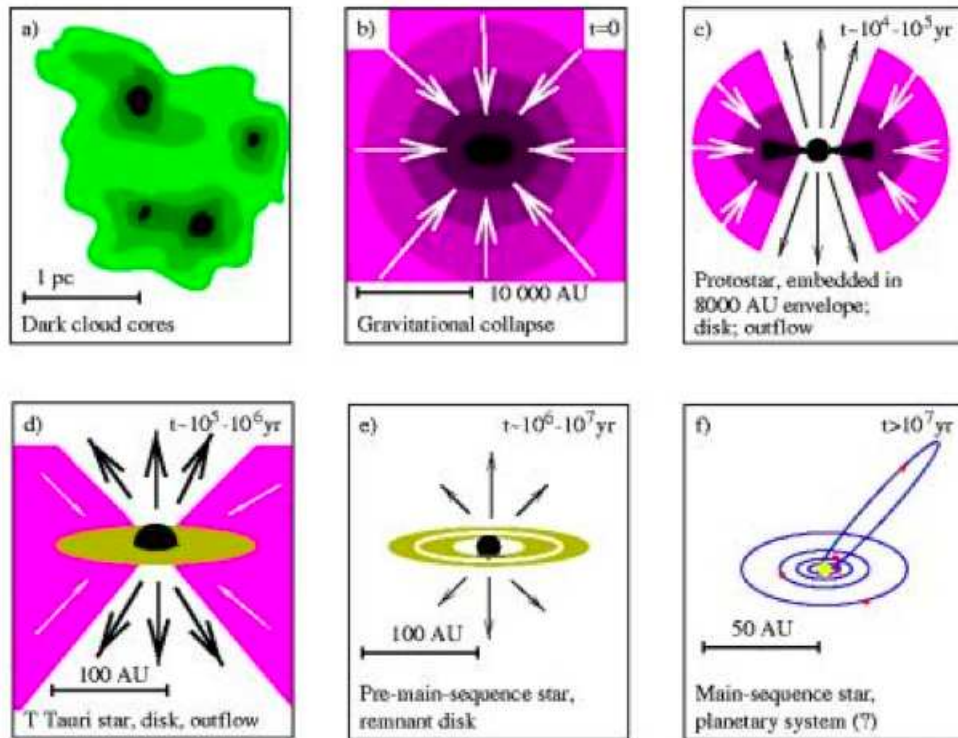


Figure 1.2: Stages of the low-mass star formation process. Taken from Hogerheijde 1998 after Shu et al 1987.

Stars are formed by the gravitational contraction of interstellar molecular gas, but as the mass of a molecular cloud is much larger than a single star, it is obvious that a star does not originate from the collapse of a cloud as a whole. There is a hierarchical and multiscale process [Efremov and Elmegreen, 1998], called *fragmentation*, in which the parent cloud breaks up into substructures like filaments or subclouds, which might themselves break into smaller and denser structures, like cores (Fig.1.3).

Starless cores represent the initial condition of (low-mass) star formation, prior to protostars, and if they are also gravitationally-bound (cf. [Andre et al., 2000];

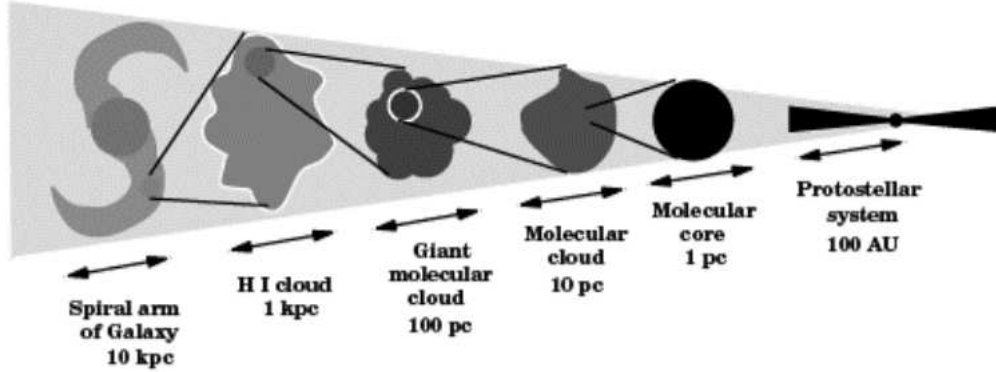


Figure 1.3: Fragmentation is a multi-scale process from spiral arms of a galaxy down to protostars whose characteristic lengths spanning from 10 kpc to 100 AU. Taken from [Schulz, 2005]

[di Francesco et al., 2007]) they are known as *prestellar cores* [Caselli, 2011].

A large number of pre-stellar condensations have been observed, both in molecular line tracers of dense gas such as NH_3 , CS , N_2H^+ and HCO^+ (e.g. [Caselli et al., 1999], [Benson and Myers, 1989], [Caselli, 2011]) and in (sub)millimeter continuum (e.g. [Motte et al., 1998], [Commercon et al., 2012]). The density peaks at about $\sim 10^5 - 10^6 \text{ cm}^{-3}$ following a flat inner profile e.g., [Ward-Thompson et al., 1994], [Motte et al., 1998]. It is believed that prestellar cores result from the gravitational fragmentation of filaments in the cold ISM (Fig.1.4) (e.g., [Könyves et al., 2010]; [Bontemps et al., 2010]; [Men'shchikov et al., 2010]; [Ward-Thompson et al., 2010]).

The dense cores are made of a few M_\odot , have diameters of about 10^4 AU , $T \leq 10 \text{ K}$ and $n(\text{H}_2) \geq 10^4 \text{ cm}^{-3}$. Abundances of C-bearing molecules drops towards the center while N-bearing species seem to survive (NH_3 enhanced) [Bacmann et al., 2002], [Tafalla et al., 2002], [Jørgensen et al., 2004]. This is consistent with the selective freeze out of molecules onto cold dust grains as the gas becomes centrally concentrated during core formation [Tafalla et al., 2004]. CO freeze-out is particularly important as the depletion of CO from the gas and the low temperatures favor the *extreme molecular deuteration* [Ceccarelli et al., 2007], [Bacmann et al., 2002].

Despite the last decade advances in the comprehension of the pre-stellar phase, there are still questions to answer. Why are clouds so fragmented but still so close to Virial Equilibrium? ([Sadavoy et al., 2012], [Dib et al., 2007]) Why do they

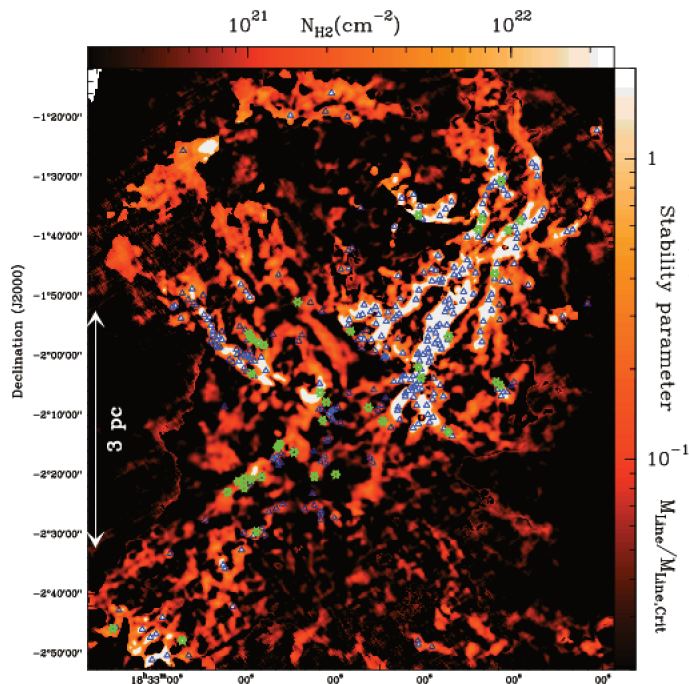


Figure 1.4: Column density map of Aquila derived from SPIRE/PACS data from the Gould Belt Survey carried out by Herschel Space Observatory. The candidate Class 0 protostars and bound prestellar cores identified in Aquila by [Bontemps et al., 2010] and [Könyves et al., 2010] are shown as green stars and blue triangles, respectively. Note the good correspondence between the spatial distribution of the cores and protostars and the regions where the filaments are unstable to gravitational collapse. For more details see [André et al., 2010].

produce a small fraction of dense cores? What is the mechanism that generates the observed clumpy structure in molecular clouds? Part of the answers could be in the small density fluctuations in molecular clouds that are amplified by their self-gravity. Or, alternatively, because of the turbulent nature of supersonic motions in molecular clouds, it has been suggested that dense structures such as filaments and clumps are formed by shocks in a turbulent flow [Padoan et al., 2001]. Turbulence, as gravity is a multiscale phenomenon in which the kinetic energy cascades from molecular clouds down to cores e.g. [Ballesteros-Paredes et al., 2007], [McKee and Ostriker, 2007]. The signature of turbulence is its contribution to thermal broadening of linewidths of molecular lines, the velocity distribution is gaussian.

Almost certainly, both gravity and turbulence play important roles in the fragmentation process from molecular clouds into the observed dense star-forming clumps (e.g. [Klessen, 2001], [André et al., 2011])

Recent results obtained with Herschel Space Observatoty (HSO) suggest that core formation occurs in two main steps: (1) Filaments form first into cold ISM, probably as a result of the dissipation of MHD turbulence . (2) The densest filaments fragment into prestellar cores via gravitational instability. This is consistent with the view that filaments form as a result of turbulent compression in low-velocity shocks. [Padoan et al., 2001]. However this is still widely debated.

1.2.2 First phase of the collapse

If the clumps in molecular clouds are the sites of star formation, what conditions must exist for collapse to occur? and what are the physics that induces and maintains collapse?

Classically, the main force counteracting gravitational collapse is thermal pressure. This sets a minimum mass that a cloud with density n , and temperature T must has to overcome pressure and to collapse. This minimum mass is called Jean Mass, M_J :

$$M_J = 1.6 \left[\frac{T}{10\text{K}} \right]^{1.5} \left[\frac{10^5 \text{cm}^{-3}}{n} \right]^{0.5} \tag{1.1}$$

The Jean mass M_J associated with the average conditions of a clump is a few M_\odot , much smaller than the mass of a clump $M_{cl} \sim 10^4 M_\odot$ [Kramer et al., 1998]. Therefore, the rate of star formation should be higher than observed (1-4 $M_\odot \text{yr}^{-1}$). If star formation takes place in molecular clouds, then the overall rate of star formation in the Galaxy is expected to be roughly the total mass in molecular clouds ($2 \times 10^9 M_\odot$) divided by their free-fall time ($4 \times 10^6 \text{yr}^{-1}$) but this gives a higher rate ($5 \times 10^2 M_\odot/\text{yr}$) of star formation than observed. Thus some other source of support, besides thermal pressure is required to prevent the molecular clouds from collapse. This conclusion is supported by the fact that the widths of spectral lines in molecular clouds are far broader than one would expect from thermal effects alone.

These alternative mechanisms of support might be, magnetic fields (e.g. [Chandrasekhar and Fermi, 1953], [Shu et al., 1987], [Mouschovias, 1987], rotation (Field 1978), or turbulence, e.g. [Larson, 1981], [Ballesteros-Paredes et al.,

2007] and [Ostriker, 2009]. As said in section 1.1.3 turbulence and magnetic fields play a key role in counteracting the gravitational force. Three cases are possible, as follows:

1. Low-mass cores are *magnetically subcritical*, namely magnetic effects prevent the collapse and support the molecular clouds. The onset of the collapse began in the densest regions, controlled by ambipolar diffusion. The characteristic timescale of ambipolar diffusion (τ_{AD}), i.e., the time required for neutrals to move a distance R against the ions is given by:

$$\tau_{AD} \simeq 2.5 \times 10^6 \text{ yr} \left(\frac{n_H}{10^2 \text{ cm}^{-3}} \right)^2 \left(\frac{B}{3 \mu G} \right)^{-2} \left(\frac{R}{1 \text{ pc}} \right)^2 \left(\frac{\chi}{10^{-6}} \right) \quad (1.2)$$

where χ is the ionization fraction, B is the magnetic field and n_H is the hydrogen density.

This ambipolar diffusion timescale is several times longer (10^7 yr [Tassis and Mouschovias, 2004]) than the dynamical contraction timescale or free-fall timescale (i.e., collapse governed by self-gravity in the absence of thermal pressure), given by

$$t_{\text{ff}} = \left(\frac{3\pi}{32G\rho_c} \right)^{1/2} \quad (1.3)$$

where $G = 6.674 \times 10^{-8} \text{ cm}^3 \text{ g}^{-1} \text{ s}^{-2}$ is the gravitational constant and ρ_c the initial density of the core, assumed to be a uniform sphere.

$$t_{\text{ff}} \simeq 0.5 \times 10^6 \text{ yr} \left(\frac{n}{10^4 \text{ H}_2 \text{ cm}^{-3}} \right)^{3/2} \quad (1.4)$$

Thus, the magnetic flux of the cloud is not be lost during the dynamical contraction (\simeq free-fall).

2. Star formation controlled by *turbulence*. Supersonic turbulence generates a complicated shock pattern. Randomly produced shock-compressed regions of high density can occasionally reach the point of instability to collapse. The time scale is shorter than the first one, about 10^6 yr.

3. Cores that are intrinsically stable are induced to collapse by a *external event* that trigger the collapse, such as a ionization front, a supernova shock wave, or a cloud-cloud collision. The time scale is the shock crossing time, which could be as short as 10^5 yr.

Finally, once magnetic forces have become dynamically unimportant, turbulence has weakened, and rotational effects have become unimportant relative to gravity in the core of the molecular cloud, and the mass of the core exceeds the Jeans mass, the gravitational collapse proceeds, the first seed of the star has been formed.

Protostellar collapse can be divided in two phases (e.g., [Larson, 1969]). (1) Isothermal phase; initially, when the collapsing fragment is optically thin to the infrared radiation of the grains, the temperature stay stable, around 10K. This phase is the result of the balance between the heating of the gas by compression and cosmic rays and, the grain and molecular cooling. The gravitational energy is all radiated away, so the thermal energy is well below gravitational energy. (2) Adiabatic phase begins once the gas collapses to the point to reach a density high enough to become optically thick. Now the gravitational energy heat the gas and the pressure increases rapidly, and the collapse slow down. However, once the central temperature has reached about 2000 K, the molecular hydrogen dissociates and the collapse resumes, because much of the gravitational energy is used to dissociated hydrogen molecule and not to increase the thermal pressure. The collapse continues until the dissociation is complete at the center and an amount of material comes into hydrostatic equilibrium, forming a protostellar core surrounded by an envelope of gas and dust.

1.2.3 Accretion phase

This phase involves the collapse of the remaining envelope onto the protostellar core. The principal source of energy of the protostar is the kinetic energy of the material infalling into the accretion shock. The accretion shock is generated by the supersonically infalling material striking the disk orbiting the protostar [Hollenbach et al., 1995].

The presence of a central source of energy produces the heating of the inner

regions of the envelope. Therefore, the molecules that were frozen onto the grains in form of ice mantles evaporate back to the gas phase forming a region with a gradient in its chemical composition called *Hot corino*, [Bottinelli et al., 2004], [Bottinelli et al., 2007] (for the low-mass case, the counterpart for the high-mass protostars is called *Hot core*).

Knowing the density and temperature profiles it is possible to understand which are the processes involved in the star forming process. Dust and density profiles are consistent with free fall motions in Class 0 protostars (e.g., [Chandler et al., 1998], [Ceccarelli et al., 2000], [Jørgensen et al., 2002], [Schöier et al., 2002]). Through observation of different species we can constrain models to know the chemical composition across the envelope to understand the physical status of the gas and the history of the protostar.

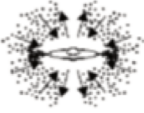
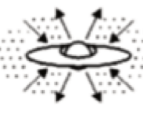



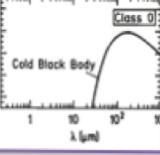
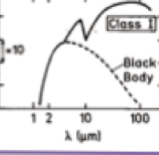
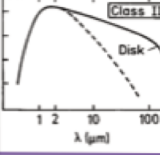
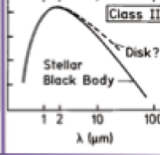
1.2.4 YSOs classification

During the collapse of the core, the dusty, cool and optically-thick collapsing layers absorb the radiation from the accretion (UV range) and re-radiate in the infrared region of the spectrum, so that the protostar becomes a bright observable infrared source.

This is why young stellar objects (YSOs) have been classified observationally by their near infrared-millimeter spectral energy distributions [Lada, 1987], [Andre et al., 1993] as, Class 0, Class I, Class II and Class III, as summarized in Figure 1.5.

The youngest observed YSOs are the Class 0 sources, with an age of about 10^4 yr [Andre et al., 2000], [Evans et al., 2009]. This age is based on the statistical detection rate. This kind of sources show (1) Indirect evidence of a central YSO, as indicated by, e.g., the detection of compact cm radio continuum emission or the presence of a collimated CO outflow. (2) Centrally peaked but extended submillimeter continuum emission tracing the presence of a circumstellar dust envelope. (3) High ratio of submillimeter to bolometric luminosity $L_{\text{submm}}/L_{\text{bol}} \gg 0.5\%$, where L_{submm} is measure longward than $350\mu\text{m}$. This ratio means that Class 0 protostars are still surrounded by a dense circumstellar envelope more massive than the central protostellar core.

Figure 1.5: Evolutionary sequence and spectral energy distributions of low-mass YSOs as proposed by André (1994). The four classes 0, I, II, and III correspond to successive stages of evolution. Adapted from [Feigelson and Montmerle, 1999].

PROPERTIES	<i>Infalling Protostar</i>	<i>Evolved Protostar</i>	<i>Classical T Tauri Star</i>	<i>Weak-lined T Tauri Star</i>	<i>Main Sequence Star</i>	
SKETCH						
AGE (YEARS)	10^4	10^5	$10^6 - 10^7$	$10^6 - 10^7$	$> 10^7$	
mm/INFRARED CLASS	Class 0	Class I	Class II	Class III	(Class III)	
DISK	Yes	Thick	Thick	Thin or Non-existent	Possible Planetary System	
SED						

The Class I sources, classified by [Lada, 1987], are detected in the near-infrared ($\lambda \approx 2 \mu\text{m}$) and have only moderate submillimeter emission. They have ages of about 10^5 yr and they are interpreted as more evolved protostars, where much of the material in the envelope has accreted onto the disk or to the central protostar. Observationally they present an optically thick disk and a residual circumstellar envelope. Outflow activity is still present but with a larger opening angle and a lower mass-loss rate than at the Class 0 stage [Bontemps et al., 1996], [Saraceno et al., 1996].

The Class II and III correspond to the pre-main sequence stars, e.g. T Tauri stars, with ages of approximately $10^6 - 10^7$ yr. In these two classes, the protostar has a prominent circumstellar accretion disk. Class II protostars are surrounded by an optically thick disk while, Class III protostars have an optically thin disk at $\lambda \leq 10 \mu\text{m}$. Class II and III objects no longer have a dense circumstellar

envelope and thus they are observable in the visible. They correspond to the T-Tauri stars. The youngest members of these classes drive outflows, and all drive strong winds with $\dot{M} \approx 10^{-7} M_{\odot} \text{yr}^{-1}$ and $v_w \approx 200$ km/s. When Class II sources are unobscured, they can be placed on the Hertzsprung-Russell diagram and compared with theoretical evolutionary tracks.

1.2.5 Outflow phase

The outflow phenomenon is associated to the star formation process, and it is observed in YSOs of nearly all masses e.g. [Lada, 1985], [Shepherd, 2003], from below the brown dwarf limit (e.g. [Whelan et al., 2011]) to the precursor of the ultra-compact HII regions (e.g. [Codella et al., 2004]), and in environments as different as isolated globules ([Froebrich et al., 2005]) and cluster-forming regions (e.g. [Zhang et al., 2001]).

As a protostar accretes, the bipolar outflow phase starts, making the collapse possible as it takes away the excess of angular momentum of the accreting material. In fact, even the relatively small-scale molecular cloud cores have far too much angular momentum to be able to collapse to stellar dimensions. Various physical effects can contribute to the solution of this problem but all these mechanisms are still heavily debated, as well as the role of the magnetic fields. One is the fragmentation of the core into a binary or multiple system, where much of the angular momentum goes into orbital motions. Another one is the collapse of the cloud onto a central stellar object surrounded by an orbiting disk, which contains most of the angular momentum. Whatever, it is clear that the removal of angular momentum by outflows is a key process.

In fact, outflows from Class 0 sources are particularly powerful [Saraceno et al., 1996] in comparison with the more evolved protostars.

Observationally and theoretically there are several explanations proposed, and still debated about the origin of the outflows. One possibility is that they are formed from the ambient gas entrained progressively by the ejected jet powered by the central protostar. However, the physics of the driving mechanism of the jet is not yet well understood. (To read more about outflows, see section 1.5.1)

1.3 The overall picture of the intermediate and high-mass star formation

The current picture of low-mass star formation is quite well established and understood, both, observationally and theoretically. There were attempts to extend the same paradigm to the intermediate and high mass star formation. However, it was found that protostars of higher masses likely evolve differently from those of low mass. There are still a lot of uncertainties on how intermediate and high-mass protostars form.

1.3.1 Global properties

High-mass forming stars should be easy to observe because they are very bright, but observations are difficult because massive star forming sites are far away, they are relatively few in number and the evolutionary time scales are shorter than those of low-mass protostars. Typically, they are found at distances of some kiloparsecs from the Sun limiting the spatial resolution [Qiu et al., 2008]. Massive star formation occurs in dense clusters (e.g. [Beuther et al., 2011]), so at their large distances its difficult to resolve the individual features of their formation. In addition, massive stars destroy their natal environment via HII regions.

The intermediate-mass (IM) protostars are objects between 2 and 8 M_{\odot} . The Class II and III sources are classified as Herbig Ae/Be stars (Herbig, 1960). We can differentiate two groups of IM protostars: those with masses between 2 and 5 M (the so called Herbig Ae stars), and between 5 and 8 M (Herbig Be stars). The formation of Herbig Ae stars shows similarities with low-mass or T Tauri stars. In fact, in these objects, the mass accretion phase of the protostar occurs prior to (and independently from) its contraction towards the main sequence. The relatively slow evolution during some tenths of million years simplify the study of these objects, since they soon disperse the parent cloud and become visible. In contrast, Herbig Be protostars are usually found in clusters, highly embedded in massive and chemically complex molecular clouds [Alonso-Albi and Fuente, 2011].

1.3.2 Formation schemes

Theoretically, the origin of the problem in the high-mass star formation is that the Kelvin-Helmholtz time scale is shorter than the infall time scale. This means that the protostar reaches the main sequence while accretion is still going on.

The resulting nuclear burning produces a huge luminosity and a corresponding large radiation pressure force on dust grains in the collapsing dense core and it can be large enough to become more important than gravity force and reverse the infall of matter, once a the star reaches a mass of roughly $20 - 40 M_{\odot}$ [Wolfire and Cassinelli, 1987] for typical Galactic metallicities. However, accretion can still be accomplished through a high accretion rate generated by the turbulent environment [McKee and Tan, 2003] and also through disks, e.g. [Krumholz et al., 2005a] with outflows that greatly reduce the radiative pressure [Krumholz et al., 2005b].

The difficulties associated with forming massive stars via accretion resulted in new theories, like that massive stars might form by collision and coalescence of lower-mass stars in the clusters [Bonnell, 2002].

It was earlier suggested that massive stars form in magnetically supercritical molecular cloud cores [Shu et al., 1987], while low-mass stars form in subcritical cores by ambipolar diffusion. Although magnetic fields are undoubtedly important in both mass ranges, there is no strong observational evidence that support this differentiation [Beuther et al., 2007]. Rather, it is becoming apparent from observations [Beuther et al., 2007], [Plume et al., 1997] that massive stars form in a highly turbulent environment from high-mass, high-density ($n \approx 10^6 \text{ cm}^{-3}$) cores, while low-mass stars form from relatively quiescent lower-mass cores of density $n \approx 10^5 \text{ cm}^{-3}$.

The protostellar evolution time is roughly the same, between high-mass stars ($\approx 10^5 \text{ yr}$) and low-mass stars ($3 \times \approx 10^5 \text{ yr}$); thus \dot{M} for accretion of high mass stars must be significantly greater than that for low-mass stars. This requirement is apparently consistent with the formation of high-mass stars in very turbulent high-density regions; this initial condition naturally provides a high mass accretion rate.

Bipolar outflows have been observed in the high and intermedia-mass proto-

stars. High-angular resolution observations show that, in general, intermediate-mass outflows are intrinsically more energetic than those driven by low-mass YSOs ([Beltrán et al., 2008]). They appear collimated, even at low velocities, and have properties that do not differ significantly from those of low-mass stars ([Beltrán et al., 2002]). Their formation, like in the low-mass case, seems to be due to the magnetic interaction near the star-disk interface with the radiation pressure. Circumstellar disks around intermediate-mass protostars have been observed at high angular resolution in the continuum and in the CO rotational lines [Fuente et al., 2006]. [Alonso-Albi et al., 2009] completed a search for circumstellar disks in a sample of six HBe stars: R Mon, MWC 1080, MWC 137, MWC 297, Z CMa, and LkH 215.

1.3.3 Chemical properties

The high-mass stars ($>9 M_{\odot}$) are extremely important for the galactic chemical evolution and the physics of the interstellar medium. Stars in this mass range can evolve into Type II supernovae which produce and release a significant amount of heavy elements that later will be the cooling agents in the interstellar gas, promoting the formation of later generations of stars.

The chemical features of the high-mass protostars are also notable. Unlike the *hot corinos*, their low mass counterparts, the *hot cores* around massive protostars have lower abundances in O- and N-bearing complex organic molecules compared to that of methanol and formaldehyde by about one order of magnitude [Bottinelli et al., 2007]. Additionally, the deuteration, large in low-mass hot corinos, is observed and found to be lower in high-mass star forming environments, like Orion.

Even though it is clear that high, intermediate and low-mass star formation differs, there is not a cutting border between them.

Besides, there is not a sharp change in the slope of the initial mass function in the high-mass region compared to 1-10 M_{\odot} region, although the initial mass function (IMF) is difficult to determinate.

1.4 Observations of outflows

In the middle of the 1980's, radio astronomers carried out the first large-scale molecular outflow surveys towards a great number of IRAS sources in extensive regions of the sky (e.g., [Margulis and Lada, 1985], [Fukui et al., 1986], and [Armstrong, 1989]) This was important in estimating the energy deposited by molecular outflows in the parental clouds, and concluded that outflows have a significant impact on the dynamical state of their host cloud.

The YSO outflows strongly interact with the surrounding molecular cloud, injecting momentum and energy at scales ranging from a few AU up to few parsecs away from their powering sources. These ejection phenomena may reveal themselves in different ways.

In the optical wavelengths, it has been observed nebulosities known as Herbig-Haro (HH) objects. They are often seen in pairs or in a chain of knots with a highest surface brightness. These HH flows are observed to be very collimated and sometimes connected by fainter emission, have length-to-width ratios of 10:1 or more, and are normally referred to as HH jets [Reipurth and Bally, 2001]. As these *collimated jets* penetrate the ambient medium, they transfer momentum and accelerate the surroundings.

Beyond the collimated jet the flow continues up to the bright and more extended bow-shaped HH objects, that can be located at distances of about 0.1 to 1 pc [Arce et al., 2007] from the central driving source (Fig. 1.10).

The optical emission comes from the shocks arising from the interaction of a high-velocity flow of gas ejected by a young stellar object and the ambient medium. These shocks are traced by the collisionally excited $H\alpha$, while forbidden line emission, such as [O I], [N II], [S II], and [Fe II] in the near-IR, trace the sites behind the shock when the gas cools and recombines.

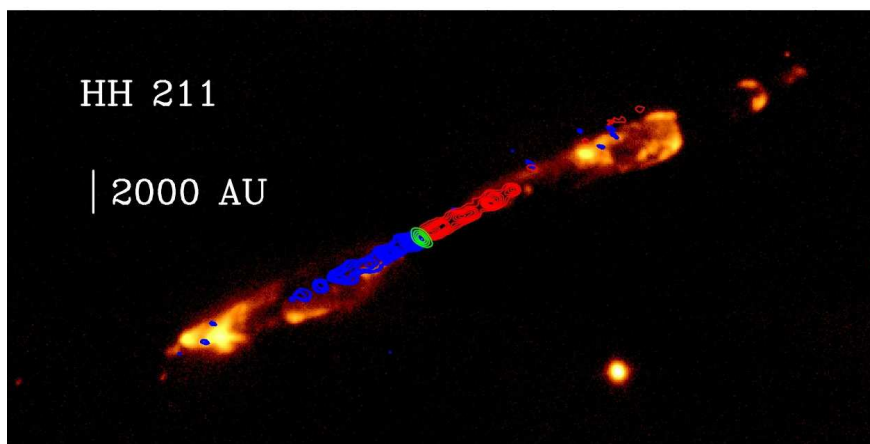
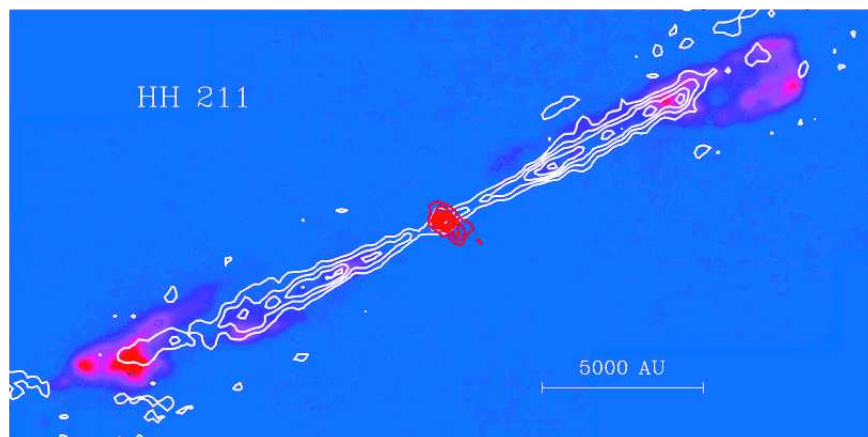
Radio interferometric observations can disentangle the morphology and dynamics of the different elements that are present i.e., to resolve the detailed structure of the low-velocity gas around the optical jet.

For example, in the HH 111 object using PdB observations [Lefloch et al., 2007] obtain a velocity channel maps of CO (1 - 0) emission that shows the emission that comes from the cavities traced by low-velocity gas.

Molecular CO transitions are the most common tracer of outflowing molecular gas (Fig. 1.6). The CO line profile can trace a low-velocity outflow cavity or even show extremely high velocities features that can reveal the presence of a jet (e.g.[Tafalla et al., 2010]). In some cases CO emission can reveal molecular bullets along the axis of the jet probably formed in the shocks resulting from time-variable ejections in the powering source [Raga et al., 2002].

It is useful to observe different molecular lines besides CO because they trace different components of the gas, due to their different excitation conditions, and

Figure 1.6: (*top*) Interferometer map of the molecular jet in the HH211 outflow. The CO J=2-1 line (white lines) [Gueth and Guilloteau, 1999] is overlaid on a false color image of H₂ [McCaughrean et al., 1994]. The red lines delineate the 230 GHz continuum emission from dust concentration around the protostar. (*bottom*) In color scale we see the near infrared H₂ emission, in contours blue and red there are the blue- and red-shifted emission of SiO (8-7), the green contours mark the dust emission at 870 micron surrounding the protostar. [Lee et al., 2007]



also because the molecular abundances can be greatly enhanced behind shocks. Examples of such molecules are SiO, HCN, SO, OH, and HCO⁺. Other molecules like the molecular hydrogen (H₂) can trace shock-excited regions if there is a enough quantity of warm (>200 K) molecular gas present in the surrounding star-jet system (Fig. 1.6). The observations of different chemical species can provide the physical conditions in different regions of the outflow.

1.4.1 The importance of the outflow phenomenon

The outflow phase is thought to play an important role into the star-formation process for two main reasons. First, outflows serve as a way to get rid of the excess angular momentum transferred from the circumstellar disk onto the forming star. Second, they can clear out cavities in their natal molecular clouds, and may eventually cause cloud disruption [Maret et al., 2009].

Finally, the involved kinetic energies ($E_{flow} \sim$ tens of 10^{44} ergs) and momenta ($P_{flow} \sim$ tens of $M_{\odot} \text{km s}^{-1}$) are very large and their formation rates so high that the outflows from young stars are an extremely important source of mechanical energy that have major effects on the dynamics and structure of their parent cloud [Reipurth et al., 2000].

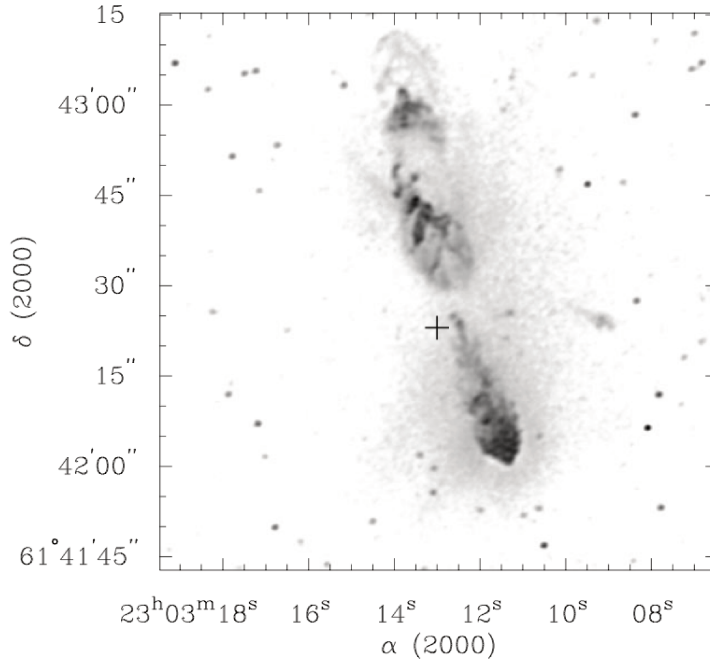
1.4.2 H₂ emission

The propagation of a supersonic protostellar wind through its surrounding medium happens primarily via shock waves that compress and heat the gas, which in turn cools down through line emission at different wavelengths. In molecular gas, shock cooling is mainly through line emission. Molecular hydrogen is by far the most abundant specie in the gas phase, and although H₂ emits only through quadrupole transitions with low radiative rates, it often represents the main gas coolant in flows from young protostars [Kaufman and Neufeld, 1996].

In general, the detection of H₂ emission is evidence of the presence of C-shocks, because a shock at high velocity should destroy the hydrogen molecules.

H₂-shocked emission in outflows has been widely studied in the past (e.g. the Infrared Space Observatory) mainly through its ro-vibrational and rotational emission in the mid-IR, (the pure rotational lines of H₂ S(0) up to S(8) e.g.,

Figure 1.7: Gray scale of the $2.12 \mu\text{m}$ S(1) line emission from molecular hydrogen. The cross marks the position of the IRAS 23011+6126 central source. Taken from [Ladd and Hodapp, 1997].



[Eislöffel et al., 2000]; [Caratti o Garatti et al., 2006]) that trace gas at $T \approx 2000$ - 4000 K.

In addition, given the different excitation temperature and critical densities of the $v = 0 - 0$ and $v \geq 1$ H_2 lines, the combination of mid-IR with near-IR observations is a very powerful tool to constrain the global physical structure and the shock conditions giving rise to the observed emission.

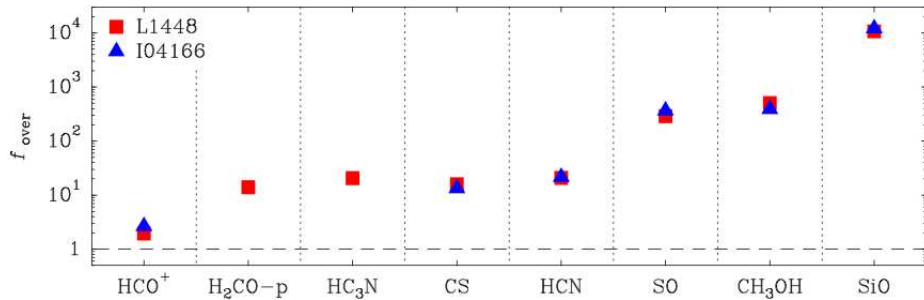
1.4.3 Radio continuum

Radio continuum emission at centimeter wavelengths has been found in association with the driving sources of many outflows in star-forming regions [Anglada, 1995]. In fact, almost all outflow sources appear to present centimeter emission above the 0.1 mJy^1 and despite the weakness of this emission, it can be observed at high angular resolution and with current sensitive interferometers.

This radio continuum emission appears to originate in shock-ionized gas very close to the outflow exciting source, and since it remains unaffected by extinction

¹1 Jy = $10^{26} \text{ W m}^{-2} \text{ Hz}^{-1}$

Figure 1.8: Overabundance factors with respect to dense core values for a number of molecules towards the outflows from L1448-mm and IRAS 04166+2706. Data from Tafalla et al. (2010). Taken from [Tafalla and Bachiller, 2011]



it allows to investigate the properties of the region closest to the origin of the outflow.

Subarcsecond angular resolution observations reveal that the centimeter emission traces collimated partially ionized jets extending typically to distances 10-100 AU from the exciting source, corresponding to material ejected from the protostar with dynamical ages of the order of a few years or less.

1.4.4 Outflow chemistry

In addition to the physical interaction of the outflowing material with the surrounding one, chemical changes are seen in the gas that has been accelerated by supersonic wind, and has been shock-processed.

Outflows drive shock waves that compress and heat the gas triggering important chemical processes, such as molecular dissociations, ice sputtering, and dust grain disruption.

Different molecular lines are observed to trace different components of the gas. While the CO line wings trace the bulk of the outflowing material, molecules such C₃H₂, N₂H⁺ and DCO⁺ trace the quiescent medium [Bachiller et al., 2001]. Other molecules like the SiO, CH₃OH and H₂CO lines trace the high-density shocked gas zones.

The SiO molecule is one of the molecules that show a high enhancement in abundance (up to 10⁶) with respect to the ambient medium, often found close to bowshocks and along the axes of some collimated outflows, where there is the maximum interaction of the outflow with the ambient gas. Very likely, this is due

to the sputtering or vaporization of Si atoms from dust mantles and grains and the grain-grain collisions [Guillet et al., 2009]. SiO lines usually present broad wings, and together with CO, reaches the highest terminal velocities among all molecular species.

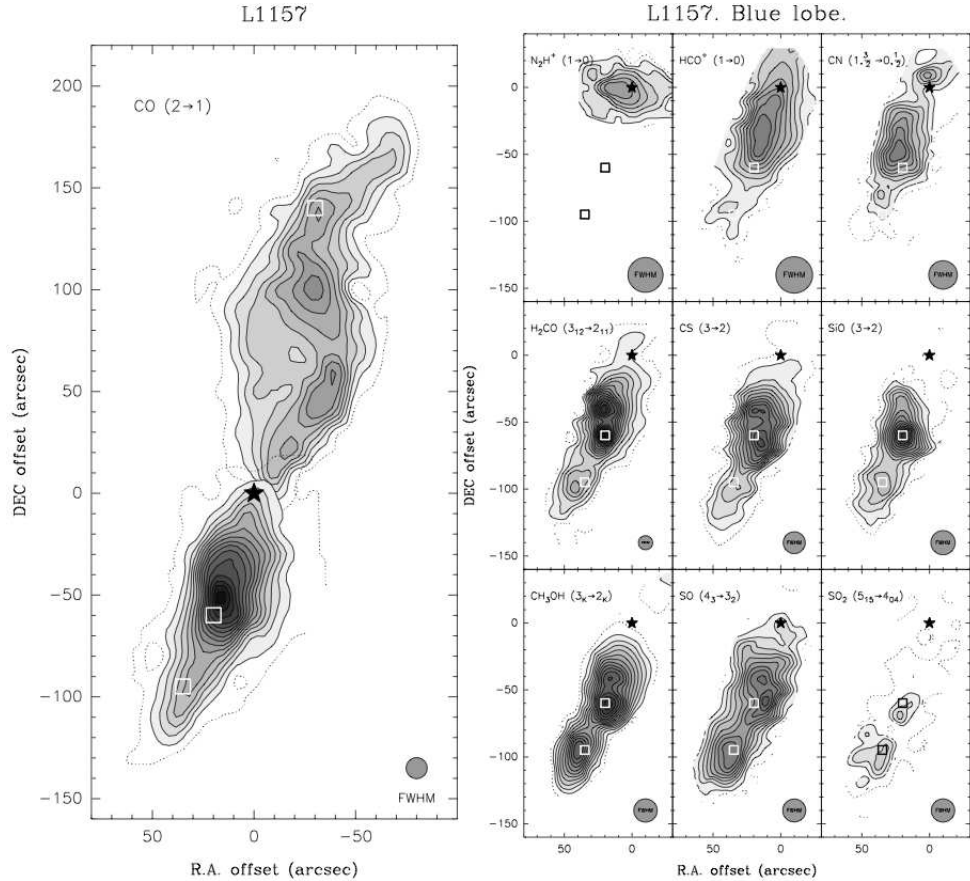
Other molecules whose abundances are enhanced in outflows are methanol (CH_3OH) and formaldehyde (H_2CO). The abundance enhancement is likely due to their release from dust grain mantles.

Molecules larger than CH_3OH have also been recently identified in L1157-B1. [Arce et al., 2008] detected for the first time in an outflow HCOOCH_3 (methyl formate), CH_3CN (methyl cyanide), HCOOH (formic acid), and $\text{C}_2\text{H}_5\text{OH}$ (ethanol). The detection of these molecules shows that outflow shocks can lead to a very rich chemistry, that in low-mass sources was previously restricted to the hot corino regions in the vicinity of some protostars like IRAS 16293-2422 [Cazaux et al., 2003].

Water is also a sensitive outflow tracer through its thermal and maser emission in outflows. The maser emission is so bright that it can be easily detected across the Galaxy, and the abundance of water required to produce the emission must have been significantly enhanced by shocks (e.g., [Kaufman and Neufeld, 1996], [Cernicharo et al., 1996]). Early observations with ISO revealed thermal water emission from a number of bipolar outflows (e.g., [Nisini et al., 1999], [Giannini et al., 2001]). Instruments like ISO, SWAS and Odin telescopes had a limited angular resolution, that only allowed to study global averages of the water emission over the whole outflow, or at least over each of their lobes. In the past two years the Herschel Space Observatory has started to provide water data with high spatial resolution thanks to its Heterodyne Instrument for the Far Infrared (HIFI), with velocity resolutions below 1 km s^{-1} . Much work still needs to be done to understand the excitation conditions of the H_2O emitting gas, and this understanding is critical to extract the full potential of the water data.

Sulfur-bearing molecules are believed to provide a useful chemical clock and allow to study the evolution of outflows. For example, the H_2S abundance, once the molecule is ejected to the gas phase by the effect of shocks, will decrease rapidly after about 10^4 yr due to oxidation with O and OH, which produces SO and SO_2 . Therefore, SO/ H_2S and $\text{SO}_2/\text{H}_2\text{S}$ ratios may be particularly useful to

Figure 1.9: *left:* CO 2→1 emission from the L1157 outflow. *right:* Maps of integrated intensity for different molecular species towards the blue (southern) lobe of the L1157 outflow. Note the different extension and peak position of each species. Taken from [Bachiller and Perez Gutierrez, 1997].



estimate the relative age of shocks in an outflows (e.g., [Wakelam et al., 2005], [Buckle and Fuller, 2003]).

The amount of the abundance enhancement depends on the species under consideration, from factors of a few for species like HCO^+ to several orders of magnitude for species like CH_3OH and SiO (Fig. 1.8). Not all the outflows show the same chemical richness. The ones that shows more chemical activity have been called ”*chemical active*” outflows [Bachiller et al., 2001].

The exact cause of the chemical richness is however unclear. One possibility is that the youngest outflows interact with denser envelopes, and therefore give rise to stronger shocks. Another possibility is that early chemical activity is associated with the higher energy known to characterize the earliest outflow phases (e.g.

[Saraceno et al., 1996]; [Bontemps et al., 1996]). Among the group of chemically active outflows is the L1157 outflow.

To summarize, millimeter spectral line surveys are the best tool to explore the chemical composition of the vicinity of YSOs. The observational study of molecular outflows at different scales provide a huge amount of information, not only about the physics and chemistry of the jets and outflows themselves, but also about the young stellar objects powering them and the molecular environment of the systems. Observations towards different regions allow to distinguish variations in the excitation conditions and/or chemical composition along the jet/outflow.

1.4.5 Herbig-Haro objects

The Herbig-Haro (HH) are nebulous knots, observed in optical images, which are distinguished by their spectrum with characteristic emission lines, especially some forbidden transition of oxygen, sulfur and neon ions.

They were discovered in the 50s by George Herbig and Guillermo Haro, believing then, that they were nebulae that contained a star in formation. Several years after their discovery, Herbig suggested that HH objects could be associated in some way with winds from young stars (Herbig 1958).

The optical spectrum of the HH objects can be reproduced if the emission is modeled as high-density gas cooling after having pass through a shock wave, i.e, the observed emission comes from the recombination zone which is located behind the shock wave. By comparing detailed observations with the theoretical predictions, it is found that it is better reproduced the HH spectra using bow shock models.

The gas that comes just at the apex of a bow shock have a larger velocity with respect to the wings, generating strong forbidden lines (e.g [OIII] 5007 to [SII] 6312 to [NeIII] 3869 Å). The gas that passes through the wings collides with a slower velocity gas producing only low excitation lines (e.g., the Lyman of H₂ molecule). This spectrum is probably produced by the interaction between a strong wind or high velocity jet (100 - 400 km s⁻¹) and the surrounding gas.

In addition, it has been observed that HH objects are often (but not always) in pairs, one redshifted and the other blueshifted, symmetrically arranged with

respect to the position of the powering star. However, in general, the redshifted HH object is much weaker than the blue counterpart. This indicates that the blueshifted part is closer to the surface of the cloud respect to the observer, so it suffers less extinction in the visible.

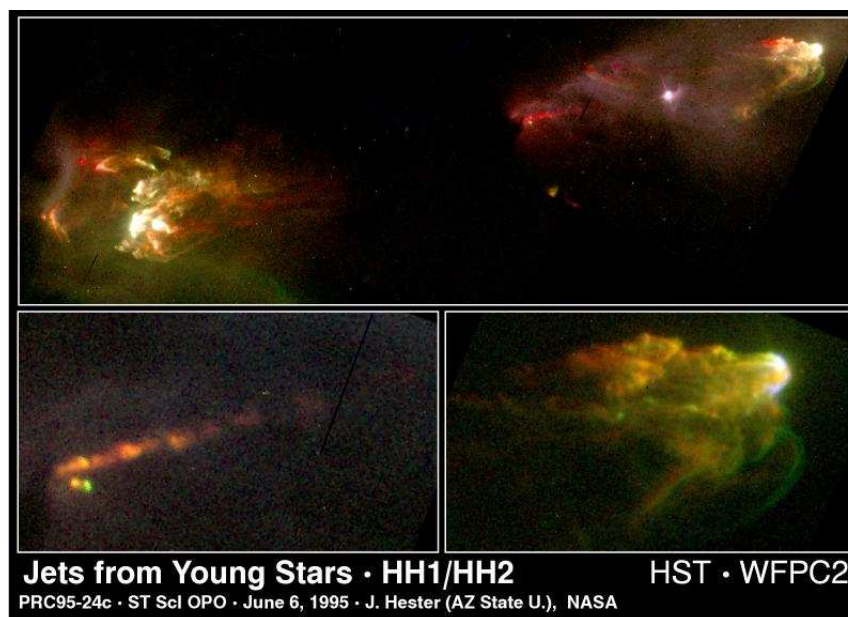
There are about 400 known Herbig-Haro objects [Reipurth, 2000].

On the other hand, the jet phenomenon itself is directly related to HH objects. The jets appear as compact chains of aligned knots, sometimes connected by weak emission and have a length/width ratio of 10:1 or more. In some cases both the collimated jet as well as the shock fronts are visible, sometimes only the shock is seen.

HH jets are always found to originate very close to their power source (less than 10^2 to 10^3 AU from their source), and they usually extend less than 0.2 pc in length. These jets present velocities from about 100 km s^{-1} up to 600 km s^{-1} .

There are two main theories for the origin of the structure of knots and the nature of the jets with a low excitation spectrum. The first mentions a series of oblique shocks traveling through the jet and perturbed by hydrodynamic, magneto-hydrodynamics or thermal instabilities. The second theory considers that jets

Figure 1.10: HH 1/2. These are among the brightest HH objects in the sky, they form bow shocks in a highly collimated bipolar outflow with dimension of 2.5 arsec (0.34 pc), symmetrically opposite from a young star which is ejecting material along its polar axis.



are not a continuous phenomenon.

Emission lines observed in the jets have properties of the ionized gas features, excited by shocks. Optical jets are usually monopolar and radial velocities observed are usually blueshifted by several hundred km s^{-1} . This is interpreted as in the case of HH objects, as a consequence of the extinction effect.

Finally, the most important evidence relating HH objects with outflowing material comes from measurements of their proper motions. The velocities of the measured proper motions can reach 200 to 300 km s^{-1} . In the case of dual systems of HH objects, they have symmetrical motions, moving in the opposite direction with respect to the position of the central source successfully.

To conclude, the gas ejected by young stars can be detected and studied in various ways, according to the spatial scale to be studied: very close to the star the radio continuum (thermal jets) are detected, at intermediate distances molecular emission lines in radio and infrared (bipolar outflows), and far from the star as it is seen in the visible like HH objects.

1.5 Theory of the outflow phenomenon

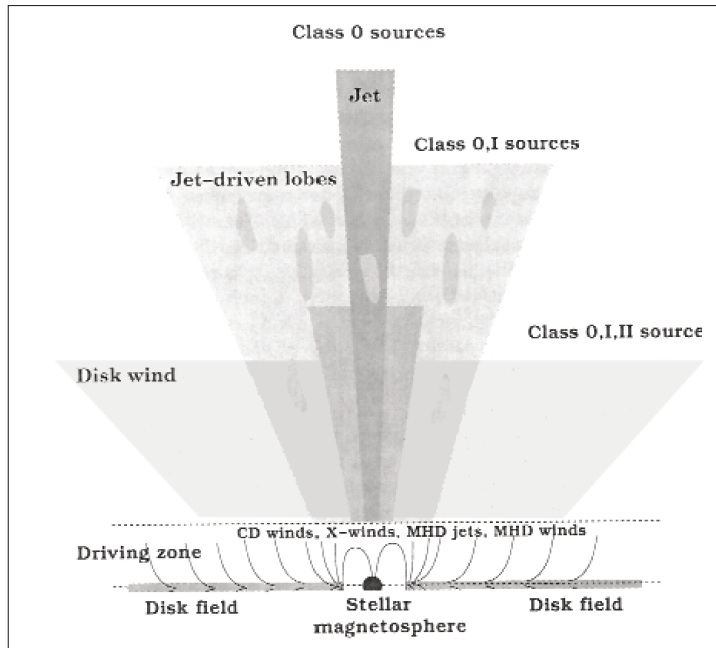
1.5.1 Origin and structure of the outflows

There are many theories about how outflows and jets are originated, and which is the relation between them, but it is still matter of discussion. However, the observed correlation between the mass outflow with the accretion rate into the disk seem to favor some magnetohydrodynamic (MHD) jet launching mechanism [Cabrit et al., 1990]. In the case of the jet, it can be generated from the interface between the star's magnetosphere and the disk (the called X-wind model) [Shang et al., 2002] or from a wide range of disk radii (the D-wind model) [Pudritz et al., 2007].

Actually, it is not clear yet what physical mechanism produces the outflows, and the fundamental stellar or protostellar wind that should sweep up the fast moving molecular gas is very hard to detect. However, there are three empirical correlations that can be summarized from many observations:

1. Progressively with the age, the outflow activity declines. It exists a tight

Figure 1.11: Several types of outflows are observed in low-mass YSOs. High velocity and very collimated jets are mainly observed in Class 0 sources. The figure indicates the trend that outflow collimation decreases with the age. Similarly the flow velocity (several hundreds km s^{-1}) decreases from the jet to the outer edges of a disk wind ($\approx 5 \text{ km s}^{-1}$). The process that originates the outflows is still not fully understood, but it seems that magnetic fields and rotation trigger the jet launching mechanism. Taken from [Schulz, 2005]



correlation between the outflow energy and the driving source; a Class I protostar produce an outflow of one order of magnitude less powerful than such produced by a Class 0 source. These outflows are also, less fast and less collimated. Class II sources produces in turn, outflows even less collimated and weaker in power than such of Class I sources. In fact, this correlation show the closer relation between the mass outflow rate and the mass accretion rate [Konigl and Pudritz, 2000].

2. The outflow velocity and the mass outflow rate increase with the bolometric luminosity of the central source. Jets associated with low-luminosity YSOs have velocities about 400 km s^{-1} and very small opening angles. In several outflows observed in Ae/Be stars and high-luminosity objects shows jet velocities up to three times higher and outflows rates up to 100 times higher [Mundt and Ray, 1994]. However, this result does not imply necessarily that the high mass accretion rate must be much higher than for low-mass

or intermediated-mass system, but, it seems that massive stars are very inefficient accreting material and that is reflected in the higher outflow rates.

3. The degree of collimation is directly determinate by the outflow rate. This correlation suggest that the apparent decrease in outflows energetics with the age reflects a decay in the mass accretion and infall rate [Bontemps et al., 1996].

1.5.2 Outflow Models

Several outflow models have been proposed to explain how molecular outflows from protostars are formed. Outflow models can be separated in four principal groups: Wind driven shells, jet driven bowshocks, jet driven turbulence flows and circulation flows. In the first three groups the molecular outflow is considered as ambient material entrained by a wide angle wind or accelerated by a collimated jet. Conversely the last one considers that the outflows is formed by deflected infalling gas.

1. *Wind driven shell models.* In this model, a wide-angle radial wind blows into the surrounding ambient molecular cloud, forming a thin swept-up shell that corresponds to the outflow shell (e.g. [Shu et al., 1991], [Matzner and McKee, 1999]). In these models it is often assumed that the ambient material has a toroidal form. These kind of models are attractive because they explain old outflows of large lateral extents and low collimation.
2. *Jet bowshock model.* In the jet driven bowshock model, a high-velocity and well-collimated internal jet entrains the ambient molecular gas through a bowshock. [Raga and Cabrit, 1993] As the jet hits into the ambient material, a pair of shocks, a jet shock and a bowshock, appear in the head of the jet. Between the shocks the gas pressure is enough high that material is ejected sideways out of the jet beam, interacting with the ambient gas through a broader bow shock surface, producing an outflow shell around the jet.
3. *Turbulent jet model.* In the jet-driven turbulent model, the interaction between the jet and the surroundings environment produces Kelvin-Helmholtz

instabilities along the jet/environmental boundary that lead to the formation of a turbulent viscous mixing layer, through which the cloud molecular gas is entrained. The mixing layer grows both into the jet and into the environment, and eventually the whole flow becomes turbulent [Canto and Raga, 1991].

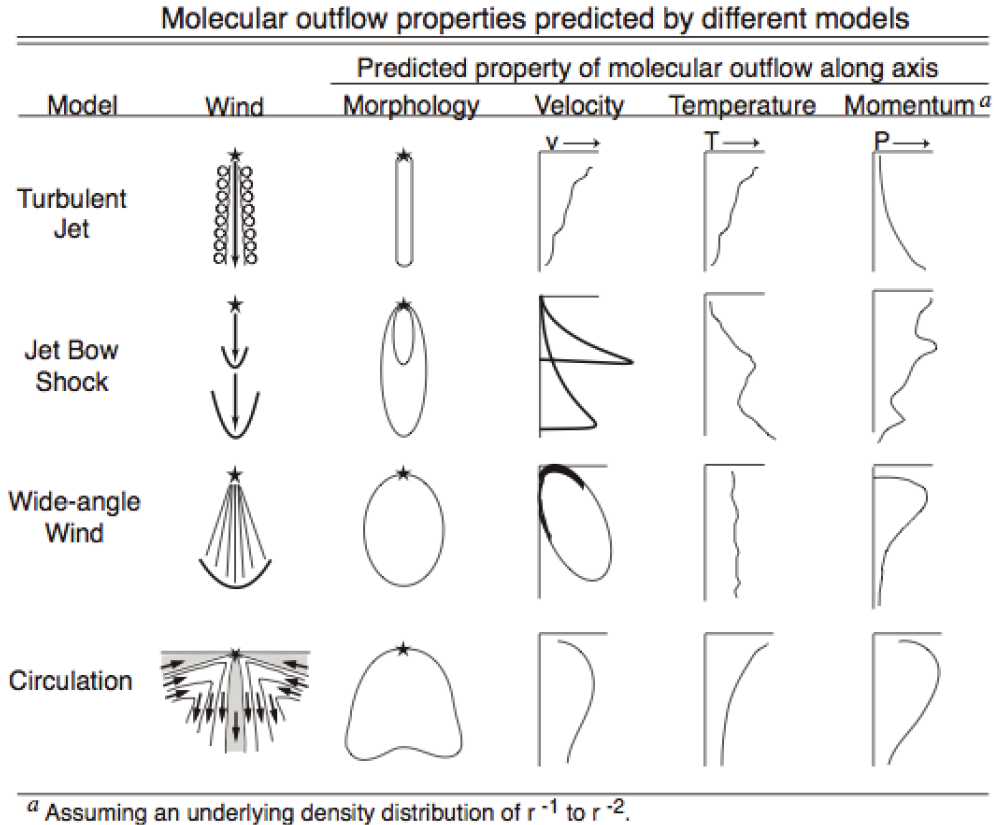
4. *Circulation models.* In the circulation model, the molecular outflow is not formed by entrained material by a jet or stellar wind. Instead, it is formed by infalling matter that it is deflected away from the protostar in a central torus of high MHD pressure through a quadripolar circulation pattern around the protostar, and accelerated above escape speeds by local heating (e.g., [Fiege and Henriksen, 1996a], [Fiege and Henriksen, 1996b]). The molecular outflow can have some contribution by entrainment from winds or a jet, but their contribution are limited to the polar regions [Lery et al., 2002].

The current observations at high angular resolution allow to confront the outflow models in detail. Comparing the jet-driven bowshock models *vs* the wide-angle wind models, there are features that one model can reproduce and that the other can not. However, there are some models that try to unified both pictures, in which both the jet and the wind play a role in driving the outflow e.g. [Shang et al., 2006].

The jet-driven bow shock models are characterized by an outflow velocity that increases toward the position of the internal leading bowshock, giving the appearance of a peak curve in the PV (position velocity) diagram, (Fig. 1.12). These models are capable to produce the observed outflow width for high collimated outflows, basically because the shocked gas in the bowshock working surface limits the transverse momentum, that can be released to the surroundings. However, these models have problems to reproduce the observed width of poorly collimated outflows. Also, there are some difficulties to produce the right momenta. In addition, the jet-driven model may need jet wandering to produce the observed outflow width and momentum for most of the outflows.

In the wide-angle wind models the outflow velocity also rises near to the source, but, in this case, they exhibit a lobe PV structure (Fig. 1.12) Most of

Figure 1.12: Observable molecular outflow properties predicted by the four leading broad classes of models: 1) turbulent jet [Canto and Raga, 1991]; 2) jet bow shock [Raga and Cabrit, 1993]; 3) wide-angle wind [Shu et al., 1991]; and 4) circulation models [Fiege and Henriksen, 1996b]. Taken from [Arce et al., 2007].



these models assume that the protostellar wind density depends on the angle from the jet axis, if not, they assume a density stratification. Anyway, these models can reproduce widths consistent with observed molecular outflows in about 10^4 yr. And again, these models have problems to reproduce discrete bowshock features. Trying with pulsed winds, they generate flat internal shocks within the internal outflow shell, inconsistent with the curved internal H_2 bowshocks, typically observed in episodic outflows. Alternatively, the wind-driven model may need to assume a collimated core with strong velocity gradient away from the core to produce the highly collimated outflows and the observed curved internal H_2 bow shock structures.

1.5.3 J versus C shocks: structure and chemistry

When the ejected material encounters the quiescent surrounding molecular gas, it creates shocks, whose nature depends on the shock velocity and the intensity of the magnetic field.

Molecular shocks generally can be described as C-shocks or as J-shocks [Draine, 1980], depending on their velocity V_s , the ambient ionization fraction, and the strength of the component of the ambient magnetic field B_o perpendicular to V_s .

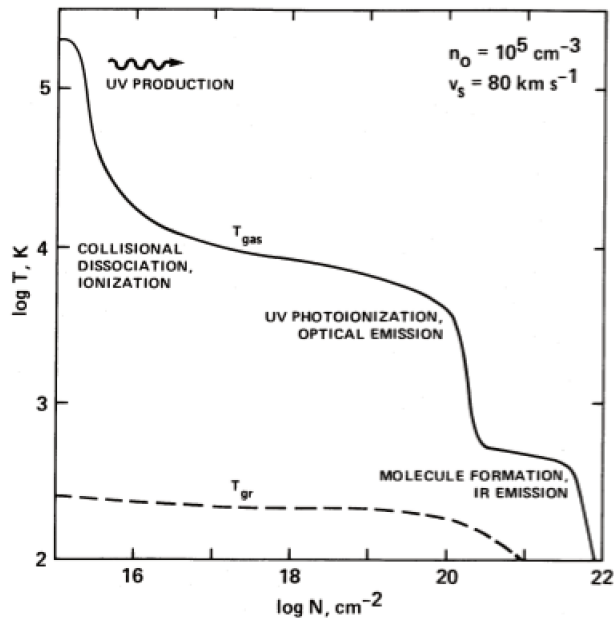


Figure 1.13: The postshock temperature structure of a fast shock. Taken from [Hollenbach and McKee, 1989]

J-shock

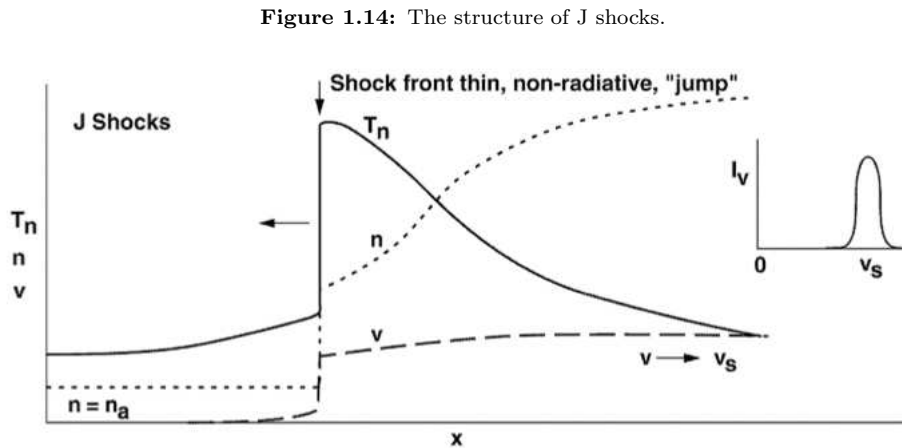
A J-shock arises when the shock velocity (V_{shock}) exceeds the local sound speed. A moving fluid element then has no time to be "warned" by sound waves of the approaching high-pressure region. It therefore undergoes a sudden change. Fast shocks are called, **J-shock**, because all fluid variables jump (on a length scale on the order of the mean free path) to their post-shock values.

The temperature, density and pressure jump upward, while the velocity is

reduced to a value that is subsonic with respect to the local sound speed (see Fig. 1.14). Downstream behind the shock front, the gas temperature falls, first quickly and then slowly, in an "relaxation region". It is the radiation generated in this cooling zone that provides the information about the shocks in star forming regions.

Following [Hollenbach and McKee, 1989], the figure 1.13 shows the typical temperature structure of a J-shock. First, the preshock gas experiences the radiation field from the shock front, the gas molecules are ionized and dissociated collisionally in the immediate postshock environment ($T \approx 10^5$ K) and UV photons arise affecting both preshock and postshock gas. Downstream, at a hydrogen column density $\approx 10^{17} \text{cm}^{-2}$ from the shock front the gas temperature cools until $T \approx 10^4$ K and the recombination starts. Temporarily an equilibrium is reached between recombinations and photoionizations by the UV photons produced upstream. This is the so-called "recombination plateau" where the Lyman continuum photons are absorbed, maintaining a $T \approx 10^4$ K. Once the ionizing photons are absorbed (at $N \approx 10^{18-19}$), the gas cools, recombines, and the molecular chemistry begins.

First to appear is H_2 , initially produced by the H^- formed out of the residual electron supply. Later, H_2 formation continues on grain surfaces. The H_2 molecules may be vibrationally excited when injected back into the gas phase. If the density is at least 10^5cm^{-3} , they decay collisionally. Under these conditions, the formation of H_2 becomes the major heating source for the gas, stabilizing



the gas temperature at a second plateau of about 500 K until all the hydrogen becomes molecular.

Other molecules also form, through purely gas-phase processes. The low ionization level and prolonged temperature elevation of the plateau result in neutral-neutral reactions being efficient.

A network of such reactions is activated which yields a variety of species, including the important coolants: CO, OH and H₂O.

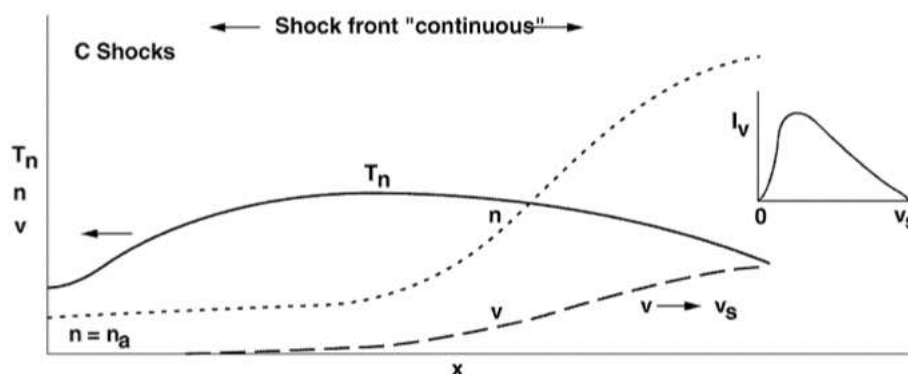
In addition to these gas-phase processes, grain cores and their mantles are affected by the shock. Millimeter and infrared observations of these shocked regions reveal the abundance enhancement of species like SiO or Fe [Nisini et al., 2007], which are usually highly depleted from the gas in quiescent regions.

This can be explained by models in which dust is destroyed (vaporization and sputtering) in the shock waves initiated by jets and outflows.

They are indeed expected to exist at the apex of bow shocks around YSOs where the observed strong lines of Fe II can be explained with J shocks modelling [Hartigan et al., 2004].

The models of [Guillet et al., 2009] show that dust destruction occurs in J-type shocks at levels comparable to that of C-type shocks of the same velocity, and that this destruction is dominated by vaporization in grain-grain collisions.

Figure 1.15: The structure of C shocks.



C-shock

In C shocks, the fluid variables are everywhere continuous, they change smoothly throughout a broad transition region by dissipative effects.

C type shocks form when the ionized fraction is low so their coupling with neutral is weak. The electron and the ion flow velocities and temperatures can differ appreciably from those of the neutrals. The charged particles that are upstream function as a magnetic precursor. The radiative dissipation process of this precursor can be so important that the neutral shock becomes a continuous transition. Then, the structure of these shock waves is dependent on several factors. (1) Ionization fraction through the ion-neutral collisions. (2) The rates of cooling through the various molecular coolants of the gas; and (3) the abundances of those coolants. [Kaufman and Neufeld, 1996]

For typical ionization fractions in dense clouds $x(e) \leq 10^{-6}$, the C-shocks occur at $V_{shock} \leq 40\text{-}50 \text{ km s}^{-1}$, causing peak temperatures of typically 2000-3000 K [Draine and McKee, 1993].

These shocks are characterized by bright molecular emission as first emphasized by [Hollenbach and McKee, 1979]. Molecules generally survive their passage, although the chemical composition of the gas can be significantly altered. On the other hand, the heating and compression of the region trigger different microscopic processes such as molecular dissociation, endothermic reactions, ice sublimation, and dust grain disruption which do not operate in the unperturbed gas.

Grain-grain destructive processes (sputtering) in C-type shocks have been extensively studied in order to confront shock models with line measurements of tracers such as SiO, H₂O and CH₃OH in molecular flows around YSOs (e.g., [Jiménez-Serra et al., 2008]; [Gusdorf et al., 2008].)

Recently, [Guillet et al., 2011] modeled the impact of the grain-grain collisions in C-type shocks propagating in dense clouds ($n_H \geq 10^4 \text{ cm}^{-3}$) on the evolution of the dust distribution, the shock dynamics and the release of chemical species into the gas phase such as SiO. They found that dust destruction by grain-grain collision (vaporization) dominates over that by gas-grain collisions (sputtering) at high densities ($n_H \geq 10^5 \text{ cm}^{-3}$), but is negligible at low densities ($n_H \leq 10^4 \text{ cm}^{-3}$).

Chapter 2

Radio observations

At present, more than 150 gaseous molecules have been detected in the interstellar medium (ISM), including alcohols, ketons, ethers, aldehydes, and others. They are mainly observed via their rotational transition, e.g. CO, CS, HCO⁺ and/or ro-vibrational transitions, e.g. H₃⁺, H₂. Depending on the mass of the molecule and its structure, these transitions lie in the radio (cm) to far infrared (>100 μ m) wavelengths. Heavier molecules have the rotational transitions at longer wavelengths. The transitions can be observed either as emission or absorption lines, depending on the continuum at the transition wavelength. Indeed, the same transition can be in emission in some regions and in absorption in others.

These line spectra can be observed using millimeter-wave single-dish telescopes on the ground or, in order to increase resolution, interferometers and, to avoid the atmosphere effects, space-borne telescopes.

2.1 The first steps of Radioastronomy

In 1931, Karl Jansky was conducting experiments for Bell Laboratories related to the production of radio-wavelength noise from thunderstorms, in the first transatlantic radio telephone between the U.S. and London.

He built an antenna, (2.1), designed to receive radio waves at a frequency of 20.5 MHz (wavelength about 14.5 meters). It was mounted on a turntable that allowed it to rotate in any direction, earning it the name "Jansky's merry-go-

round". By rotating the antenna, one could find what the direction was to any radio signal.

During the course of his investigation, Jansky discovered that the noise originated from three sources: local thunderstorms, distant thunderstorms and a constant noise of unknown cause. Over time, he realized the noise gradually changes of position, as if it came from a fixed direction in the sky. He also noted that the signal was detected 4 minutes earlier each day, as the stars do, due to the translational motion of the Earth. This fact made Jansky suppose that the signal did not have a terrestrial origin.

By 1935, he had correctly concluded that much of the signal he was measuring originated in the plane of the Milky Way, with the strongest emission coming from the constellation Sagittarius, which lies in the direction of the center of our Galaxy. Jansky's pioneering work represented the birth of *radio astronomy*, a whole new field of observational study.

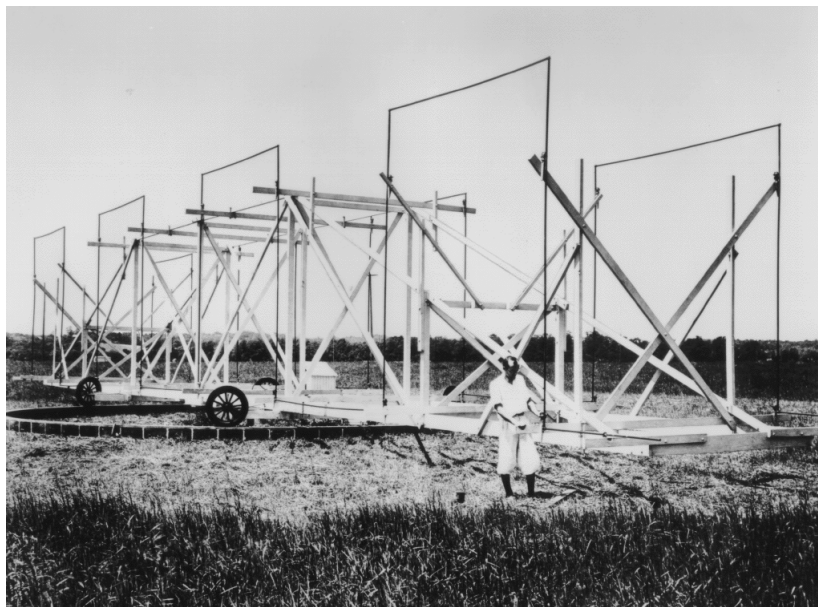
During the years of the Second World War radio physics had made great progress, mainly due to efforts directed towards the development of sensitive and efficient radar equipment.

On the other hand, the international scientific community lost almost all communications. The exchange of information was minimum, with a great exception. A copy of the article published by Reber (who followed the Jansky's work) in the *Astrophysical Journal* arrived at the Leiden Observatory during the occupation of Holland. This publication caught the attention of Dr. Oort, who immediately envision the possibility of radio astronomical observations.

Oort was one of the few astronomers who recognized the scientific potential of the radio data, previously regarded only as a curiosity in the field of engineering. He understood that observing emission lines of species that populate interstellar space would provide a tremendous tool for determining not only the quantity of the species but also of the energy necessary to excite it, and the information on the radial velocity, from which to derive the dynamics of the Galaxy.

Oort commissioned a young astronomer, Hendrick van de Hulst, the estimation of the probability of observing emission lines in radio wavelengths. Van de Hulst, after studying the issue, concluded that the element the most likely to be detected in interstellar space was neutral hydrogen. The frequency of the emis-

Figure 2.1: In 1931 Karl Jansky built the first radiotelescope. This 14.6 meter rotatable, directional antenna system was designed, to investigate interference problems on long distance communication circuits. Using this antenna, Jansky was able to make the first positive identification of radio waves of extra-terrestrial origin.



sion, caused by the transition between the two hyperfine sublevels of the ground state of HI, is 1420 MHz ($\lambda = 21$ cm). The life time for each excited atom is about 11 million years so that the probability of spontaneous transition is very low, but this could be offset by the large number of atoms in the interstellar medium and the frequent collisional excitations and desexcitation between the atoms, so such emissions could be observable.

Once in 1945 the predictions by Hendrick Van de Hulst were published, it started a race between several countries to detect the 21 cm line of HI. The detection occurred almost simultaneously (with differences of a couple of weeks) in 1951 in three places: Harvard, Leiden and Sydney. Thereafter, radio astronomy acquired enormous importance which resulted in several projects of radio telescopes in the world and an explosive growth in the amount of information that was collected. The line of HI could be detected in almost any direction from the sky [Verschuur, 1987].

We will not follow this historical development any further, except to note that the instrumental development has been toward higher sensitivity, shorter wavelength, and higher angular resolution.

The radio - far infrared window covers from $\lambda \sim 10$ m to shortward of $\lambda \sim 0.1$ mm.

2.2 **Some basic concepts**

Electromagnetic radiation in the radio is a wave phenomenon, but when the scale of the system greatly exceeds the wavelength of radiation, we can consider the radiation to travel in straight lines called *rays*.

A single ray carries essentially no energy, so it is necessary to consider the energy carried by sets of rays, which differ infinitesimally from the given ray. Consider a set of rays from the sky falling through an horizontal area σ at the surface of the earth. The infinitesimal power dP from a solid angle $d\Omega$ of the sky incident on a surface of area $d\sigma$ is

$$dP = I_\nu \cos \theta d\Omega d\sigma d\nu \quad (2.1)$$

where

dP = infinitesimal power, in watts,

$d\sigma$ = infinitesimal area of surface, cm^2 ,

$d\nu$ = infinitesimal bandwidth, in Hz,

θ = angle between the normal to $d\sigma$ and the direction to $d\Omega$,

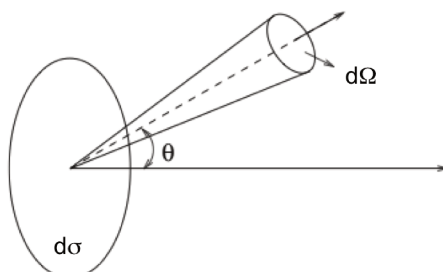
I_ν = brightness or specific intensity, in $\text{W m}^{-2} \text{Hz}^{-1} \text{sr}^{-1}$.

Equation 2.1 is the definition of the *brightness* I_ν . The total flux of a source is obtained by integrating 2.1 over the total solid angle Ω_s subtended by the source (See fig. 2.2).

$$S_\nu = \int_{\Omega_s} I_\nu(\theta, \phi) \cos\theta d\Omega \quad (2.2)$$

where the *flux density* S_ν is measured in units of $\text{W m}^{-2} \text{Hz}^{-1}$ [Kraus, 1950].

Figure 2.2: Schematic diagram which shows how the specific intensity is defined.



2.2.1 The radiative transfer

If a ray passes through matter, energy may be added or subtracted from it by emission or absorption, and this change of I_ν is described by the *equation of transfer*.

For a change in I_ν along the line of sight, a gain in the intensity will be describe in terms of the spontaneous emission coefficient as $\epsilon_\nu ds$ and the loss of intensity in a beam as it travels a distance ds will be $-\kappa_\nu I_\nu ds$. So that the change of intensity in a slab of material of the thickness ds will be

$$\frac{dI_\nu}{ds} = -\kappa_\nu I_\nu + \epsilon_\nu \quad (2.3)$$

There may be situations for which ϵ_ν depends strongly on I_ν , such as an environment in which radiation is strongly scattered. However, there are many other important situations where ϵ_ν is independent of I_ν .

The transfer equation provides a useful formalism within which to solve for the intensity in an emitting and absorbing medium. It incorporates most of the macroscopic aspects of radiation into one equation, relating them to two coefficients κ_ν and ϵ_ν . Once spontaneous emission and absorption coefficients, are known, it is relatively easy to solve the transfer equation for the specific intensity [Rybicki and Lightman, 1979].

2.2.2 Antenna and brightness temperature

The radio telescopes measure the power coming from the sky per unit area per unit frequency, or as we already see the *flux density*.

When the antenna is pointed toward a cosmic source this provides the *antenna temperature*, T_a , defined as the temperature of an equivalent resistor which would give the same power, as measured at the final output terminals, as the cosmic source.

When we point the antenna on a source and then away from it, the difference in the two outputs gives the contribution from the source alone. This provides the *brightness temperature*, T_b , defined as the Rayleigh-Jeans temperature of an equivalent black body which would give the intrinsic temperature of the source.

Note that the antenna temperature is antenna-specific, and will vary from telescope to telescope. They are usually easy to measure, and are useful for understanding the system performance. In contrast the brightness temperatures is a property of the sources on the sky; provided the sources are resolved, different radio telescopes will measure the same value.

The concepts of antenna and brightness temperatures allow us to calculate the power received by single dishes without knowing the details of the Fourier coverage of the aperture. The consequences of the grating are taken into account through global factors, the most important being aperture efficiency and beam efficiency. The *aperture* ϵ_{ap} is defined as

$$\epsilon_{ap} \equiv A_e/A \tag{2.4}$$

where A_e is the effective collecting area, and A is the geometric area of the antenna.

The *effective beam efficiency*, B_{eff} , corresponds to the amount of signal that is contained in the main lobe and is defined by

$$B_{eff} \equiv T'_a/T_{MB} \tag{2.5}$$

where T'_a is the antenna temperature corrected for atmospheric extinction, it is: $T'_a = T_a e^{\tau_\nu}$ and T_{MB} is the *main beam temperature*. The main beam temperature

relate the forward efficiency (the the total amount of the signal that comes from the front of the telescope) with the beam efficiency as follows:

$$T_{MB} = T_a \frac{F_{eff}}{B_{eff}} \quad (2.6)$$

Under the assumption that both the source and the beam are Gaussian shaped, the brightness temperature, T_b , is related to the main beam temperature, T_{MB} (see Eq. 2.9), by:

$$T_b = T_{mb} \frac{\theta_s^2 + \theta_{MB}^2}{\theta_s^2} \quad (2.7)$$

The aperture efficiency is usually measured via a celestial source of known flux density, whose antenna temperature is obtained by comparison with a noise standard, such as the difference between hot and cold loads. The beam efficiency may be calculated from the beam pattern [Wilson and Huttemeister, 1987].

2.2.3 The beam

The sky brightness is in general a function of the angle. This may be expressed explicitly by $I(\theta, \phi)$. Thus, the spectral power or power per unit bandwidth, becomes

$$dP = I(\theta, \phi) \cos\theta \, d\sigma \, d\Omega \quad (2.8)$$

where it is considered the case where $d\sigma$ is the flat horizontal surface of a receiving antenna with the power pattern of the antenna directed toward the zenith ($\theta=0$). In this case the equivalent area is called the *effective aperture* of the antenna. The power pattern $P_n(\theta, \phi)$ is a measure of the response of the antenna to radiation as a function of the angles θ and ϕ . It is a dimensionless quantity and is normalized at its most sensitive direction (ideally, this will be along the physical axis of the antenna).

$$P_n(\theta, \phi) = \frac{1}{P_{max}} P_n(\theta, \phi) \quad (2.9)$$

The pattern solid angle Ω_A or more commonly called beam area or solid angle of

an antenna is

$$\Omega_A = \iint_{4\pi} P_n(\theta, \phi) d\Omega \quad (2.10)$$

this is measured in steradians (sr). The integration is extended over the full sphere 4π , such that Ω_A is the solid angle of an ideal antenna having $P_n = 1$ for all of Ω_A and $P_n = 0$ everywhere else. Such an antenna does not exist; for most antennas the normalized power pattern has considerably larger values for a certain range of both θ and ϕ than for the remainder of the sphere. This range is called the *main beam* or *main lobe* of the antenna; the remainder are the side lobes (See fig 2.3). In analogy to 2.10, it can be define as the *main beam solid angle* Ω_{MB} by

$$\Omega_{MB} = \iint_{\substack{\text{main} \\ \text{lobe}}} P_n(\theta, \phi) d\Omega \quad (2.11)$$

For a Gaussian shaped main beam, the solid angle is given by

$$\Omega = 1.133 \theta_b^2 \quad (2.12)$$

where θ_b is the full width to half maximum (FWHM), also know as full width to half power (FWHP). The full width half maximum of the main beam defines the *resolution* of the telescope and therefore it is important to have an accurate measurement of the telescope's main beam.

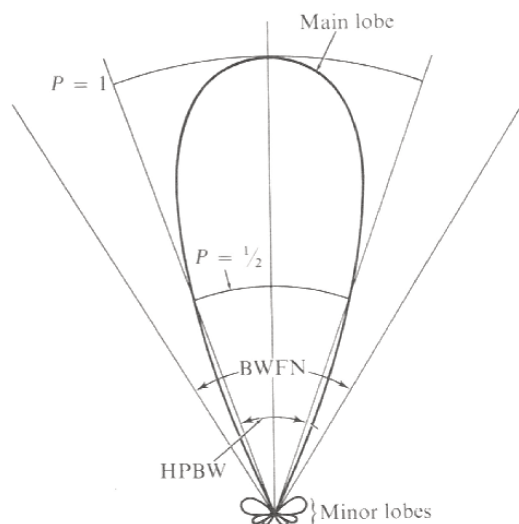
If the beam is convolved with a gaussian source of halfwidth θ_s , the response pattern will also be gaussian, with halfwidth θ_r given by

$$\theta_r^2 = \theta_s^2 + \theta_b^2 \quad (2.13)$$

(in practice, this relation can be trusted only for $\theta_s > \theta_b/2$) [[Wilson and Huttemeister, 1987](#)].

Since the response of the telescope is a convolution of the telescope's beam with a source's signal, a bright and isolated point source should be used to measure the shape of the main beam. Using such an object allows one to be confident

Figure 2.3: Schema of an antenna pattern.



that all of the flux from the source is contained in the beam shape and that the flux measured is from that single object. Thus, one is effectively convolving a delta function with the telescope's beam. When the point source is in the most sensitive part of the main beam, the measured signal will be highest. As the point source is moved away from the centre of the main beam, the measured signal will decrease.

The quality of an antenna as a direction measuring device depends on how well the power pattern is concentrated in the main beam. If a large fraction of the received power comes from the side lobes it would be rather difficult to determine the location of the radiation source, the so-called *pointing*.

It is appropriate to define a main beam efficiency or (usually) *beam efficiency*, η_{MB} , by

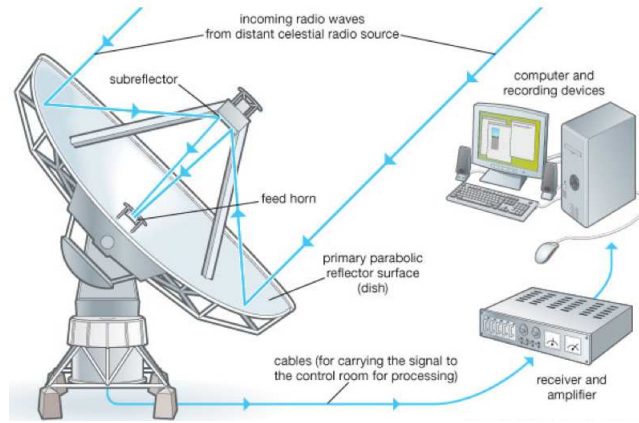
$$\eta_{\text{MB}} = \frac{\Omega_{\text{MB}}}{\Omega_A} = B_{\text{eff}} = \frac{T'_a}{T_{\text{MB}}} \quad (2.14)$$

the second equality use the IRAM notation used in eq; 2.5.

2.2.4 The signal and the receiver

Radio telescopes vary widely, but they all have two basic components: a radio antenna and a radio receiver. The sensitivity of a radio telescope depends on the

Figure 2.4: Typical radio telescope, a large parabolic antenna collects incoming radio waves and focuses them onto a smaller antenna called the feed horn. The signal is then carried to the radio receiver.



area and efficiency of the antenna and the sensitivity of the radio receiver used to amplify and detect the signals.

When the wavefronts reaches the antenna the input signal has to be amplified, because cosmic radio sources are weak, and modulated at a certain frequency that matches with the electronics of the telescope system.

The equipment behind the antenna feed is usually formed by a receiver and a pre-amplifier, followed by a mixer to obtain an *intermediate frequency* (IF). In millimeter astronomy, because of the absence of good amplifiers at the radio frequency, the signal from the sky is fed directly to the mixer. The output of the mixing of the *radio frequency* (RF) signal with a local oscillator signal passes through one or several IF amplifier stages, and is then fed to a backend detector, whose output goes to a computer.

The noise of the radiometer is characterized by a receiver temperature, T_R , the temperature of an equivalent resistor with the same noise power, as given by the Nyquist formula, $P = kT_R\Delta\nu$. Normally, the receiver temperature consists of contributions from the mixer plus the IF stages, the latter being multiplied by the conversion loss, L , of the mixer, $T_R = T_M + LT_{IE}$.

The system temperature is the temperature of an equivalent resistor which would give the same noise power as the entire system, that is, the receiver, and

the contributions received by the antenna from the sky and the ground:

$$T_{sys} = T_R + T_{sky} + T_{ground} \quad (2.15)$$

where

$$T_{sky} = F_{eff} T_{amb}(1 - e^{-\tau\nu}) \quad (2.16)$$

and

$$T_{ground} = (1 - F_{eff}) T_{amb} \quad (2.17)$$

where T_{amb} is the ambient temperature (assumed to be the same for the air and the ground, in this example), and F_{eff} is the forward efficiency of the antenna. The r.m.s sensitivity, ΔT_a , of the system is given by

$$\Delta T_a = T_{sys} (\Delta\nu \tau)^{-0.5} \quad (2.18)$$

where $\Delta\nu$ = bandwidth per observing channel, and τ is the integration time on source. The *signal to noise* ratio S/N is then define as

$$S/N = \frac{T_a}{T_{sys}} \sqrt{\Delta\nu \tau} \quad (2.19)$$

2.3 Observing below the atmosphere

2.3.1 Atmospheric transmission

The Earth's atmosphere below 80km is a mixture of gases with the principle constituents nitrogen (N₂ : 78.09% by volume), oxygen (O₂: 20.95%) and argon (Ar : 0.93%). This mixture is almost constant in the lower atmosphere, but there are several minor constituents whose relative percentage may vary both with altitude and time.

The most important of these is water vapor (H₂O). Its concentration varies erratically with the local weather conditions and with altitude. Carbon dioxide (CO₂) with an average percentage of 0.03% shows both seasonal variations and a secular trend. In recent years it has come to prominence in connection with the

greenhouse effect.

The atmosphere absorbs electromagnetic radiation particularly at ultraviolet, infrared, X-ray, and gamma-ray wavelengths, while it is mostly transparent in the visible, near-infrared and radio-submm wavebands. Thus, ground-based astronomy is confined to those *atmospheric windows*. Then the ground-based astronomy observations is constrained to these windows (See Table 2.1 for a list of telescopes in the radio-FIR range).

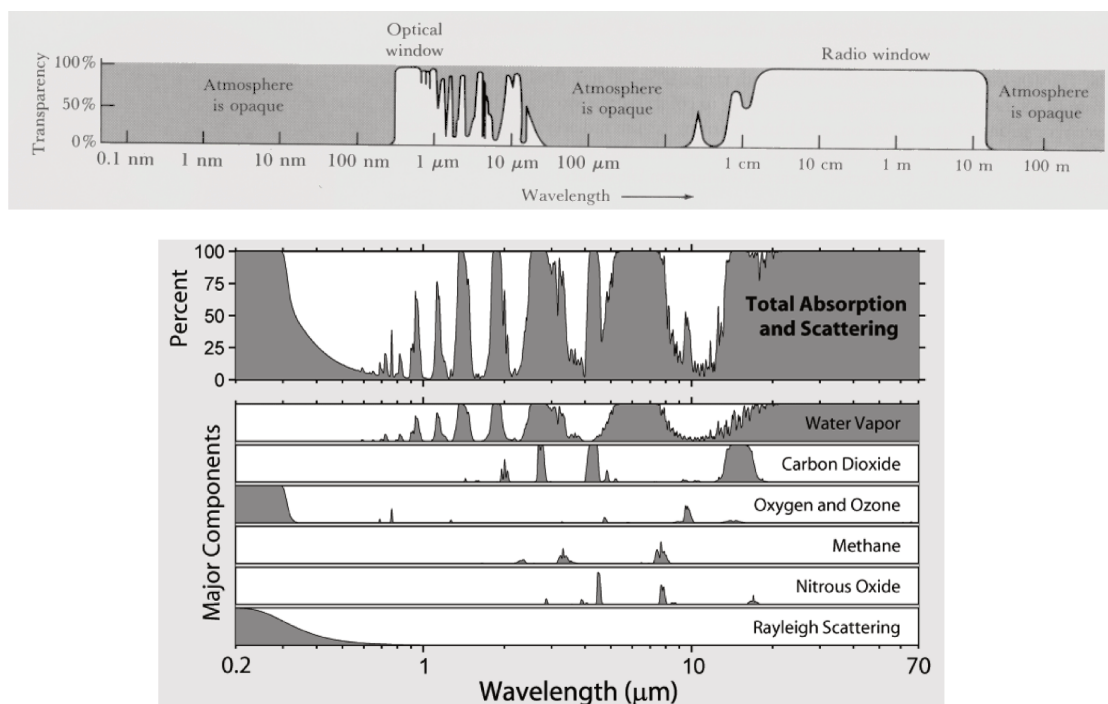
The visible window is relatively narrow in terms of frequency or wavelength from 0.3 to about 1 μm . The absorption at the short-wavelength side of the optical window is mainly caused by oxygen and ozone (O_3). (See Fig. 2.5).

As the wavelength of the radiation approaches X-rays, atomic absorption dominates, and in a very hard X-ray and gamma-ray region, nuclear absorption is the most important.

Table 2.1: The largest radio-mm-submm telescopes and interferometers to observe in radio to submm wavelengths.

Single-dish			
Telescope	Frequency range (GHz)	Diameter (m)	Localization
Arecibo	0.3 – 10	305	Puerto Rico
Effelsberg	0.3 – 96	105	Germany
GBT	0.1 – 116	100	US
Onsala	18 – 116	20	Sweden
IRAM	72 – 350	30	Ge/Fr/Spa
JCMT	215 – 680	15	UK/Nl/Ca
CSO	180 – 950	10.4	US
APEX	211 – 1390	12	Chile
Interferometers			
Telescope	Frequency range (GHz)	Antennae (m)	Localization
EVLA	0.07–50	27	US
VLBA	0.3 – 45	10	US
PdB	80 – 370	6	FR/Ge/Spa
SMA	180 – 700	4	US
ALMA	84 – 720	66	EU/N America Chile/Asia

Figure 2.5: *Top* Atmospheric transmission of the Earth's atmosphere for electromagnetic radiation. *Bottom* Radiation transmitted by the atmosphere between 0.2 and 70 μm . The pannel shows the absorption bands in the Earth's atmosphere and above the individual absorption spectrum for major greenhouse gases plus Rayleigh scattering.



The absorption band between the long-wave side of the optical window and the short-wave side of the radio window is caused mainly by infrared absorption bands of water and carbon dioxide. There are a few bands of partial transparency between 1 and 24 μm .

On the other hand, the radio window extends from frequencies around of 1 THz ($\lambda \sim 0.3$ mm) to 10 MHz ($\lambda \sim 30$ m) (Fig. 2.5). It is limited at low frequencies by the ionosphere and at high frequencies by the troposphere. The lower limit is due to the solar UV and X-rays creating a permanent, weakly ionized plasma around the Earth. Most radio astronomical measurements are made at frequencies well above this limit. At higher frequencies, observations are limited by water vapor and oxygen lines in the troposphere, of which only the 22 GHz H_2O line is partially transparent.

The partially absorbing atmosphere does not just attenuate the incoming radio signal; it also emits radio noise that can seriously degrade the sensitivity of

ground-based radio observations and refracts the signal and there are changes in the path length. Usually these effects change slowly with time, but there can also be rapid changes such as scintillation and anomalous refraction. Thus, the propagation properties of the atmosphere and detailed features of its radiation must be taken into account, if the astronomical measurements are to be interpreted properly.

2.3.2 Calibration procedure

In the millimeter and submillimeter wavelength range, the atmosphere has a large influence because the atmospheric absorption at these wavelengths can be significant, and varies with elevation. Therefore, we must make accurate corrections to obtain useful calibrated data. In addition, in the mm range, most large telescopes are close to the limits caused by their surface accuracy, so that the power received in the error beam may be comparable to that received in the main beam. Thus, one must use an appropriate value of beam efficiency.

In order to solve this atmospheric problem it is useful to take the sky itself as a calibrator source, as its signal also varies with elevation in the same way as the attenuation, so such a calibration yields the source temperature outside the atmosphere.

This calibration method, often called the *chopper wheel method* [Penzias and Burrus, 1973], defines the calibration signal to be the difference between an absorber at ambient temperature and the sky.

The procedure consists of: (1) the measurement of the receiver output when an ambient (room temperature) load is placed before the feed horn, and (2) the measurement of the receiver output, when the feed horn is directed toward cold sky at certain elevation. For (1), the output receiver while measuring an ambient load, T_{amb} , is V_{amb} :

$$V_{amb} = G(T_{amb} + T_R) \quad (2.20)$$

For step (2), the load is removed; then the response to empty sky noise, T_{sky} and receiver cabin (or ground), T_{ground} from eqs. 2.16 and 2.17, is

$$V_{sky} = G[F_{eff} T_{sky} + (1 - F_{eff}) T_{ground} + T_R] \quad (2.21)$$

where F_{eff} is the forward efficiency, this is basically the fraction of power in the forward beam of the feed. G is the varying gain factor to be calibrated out, T_R is the receiver temperature. If we take the difference of V_{amb} and V_{sky} , we have

$$\Delta V_{cal} \equiv V_{amb} - V_{sky} = G F_{eff} T_{amb} e^{-\tau_\nu} \quad (2.22)$$

where τ_ν is the atmospheric absorption at the frequency of interest. The response to the signal received from the radio source is

$$\Delta V_{sig} = G T'_A e^{-\tau_\nu} \quad (2.23)$$

Hence, solving for T'_A ,

$$T'_A = \frac{\Delta V_{sig}}{\Delta V_{cal}} F_{eff} T_{amb} \quad (2.24)$$

where T'_A is the antenna temperature of the source outside the earth's atmosphere. We define

$$T_A^* \equiv \frac{T'_A}{F_{eff}} = \frac{\Delta V_{sig}}{\Delta V_{cal}} T_{amb} \quad (2.25)$$

The quantity T_A^* is commonly referred to as the corrected antenna temperature. It can be thought of as a "forward-beam brightness temperature". It is the brightness temperature of an equivalent source which fills the entire 2π steradians of the forward beam pattern. Note that although the chopper wheel method corrects for atmospheric attenuation, it does not correct antenna temperature for all telescope losses. In particular it does not correct for the very significant telescope losses due to surface irregularities [Downes, 1989].

For an extended source filling a large part of the sky T'_A is the T_{MB} . For small sources, one must still correct for the telescope beam efficiency, which is commonly referred to as B_{eff} . Then

$$T_{MB} = \frac{F_{eff}}{B_{eff}} T_A^* \quad (2.26)$$

2.3.3 Spectral line Observations

Observing spectral lines, we can probe the physical, chemical and dynamical conditions of the interstellar matter (ISM) in the Milky Way and in external galaxies.

The intensities of the lines can tell us about gas temperature and density, the chemical composition and therefore about the abundances and the evolutionary state, the ionization and the magnetic fields.

Besides, frequencies and line widths can be used to constrain dynamical models (clouds collapse, protostellar outflows) and to derive redshifts (age and distance).

Spectral lines form through the interaction between a quantum system (molecules or atoms) and a single photon. These systems can change their states only in discrete amounts of energy ΔE . The transition between these states leads to emission or absorption of light at a single frequency $\nu = \Delta E/h$, the so called *rest frequency*.

Spectrally, this transition is seen as a line. Molecules, which consist of multiple atoms, can vibrate or rotate around an axis. When a vibrational or rotational state of molecules discretely changes, obeying quantum dynamics, they emit or absorb line radiation. Electron energy transitions as well as vibrational and rotational transitions make molecular lines.

These lines are excited, near HII regions radiatively via UV fields, in cold molecular clouds via CMB but predominantly via collisions with H_2 . In case of a level inversion one gets a maser.

Depending on the density and temperature, spectral line emission can be optically thin or thick. In the case of optical depth $\tau \ll 1$, one can look through a cloud and determine column densities and internal dynamics. For $\tau \gg 1$, one can see only the surface of an object. Using radiative transfer codes one can calculate the cloud temperature and density.

Energy uncertainty causes a small broadening, the "natural line width". Thermal motion of emitters leads to Doppler shifted line frequencies. Considering statistical ensembles one can derive a gaussian shape for the broadened line, but only the line of sight, i.e. the radial component adds to this effect. Larger Doppler

shifts can occur due to dynamical processes in molecular clouds and stars as ejecta phenomena (outflows).

To observe these spectral lines we need an heterodyne frontend, usually a down-converter from observing frequencies to a low (0-4 GHz) intermediate frequency (IF) band and a spectrometers to analyze the signal.

Spectrometers measure the frontend signal in many frequency bins across the available bandwidth. There are several techniques: (1) filter banks: a series of analog filters; complex electronics or (2) auto-correlators: special purpose computers; correlation function of time series signals; low number of bits.

As we already see the source signal is partially absorbed by the Earth atmosphere and the atmosphere itself radiates and thus contributes to the signal, the telescope beam picks up ground spillover, the receiver etc. add a signal too. To remove the atmospheric and instrumental emissions one observes the target and then a position on sky out-source. The difference of the two measurements contains only the source signal (still weakened by the differential atmospheric absorption).

On-Off measurements can be taken by moving the telescope between two positions. If the source is small, then one can use wobbler switching which is faster.

In IRAM 30-m telescope there are four different procedures available for line observations: position switching, frequency switching, wobbler switching and raster map in position switching.

Position Switching In this observing mode the antenna moves between the source position and a reference position (also called *off position*) where there is "blank sky" making a given angle. This procedure will provide the simplest means to eliminate the standing waves in the baselines. Note that the half of the observation time is spent off source.

Frequency Switching In this observing mode the local oscillator is shifted by several MHz at a rate of several Hz. The result is two spectra one shifted respect to the other. One subtract the two spectra and make an average to improve the signal to noise ratio. This mode eliminates bandpass shape from components

after the mixer. The advantage of this mode is that the integration time is larger than in the other modes because this frequency switching can be done much quicker than moving the telescope, and the antenna is always on-source.

Wobbler Switching In this observing mode the secondary reflector switch between the source and a reference position located at a wobbler throw distance from the source. The subscans are taken alternatively with telescope pointing at minus and plus the wobbler throw distance from the source (maximum 240 arcseconds), so that the reference positions are alternatively at each side of the source.

Raster mapping This procedure is equivalent to the position switching, but spectra for several positions are obtained during a single scan. Raster mapping allows to use the same reference subscan for several positions.

2.3.4 Single-dish IRAM-30m telescope

Figure 2.6: IRAM30-m antenna at Pico Veleta in Spain.



The IRAM 30-meter telescope is a single-dish antenna that was built between 1980 and 1984. It is located on Pico Veleta in Sierra Nevada, Spain, it is one of the two radio astronomy facilities operated by IRAM. In table 2.2 are indicated the principal parameters of this telescope.

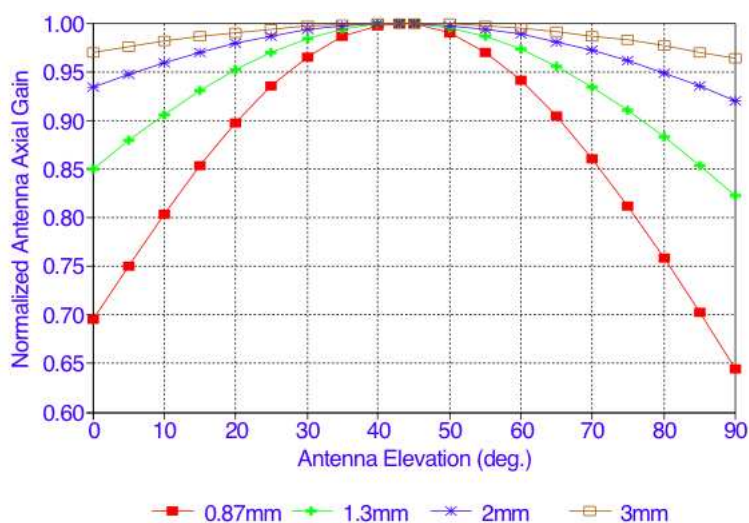
Table 2.2: IRAM 30m telescope parameters

Position	Longitude	3°23'33.7" (W)
	Latitude	37°03'58.3" (N)
	Altitude	2920 m
Parabolic main reflector	Diameter	D= 30
	Focal length	f=10.5m
	Focal ratio	f/D=0.35
Hyperbolic subreflector (wobbling)	Diameter	d=2.0m
	Eccentricity	e=1.0746
	Max. beam throw	240"
	Max. used wobblor frequency	1 Hz'
Nasmyth mirrors (flat)	Size	1.0×0.7 m
Optics	Cassegrain magnification factor	M=27.8
	Effective (equivalent) focal length	$f_e = Mf = 291.9\text{m}$
	Effective focal ratio Cassegrain system	$n = f_e/D = 9.73$
	Distance subrefelctor to Nasmyth focus	$f_c = 19.79\text{ m}$
	Focal plane scale	1" = 1.41 mm
Surface accuracy	Main reflector (1998)	70±5μm (rms)
	Reflector panels (fabrication)	26 μm (rms)
	Subreflector	15 μm (rms)
	Nasmyth mirrors	10 μm (rms)
Pointing	Pointing accuracy	2–3" (rms)
	Tracking accuracy (wind ≤ 15 m/s)	1"
Beam width (FWHM)	86 GHz	28"
	115 GHz	21"
	140 GHz	17"
	230 GHz	11"
	345 GHz	8"

The telescope is an alt-azimuth mounted Cassegrain-Nasmyth system. In order to minimize thermal deformations, the telescope is covered on the entire

outside by thermal insulation, only the panels of the panels of the main reflector are exposed to the atmospheric conditions. In addition, an active control system keeps the temperature homogeneity and gradients of the reflector backup structure well within one degree.

Figure 2.7: Gain elevatin dependence.



The main reflector is constructed on the principle of homology [von Hoerner, 1967]. It deforms under the influence of gravity such that at any elevation angle ε the best-fit surface of the deformed reflector is a parabola with deviations within the tolerance specifications of the reflector precision (generally $< \lambda/20$ of shortest wavelength of observation). Figure 2.7 shows the gain correspondant to homology deformation for four wavelengths as a function of elevation. The position of the focus and the focal length of the best-fit parabola may change with elevation, however, these effects are to a large extent compensated by corresponding shifts and tilts of the subreflector (built in computer controlled corrections). The panels are optimally adjusted for an elevation $\varepsilon_o = 43^\circ$ where gravitational deformations are eliminated by a corresponding pre-derfomation of the surface.

The 30-meter telescope is equipped with a series of single pixel receivers operating at 3, 2, 1 and 0.8 millimeters. The atmospheric conditions for increasing amount of precipitable water vapor (pwv) in air are the worst, especially for higher frequencies. The shorter wavelengths (1 and 0.8 mm) are best suited in winter, when the air is colder and drier.

It is also equipped with two cameras working at 1 millimeter: HERA with 9 pixels for the mapping of molecular gas in extended nebulae.

2.3.4.1 Receivers and backends

The IRAM 30m telescope is equipped with a series of heterodyne receivers and bolometers operating at four different wavelength bands: 3 mm (100 GHz), 2 mm (150 GHz), 1.3 mm (230 GHz), and since 2010, the 0.9 mm (330 GHz) is available.

The heterodyne receivers that can be used at the 30-m telescope are:

EMIR (Eight MIxer Receiver) It is working since April 2009. It provides a minimum instantaneous bandwidth of 4 GHz in each of the two polarizations. The four EMIR bands cover the four main atmospheric windows in the millimeter range they are denominated as E090, E150, E230, and E330 according to their center frequencies in GHz. The E150 band has SSB mixers with a single sideband available at a time, and the E090, E230, and E330 bands can be operated in 2SB mode where both sidebands are available for connection to backends. In figure 2.8 shows an overview of EMIR receiver and possible combination bands and figure 2.9 shows the atmospheric transmission for 2mm and 4mm precipitable water vapors with the EMIR bands marked together with the frequencies of a few important molecular transitions.

HERA (HEterodyne Receiver Array) consists of two arrays of 3×3 pixels with 24" spacing. This receiver has a bandwidth of 1 GHz. HERA covers a band between 215 and 272 GHz (See fig 2.9) The beam width varies between 12" and 9". The main purpose of this first multibeam spectral line receiver on the 30m telescope is to allow, together with the related backends, for rapid raster and on-the-fly imaging of spectral lines in the 1.3mm atmospheric window.

The receivers deliver 18 IF bands, every one being one GHz wide. The autocorrelator VESPA (VErsatile SPectrometer Array), is very flexible and offers a high spectral resolution but narrow band width (10–512 MHz) and thus it is not

Figure 2.8: Overview of EMIR bands. Possible band combinations: E090, E150, E230, E330, E090&E150, E090&E230 and E150&E330.

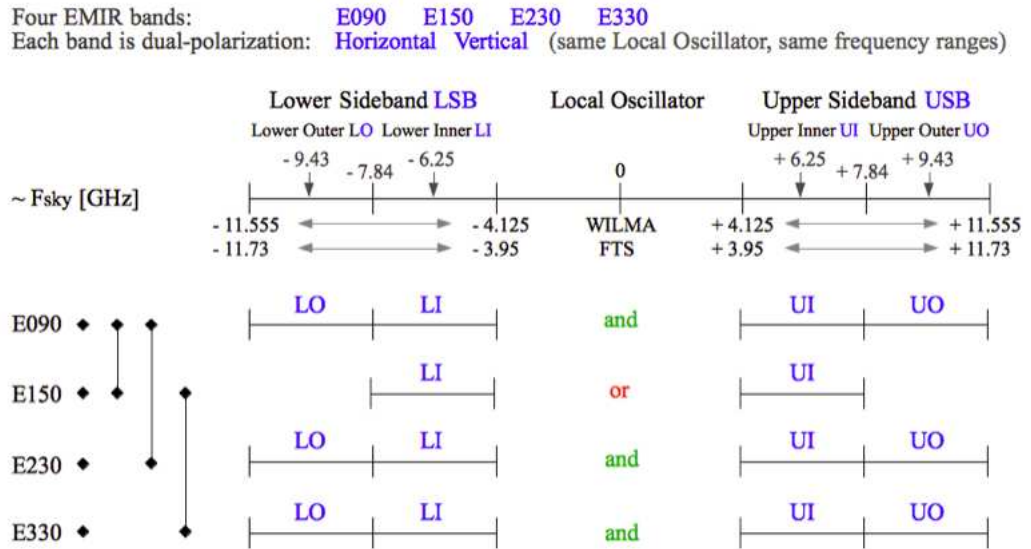
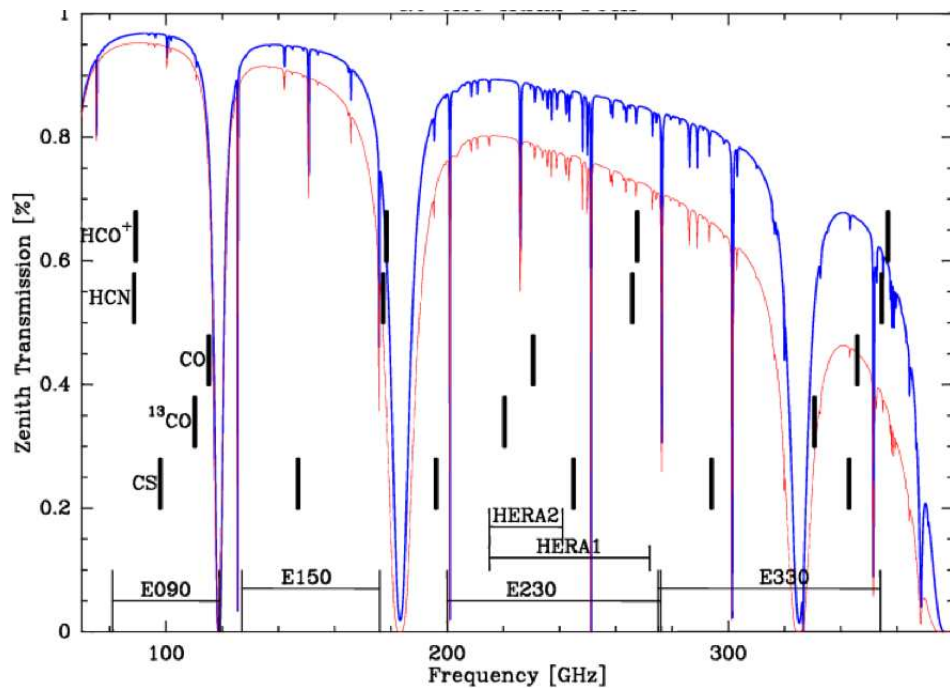


Figure 2.9: Atmospheric transmission for 2mm and 4mm of precipitable water vapors at IRAM 30m. The EMIR and HERA bands are marked together with the frequencies of a few important molecular transitions.



capable of processes the totality of the bandwidth delivered by the receivers. For this reason a special spectrometer has been designed: WILMA (Wideband Line Multiple Autocorrelator), which has no flexibility at all, but which is capable of crunching all the bandwidth at once (16 GHz ot 18×930 MHz), but with a low spectral resolution.

2.3.4.2 Software

The software used to reduce and/or analyze the data acquired with the IRAM 30M telescope and Plateau de Bure Interferometer PDBI is called GILDAS (Grenoble Image and Line Data Analysis System) software. It is a collection of softwares oriented toward millimeter and submillimeter radioastronomical applications including both single-dish or interferometric observations.

The utilities offered by GILDAS are the following:

CLASS (Continuum and Line Analysis Single-dish Software) is a software package for reducing and analyze spectroscopic data obtained on a single-dish telescope.

GREG (GREnable Graphics) is a graphic utility package whose goal is to help people prepare plots of their data or of the results of theoretical computations.

ASTRO (A Software To pRepare Observations) is a software developed to help astronomers to prepare their observations with the IRAM telescopes, for example, computing the position of sources as seen at a given time from a given location.

PAKO is a user interface used during the observations to command the telescope.

MIRA (Multichannel Imaging and Calibration Software for Receiver Arrays) is used also during the observations are carried out to reduced and view the data immediately after it has been taken.

2.4 Observing above the atmosphere

The availability of astronomical satellites starting with IRAS, and then ISO, ODIN, MSX, CHANDRA and SPITZER have increased the number of spatial

observations. Somewhat more specialized are the radio telescopes dedicated to the study of the 3 K microwave background. These include the satellite missions COBE and WMAP (See table 2.3). Taken together, these have changed our concepts of astronomy. This trend continues with the launch of the Herschel Satellite Observatory and the start of scientific measurements with the Stratospheric Observatory for Infrared Astronomy, SOFIA.

Figure 2.10: Herschel space observatory.



The Herschel Space Observatory observe at sub-mm and far infrared wavelengths with bolometer and heterodyne instruments. The antenna is a 3.5 m paraboloid made of silicon carbide, more than four times larger than any previous infrared space telescope and almost one and a half times larger than that of the Hubble Space Telescope. The structure behind the antenna is a sun shield; the structure below the main reflector is the cryostat containing the receiver systems.

Herschel is equipped with two bolometer cameras, SPIRE (covering 250-520 μm) and PACS (covering 75-170 μm , and a very high-resolution spectrometer, HIFI (covering 157-212 and 240-625 μm). The bolometers also have spectroscopic capability. The detectors in these instruments are cooled to temperatures close to absolute zero by a sophisticated cryogenic system. It is estimated that its lifetime will end in February/March 2013 until the cryostat runs out of helium.

Herschel is being operated as an observatory. About two-thirds of its observing time is available to the worldwide scientific community. The rest of the observing time is being allotted to the instrument consortia. Herschel is operating autonomously, sending acquired data to Earth over a three-hour period every

Table 2.3: List of some satellites that work(ed) from near-infrared to radio wavelengths.

Satellite	Cover band	Diameter (m)	Lifetime
IRAS	12, 25, 60 and 100 μm	0.6	Jan1983 – Nov1983
ISO (ESA)	2-240 μm	0.6	Nov 1995-May 1998
SWAS (NASA)	81.5 –92.3 GHz	0.6	Dec1998- Dec 2004
ODIN (SSC)	118.25 – 119.25GHz 486 – 504 GHz 541 – 580 GHz	1.1	Feb 2001–2012
HSO (ESA)	550 – 1900 GHz	3	Abril 1990–Jul 2007
SPITZER	3-180 m	0.85	Agust2003 –May2009
HERSCHEL	480 – 1910 GHz	3.5	May2009–Feb2013
PLANCK (ESA)	30 – 850 GHz	1.5	May2009–Dec2014

day.

Chapter 3

The source: Cep E-mm

3.1 The Cep E molecular cloud

The Cepheus E molecular cloud is one of the six molecular clouds inside the Cepheus OB3 association. This association has 40 early-type members at 725 pc [Blaauw et al., 1959] divided in two subgroups [Blaauw, 1964], Cep OB3a and Cep OB3b with ages of 7.5 and 5.5 Myr respectively [Jordi et al., 1996]. The Cepheus OB3 association has an extension of 20×60 pc and a average radial velocity of -10 km s^{-1} [Sargent, 1977] (See Figure 3.1).

The Cepheus E molecular cloud was first identified by [Sargent, 1977] by CO (1-0) maps over the region of Cepheus OB3. Sargent's CO observations revealed the presence of several molecular clouds in the Cepheus OB3 association. She labeled them as Cep A, B, C, D, E, F (See Figure 3.2).

The Cep E molecular cloud has a size of ~ 1.5 pc, $T_{ex} \sim 17$ K and a density $n(\text{H}_2)$ about $2.1 \times 10^3 \text{ cm}^{-3}$ estimated from $^{18}\text{CO}(J=1-0)$ maps following the assumption of LTE [Yu et al., 1996].

The Cepheus OB3 association was mapped at the positions of the strongest CO emission detected by [Sargent, 1977] in the $1_{11}-1_{10}$ transition of formaldehyde at 6cm wavelength, showing that the Cep E molecular cloud is the second most massive (M_{H_2} of $2100 M_{\odot}$) and dense of the Cep OB3 molecular clouds [Few and Cohen, 1983]. Thermal NH_3 and OH (1665/1667 MHz) emission [Wouterloot et al., 1988] have been also detected toward Cepheus E molecular cloud.

Figure 3.1: The Cepheus OB3 active star formation region overlaid on the map of visual extinction, obtained from 2MASS [Lombardi and Alves, 2001]. Large circles denote the clouds associated with young stars. The meaning of the different symbols are as follows: Filled triangles are T Tauri stars, filled squares are Herbig Ae/Be stars, filled circles are weak-line T Tauri stars, open squares are photometric candidate and possible PMS members, X are H_{α} emission stars, crosses are T Tauri candidates. For details see [Kun et al., 2008].

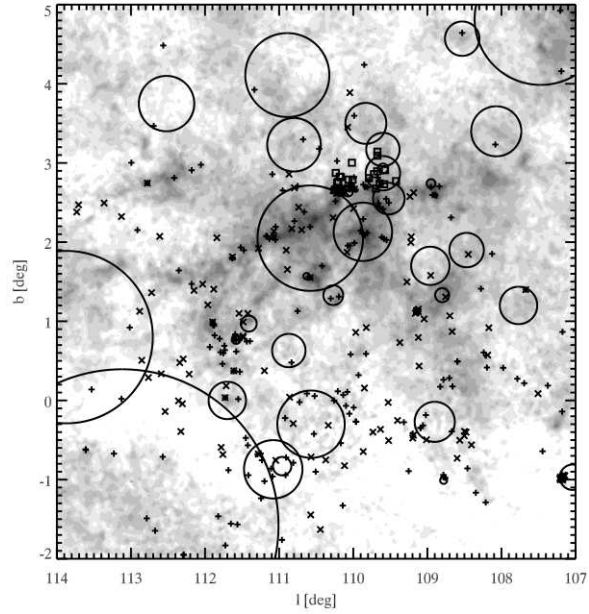
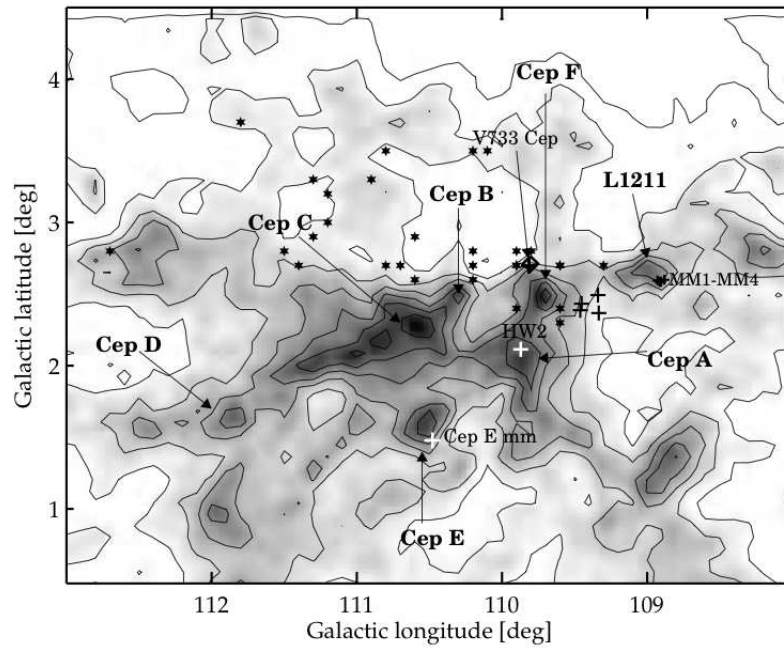


Figure 3.2: Cep OB3b region. In the image the molecular clouds Cep A to Cep F, the dark cloud Lynds 1211, as well as the most prominent associated young stars are labeled. In contours the distribution of the visual extinction [Dobashi et al., 2005]. The lowest contour of the extinction is at $A_V = 1$ mag, and the increment is 0.7 mag. For details see [Kun et al., 2008].



Finally, during a survey carried out by [Wouterloot and Walmsley, 1986] using 100-m Effelsberg telescope to detect H₂O maser-emission from the Cepheus molecular clouds, they found eleven new sources, among them Cep E-mm source, or IRAS 23011+6126.

3.2 The Cepheus E-mm source

In the interior of the Cep E molecular cloud is embedded the Cep E mm source, (hereafter called just Cep E). Cep E coordinates are $\alpha(2000)$ 23h 03m 13s, $\delta(2000)$ 61° 42' 21". (See Figure 3.2.)

Several authors have studied this source, after the first identification by [Lefloch et al., 1996] as a bona fide Class 0, according to the criteria established by André, Ward-Thompson, & Barsony 1993 (See section 1.2.4). [Crimier et al., 2010], [Moro-Martín et al., 2001] studied the properties of the molecular gas and dust envelope. [Froeblich et al., 2003b] studied the nature of the central protostellar source, which was questioned at about the same time by [Noriega-Crespo et al., 2004].

All these studies allow to constrain the source Cep E parameters as reported in Table 3.1.

Table 3.1: Cep E protostar parameters.

Parameter	Value	Reference
Distance	730 pc	[Blaauw et al., 1959]
Age	3×10^4 yr	[Froeblich et al., 2003b]
L_{bol}	100 L _⊙	[Lefloch et al., 2011]
Envelope mass	35 M _⊙	[Crimier et al., 2010]
Envelope size	~50"	[Crimier et al., 2010]

3.2.1 The dusty envelope

The protostellar envelope emits in the millimeter continuum, due to the dust emission of all the material surrounding the protostar.

There was some debate on Cep E belonging to Class 0 or Class I classes. Based on millimetric observations [Moro-Martín et al., 2001] affirmed that the SED of

Figure 3.3: Spectral energy distribution of Cep E-mm (IRAS 23011+6126) source observed and modeled. Taken from [Crimier et al., 2010].

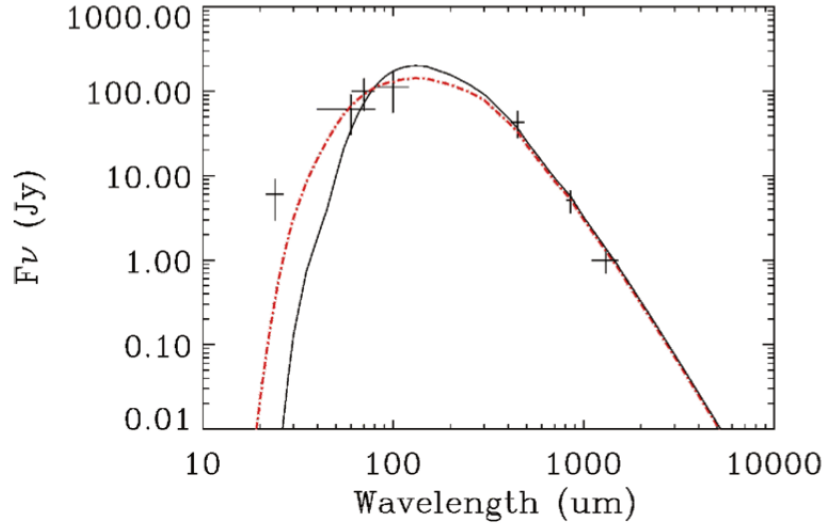
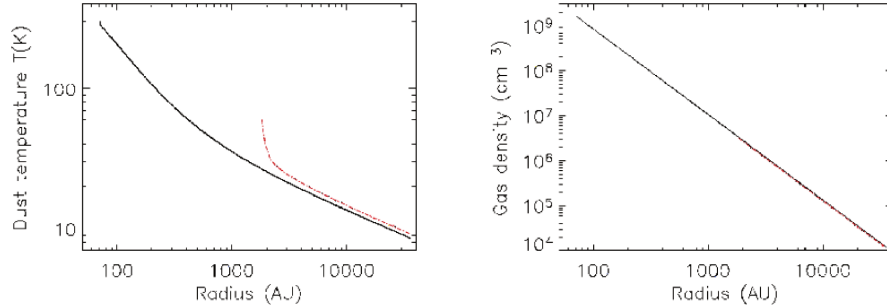


Figure 3.4: Cep E-mm dust temperature (*left panel*) and H₂ density (*right panel*) profiles from the best-fit model. For details see [Crimier et al., 2010].



Cep E resembles that of a Class I source rather than a Class 0 as proposed by [Lefloch et al., 1996]. In order to clarify the nature of Cep E, several studies were carried out (e.g., [Chini et al., 2001] with SCUBA, [Froebrich et al., 2003b] with ISO and [Noriega-Crespo et al., 2005] with Spitzer). All these studies confirm the Class 0 status of Cep E.

The observed Spectral Energy Distribution (SED) (see Fig. 3.3) and the 350, 450 and 800 μm maps together with modeling of the emission permit to derive the physical structure as the density and temperature profiles (see Fig 3.4 from [Crimier et al., 2010]).

In their study, [Crimier et al., 2010] derived the dust temperature and density

profiles for a IM-protostars sample, finding that Cep E shows a density profile consistent with the inside-out collapse theory [Shu, 1977], where the envelope density follows a single index power law with $\alpha=1.9$ at wavelengths larger than $60 \mu\text{m}$. This is;

$$n(r) = n_0 \times \left(\frac{r_0}{r}\right)^\alpha \quad (3.1)$$

where the power law index, α , the density, n_0 , at r_0 are free parameters of their model. The envelope is assumed to start at a radius r_{in} and extends to r_{out} .

In the Table 3.3 are listed the input parameters as well as the best fit parameters and some relevant physical quantities obtained from the radiative transfer analysis of Cep E protostar. Crimier et al. found that the maximum difference between T_{dust} and T_{gas} is 5K so gas and dust are coupled.

This model yields a mass envelope of $35 M_\odot$ and a best fit value for the luminosity of $100 L_\odot$.

Others envelope mass values have been obtained by others authors assuming power law-density $\sim 13 M_\odot$ and bolometric luminosity of $\sim 30 L_\odot$ [Moro-Martín et al., 2001]; [Noriega-Crespo et al., 2004] a constant density over a spherical volume; $10 M_\odot$ [Ladd and Howe, 1997] and in dust temperature dependent models; $18 M_\odot$ [Lefloch et al., 1996]. SED models based on a grey body approximation [Froeblich et al., 2003b] predict $\sim 78 L_\odot$ and a envelope mass of $7 M_\odot$ taking a $\beta=1.0\pm 0.3$, where β is the submm slope of the SED. The summary of these studies are listed in Table 3.2.

Table 3.2: Cep E envelope parameters calculated from different models.

Model	M_{env}	L_{bol}	Reference
grey body approximation		$78 L_\odot$	[Froeblich et al., 2003b]
power-law density and temperature distributions		$30 L_\odot$	[Moro-Martín et al., 2001]; [Noriega-Crespo et al., 2004]
dust temperature dependent models		$100 L_\odot$	[Lefloch et al., 1996]
power-law density	$35 M_\odot$		[Crimier et al., 2010]
grey body approximation	$7 M_\odot$		[Froeblich et al., 2003b]
power-law density	$13 M_\odot$		[Moro-Martín et al., 2001]; [Noriega-Crespo et al., 2004]
constant density over a spherical volume	$10 M_\odot$		[Ladd and Howe, 1997]
dust temperature dependent models	$18 M_\odot$		[Lefloch et al., 1996]

Table 3.3: Summary of the dust radiative transfer analysis for Cep E protostar. Adapted from [Crimier et al., 2010].

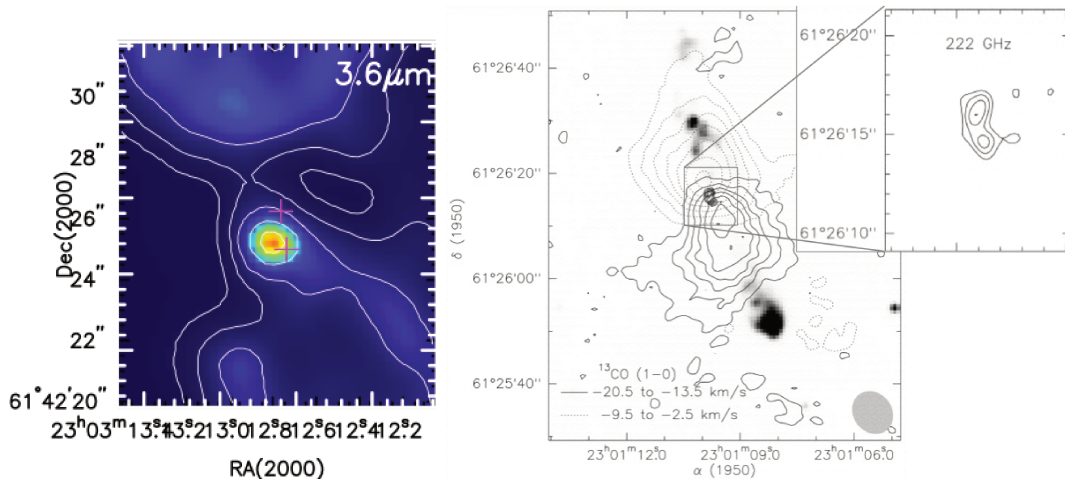
Fixed input parameters	
Stellar temperature, T_\star	5000 K
Dust temperature at r_{in} , T_{in}	300 K
Dust opacity (OH5) at 100 μm , κ_{100}	86.5 $\text{cm}^2 \text{g}^{-1}$
Best-fit parameters & physical quantities	
Source	Cep E
Distance, (pc)	730
Luminosity, (L_\odot)	100
Dust optical depth at 100 μm , τ_{100}	5.0
Density power law index, α	1.9
Envelope thickness, Y ($= r_{\text{out}}/r_{\text{in}}$)	500
χ_{red}^2 -maps	0.11
χ_{red}^2 -SED	0.80
Inner envelope radius, r_{in} , (AU)	70
Outer envelope radius, r_{out} , (AU)	35 800
Radius at $T_{\text{dust}} = 100 \text{ K}$, $r_{100 \text{ K}}$, (AU)	223
H ₂ density at $r_{100 \text{ K}}$, n_0 , (cm^{-3})	2.0×10^8
Envelope mass, M_{env} , (M_\odot)	35
$(T_{\text{dust}} - T_{\text{gas}})_{\text{max}}$, (K)	5

3.2.2 Single or binary protostar

Cep E is proposed to be a double source separated by 1.4'' (~ 1000 AU) based on continuum images at 22 GHz [Moro-Martín et al., 2001]. (See Fig. 3.5 at the right).

Moreover, line and continuum observations (See section 3.3), showed two separate outflows structures emanating from the mm central source suggesting the presence of a second driving source (e.g. [Eisloffel et al., 1996], [Ladd and Hodapp, 1997]) See Figures 3.5 and 3.10. However, [Velusamy et al., 2011] do not find any evidence of a double source in the IR bands using the Spitzer imaging with a subarc resolution ($\sim 0.6'' - 0.8''$) enough to resolve any double source separated by 1.4''. These observations imply that Cep E-mm is a binary with a separation smaller than $\sim 1''$. This issue is still under discussion.

Figure 3.5: (left) HiRes (Spitzer) maps of the inner 10'' region around the Cep E protostar. The crosses represent the positions of the mm double source from [Moro-Martín et al., 2001]. Taken from [Velusamy et al., 2011]. (right) Superposition of the H₂ 1-0 S(1) 2.12 μm emission (gray scale) on the ¹³CO and 222 GHz continuum in contours. The dashed contours toward the north correspond to the redshifted lobe ($v_{LSR} = -9.5$ to -2.5 km s⁻¹), while the solid contours to the south correspond to the blueshifted lobe ($v_{LSR} = -20.5$ to -13.5 km s⁻¹). Note that the 222 GHz continuum trace a double component. Adapted from [Moro-Martín et al., 2001].



3.2.3 Chemical properties

A chemical study of Cep E envelope was carried out by [Alonso-Albi et al., 2010] among a sample of seven intermediate-mass Class 0 candidates: Cep E, Serpens-FIRS 1, L1641 S3 MMS 1, IC1396N, CB3, OMC2-FIR4 and NGC 7129-FIRS 2 and two Class 1 IM stars; S140 and LkH α 234. They studied the CO depletion and N₂H⁺ deuteration. Based on millimeter line observations of C¹⁸O, C¹⁷O, N₂H⁺ and N₂D⁺ they found hints on the chemical evolution from Class 0 to Class 1 stars.

While the emission of the N₂H⁺ (1–0) peaks towards the star position in Class 0 protostars, it surrounds the FIR source in the case of Class 1 stars due to the recently formed star which heat and disrupts the core.

On the other hand, the deuterium fractionation N₂D⁺/N₂H⁺ is low (<a few 0.001) in the Class 1 sources. But for Class 0 sources the values range between a few 0.001 to a few 0.01. These authors found that Cep E belongs to a group of high deuterated sources that have values of $N(N_2D^+)/N(N_2H^+) > 0.01$ (See Section 4.7). The deuterium fractionation of N₂H⁺ strongly depends on the CO

depletion factor and the gas temperature [Roberts et al., 2003].

However, it is not possible to establish an evolutionary trend among Class 0 sources based on simple parameters such as the average CO depletion and the average N_2H^+ deuterium fractionation. This is due to the complexity of these regions and because the observations do not reach the sufficient angular resolution to trace the inner regions of the envelopes.

Alonso-Albi et al. derived also the radial abundance profiles across the sample envelopes of C^{18}O , N_2H^+ and N_2D^+ . Their results on Cep E are showed in the Figure 3.6.

Using a spherical-envelope steady-state chemical models [Caselli et al., 2002] and assuming a CO binding energy of ~ 1100 K [Alonso-Albi et al., 2010] failed to reproduce their observations towards Cep E. The qualitative behavior is reproduced for the C^{18}O and N_2H^+ emission, but the model reproduces the line integrated intensities poorly. The line intensity predictions are a factor of 2-4 higher than the observations. Increasing the CO binding energy and thus reducing the efficiency of cosmic-ray-induced desorption does not improve the fit (see model 2 in 3.6). In addition, this also causes an increase in deuterium fractionation, which is not observed.

The authors propose that this discrepancy is due to the assumption of spherical geometry in the model and which do not take into account important phenomena like bipolar outflows and UV radiation from the star.

3.3 Cepheus E bipolar outflow

Cep E drives a bipolar outflow. The first detection was obtained by Fukui in 1989, as part of an IRAS data base survey. Years later, in 1994 the first image of Cep E was taken by Hodapp during the near-infrared K'-band imaging survey of all regions associated with CO molecular outflows from the list of Fukui 1989 (Fig. 3.7). Hodapp described the bright and compact object as a bipolar nebula, however it was not possible to know if it was a reflexion nebula or a line emission region.

The next year, Eislöffel and colleagues, carried out a near-infrared imaging survey for molecular hydrogen emission in CO outflows. They found that Cep E

Figure 3.6: (*top*) Model 1: In the first panel shows the standard chemical model for Cep E assuming a binding energy of 1100 K. The $C^{18}O$ abundance is shown in black, N_2H^+ in red, and N_2D^+ in blue. In the center; comparison between the predicted $C^{18}O$ 1 \rightarrow 0 line intensities (continuous line) and the observed values (filled squares). At the right: the same for N_2H^+ 1 \rightarrow 0. (*middle top*) Model 2. (*middel bottom*) Model 3 (*bottom*) Model 4. Taken from [Alonso-Albi et al., 2010].

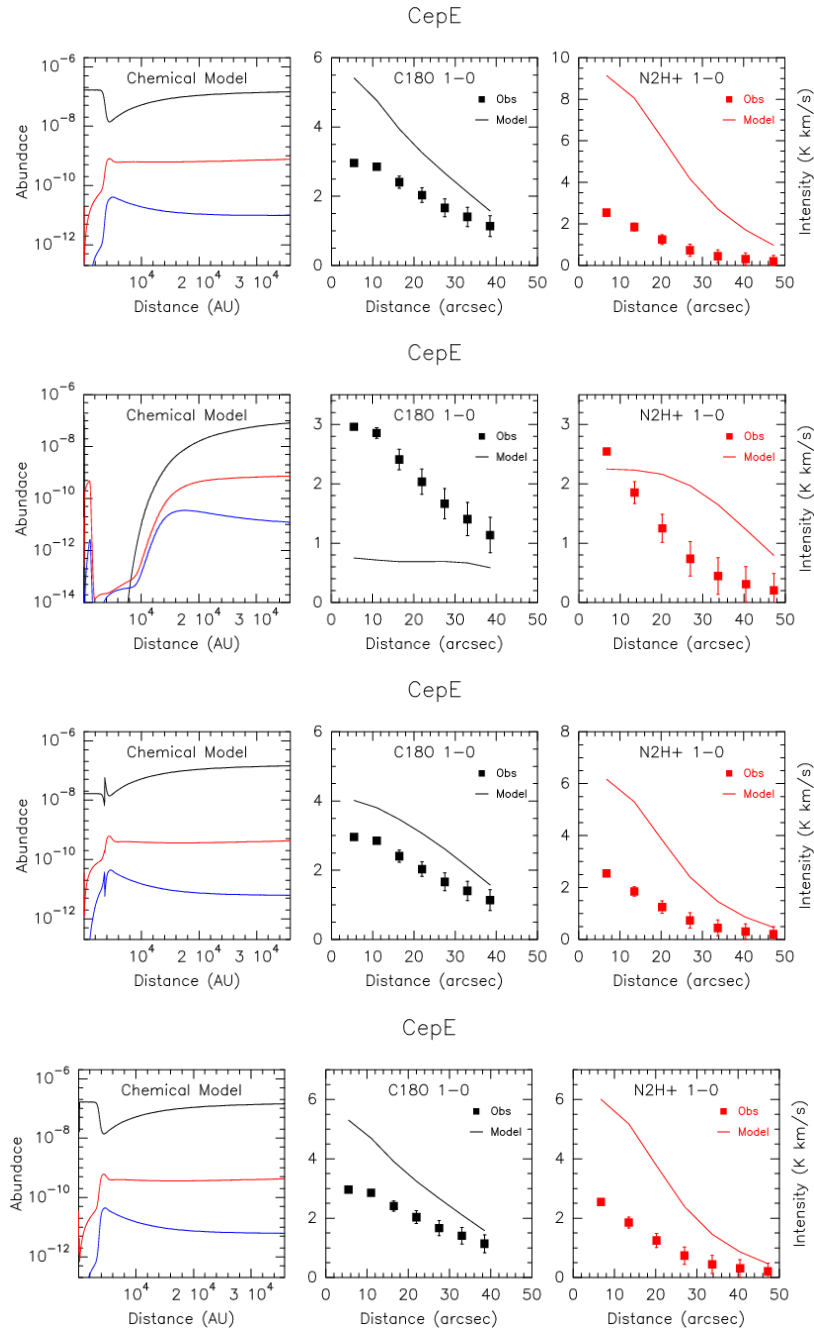
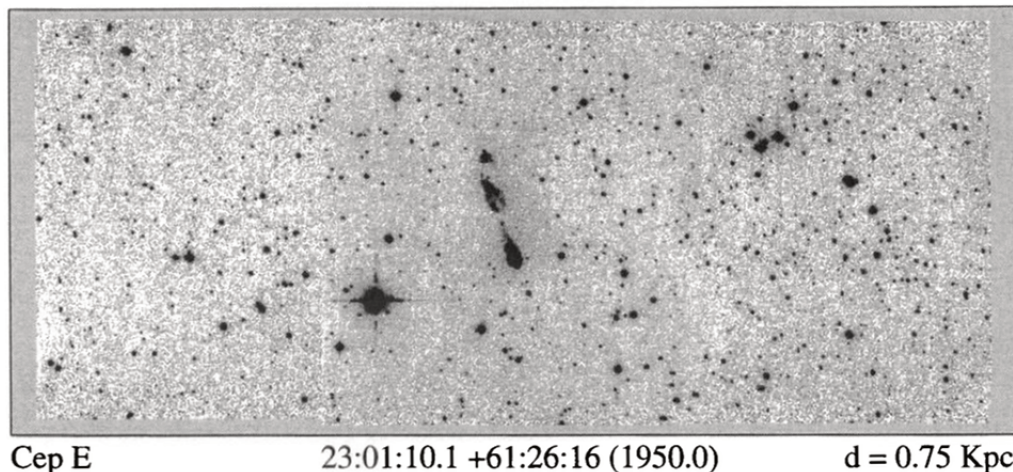


Figure 3.7: K' band image of the Cep E region in a $\sim 8' \times 3'$ field. In the center of the image we see the double lobe morphology of the Cep E outflow. Taken from [Hodapp, 1994].



is very bright in the H_2 1–0 S(1) line at $2.12 \mu\text{m}$.

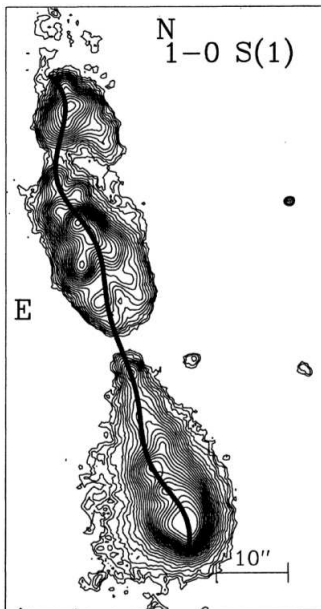
[Eisloffel et al., 1996] studied in detail the excitation of the molecular hydrogen in the outflow trying to elucidate what kind of shocks explained the observations and they concluded that as the line ratios were essentially constant everywhere in the outflow neither model of slabs or planar J- or C-shocks can explain the data, but bow-shock do, especially C-bow shocks.

As we already mentioned in section 3.2.2, they also found two H_2 knots almost perpendicular (70°) to the north-south bipolar outflow that they interpreted as a second outflow (Fig.3.10).

The wiggly morphology of the southern lobe and regular sideways positional offsets of the bows in the northern lobe were interpreted as due to precession. The model for this precession estimates an angle of 4° , a length scale of $22''.8$, and a precession period of 400 yr, assuming an outflow velocity of 200 km s^{-1} (this assumption is consistent if we take into account the proper motion and CO line observations that show outflow radial velocities between -150 and 100 km s^{-1}) and a distance of 730 pc to Cep E. (See Figure 3.8).

In the same period, observations of $^{12}\text{CO}(2-1)$ and the $\text{SiO}(3-2)$ lines were carried out with IRAM 30m by [Lefloch et al., 1996]. This molecular emission traced again the bipolar structure seen by [Eisloffel et al., 1996] in molecular hydrogen

Figure 3.8: Contour plot of Cep E in H_2 1-0 S(1) emission line. The solid line trace the precession model plotted over the 1-0 S(1) line contours of Cep E that can explain the wiggle structure in the southern lobe and the regular sideways positional offsets of the bows of the northern lobe. Taken from [Eisloffel et al., 1996].



lines. [Lefloch et al., 1996] estimated an age for the outflow of about 3×10^3 yr. The $^{12}\text{CO}(2-1)$ line presents high velocity wings extended up to -125 km s^{-1} relative to the ambient gas ($v_{lsr} \approx -11 \text{ km s}^{-1}$) in the blue-shifted lobe and to 80 km s^{-1} in the red-shifted lobe (Fig. 3.9).

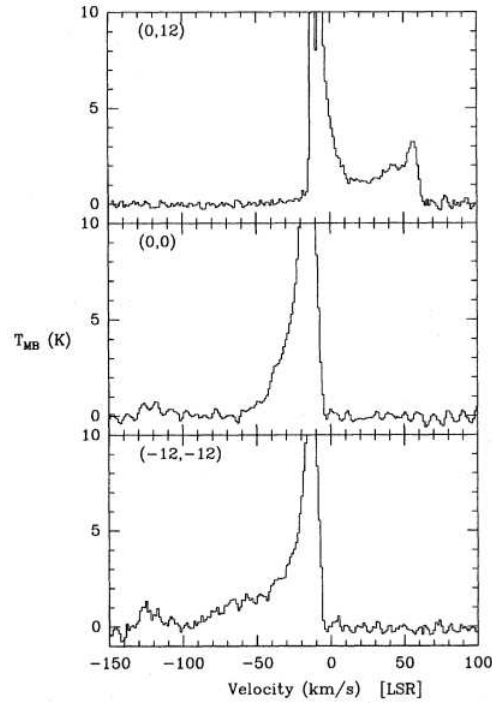
In addition, the Cep E outflow shows the presence of *bullets* of high-velocity material, in both lobes, situated symmetrically at almost the same distance from the central source, with average velocities of 100 km s^{-1} and 70 km s^{-1} relative to the ambient gas.

The outflow lobes are relatively compact, with a typical size of $\approx 30'' \times 10''$ at half power. The estimated kinematical ages for the blue and red lobe are 1.1×10^3 and 1.8×10^3 yr respectively [Lefloch et al., 1996].

The $\text{SiO}(3-2)$ emission traces the high-density material of the bullets detected by ^{12}CO lines, and not the ambient gas. Comparison with the H_2 observations [Eisloffel et al., 1996], and the continuum 1.25 mm dust emission [Lefloch et al., 1996] suggests that outflow interacts strongly with the circumstellar material, sweeping up the gas and dust of the parental envelope.

In addition, water emission has been detected in the high-velocity gas close to

Figure 3.9: $^{12}\text{CO}(2-1)$ emission at three different positions respect to the reference position of the IRAS 23011+6126 source. The *top* panel shows line emission comes from north lobe, a first component is centered at the ambient velocity ($\approx -11 \text{ km s}^{-1}$) and it extends to red velocities up to reach a second component that peak at about 50 km s^{-1} . The *middle* panel shows emission comes from the central source, the spectrum display a main component centered at ambient velocity and weak emission comes from the blue-shifted velocities. The *bottom* panel exhibit the spectrum comes from the south lobe. It shows again a bright component at ambient velocity and a second component that peak around -125 km s^{-1} . These second components at high velocities are interpreted as evidence of the presence of jets. [Lefloch et al., 1996].



the protostar by [Lefloch et al., 2011]. They observed a masing line at 183 GHz, in order to elucidate the origin of water emission in protostellar systems. This water emission can be observed only at the IRAM 30m telescope, under excellent and stable weather conditions in winter. Although this emission is unresolved in the main-beam of the IRAM30m telescope, the authors used PdB observations at $2''$ of resolution to help establish the origin of the emission detected, and the physical conditions in the emitting gas. Assuming an ortho-to-para ratio of 3, it is possible to derive a water column density of $N(\text{H}_2\text{O}) \approx (1.2-8.0) \times 10^{17} \text{ cm}^{-2}$.

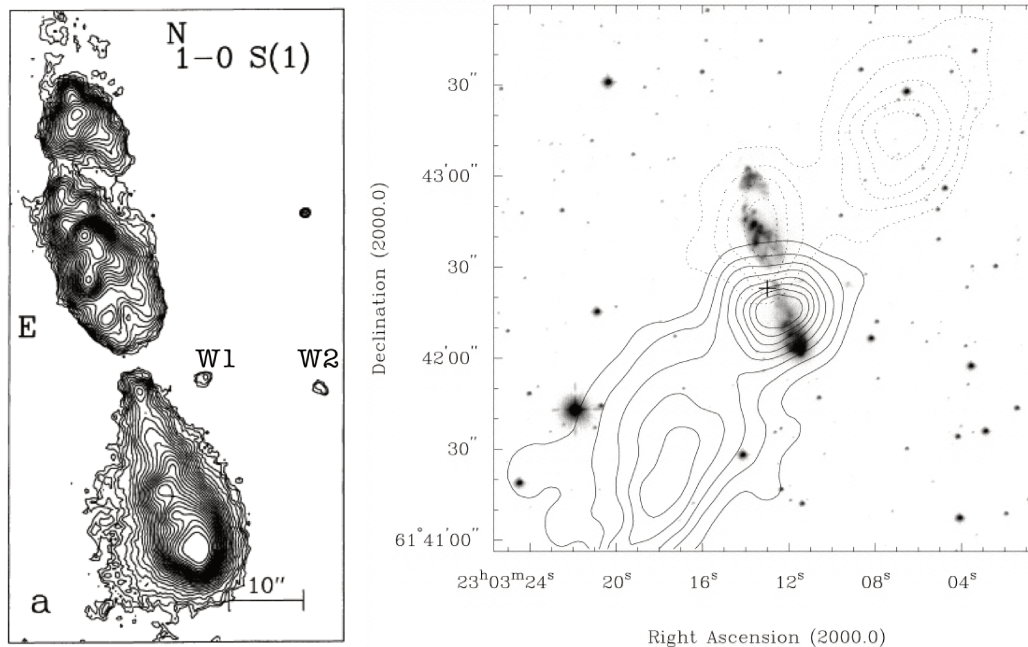
The jet gas kinetic temperature and column density values were determined by [Lefloch et al., 2011] obtaining a $T_K \approx 120 \text{ K}$ and a $N(\text{CO}) \approx 2.5 \times 10^{17} \text{ cm}^{-2}$, adopting the standard value for the CO abundance in the gas, we have $N(\text{H}_2) \approx 2.5 \times 10^{21} \text{ cm}^{-2}$. Based on the ratio SiO $J=8 \rightarrow 7$ to $J=3 \rightarrow 2$ the authors estimate

a column density of $N(\text{SiO}) \approx (2.0\text{--}3.3) \times 10^{14} \text{ cm}^{-2}$ for gas at 120 K in the blue- and redshifted components.

As part of an attempt to clarify the nature of Cep E source and its outflows, other studies were carried out towards Cep E region. [Ladd and Hodapp, 1997] reported the presence of another bipolar outflow structure traced in $^{12}\text{CO}(2\text{--}1)$ emission with the James Clerk Maxwell Telescope (see Fig. 3.10), in addition to the H_2 north-south bipolar outflow reported by [Eisloffel et al., 1996].

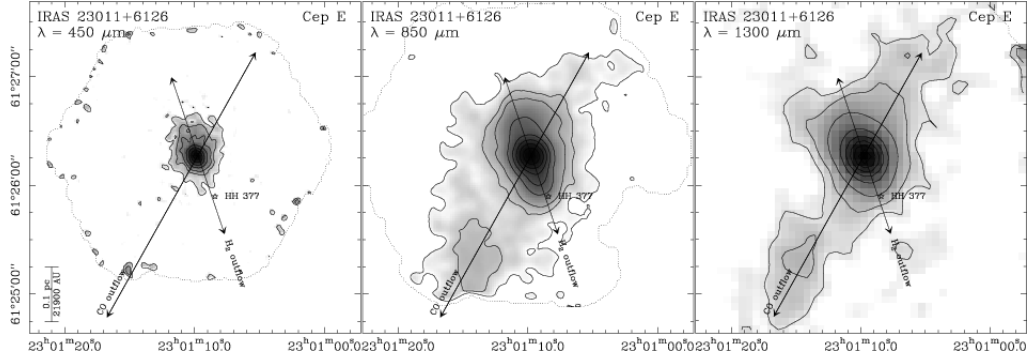
At small scale a north-south flow of 0.1 pc (projected size scale) is traced by the shock-excited H_2 emission. And at large scales another CO outflow of 0.35 pc is centered on the IRAS source but not associated with the S(1) emission [Ladd and Hodapp, 1997] (See Fig. 3.10).

Figure 3.10: (left) H_2 1 – 0 S(1) contour map shows the bipolar structure of Cep E. There are also two H_2 knots at the west of the IRAS source region labeled as W1 and W2. [Eisloffel et al., 1996] interpret these knots as a second independent outflow and, therefore, the presence of a second outflow source can be inferred. (right) Cep E could be a double or multiple system. In gray scale, the $2.12 \mu\text{m}$ S(1) emission from H_2 overlaid to contours of redshifted $[-6 \text{ to } 0 \text{ km s}^{-1}]$ (dotted) and blueshifted $[-14 \text{ to } -20 \text{ km s}^{-1}]$ (solid) ^{12}CO J= 2–1 emission. Both maps are centered on the IRAS source. For details see [Ladd and Hodapp, 1997].



Additional studies of the circumstellar dust around Cep E [Chini et al., 2001] carried out with SCUBA in the 850 and 1300 μm confirm the presence of these two bipolar outflow structures observed by [Ladd and Hodapp, 1997] (See Fig.

Figure 3.11: The figure shows the 450, 850 and 1300 μm images of the IRAS 23011+6126 region. The dust emission trace the quadrupolar outflow observed by [Ladd and Hodapp, 1997] (See text). Taken from [Chini et al., 2001].



3.11). The elongation of the central source at the higher level contours at 450 μm in the north-south direction is coincident with the bipolar outflow detected in molecular hydrogen by [Eisloffel et al., 1996]. The southern lobe is coincident with HH 377 (See section 3.4). The low-level emission seen at 850 and 1300 μm to the south-east is coincident with the bipolar outflow structure detected in ^{12}CO J= 2–1 by [Ladd and Hodapp, 1997].

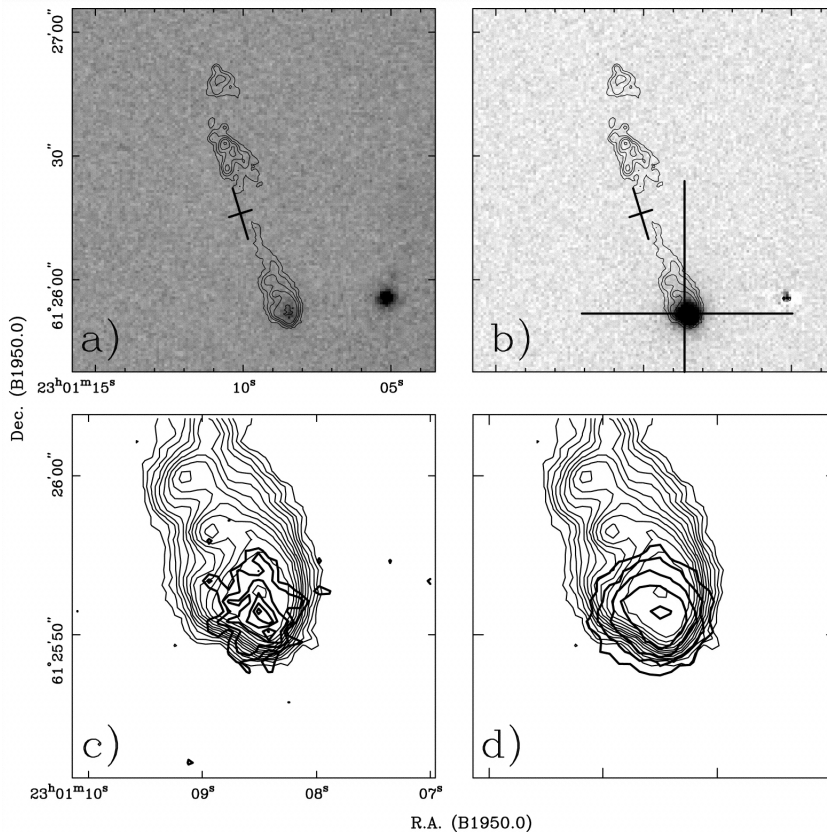
In summary, the observations indicate the presence of two bipolar outflow structures, a north-south bipolar outflow traced by H_2 1 – 0 S(1), a south-east bipolar outflow traced by ^{12}CO J= 2–1. A group of knots suggest the presence of a single lobe traced also by H_2 1 – 0 S(1) eastward. However, it is not clear so far if this is a binary or multiple source or a time and angle variable driving source that generate these outflow structures. This issue is still open.

3.4 HH 377

[Noriega-Crespo and Garnavich, 1997] detected the optical counterpart of the southern bowshock observed at 2 μm by [Eisloffel et al., 1996]. This optical knot was observed in $\text{H}\alpha$ and [SII] $\lambda\lambda 6717, 6731$ emission and has been named HH 377 by [Devine et al., 1997].

The structure of the H_2 outflow and the optical emission of only one compact knot is illustrated in Figure 3.12. In this figure there are H_2 1-0 S(1) contour maps of Cepheus E, overlaid on gray-scale and contour representations of optical

Figure 3.12: Panel (a) shows a H_2 1-0 S(1) contour map overlaid with gray-scale representations of the $H\alpha$ image. In panel (b) again the H_2 1-0 S(1) contour map overlaid with the [S II] $\lambda\lambda 6717, 6731$ image. Panels (c) and (d) are closed-ups to the bowshock region. They show the $H\alpha$ and [S II] 6717, 6731 images (respectively) as dark contour maps, over the H_2 light contours. Taken from [Ayala et al., 2000].



images at left with $H\alpha$ and at the right with [SII]. These maps clearly show the coincidence between the optical knot and the brightest region of the southern lobe of the IR flow. Cep E Herbig Haro object is one cases like HH 1–2 [Davis et al., 1994] where the J-type (inferred from the optical spectra) and C-type (inferred from the IR spectra) seems to coexist spatially [Ayala et al., 2000].

HH377 has characteristics typical of low-excitation ($\sim 1\%$ ionization) Herbig-Haro objects and an anomalous high electron density, $n_e \sim 4100 \text{ cm}^{-3}$, suggesting an unusually high preshock density of $\sim 10^5 \text{ cm}^{-3}$ [Ayala et al., 2000]. The proper motion of this optical knot is $107 \pm 14 \text{ km s}^{-1}$ [Noriega-Crespo and Garnavich, 2001] with a radial velocity of $-70 \pm 10 \text{ km s}^{-1}$ [Ayala et al., 2000].

Hydrodynamic models of molecular jets have been produced to simulate observed molecular outflows from protostellar sources e.g., [Suttner et al., 1997]. In

their work they carried out 1D, 2D and 3D simulations of molecular jets to model observed complex structure of the jets. The simulated emission maps are in good correspondence to a number of observations of deeply-embedded outflows. They compare the 3D simulated images of the 1–0S(1) H₂ emission to a sample of observed outflows; Cep E, HH21, HH212, HH288 and L1634. They remarked that the H₂ lines peak at the bow shock, 1–0S(1) being somewhat more extended than 2–1S(1). At the tip the emission originates mainly from shocked jet gas, in the wings ambient H₂ survives and radiates. A bow-like arc upstream of the main bowshock is formed and similar features had been observed in protostellar jets e.g. HH288, L1448, DR 21 [Davis and Smith, 1996]. Rotating the simulated images this bowshock looks like an elongated knot similar to HH212 [Zinnecker et al., 1996] and HH211 [McCaughrean et al., 1994]. So authors achieve to reproduce features which seem to be multiple bow shocks are generated naturally by continuous jet.

[Suttner et al., 1997] found that Cep E jet require a jet density of 10⁵ cm⁻³, they remark that even if the density in optical jets is hardly above 10³ cm⁻³ this value is due to: (1) the hydrogen molecule is observed to be close to LTE, (2) the overall energetics require high densities (3) dense clumps and cores have been deduced from observations, (4) jets would take excessively long time to escape from cores if their density were relatively low. This value is consistent with the [Ayala et al., 2000] and later with the [Smith et al., 2003] results. This could be a sign of a very early stage of jet development and support the scene in which Cep E is a very young outflow breaking through its parental molecular core.

In Table 3.4 we present a summary of Cep E outflow properties, how they were deduced and their references.

3.5 Shock models of Cep E

Many authors have tried to interpret the wealth of observations toward Cep E making use of shock models (e.g., [Eisloffel et al., 1996], [Ayala et al., 2000], [Smith et al., 2003], [Noriega-Crespo et al., 2004]). The comparison between the measured fluxes and the predictions from two different shock models, C-type and J-type, can help to constrain the properties of the outflows (shock velocity,

Table 3.4: Summary of the Cep E outflow properties.

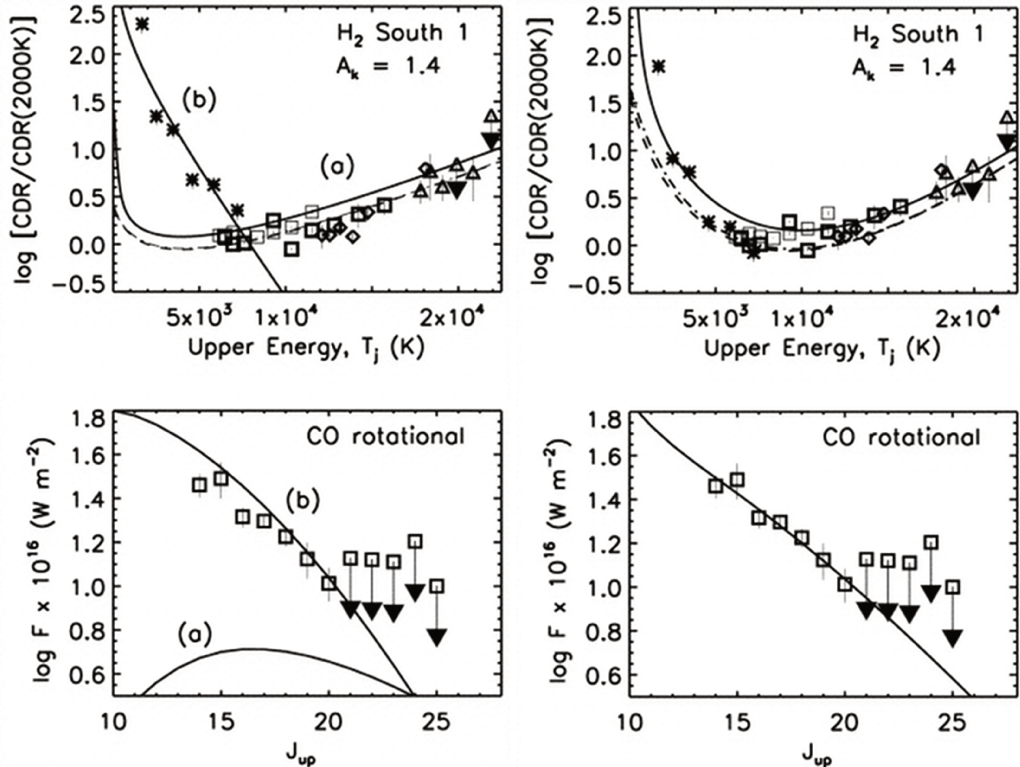
		Tracer	Resolution	Reference
Outflow structure	bipolar	^{12}CO (1-0)	$\sim 3'$	[Fukui, 1989]
Driven source	IM Class 0 Cep E			[Lefloch et al., 1996]
Distance	730 pc			[Blaauw et al., 1959]
Bolometric luminosity	$10 L_{\odot}$			[Lefloch et al., 2011]
CO kinetic luminosity	$0.2 L_{\odot}$	CO		[Moro-Martín et al., 2001]
FIR line luminosity	$2.8 L_{\odot}$	[OI], CO, H ₂ , OH		[Giannini et al., 2001]
H ₂ rovibr. line lum.	$0.7 L_{\odot}$	H ₂ 1 – 0S(1)	45×46/pixel	[Froeblich et al., 2003b]
n(H ₂)	$2 \times 10^8 \text{ cm}^{-3}$	450,850μm	7.5", 14.8"	[Crimier et al., 2010]
N(H ₂)	$2.5 \times 10^{21} \text{ cm}^{-2}$	CO(4-3), (2-1)	11"–21"	[Lefloch et al., 2011]
N(H ₂ O)	$(1.2 - 8.0) \times 10^{17} \text{ cm}^{-2}$	p-H ₂ O 3 ₁₃ -2 ₂₀	13.2"	[Lefloch et al., 2011]
N(CO) (redshifted jet)	$2.5 \times 10^{17} \text{ cm}^{-2}$	CO(4-3), (2-1)	11"–21"	[Lefloch et al., 2011]
N(CO) (redshifted lobe)	$1.3 \times 10^{17} \text{ cm}^{-2}$	CO		[Giannini et al., 2001]
N(CO) (blueshifted lobe)	$5 \times 10^{16} \text{ cm}^{-2}$	CO		[Giannini et al., 2001]
N(SiO)	$(2.0 - 3.3) \times 10^{14} \text{ cm}^{-2}$	SiO(8-7)	14.2"	[Lefloch et al., 2011]
T _K	120 K	CO(4-3), (2-1)	11"–21"	[Lefloch et al., 2011]
V _{LSR}	-11 km s ⁻¹	^{12}CO (1-0)	2'.5	[Sargent, 1977]
Outflow velocity range	-150 to 80 km s ⁻¹	^{12}CO (1-0)	21'	[Lefloch et al., 1996]
Precession angle	4°	SiO (3-2)	19'	
Size	30" × 10"	H ₂ 1 – 0S(1)	0.33"/pixel	[Eisloffel et al., 1996]
Precession period	400 yr	^{12}CO (2-1)	11"	[Lefloch et al., 1996]
Dynamical age	$\sim 2 \times 10^3$ yr	H ₂ 1 – 0S(1)	0.33"/pixel	[Eisloffel et al., 1996]
Visual extinction	3.2–3.4 mag	^{12}CO (1-0)	21"	[Lefloch et al., 1996]
	north lobe: 2.1 – 2.4 mag	SiO (3-2)	19"	
	south lobe: 1.4 mag	1.25mm	11"	[Lefloch et al., 1996]
		H ₂	(KSPEC)	[Smith et al., 2003]
			medium-resol.	
HH377				
Ionization degree	1 %	[NI],[NII]	0".482/pixel 0".85/pixel	[Ayala et al., 2000]
Proper motion	107±14 km s ⁻¹	[SII]λλ6717/6731	0".63/pixel 0".40/pixel	[Noriega-Crespo and Garnavich, 2001]
Radial velocity	-70±10 km s ⁻¹	[SII]λλ6717,6731, H _α	0".482/pixel 0".85/pixel	[Ayala et al., 2000]
Preshock jet density	10^5 cm^{-3}	[OI]λ6300/H _α	0".482/pixel 0".85/pixel	[Ayala et al., 2000]
Electron density	$n_e \sim 4100 \text{ cm}^{-3}$	[SII]λλ6731/6717	0".482/pixel 0".85/pixel	[Ayala et al., 2000]

velocity distribution) and of the surrounding gas (density, atomic fraction, ortho to para ratio of H₂ and molecular abundances).

Steady-state planar models are usually used to explain the H₂ outflows [Froeblich et al., 2003a]. However in the case of Cep E, simple planar J-shock or planar C-shock models do not reproduce the observations. Single J-type shock waves predict high excitation H₂ spectra and C-type shock waves predict constant excitation across a wide range of upper energy levels [Smith et al., 2003].

Better results come from multi-shock fits, as shown in left panels in the Fig. 3.13 for the southern lobe. [Smith et al., 2003] found two steady-state C-type planar shocks that fit the full set of data. However it is not clear how two shocks

Figure 3.13: The upper panels displays the H₂ data. The lower panels displays the CO rotational fluxes. Taken from [Smith et al., 2003]. (left) **Planar shock models for Cep E south.** (a) A hot C-shock component with 32 km s⁻¹ provides a fit to the vibrationally excited columns but does not contribute to the CO rotational lines. (b) A cool C-shock with speed 11 km s⁻¹ provides a fit to the rotationally excited H₂ and CO but does not contribute to the vibrational lines. (right) **C-type bow shock model for Cep E South 1** with speed 120 km s⁻¹. In all the cases the density is 10⁵ cm⁻³. The H₂ models values are displayed for the ground (solid line), first (dashed line) and second (dot-dashed line) vibrational levels.

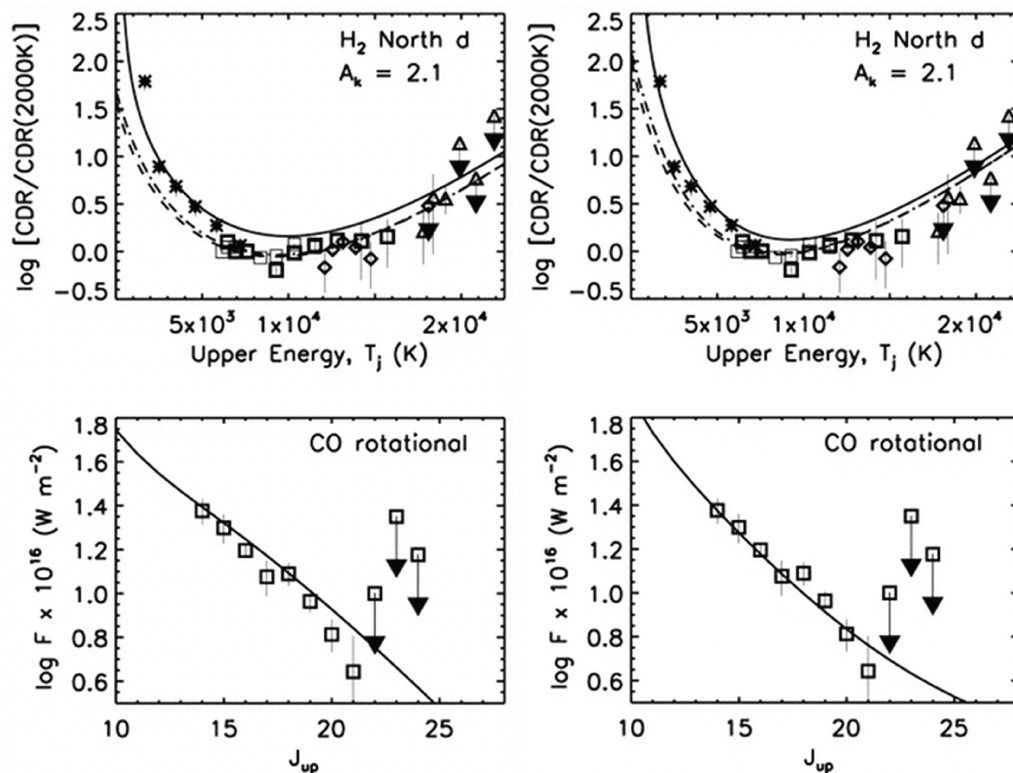


with almost the same parameters can be found in the three separate locations since the excitation produced in planar shocks is very sensitive to the shock velocity, field strength, and ionization fraction.

However, images of Cep E protostellar outflow show that the shocks are not planar, but curved. This curvature leads to a distribution of shock speeds. It is usually used models with a shape $Z \propto R^s$ (cylindrical coordinates) and the distribution of shock speeds is modeled as a power law distribution with power law index of $\alpha = 2s/(s-1)$ [Froebrich et al., 2003a].

[Smith et al., 2003] tried to model simultaneously the emission lines from carbon monoxide and hydrogen molecules with a single paraboloidal steady-state C-type bow shock. The resulting fits are displayed in right panels in Figs. 3.13

Figure 3.14: The upper panels displays the H₂ data. The lower panels displays the CO rotational fluxes. Taken from [Smith et al., 2003]. (left) C-type bow shock model for Cep E North (Nd). The model bow speed is 120 km s⁻¹. (right) J-type bow shock model for Cep E North (Nd) with shape parameter s=1.5 and a speed of 60 km s⁻¹.



and 3.14.

Bow shock configurations are strongly supported in the case of Cep E by H₂ images that display numerous bow-shaped structures in the outflow (See Fig 3 in [Ladd and Hodapp, 1997]).

To distinguish between J- and C-type bow models, the authors examined other signatures like the gas cooling and the luminosity of the outflowing gas in the CO and H₂ lines (See Table 5 in [Smith et al., 2003]).

These authors failed to fit a single J-type bow shock but J-shocks produce extremely high fluxes in the lines from the cooler molecular gas of CO and H₂. This is inconsistent since the total cooling then exceeds the bolometric luminosity of the protostar. In right panels of Figure 3.14 are displayed the fits for a J-type bow shock in the Cep E northern lobe.

In summary:

Steady-state C-type shocks with a paraboloidal **bow shock geometry** seem account for the molecular excitations of H₂ 1-0 S(1) rovibrational and CO rotational transitions from the with a bow speed of $>38\text{km s}^{-1}$ [Smith et al., 2003].

Steady-state C-type shocks are strongly favored in the case of Cep E (e.g., [Eisloffel et al., 1996], [Ladd and Hodapp, 1997], [Ayala et al., 2000], [Smith et al., 2003]).

A further diagnostic is provided by the integrated intensity of the CO emission. The C-bow shock model predicts a CO(3-2)/CO(18-17) ratio of 6, close to the measured ratio of 4 for the north lobe and 2 for the southern lobe [Smith et al., 2003].

High-resolution H₂ 1-0 S(1) imaging show that lobes consist of numerous emission knots of size $(1-3)\times 10^{15}$ cm [Ladd and Hodapp, 1997]. To reproduce the integrate emission H₂ 1-0 S(1) of each lobe the model required around 20 bow shocks, close to the paraboloidal shape [Smith et al., 2003].

Chapter 4

The spectral survey of Cep E

4.1 Introduction

Spectral surveys are a powerful tool to obtain a complete census of the molecular complexity in star forming regions, and to understand the interplay between the molecular composition and the star forming process.

The dynamic of the collapse is regulated by the molecular composition, as well as the gas temperature and the coupling between matter and the magnetic fields. Conversely, the gravitational collapse influences the gas physical conditions, as the infalling material releases its energy into photons that heat the collapsing envelope, and, consequently change the chemical composition and gas cooling.

In fact, the thermal balance of the gas depends on the molecular composition, through the gas cooling function. Conversely, the temperature and density controls the molecular composition through the chemical network which depend on the gas temperature, density and their abundance.

In addition, the ambipolar diffusion (the coupling of matter to the magnetic field) is controlled by the ionization fraction.

Besides, the emission lines can be a powerful diagnostic tool, because different lines from the same molecule probe different excitation conditions and permit to trace regions of different physical conditions, from multifrequency analysis and modeling. Likewise, lines are the only way to study the dynamics.

The few unbiased spectral surveys carried out in the millimeter and submil-

limeter bands accessible from the ground were obtained mostly toward high-mass stars (e.g. Orion KL [Tercero et al., 2010],[Tercero et al., 2011] and [Tercero et al., 2012], AFGL 2591, IRAS 20126+4104 [Plume et al., 2007], IRAS 23385+6053 [Thompson and Macdonald, 2003], NGC 6334 I, I(N)) [Thorwirth et al., 2007] and compact HII regions as W3 IRS5, IRS4 [Kim et al., 2006], G34.3+0.15 [Kim et al., 2000], G5.89-0.39 [Thompson and MacDonald, 1999]. This is mainly because of their strong molecular lines and their rich chemistry [Herbst and van Dishoeck, 2009]. Only two solar-type sources have been studied in the mm/submillimeter window: IRAS 16293-2422 [Caux et al., 2011], L1527 [Sakai et al., 2008].

Finally, the launch of the Herschel Space Observatory has permitted the spectral surveys in the 500 – 2000 GHz in sample of low to high mass star forming regions [Ceccarelli and CHESS Consortium, 2010]. It is important to note that the intermediate-mass regime has not been covered yet in the mm/submm range. Hence their chemistry, the influence of the central object and its radiation field are not well known.

Before this thesis, there was no **unbiased** line surveys of a molecular outflow. At the same time when Cep E was been observed, spectral line surveys were carried out towards L1157-B1 (IRAM and Herschel); and another one at 3 mm with Nobeyama Radio Observatory (NRO) 45m telescope [Sugimura et al., 2011].

Line surveys towards outflows and jets give access to unique information to the feedback of outflows on the surrounding molecular gas, in particular the impact on the gas chemical composition in the region.

In the last years, observational studies were carried out towards young protostellar outflows, though mostly fragmentary studies e.g. [Bachiller, 1996], [Bachiller et al., 2001], [Jiménez-Serra et al., 2004]. The most studied source, until now, has been L1157-B1, whose investigation of the chemical composition was restricted to bright molecular line emission. The exceptional line richness of L1157-B1, associated with a peculiar gas composition, distinct from that of the protostellar envelope, led R. Bachiller to propose the existence of a class of young protostellar outflows, "chemically active" (See section 1.4.4). These biased surveys together with the new generation of models with both, collimated and wide-angle wind components (e.g. [Ferreira et al., 1997] [Shang et al., 2006], [Machida et al., 2008]), are an attempt to achieve a consistent picture of outflows

morphology, kinematics and chemical abundance enhancements.

The motivation to carry out an unbiased survey of CepE with the IRAM 30m telescope are: **1)** To constrain the actual composition of a typical intermediate-mass star forming region (envelope and molecular outflow); **2)** to understand how the gas chemical composition is altered by the outflow process; **3)** comparison with shock models for the outflow emission.

4.2 Kinematics and morphology of the outflow

Figures 4.1 and 4.2 show velocity maps of CO (2-1) and SiO (2-1), giving the morphology of Cep E outflow. Towards the central position, at low velocity ($\leq 30 \text{ km s}^{-1}$), emission is associated with the large scale, extended outflow entrained material; at moderate (between 30 and 45 km s^{-1}) velocity emission is associated with the cavity at the base of the north jet; the high ($\geq 45 \text{ km s}^{-1}$) velocity is associated with the north jet. Towards the south outflow lobe, (between -65 and -80 km s^{-1}) it can be distinguish a concentration of CO (2-1) at the apex of the south jet and at extremely high velocity ($\leq -110 \text{ km s}^{-1}$) is detected emission associated with the south jet.

4.3 Observations

The unbiased line spectral survey towards Cep E was carried out with the IRAM 30-m radiotelescope at Pico Veleta, Spain, in three different runs: March and July 2010 and February 2011.

Two positions were observed: toward the driving protostellar at source offset position (0, 0), at $23\text{h}03\text{m}13.0\text{s} +61^\circ42'21''$ (J2000) and towards the apex of the south outflow lobe at offset position ($-12''$, $-18''$). These two positions were chosen in order to **a)** obtain a census of the molecular composition of the protostellar envelope, including a possible hot corino, **b)** obtain a census of the molecular composition of a typical bowshock region (HH377), at $(-12,-18)$, **c)** distinguish between protostellar and shock origin for the molecular species detected.

The observed positions are marked by yellow crosses in the CO (2-1) emission map of Figure 4.3.

Figure 4.1: CO (2-1) velocity maps taken with PdB toward Cep E region. (*top*) The cross mark the position of the central source. The gas emission comes from two main components, the cavity between 30 and 45 km s^{-1} and the jet between 50 and 80 km s^{-1} . (*bottom*) Cep E south jet, the emission comes mainly from the gas between -100 and -130 km s^{-1} .

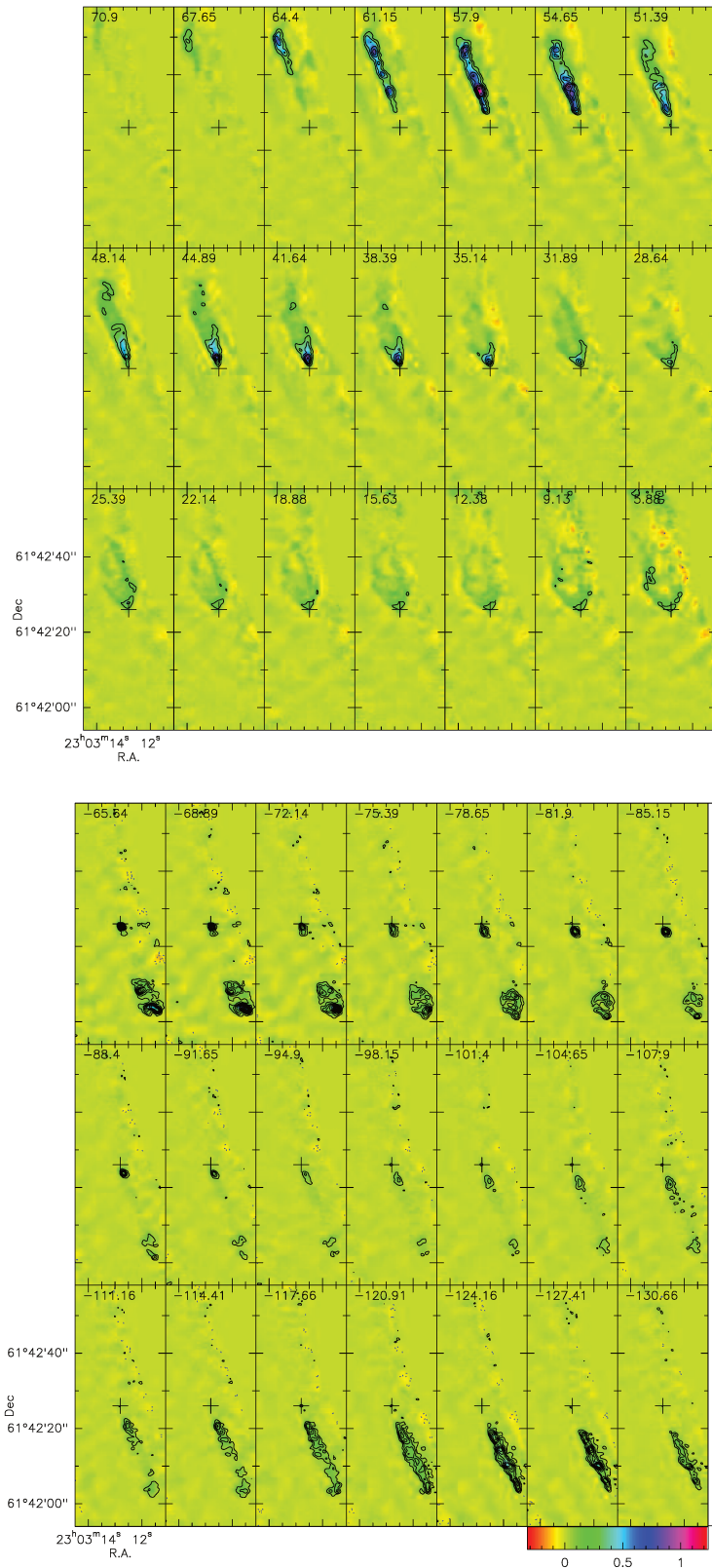


Figure 4.2: SiO (2-1) velocity maps taken with PdB toward Cep E region. Clearly the emission at positive velocities comes from two components, the first one around 25 and 45 km s^{-1} and the second one between 50 and 70 km s^{-1} . At negative velocities, the emission similarly is mainly from one component between -25 and -50 km s^{-1} and a second component from -50 to -90 km s^{-1} . In this transition the EHV emission is not observed.

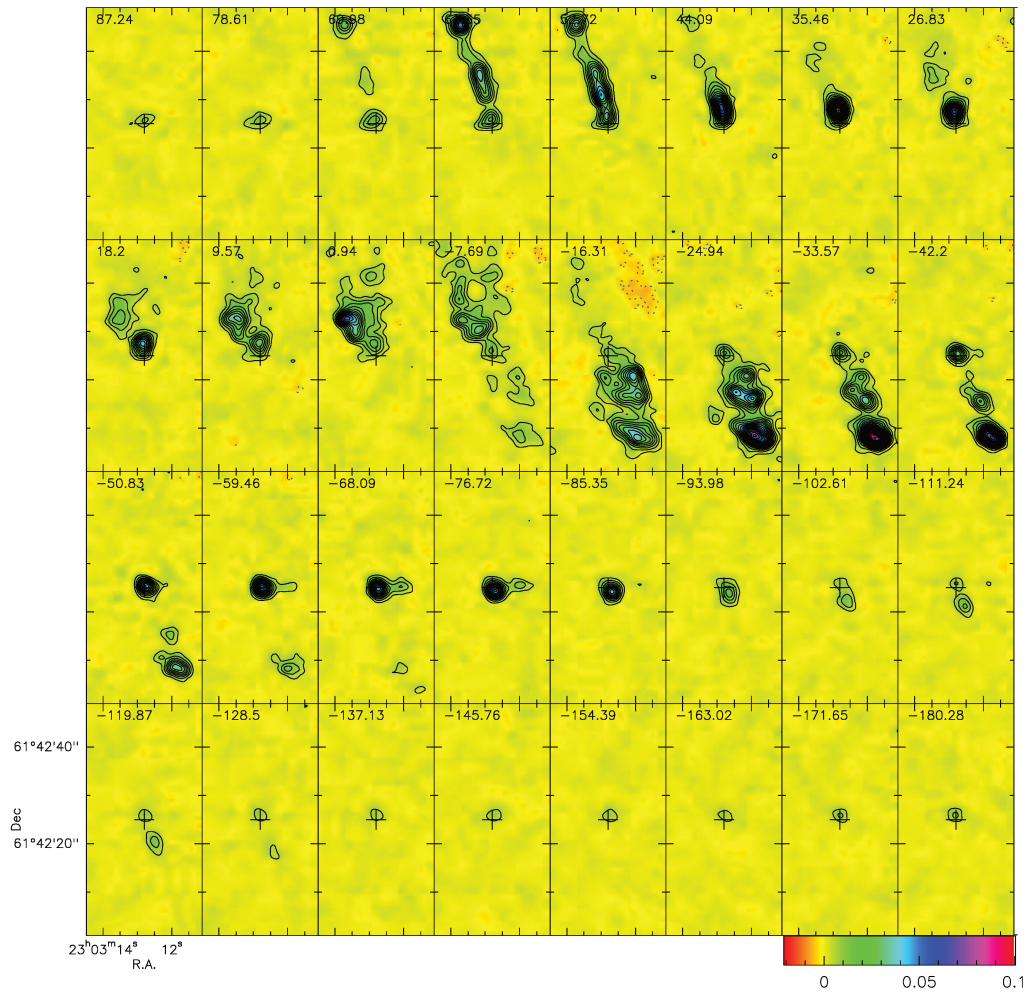
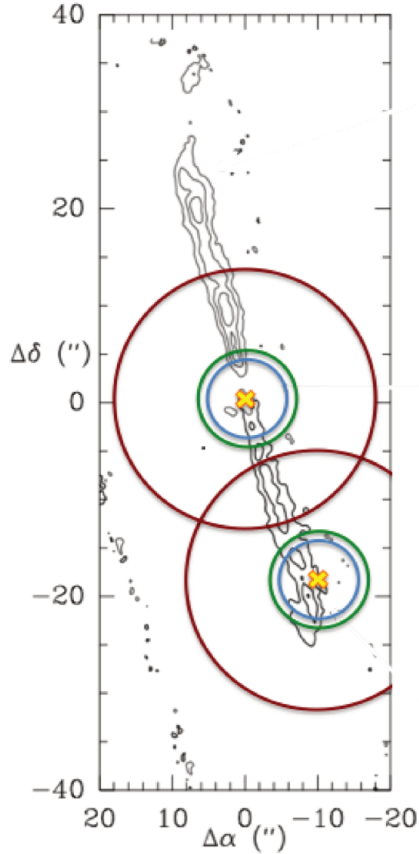


Figure 4.3: The high-velocity jet emission from CepE CO (2–1) emission map at 1'' resolution obtained with the PdBI (Lefloch et al. 2011). Central position is placed at 23h03m13.0s +61°42'21'' (J2000). The red circle represents the IRAM beam at 3mm, the green one at 1.3mm and the blue one at 0.8mm.



We used the EMIR receiver and the WILMA autocorrelator as spectrometer (See section 2.3.4.1), which provide us with a spectral resolution of 2 MHz (~ 1.7 km s $^{-1}$ at 0.9 mm, ~ 2.5 km s $^{-1}$ at 1.3 mm and ~ 6.5 km s $^{-1}$ at 3 mm). Each spectral band covered a spectral range of about 4 GHz. (3.72 GHz). The spectral survey covered each band in tunings every 2 GHz to have a redundancy of two.

The observations were obtained in wobbler-switching mode to ensure flat baselines. Calibration, pointing and focus were regularly checked on planets or on the radio continuum source NGC 7538.

The unbiased spectral survey cover the bands: 0.9mm (260-350 GHz), 1.3 mm (200 - 270 GHz), 2mm (164 -170 GHz) and the 3 mm (80 - 115 GHz). (see Table 4.1). The 0.9mm band could be covered thanks to the exceptional

Table 4.1: Observational parameters.

Band	Frequency (GHz)	Resolution (km s ⁻¹)	rms (mK)	HPBW (arcsec)	Feff %	Calibration error (α)
E090	83–117	7.2–5.1	2–5	30–21	(86)95	10%
E150	164–170	3.7–3.5	5	14.8–14.3	(145)93	15%
E230	201–267	3–2.2	5–9	12.1–9.1	(210)94	20%
E330	260–305	2.3–1.2	6–10	9.4–8	(260)88	30%
	330–348	1.8–1.7	12–23	7.4–7	(340)81	30%

Note. The numbers between curly brackets indicate the frequency at which the Feff was measured.

weather conditions, with a precipitable water vapor (p_{wv}) of ~ 1 mm, a system temperature in the range of 250 to 600 K and an opacity between 0.1 to 0.4 during the observations. Overall, the observations required a total of about 80 hours of observation time.

The beam of the telescope varies from 7 arcsec for the highest frequencies (350 GHz) to 30 arcsec for the lowest frequencies (80 GHz) (see Fig. 4.3). The achieved rms after averaging all the observations for each band is reported in Table 4.1.

4.3.1 Data calibration

4.3.1.1 Atmospheric calibration

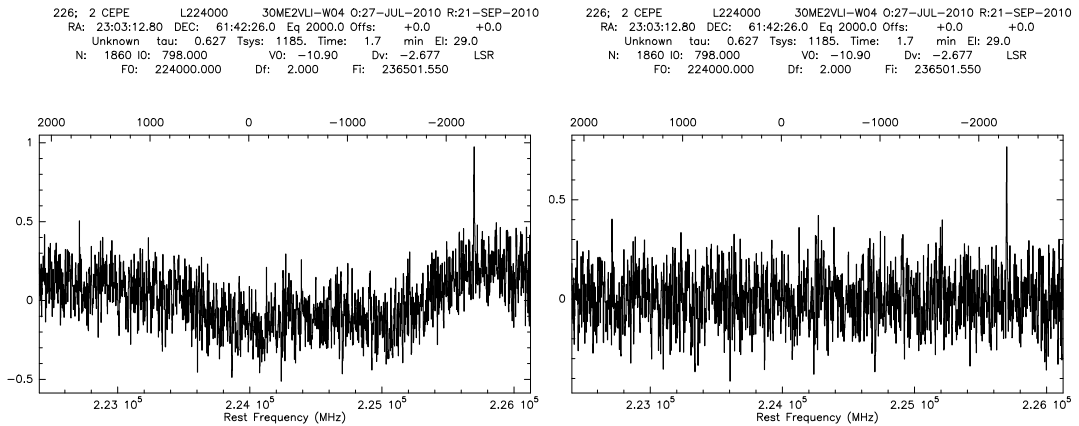
In the millimeter and submillimeter wavelength range, the atmosphere has a large influence and can change rapidly, affecting the signal received by the telescope. Such perturbations will be recorded as fluctuations over the continuum along all the spectra, as it is showed in Fig.4.4.

In the survey the atmospheric calibration was obtained performing three measurements in the "cal" procedure, including a measure on the sky. The sky opacity and calibration was obtained using the program ATM (Atmospheric Transmission at Microwaves) installed at the IRAM 30m telescope (Cernicharo 1985). The observing mode Wobbler switch was chosen precisely to minimize the drifts in atmospheric calibration by subtracting the emission of the reference position every sec.

Thus, the first step is to remove the effect of the changing baselines, caused

by variations in the receiver gain with antenna temperature. Usually, only linear baselines were removed from the spectra. In some spectra, we found it difficult to fit the raw spectra with only the first order of polynomial function, and in these cases we extract the baselines with a higher polynomial order or in some cases we also used sinusoidal functions. Then we can start to work with these clean spectra.

Figure 4.4: (*left*) A spectra with fluctuations in the continuum baseline, it is different to zero along the spectra. (*right*) The same spectra of the left but corrected, it has been removed a baseline in order to obtain a continuum close to zero.



Later, in order to convert T_a^* (flux units of the spectra) into an intensity as close as possible to the true brightness temperature of a source that has a size of the same order as the main-beam, we correct for the telescope beam efficiency.

For the IRAM 30 m telescope, the forward efficiency (this is basically the coupling of the telescope with the sky. See section ??) is $F_{eff} \sim 0.9$ down to 3 mm wavelength (See table 4.1), as provided by IRAM's website. On the other hand, B_{eff} varies with the wavelength according to the Ruze formula¹:

$$\eta_a = \eta_{ill} \times \exp((4\pi\sigma_s/\lambda)^2) \quad (4.1)$$

For our data analysis we made a (simplified) linear interpolation between values determined by the IRAM staff at given frequencies. These interpolation functions are listed in table 4.2.

¹www.iram.es/IRAMES/telescope/telescopeSummary/telescope_summary.html

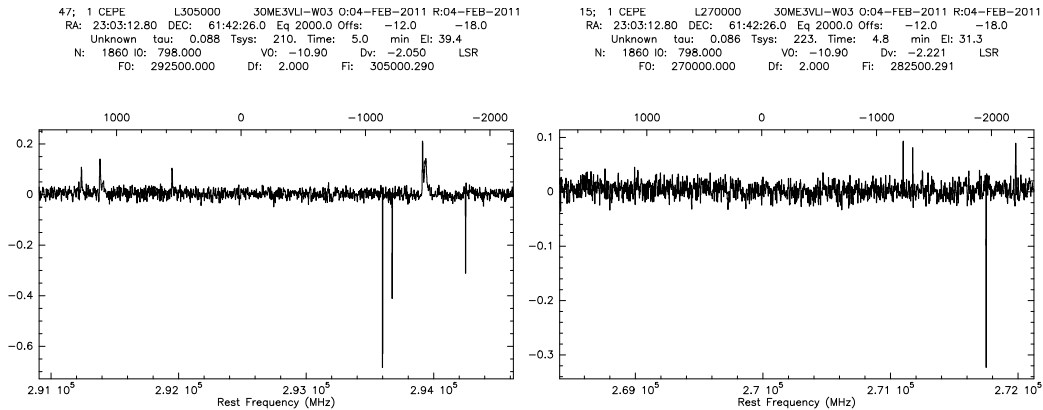
Table 4.2: Frequency ranges and interpolation functions used to derive the Beff for each line frequency in the Cep E survey. The Beff values were taken from IRAM’s website.

Frequency range (GHz)	Beff %	Interpolation function
86 - 145	80 - 74	$-0.12 x + 91.20$
145 - 210	74 - 63	$-0.17 x + 98.54$
210 - 260	63 - 53	$-0.20 x + 105.00$
260 - 340	53 - 35	$-0.23 x + 111.50$

4.3.1.2 Spurious features

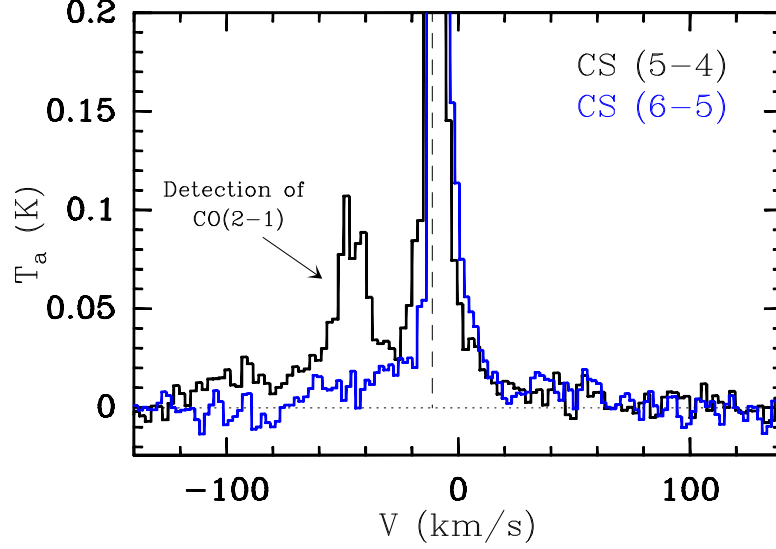
Spikes There is another problem that can appear in the spectra, the presence of spurious lines in form of spikes. These ”spikes” come from interferences in the electronic chain of nearby receivers; they are tracked and catalogued by the IRAM’s staff. However, there are other spikes that can appear and these can be recognized because they appear as an extremely bright emission or absorption features in just one or two channels. These spikes were flagged from the spectra.

Figure 4.5: Examples of spikes present in the spectra. Note that the intensity of these spikes are 4 times brighter than the emission from the lines.



Contamination from image band The rejection of the image band is limited to 10 – 15 dB. This is not sufficient anymore at the level of sensitivity reached by our observations. We indeed observed ”ghost” lines from bright lines in the image band (See figure 4.6). This ghost lines were flagged in the individual spectra.

Figure 4.6: Example of a ghost line: CS (5-4) spectra (*black line*) with a contamination in the wing by CO (2-1). For comparison we overplot the CS (6-5) spectra in *blue*.



4.3.2 Errors

The detection limit for emission lines in the survey was established at 3 rms noise level, in order to assure a reliable line identification.

In practice, the integrated flux over a velocity range is limited at 3σ , where the σ and the rms are related as follows:

$$\int T_{mb} dv \leq 3\sigma = 3 * rms \sqrt{\Delta v \delta v} \quad (4.2)$$

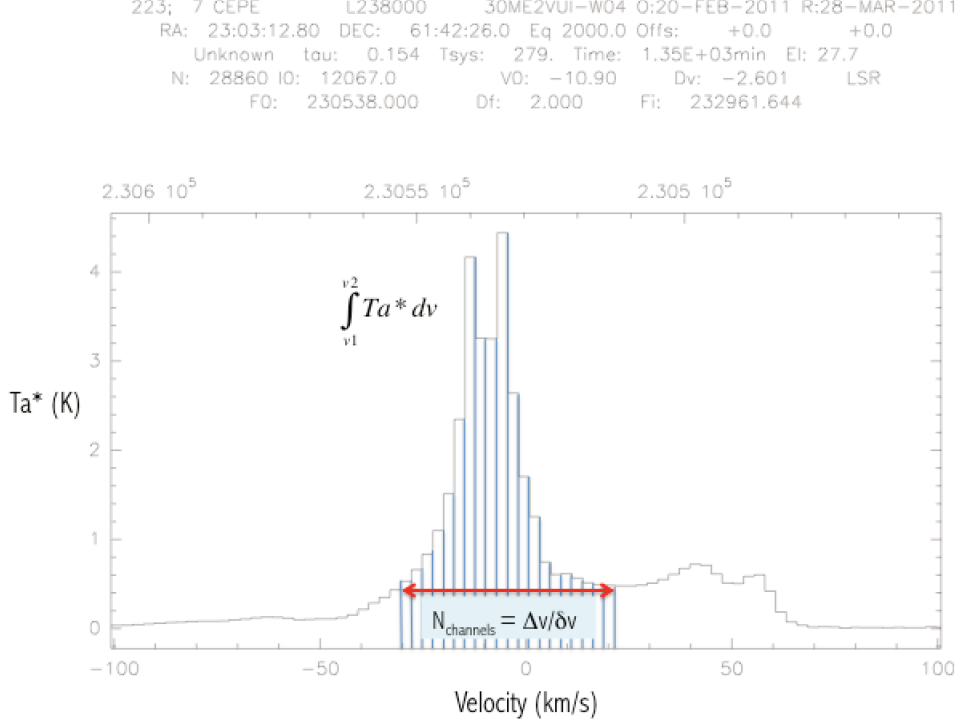
where, rms is the noise over one channel, δv the spectral resolution (2MHz), and Δv the width of the velocity range over which we are integrating.

This expression was calculated as the quadratic sum of the errors of each channel along the velocity interval in which one makes the integral (Fig. 4.7). Then, the error of the integrated flux over a velocity interval is:

$$\begin{aligned} \sigma_{Int.flux}^2 &= \sigma_{channel_1}^2 \delta v^2 + \sigma_{channel_2}^2 \delta v^2 + \sigma_{channel_3}^2 \delta v^2 + \dots \\ \sigma_{Int.flux}^2 &= \sum_{i=1}^N \sigma_{channel}^2 \delta v^2 \end{aligned} \quad (4.3)$$

but the $\sigma_{channel}$ is the rms and if we assume that it is the same over each tuning,

Figure 4.7: Cep E CO (2-1) spectra. This image illustrates the addition of errors of each channel along the velocity interval from v_1 to v_2 .



then we can write:

$$\sum_{i=1}^N \sigma_{channel}^2 = N \text{ rms}^2 \quad (4.4)$$

where N is the number of channels.

Using equation 4.3, it holds

$$\sigma_{Int.flux}^2 = N \text{ rms}^2 \delta v^2 \quad (4.5)$$

The number of channels can be deduced easily because we defined the velocity range and we know the width (spectral resolution) of each channel, $N = \Delta v / \delta v$, then,

$$\sigma_{Int.flux}^2 = N \text{ rms}^2 \delta v^2 = \left(\frac{\Delta v}{\delta v} \right) \text{ rms}^2 \delta v^2 \quad (4.6)$$

$$\sigma_{Int.flux}^2 = \text{rms}^2 \Delta v \delta v \quad (4.7)$$

$$\Rightarrow \sigma_{Int.flux} = rms\sqrt{\Delta v\delta v} \quad (4.8)$$

Finally, the errors reported in Table 5.5 are computed taking into account the calibration uncertainties.

Thus the total error from the observations taking into account the rms and the calibration errors is,

$$\sigma_{total} = \sqrt{\sigma_{area}^2 + (\alpha * flux)^2} \quad (4.9)$$

where, α is the calibration error.

The calibration uncertainties include the errors due to variations in atmospheric calibration, as well as for uncertainties in the band rejection. Note we adopted the calibration uncertainties as is showed in Table 4.1.

4.4 Results

Figures 4.10 to 4.13 show the overview of the full survey in the three bands and the richness of Cep E line spectrum. Overall, we have detected ($\sigma \geq 3$) 559 lines from more than 60 different species with a wide range of upper level energies, from a few K up to around 200 K (See Tables 4.11 and 4.12). Figure 4.8 shows the fraction of lines with upper level energy in different ranges: 0 to 50K, 50 to 100K, 100 to 150K and 150 to 200K.

Figure 4.8: Upper level energy distribution in the Cep E unbiased spectral survey.

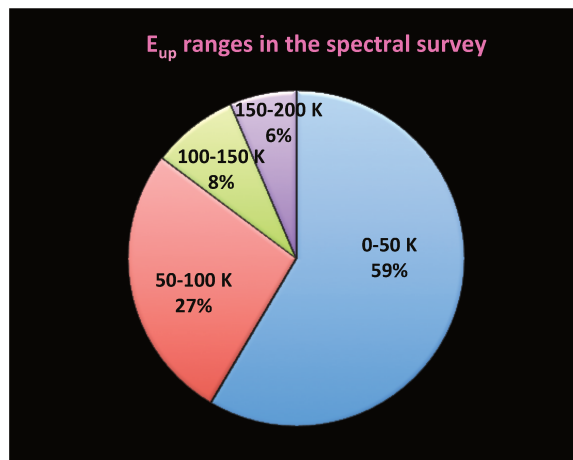
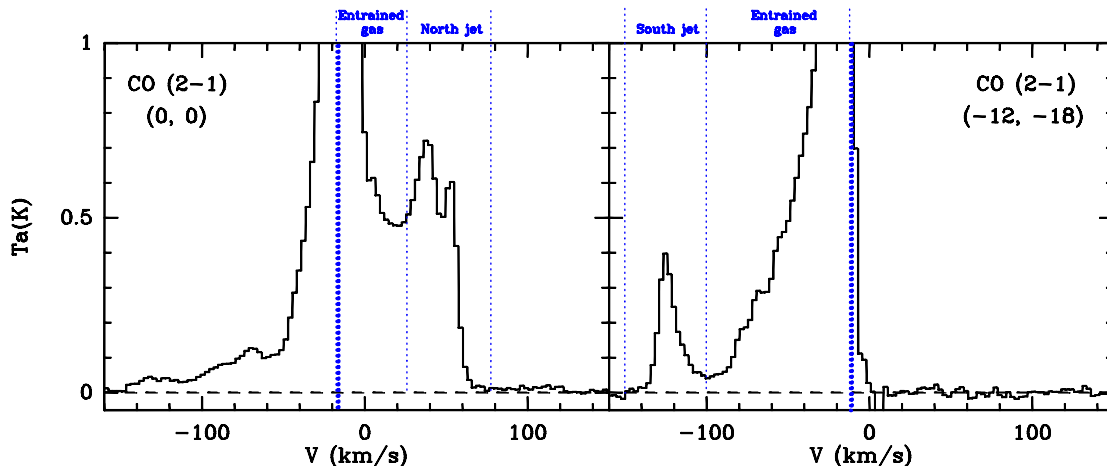


Figure 4.9: Three kinematical components were found: the ambient gas at $\sim -10.9 \text{ km s}^{-1}$, the entrained gas between $-90 \rightarrow -12$ and $-9 \rightarrow +30$ and the jet, detected at -125 km s^{-1} (south jet) and at around $+50 \text{ km s}^{-1}$ (north jet).



Most of the detected lines have upper level energies lower than 50K, normally are associated with cold gas. Conversely, only 14% of the lines have upper level energies larger than 100K, suggesting that Cep E spectrum is unlikely dominated by hot gas emission.

Some line profiles, notably those of CO and HCO^+ , show the existence of three velocity components (Fig.4.9), likely associated with three different physical components: **the ambient gas** at $\sim -10.9 \text{ km s}^{-1}$, **the entrained gas** at $(-90 \rightarrow -12)$ and $(-9 \rightarrow +30)$ and **the jet**, mostly detected at -125 km s^{-1} (south jet) in the $(-12,-18)$ position and at $+50 \text{ km s}^{-1}$ (north jet) in the $(0,0)$ position. All the components are detected in both positions, but not in all molecular tracers (Table 5.1).

In Figure 4.9 we can see that some line spectra like CO show extremely high velocity (EHV) features, that was already seen in [Lefloch et al., 1996]. This means that molecular spectra present a secondary component less intense than the main emission peak from the ambient gas but enough intense and placed at high velocities to be identified as emission from a driving jet. e.g., [Bachiller et al., 2001], [Jørgensen et al., 2007], [Santiago-García et al., 2009], [Hirano et al., 2010].

In an preliminary analysis, we detect a total of 559 lines whose 428 identified. Tables 4.11 and 4.12 list all the detected lines and the integrated emission be-

Table 4.3: Component velocity limits. The jet component present two components, MV (moderate velocity) and the HV (high velocity) gas.

Component	Velocity limits (km s ⁻¹)	
	Offset 0,0	Offset -12, -18
Ambient gas	-10.9km s ⁻¹	-10.9km s ⁻¹
Entrained gas	-9 → 30	-12 → -100
Jet gas: MV	30 → 45	
Jet gas: HV	50 → 80	-100 → -150

tween the velocity ranges of the three different kinematical components in both positions.

Figures 4.19 to 4.26 present the spectra with the labels of each line identification listed in Tables 4.11 and 4.12 for (0,0) and (-12,-18) offset respectively.

In chapter 5 we are going to present the results of the detailed study of the jet component.

4.5 Line identification

The systemic velocity of Cep E is -10.9 km s⁻¹ [Sargent, 1977]. Line identification was carried out using the package of CLASS called WEEDS [Maret et al., 2011]. Two databases available online were used in order to identify lines: (1) Cologne Database for Molecular Spectroscopy ¹ (CDMS; see Mller et al. 2001, 2005) and (2) Molecular Spectroscopy database of Jet Propulsion Laboratory ² (JPL; see Pickett et al. 1998).

A close match in frequency between an observed and cataloged line is a necessary, but not sufficient, condition for identification. One must take into account all the transitions available in the observed spectral band(s), the spontaneous emission Einstein coefficient and verify the consistency. In total we have 132 unidentified lines out of 559 lines, namely 23% in our preliminary analysis. Table 4.5 lists the species detected in the survey. Furthermore, the chemical richness is more important towards the central source than towards the south lobe.

¹<http://www.astro.uni-koeln.de/cgi-bin/cdmssearch>

²<http://spec.jpl.nasa.gov/ftp/pub/catalog/catform.html>

Figure 4.11: Overview of all the detected lines in the 2 mm band from 164-170 GHz. At the *bottom* the (0,0) position and at the *top* the (-12, -18) position. The temperature axis is zoomed to appreciate the line richness in both position. Signals are in antenna temperature (K).

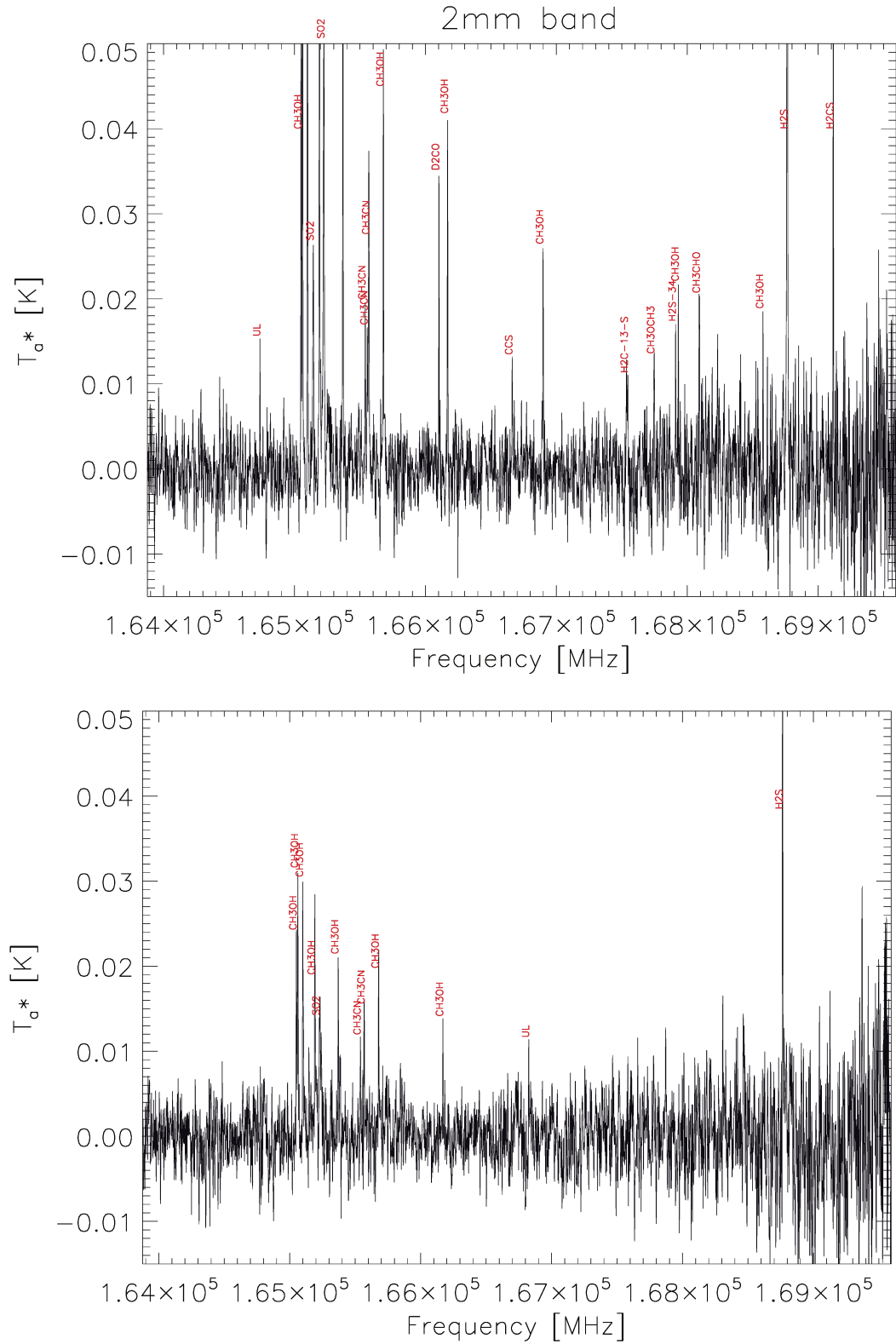
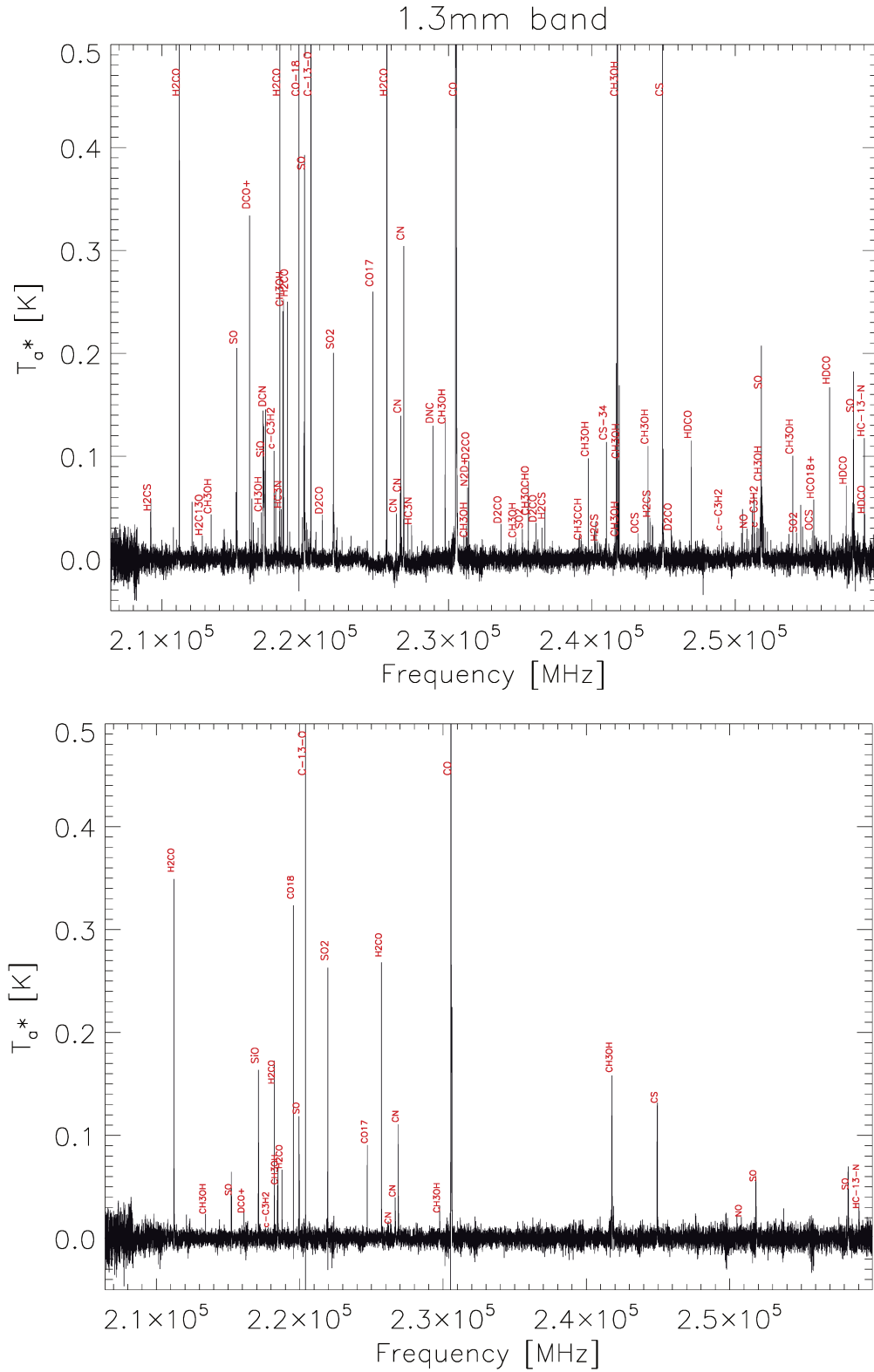


Figure 4.12: Overview of all the detected lines in the 1.3 mm band from 207-260 GHz. At the *bottom* the (0,0) position and at the *top* the (-12, -18) position. The temperature axis is zoomed to appreciate the line richness in both position. Signals are in antenna temperature (K).



4.6 Rotational diagrams

The abundance and excitation conditions of the molecular species detected were derived in first approximation under the hypothesis of LTE and optically thin emission, carrying out a simple rotational diagram analysis. (See Appendix A).

The method consists in plotting the column density per statistical weight of a number of molecular energy levels as a function of their energy above the ground state, following the standard formula e.g. [Goldsmith and Langer, 1999]:

$$\ln \frac{N_u}{g_u} = -\frac{1}{T_{\text{rot}}} \frac{E_u}{k} + \ln N - \ln Z, \quad (4.10)$$

where N_u is the column density of the upper energy level with statistical weight g_u , N is the total column density, T_{rot} is the rotational temperature (\sim kinetic temperature, if LTE applies) and Z is the partition function. From a straight line least-squares fit to the observed values of $\ln(N_u/g_u)$ versus E_u , the y-intercept gives the column density, and the negative reciprocal of the slope gives the rotational temperature.

As a result of the LTE analysis we derived the T_{rot} and column density values for the different species. The line emission was integrated between -20 and 10 km s^{-1} for each line. The quoted values refer therefore to the quiescent gas, namely the envelope toward the central position and the cloud toward the south lobe position. Note that we did not include a beam dilution correction as the source size is large (about 50 arcsec, $\sim 35\,000$ AU [Crimier et al., 2010] at 730 pc of distance) than the largest telescope beam. The values of T_{rot} and the column densities are listed in Table 4.4.

4.7 Overview of the chemical structure of the envelope

The detection of lines from *complex molecules* like the acetaldehyde (CH_3CHO), the methylformate (CH_3OCHO) and probably the dimethyl ether (CH_3OCH_3) reveals that Cep E has a "hot core" like region. See Table 4.8.

These chemical characteristics are thought to arise from thermal evaporation

Table 4.4: Molecular column densities and rotational temperatures derived towards Cep E for ambient velocity component (See Figs 4.14 and 4.15). The abundances are expressed respect to H₂ and CO-normalized, i.e., $X_4^{\text{CO}} = N/N_{\text{CO}} \times 10^4$.

Molecule	N (cm ⁻²)	T _{rot} (K)	X ₄ ^{CO}
CO	$4.4^{+0.3}_{-0.2} \times 10^{15}$	19^{+2}_{-1}	1×10^4
SiO	$3.1 \times 10^{11} \pm 0.4$	33^{+8}_{-5}	0.7 ± 0.1
SO	$7.4^{+2}_{-1.3} \times 10^{12}$	32^{+4}_{-3}	$16.8^{+5.7}_{-3.7}$
HCO ⁺	2.4×10^{12}	36	$5.4^{+0.3}_{-0.2}$
HCN	2.1×10^{12}	15	$4.8^{+0.3}_{-0.2}$
CH ₃ OH	$8.0^{+5}_{-3} \times 10^{13}$	33^{+34}_{-11}	$181.8^{+126.0}_{-76.4}$
H ₂ CO	$1.5^{+0.8}_{-0.5} \times 10^{13}$	84^{+448}_{-39}	$34.1^{+20.5}_{-12.9}$

Figure 4.14: Rotational diagrams of CO, SiO and SO. The *squares* are the data and the red line are the fit. In some cases the error bar is smaller than the symbol. The resulting column density and rotational temperature are listed in table 4.4.

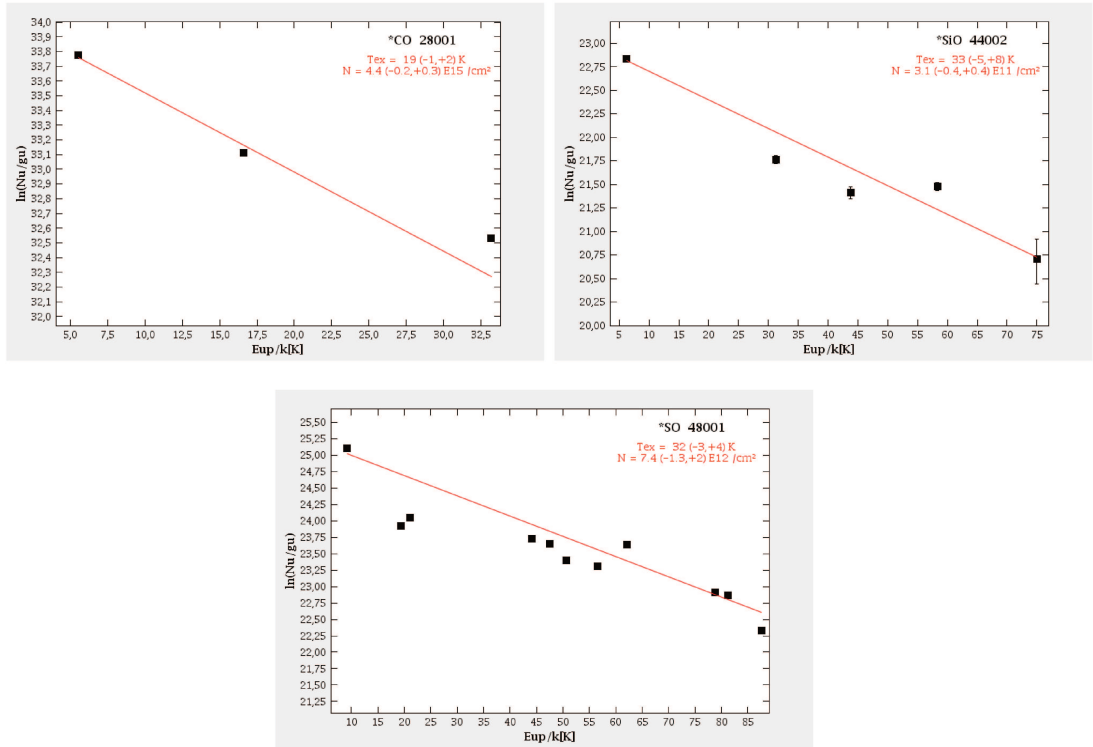
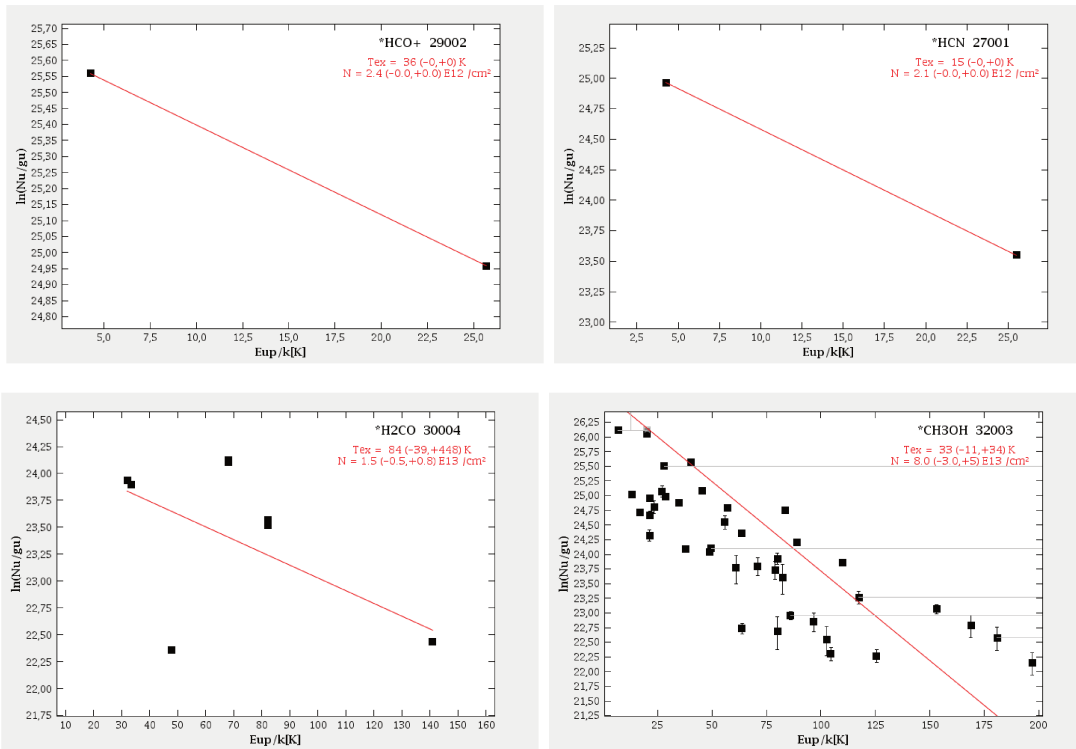


Figure 4.15: Rotational diagrams of HCO⁺, HCN, CH₃OH and H₂CO. The *squares* are the data and the red line are the fit. In some cases the error bar is smaller than the symbol. The resulting column density and rotational temperature are listed in table 4.4. In the CH₃OH rotational diagram are grey lines that indicate that there are transitions at different Eup for a same frequency.



of ice mantles from the grains close to the protostar, possibly followed by rapid high-temperature gas-phase reactions. In this scenario, the fully hydrogenated species are first generation molecules produced by surface chemistry on the grains, whereas complex organic molecules like HC_3N , CH_3OCH_3 and HCOOCH_3 are second generation produced by gas-phase chemistry between evaporated species e.g., [Ceccarelli, 2007]; [Herbst and van Dishoeck, 2009].

We detected emission from *ions* at both positions, towards the source (HCO^+ , DCO^+ , H^{13}CO^+ , HC^{18}O^+ , HCS^+ , N_2D^+ and N_2H^+) and towards the south lobe (HCO^+ , DCO^+ , H^{13}CO^+ , HCS^+ and N_2H^+). The spectra are shown in Fig. 4.16. The list of species are in Table 4.6.

4.8 Molecular deuteration

Cep E presents a strong *deuteration* with 11 different detected species in all the survey (See Table 4.7).

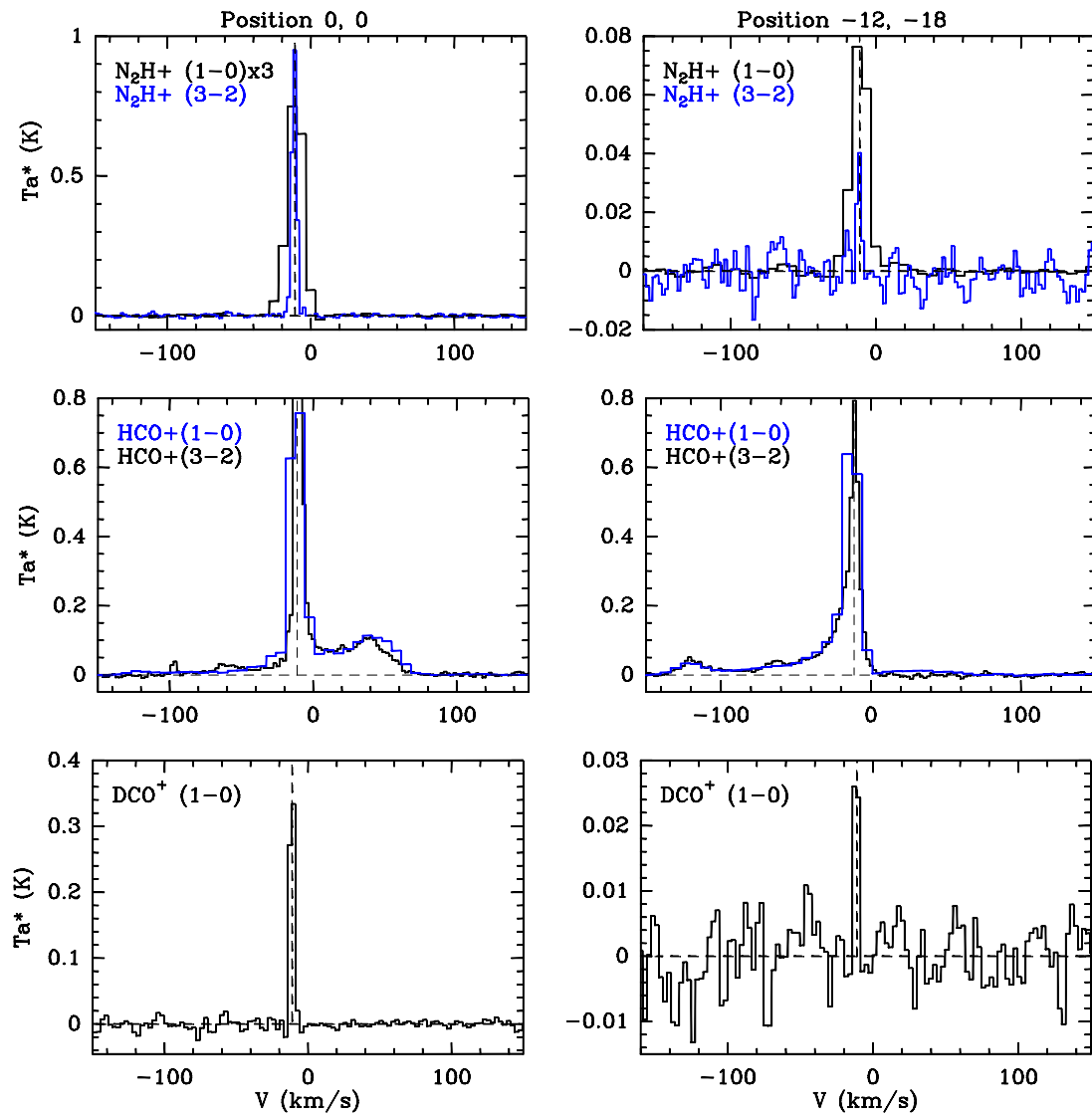
Toward the central position, we detected CH_2DOH , DCO^+ , D_2CO , HDCO , HDO , DNC , CCD , all species already detected toward IRAS 16293-2422 protostar [Caux et al., 2011] just to mention the low mass protostar where a similar spectral survey has been carried out in the past. In addition, we detected DCN , NH_2D , N_2D^+ and HDCCO . The brightest deuterated species line is from DCO^+ , with intensity ~ 0.33 K.

Toward the position (-12,-18), we detected in addition species like CH_2DOH , NH_2D , HDCO already detected toward LL1157-B1 (Codella et al. 2012), DCO^+ and HDCCO . The brightest line are from DCO^+ , HDCO and HDCCO with an intensity about 0.030 K. Figure 4.17 shows some of the line profiles of the different deuterated species observed towards Cep E. They are, therefore, emitted by the cloud hosting Cep E.

To derive the rotational temperatures and the column densities of these species we carried out a rotational diagram analysis for the deuterated and non deuterated molecules in order to compare their abundances. The results are shown in Table 4.9 and in Table 4.10 are listed the abundance ratios.

The $\text{CH}_2\text{DOH}/\text{CH}_3\text{OH}$ ratio is found to be $0.6_{-0.3}^{+0.5}$ for the ambient gas at central position. This ratio is similar to what found in IRAS 16293-2422 with a

Figure 4.16: Some brightest ion spectra at both positions. At the *top* we show the N_2H^+ lines at the *middle* the HCO^+ lines and at the *bottom* the DCO^+ spectra. Vertical dotted line indicates the systemic velocity.



value of $0.37^{+0.38}_{-0.19}$ [Parise et al., 2006] and higher than the $\text{CH}_2\text{DOH}/\text{CH}_3\text{OH}$ ratio found towards L1157-B1 $(0.2-2) \times 10^{-2}$ [Sugimura et al., 2011]; [Codella et al., 2012]. The DNC/HNC ratio in Cep E is 0.1 larger than in IRAS 16293-2422 (0.03 ± 0.015 [?]). In the case of $\text{N}_2\text{D}^+/\text{N}_2\text{H}^+$ ratio, the value found for Cep E is 0.08 in agreement with the value of 0.03 derived by [Alonso-Albi et al., 2010]. It is also similar to the values found in other Class 0 sources, ~ 0.1 for L1448mms and ~ 0.2 for IRAS 03282 [Emprechtinger et al., 2009]. For $\text{HDCO}/\text{H}_2\text{CO}$, we find a ratio of $0.1^{+0.08}_{-0.05}$, similar to that reported by [Parise et al., 2006] $0.29^{+0.23}_{-0.15}$ towards L1448mms and 0.15 ± 0.07 towards IRAS 16293. It is instead higher than in L1157 ($5 - 8 \times 10^{-3}$) [Codella et al., 2012]. The $\text{D}_2\text{CO}/\text{H}_2\text{CO}$ ratio in Cep E envelope is $0.09^{+0.06}_{-0.04}$. The summary of these comparisons is reported in Table 4.10.

Figure 4.17: Assembly of the line profiles of deuterated molecules observed towards Cep E (Offset 0,0). The dash line indicates the systemic velocity.

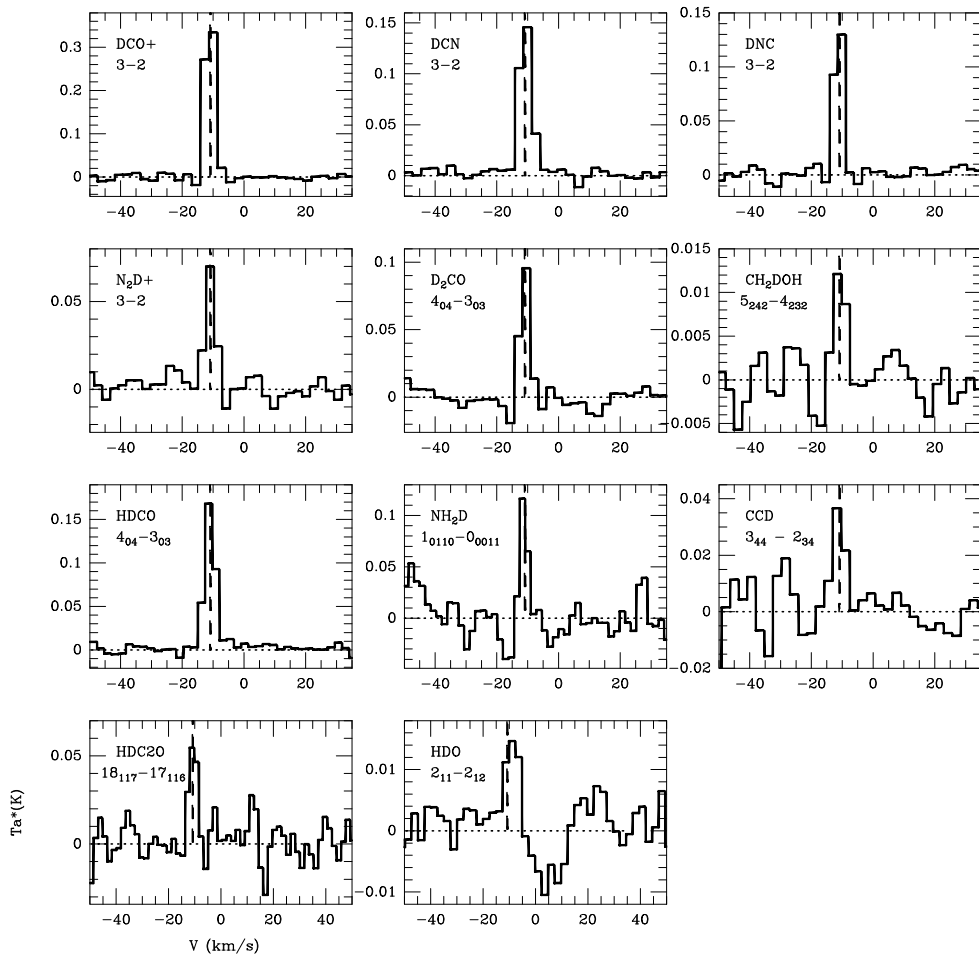


Figure 4.18: Rotational diagrams of CH₂DOH, DCN, N₂D⁺, HDCO and D₂CO . The *squares* are the data and the red line are the fit. The resulting column density and rotational temperature are listed in table 4.9.

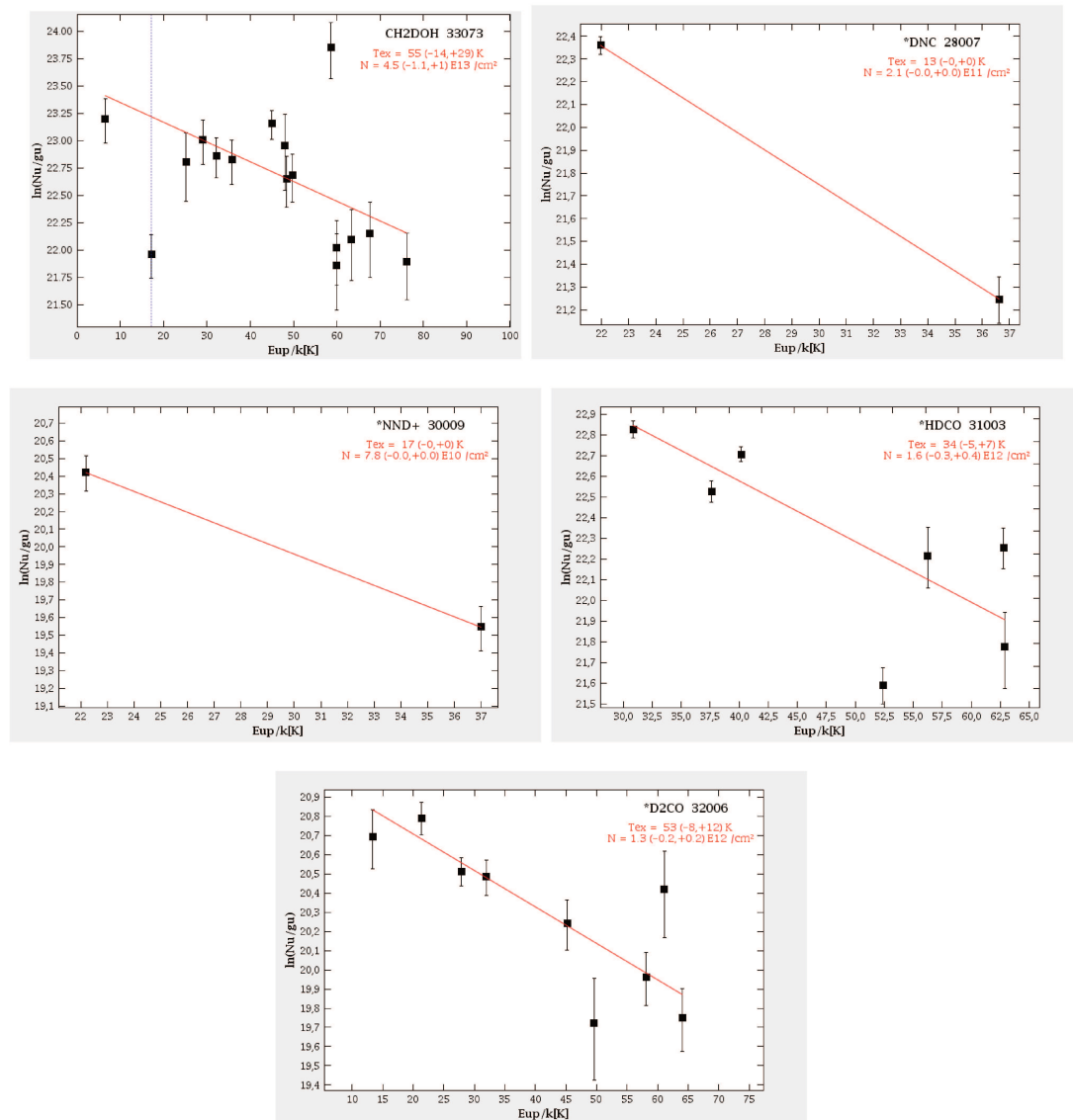


Table 4.5: Summary of the molecules detected. The first and second columns number indicate the number of lines detected toward the central and the south position respectively. Between brackets the total number of transitions in the case of multiplets are indicated. In the third column are the reference numbers from Tables 4.11 and 4.12.

Species	Position (0,0)	Position (-12,-18)	No. Ref.
C-bearing			
CO	3	3	140, 243, 547
¹³ CO	3	3	117, 209, 504
C ¹⁷ O	3	3	128, 224, 517
C ¹⁸ O	3	3	113, 119, 498
CH ₃ OH	56(96)	24(40)	See Table 4.11
CH ₂ DOH	16	1	39,44,192,204,221,222, 281,339,341,347,366, 374,375,378,385,486
CH ₃ CHO	14	7	64,65,72,73,75, 84,85,126,127,135, 136,159,415,495
CH ₃ OCHO	5	3	19,133,258,411,475,501
CH ₃ OCH ₃	2	2	156, 358, 413
CH ₃ CCH	9	6	14,15,96,97,217, 218,271,272,388
CCH	3(18)	0	30, 363, 559
CCD	1(3)	1	182
HCO	2	1	25, 26
DCO ⁺	1(6)	1(6)	180
HCO ⁺	2	2	43, 373
H ¹³ CO ⁺	3	1	27, 355, 554
HC ¹⁸ O ⁺	3	0	11, 337, 527
c-C ₃ H ₂	16	2	4,8,13,181,188, 189,190,233,295,307, 318,319,335,368
C ₄ H	2	0	16, 17
S-bearing			
SO	15	11	22,86,111,178,203

			322,349,361,445,455 466,522,528,542,552
^{34}SO	3	1	32, 168, 179
SO_2	22	7	5,100,101,143,144,163, 216,256,260,287,297,316, 317,331,338,382,419,422, 425,450,488,510,544
OCS	10	1	10,79,112,197,244 291,336,372,408,431
CS	4	4	83, 298, 440, 534
^{13}CS	3	1	60, 246, 398
C^{33}S	2	0	77, 429
C^{34}S	3	1	74, 284, 518
CCS	8	4	2,54,66,91,104, 131,152,350
C^{13}CS	2	1	1, 259, 301
CC^{34}S	0	1	211
H_2S	2	1	161, 183
H_2^{34}S	1	0	157
H_2^{13}CS	2	0	155, 376
H_2CS	19	4	93,98,99,102,162,164,264 276,277,278,279,280,294 379,390,406,469,520,536
HCS^+	2	1	12, 451
N-bearing			
CN	6(24)	5(21)	129,132,230,231,524,525,
DCN	1(5)	0	186
HCN	2(4)	2(4)	40, 369
H^{13}CN	3	2	23, 352, 545
HC^{15}N	2	1	21, 348
CH_3CN	9(28)	5(10)	56,121,145,214,270 342,394,444,508
DNC	2	0	239, 471

HNC	2	2	53, 384
HN ¹³ C	3	1	29, 359, 556
H ¹⁵ NC	1	1	42
HNCO	5	3	32,115,201,290,364
HCNO	1	0	541
HC ₃ N	15	5	3,55,92,110,165,193,234,263 300,334,365,386,421,426,452
NH ₂ D	3(10)	1(4)	20, 116, 511
NH ₂ OH	1	0	18
N ₂ D ⁺	2	0	248, 480
N ₂ H ⁺	2	2	63, 407
NO	4(6)	2	308,309,310,313,314,315
O-bearing			
SiO	5	5	28, 185, 356, 465, 555
HDCO	7	2	304,340,346,354, 377,479,492,512
HDCCO	2	1	420, 533
HDO	1	0	286
D ₂ CO	13	0	122,150,215,249,253,259,299, 395,430,446,476,505,532
H ₂ CO	10	9	169,191,195,196,225, 418,427,428,232,454
H ₂ ¹³ CO	6	1	174,202,391,424,435,537
H ₂ CCO	3	1	95, 274, 410

Table 4.6: Summary of ions detected. Between brackets the total number of transitions in the case of multiplets are indicated. In the third column are the reference numbers from Tables 4.11 and 4.12.

Species	Position (0,0)	Position (-12,-18)	No. Ref.
DCO ⁺	1(6)	1(6)	180
HCO ⁺	2	2	43, 373
H ¹³ CO ⁺	3	1	27, 355, 554
HC ¹⁸ O ⁺	3	0	11, 337, 527

HCS ⁺	2	1	12, 451
N ₂ D ⁺	2	0	248, 480
N ₂ H ⁺	2	2	63, 407

Table 4.7: Summary of deuterated molecules detected. Between brackets the total number of transitions in the case of multiplets are indicated. In the third column are the reference numbers from Tables 4.11 and 4.12.

Species	Position (0,0)	Position (-12,-8)	No. Ref.
CH ₂ DOH	16	1	39,44,192,204,221,222,281,339, 341,347,366,374,375,378,385,486
CCD	1(3)	1	182
DCO ⁺	1(6)	1(6)	180
DCN	1(5)	0	186
DNC	2	0	239, 471
NH ₂ D	3(10)	1(4)	20, 116, 511
N ₂ D ⁺	2	0	248, 480
HDCO	7	2	304,340,346,354,377,479,492,512
HDCCO	2	1	420, 533
HDO	1	0	286
D ₂ CO	13	0	122,150,215,249,253,259,299, 395,430,446,476,505,532

Table 4.8: Summary of complex organic molecules detected. Between brackets the total number of transitions in the case of multiplets are indicated. In the third column are the reference numbers from Tables 4.11 and 4.12.

Species	Position (0,0)	Position (-12,-18)	No. Ref.
CH ₃ OH	56(96)	24(40)	See Table 4.11
CH ₂ DOH	16	1	39,44,192,204,221,222, 281,339,341,347,366, 374,375,378,385,486
CH ₃ CHO	14	7	64,65,72,73,75, 84,85,126,127,135, 136,159,415,495

CH ₃ OCHO	5	3	19,133,258,411,475,501
CH ₃ OCH ₃	2	2	156, 358, 413
CH ₃ CN	9(28)	5(10)	56,121,145,214,270 342,394,444,508
NH ₂ OH	1	0	18
H ₂ CO	10	9	169,191,195,196,225, 418,427,428,232,454
H ₂ ¹³ CO	6	1	174,202,391,424,435,537
CH ₃ CCH	9	6	14,15,96,97,217, 218,271,272,388
H ₂ CCO	3	1	95, 274, 410

Table 4.9: Column densities and T_{rot} derived using a rotation diagram analysis. These values are used to compute the deuterated fraction (see Table 4.10). The abundances are expressed respect to H_2 and CO-normalized, i.e, $X_4^{\text{CO}} = N/N_{\text{CO}} \times 10^4$.

Molecule	$N \text{ (cm}^{-2}\text{)}$	$T_{\text{rot}} \text{ (K)}$	X_4^{CO}
CH_2DOH	$4.5_{-1.1}^{+1} \times 10^{13}$	55_{-14}^{+29}	102.3 ± 29.7
CH_3OH	$8.0_{-3}^{+5} \times 10^{13}$	33_{-11}^{+34}	$181.8_{-76.4}^{+126.0}$
DNC	2.1×10^{11}	13	$0.5_{-0.02}^{+0.03}$
HNC	2.1×10^{12}	15	$4.8_{0.2}^{+0.3}$
N_2D^+	7.8×10^{10}	17	0.2 ± 0.01
N_2H^+	1.0×10^{12}	21	2.3 ± 0.1
D_2CO	$1.3 \pm 0.2 \times 10^{12}$	53_{-8}^{+12}	$3.0_{-0.6}^{+0.7}$
HDCO	$1.6_{-0.3}^{+0.4} \times 10^{12}$	34_{-5}^{+7}	$3.6_{-0.8}^{+1.1}$
H_2CO	$1.5_{-0.5}^{+0.8} \times 10^{13}$	84_{-39}^{+448}	$34.1_{-12.9}^{+20.5}$

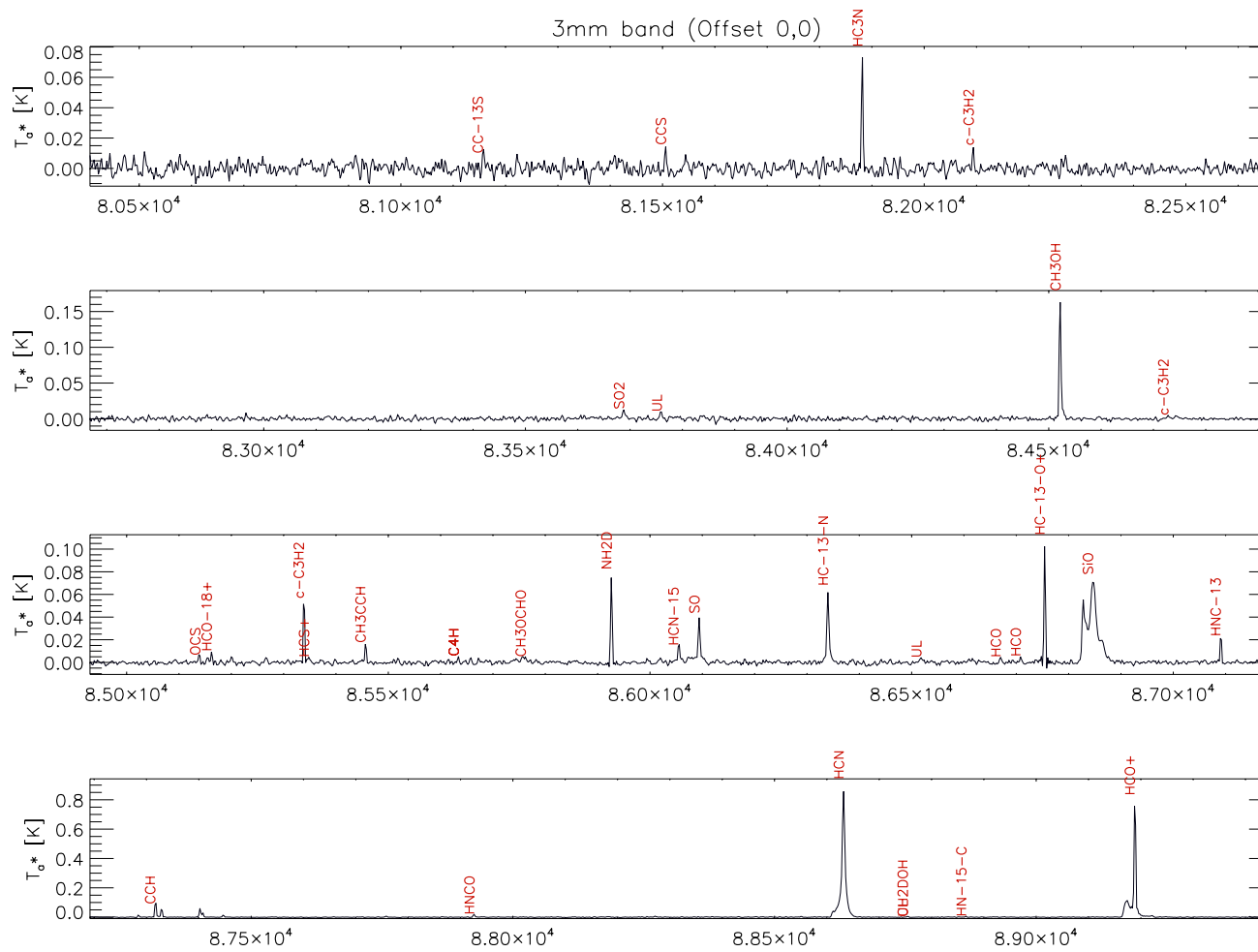
Table 4.10: Ratios between some of the deuterated molecules and its corresponding non-deuterated molecule. In the first column there are the values obtained in our survey towards (0,0) position. The values listed here correspond to the ambient gas component (envelope) towards offset (0, 0). See the text. The other columns show the same ratios towards Class 0 low-mass protostars, pre-stellar cores, L1157-B1 and IM protostars in order to compare our results.

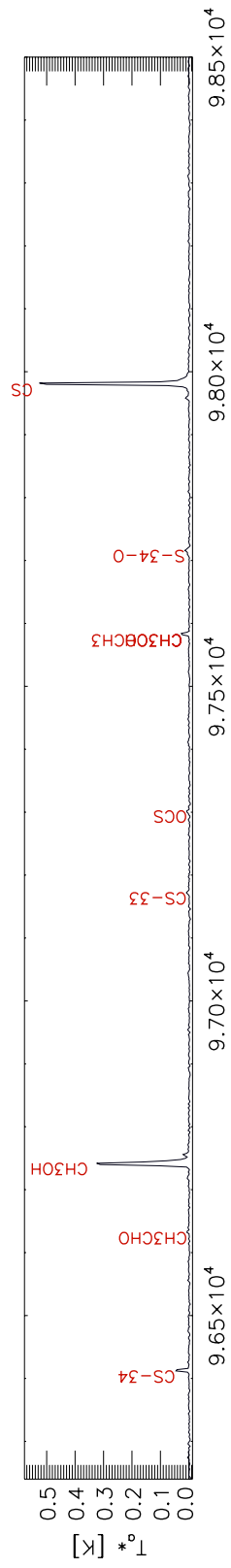
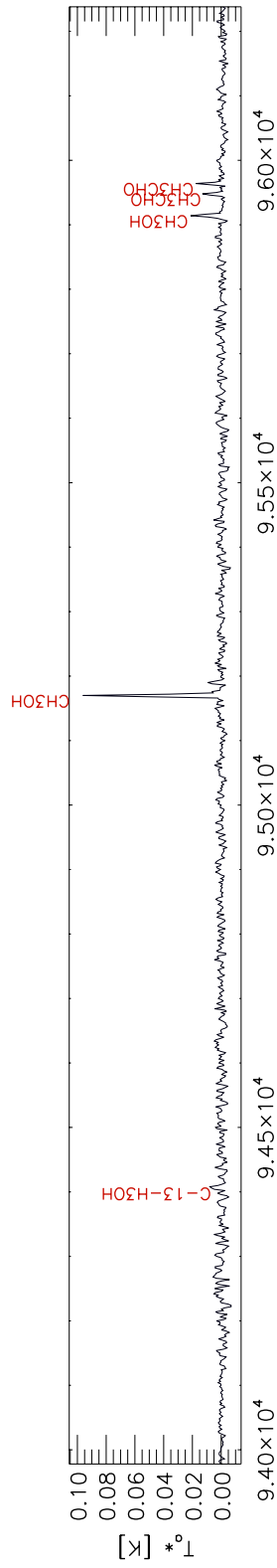
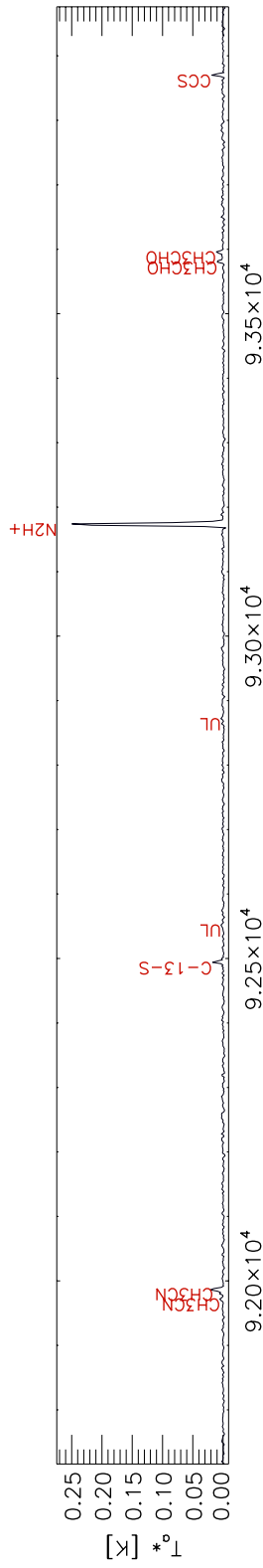
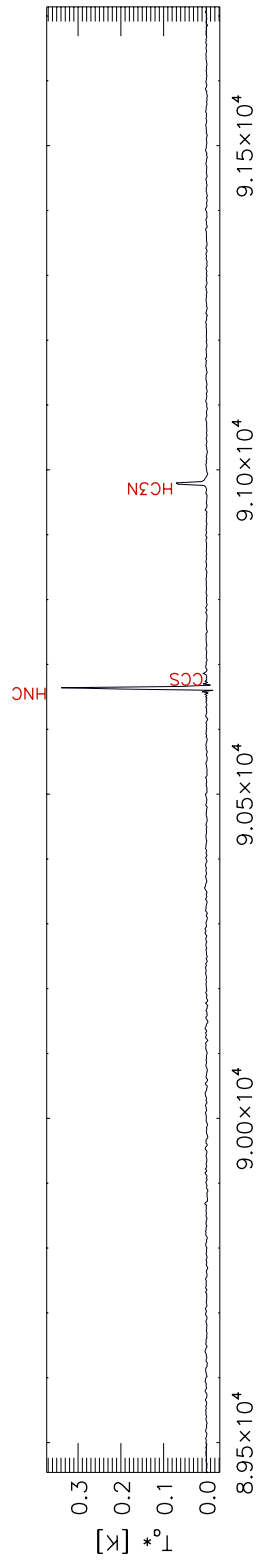
	Cep Envelope	Low-mass protostars ^a	Pre-stellar cores	L1157-B1 ^d	IM protostars ^e
$\text{CH}_2\text{DOH}/\text{CH}_3\text{OH}$	$0.60_{-0.3}^{+0.5}$	$0.37_{-0.19}^{+0.38}$		$0.2 - 2 \times 10^{-2}$	
DNC/HNC	0.10	0.03 ± 0.015^g			
$\text{N}_2\text{D}^+/\text{N}_2\text{H}^+$	0.08	0.10 ± 0.02^f	0.05 ± 0.01^b		0.03
HDCO/ H_2CO	$0.10_{-0.05}^{+0.08}$	0.15 ± 0.07		$5 - 8 \times 10^{-3}$	
$\text{D}_2\text{CO}/\text{H}_2\text{CO}$	$0.09_{-0.04}^{+0.06}$	0.05 ± 0.025	$0.04_{-0.03}^{+0.06^c}$		

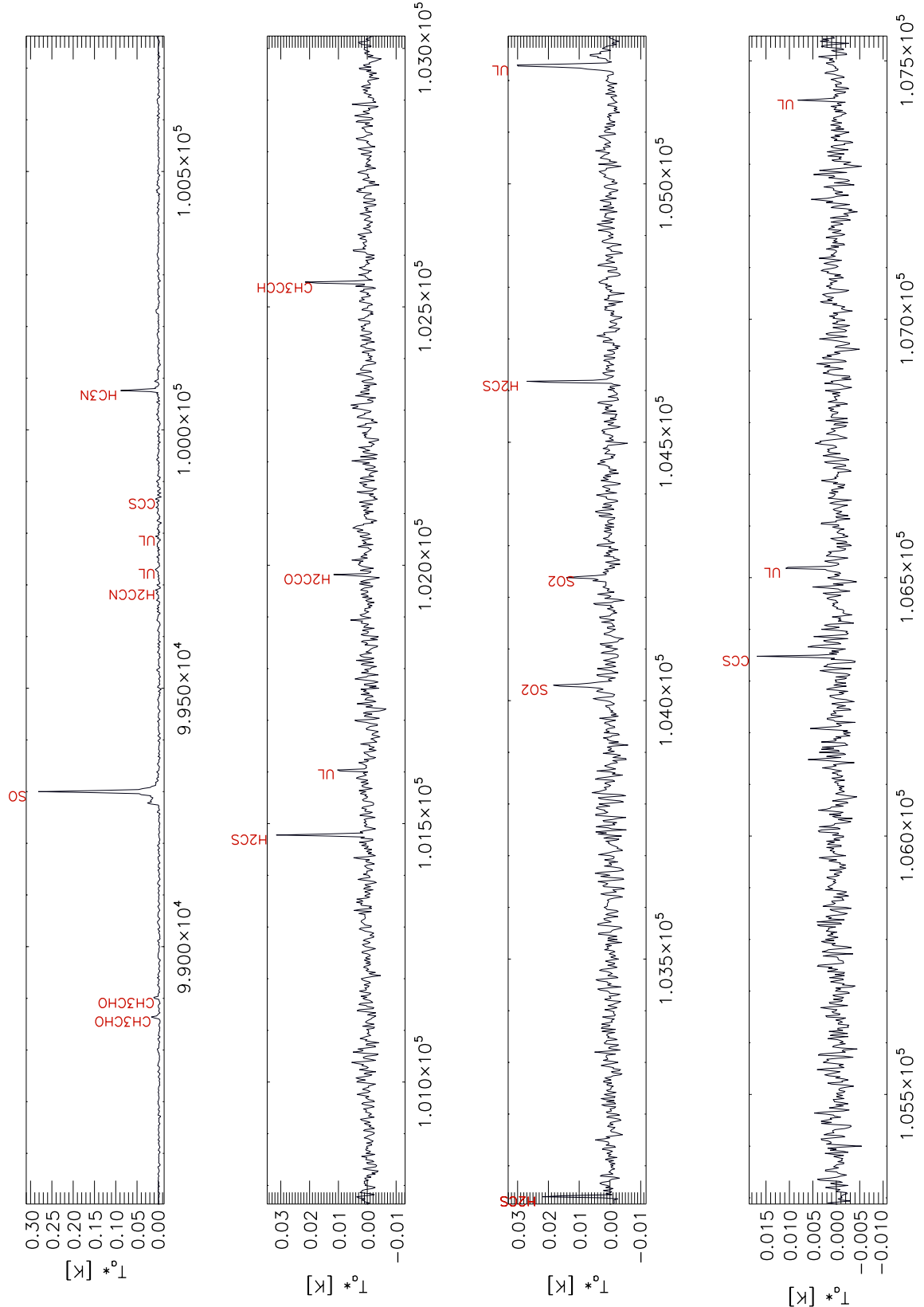
REFS: ^a [Parise et al., 2006] towards IRAS 16293; ^b [Crapsi et al., 2005] towards L1495; ^c [Bacmann et al., 2003] towards L1544; ^d [Codella et al., 2012]; ^e [Alonso-Albi et al., 2010] towards Cep E; ^f [Emprechtinger et al., 2009] towards L1448mms; ^g [van Dishoeck et al., 1995] towards IRAS 16293.

Line catalogue

Figure 4.19: 3 mm band taken toward Cep E region. Each line is labeled with the molecular specie (See Table 4.11). Features appearing as absorption spikes were removed because they are artifacts. Signals are in antenna temperature (K).







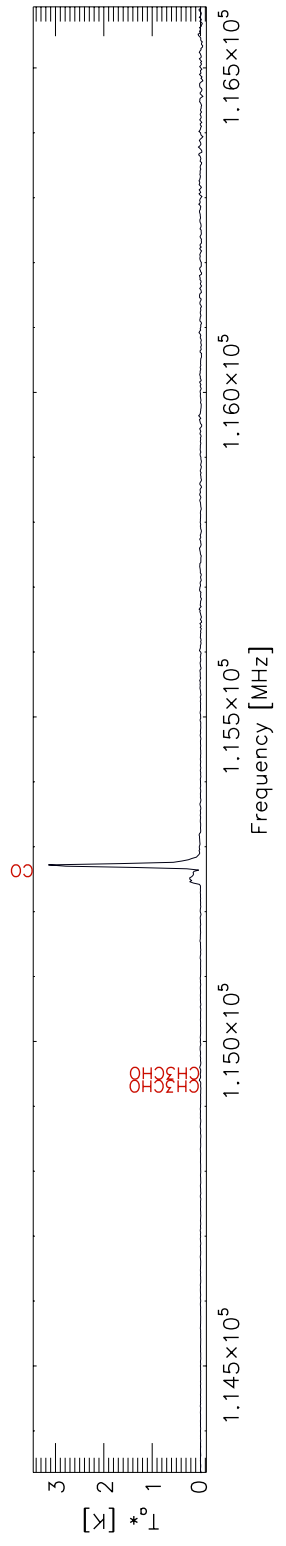
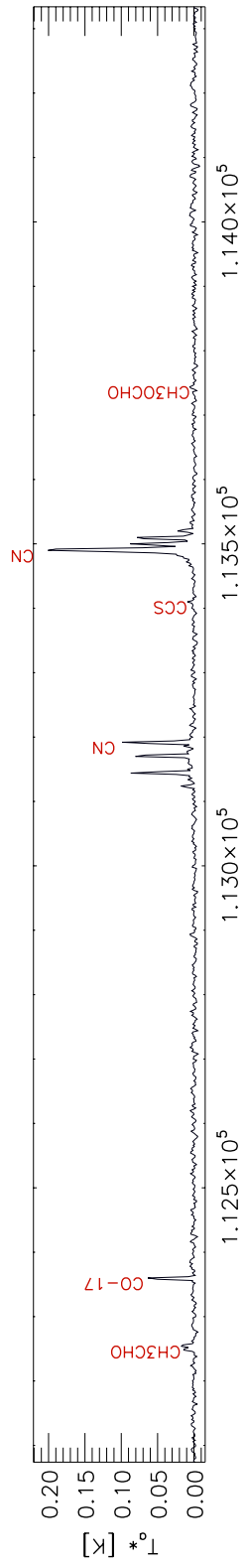
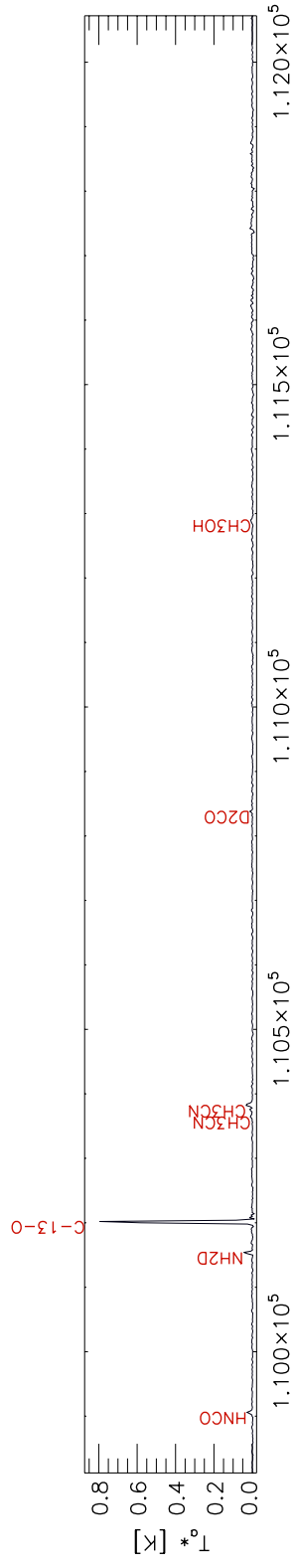
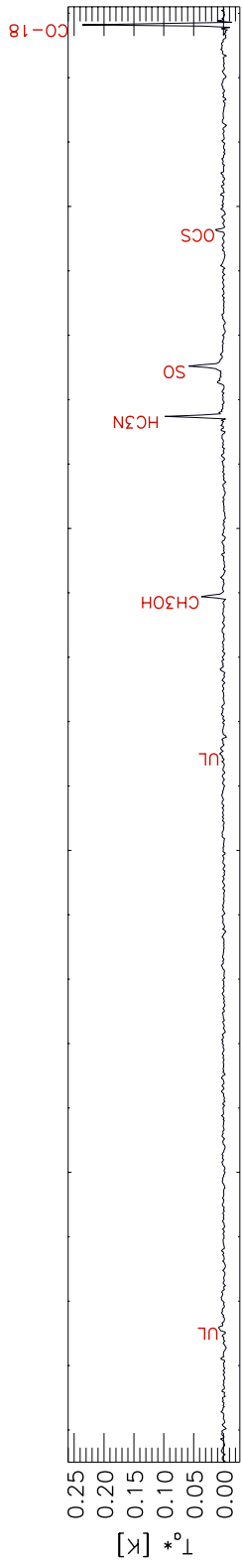


Figure 4.20: 2 mm band from 164-170 GHz. Each line is labeled with the molecular specie (See Table 4.11). Features appearing as absorption spikes were removed because they are artifacts. Signals are in antenna temperature (K).

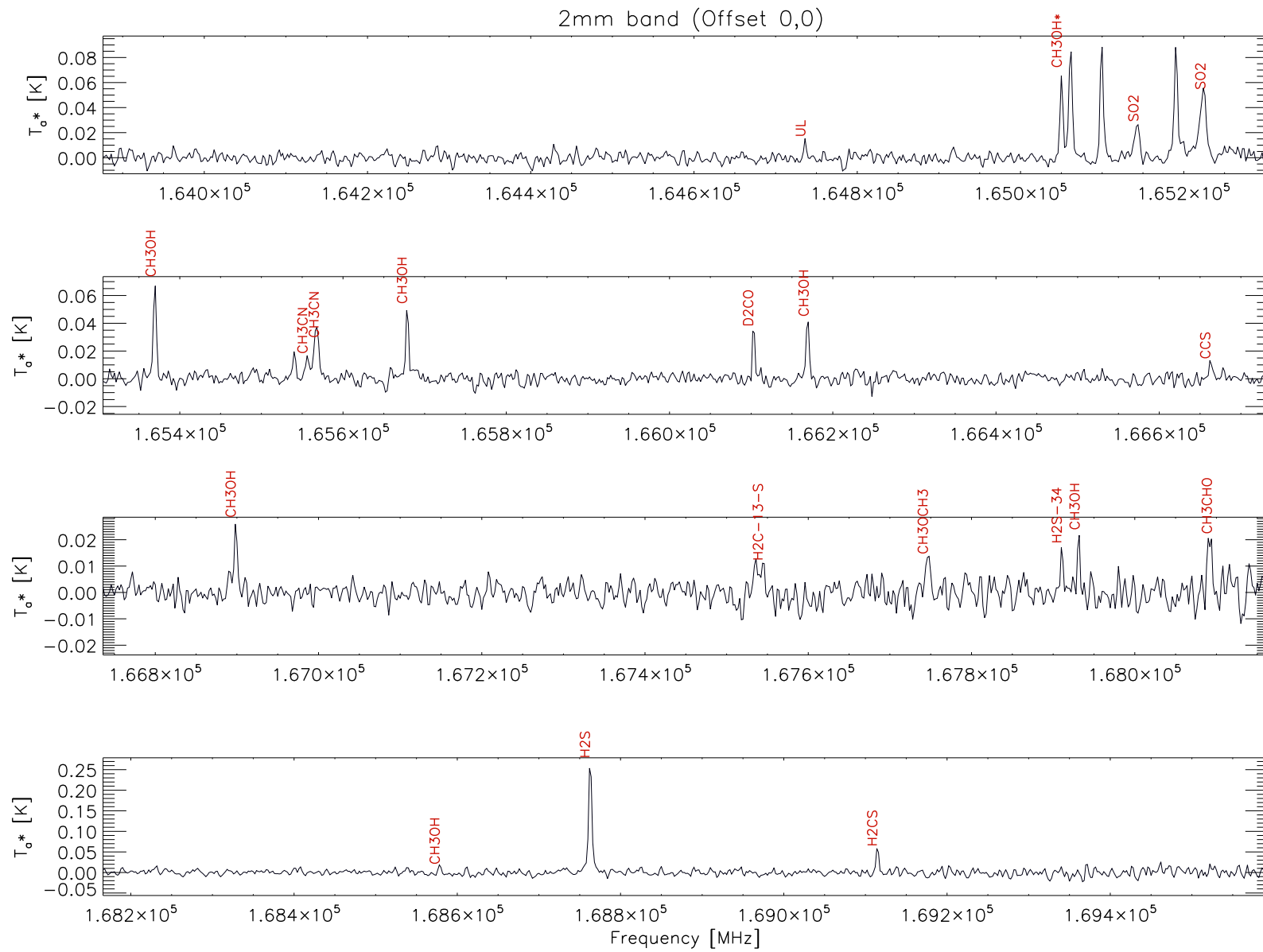
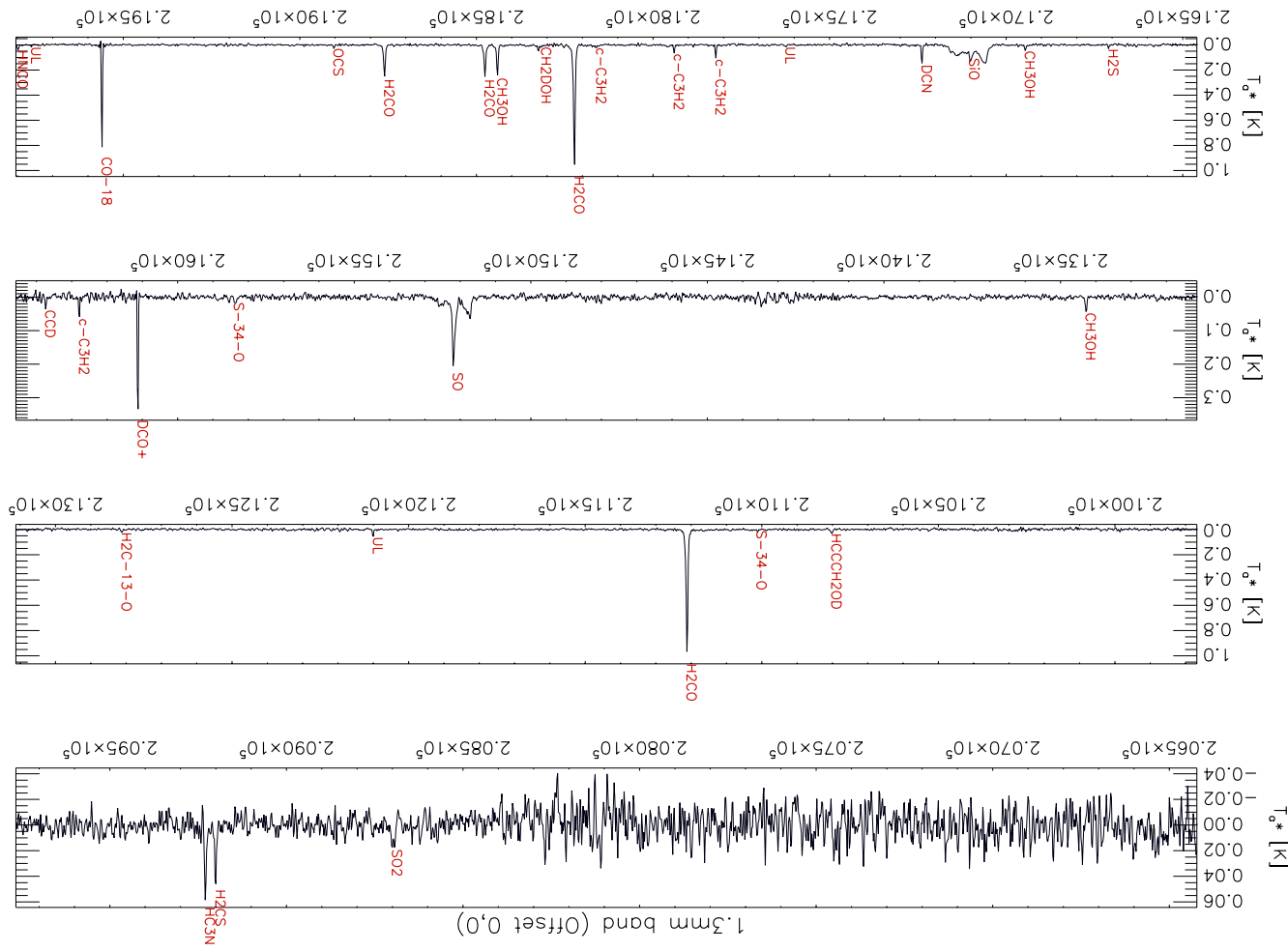
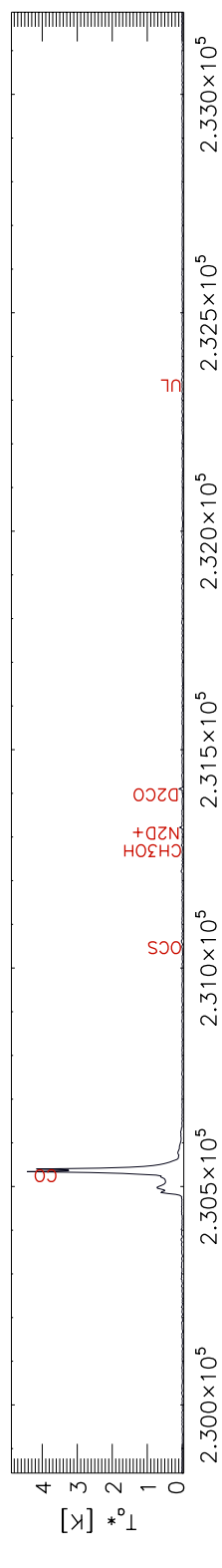
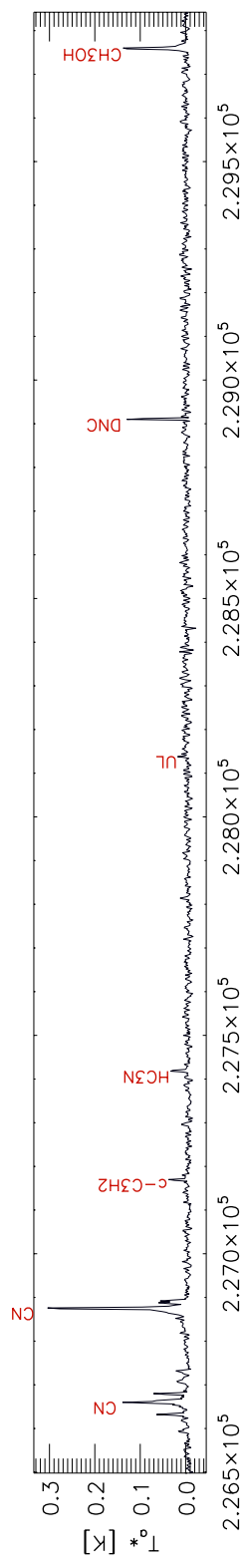
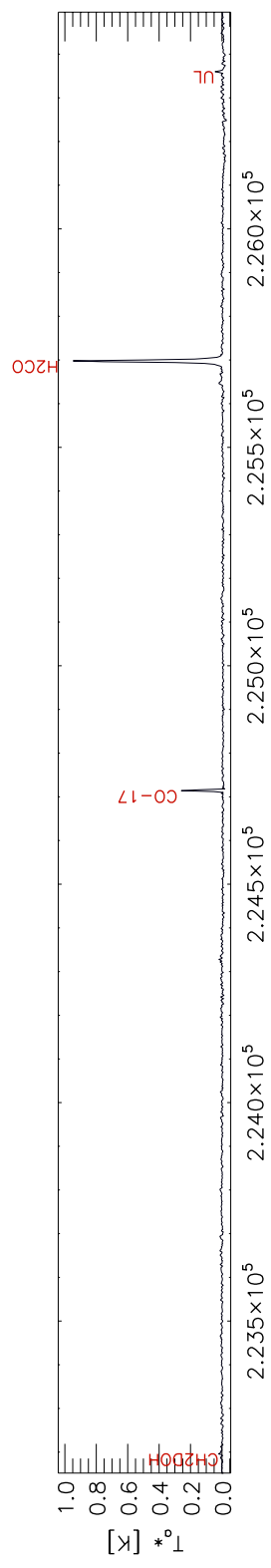
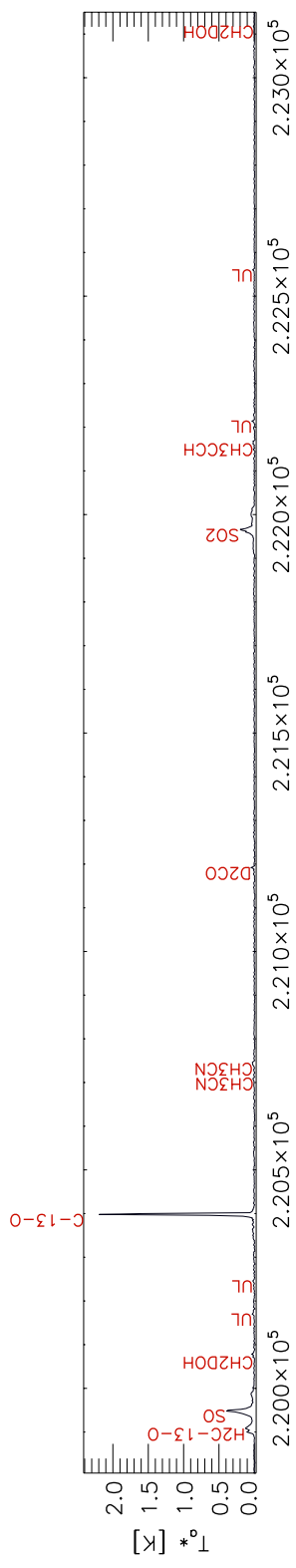
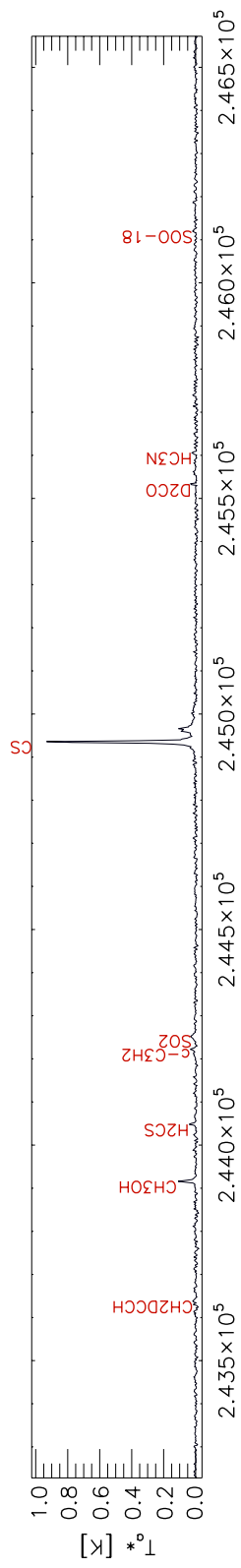
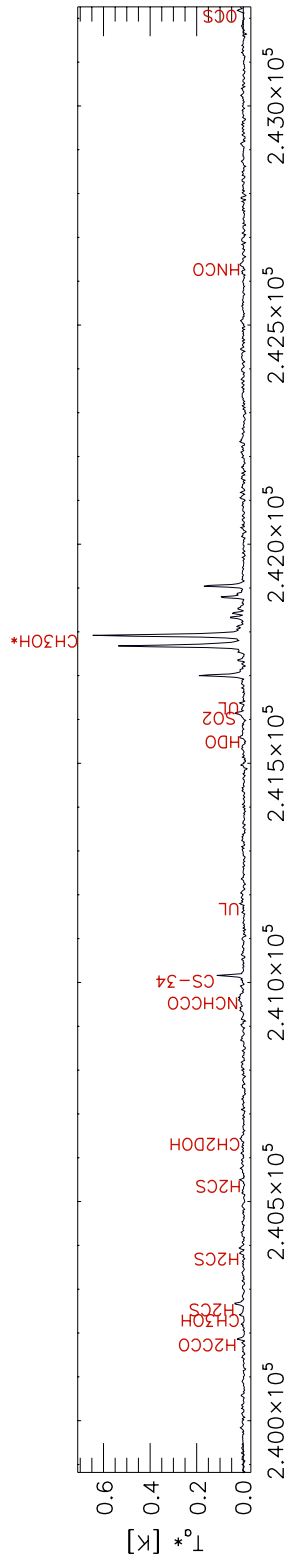
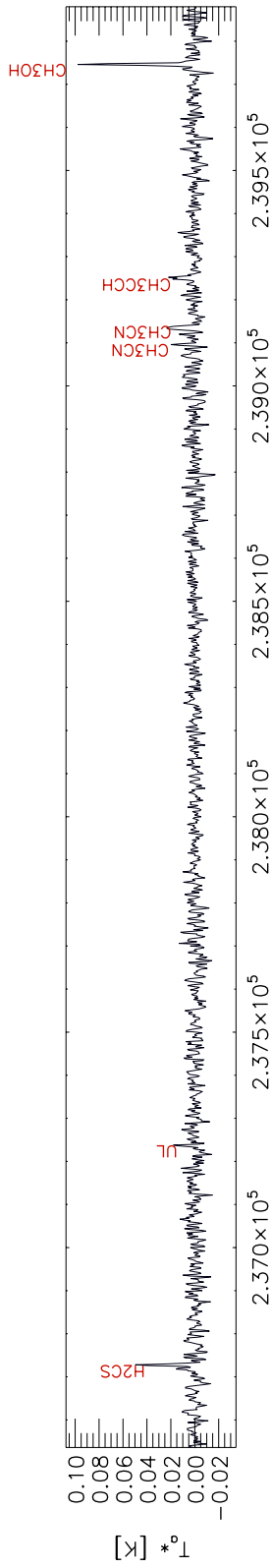
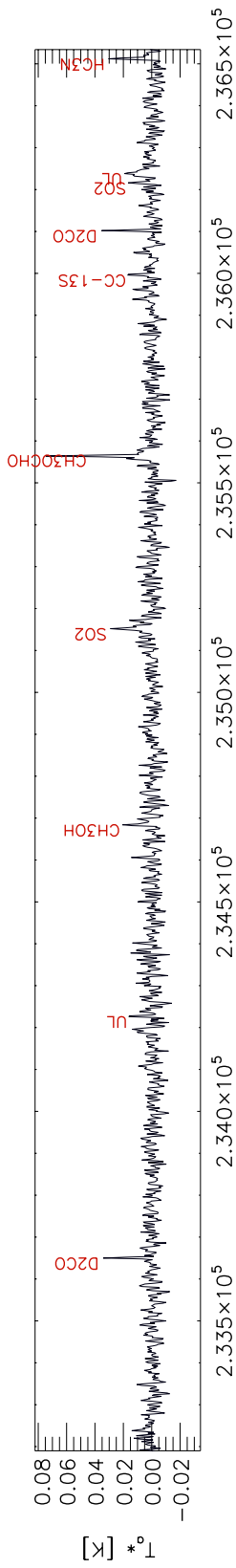


Figure 4.21: 1.3 mm band from 207-260 GHz. Each line is labeled with the molecular specie (See Table 4.11). Features appearing as absorption spikes were removed because they are artifacts. Signals are in antenna temperature (K).







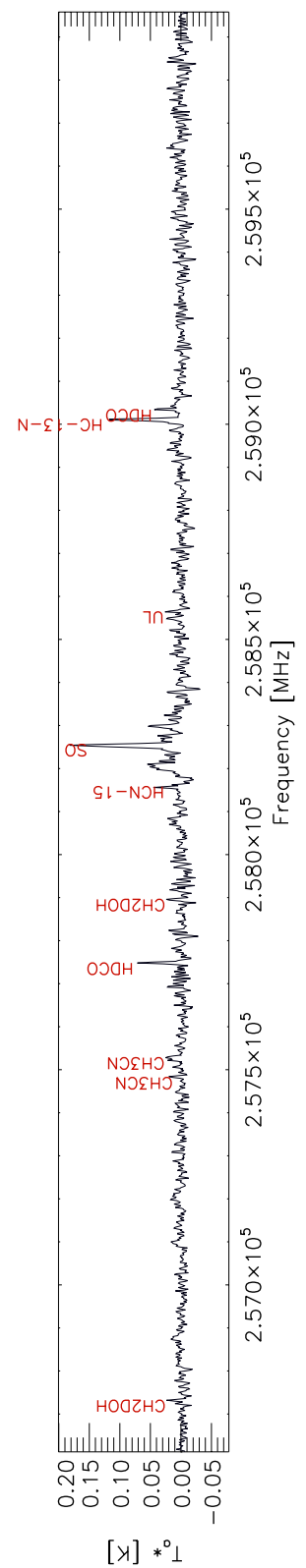
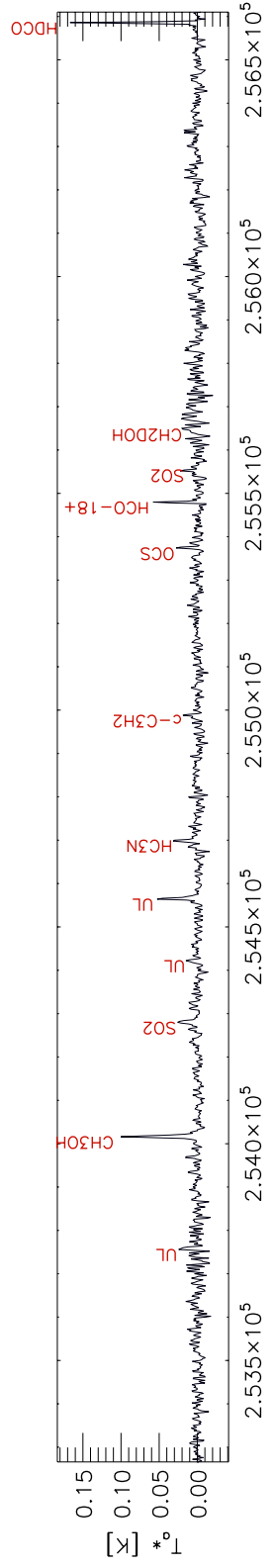
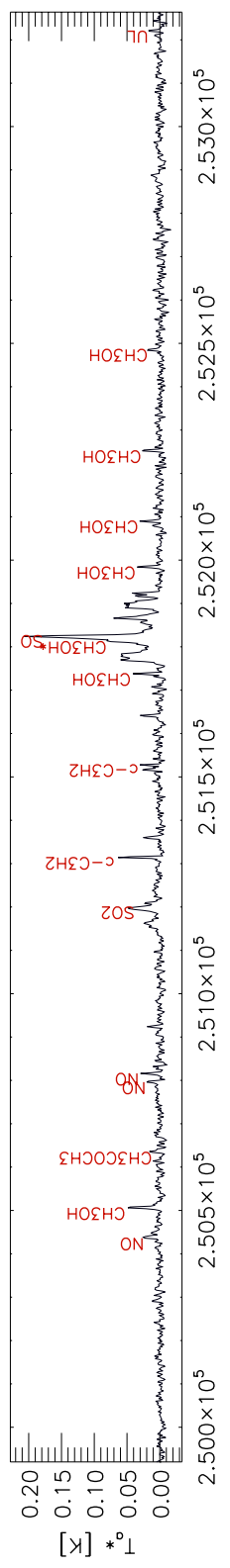
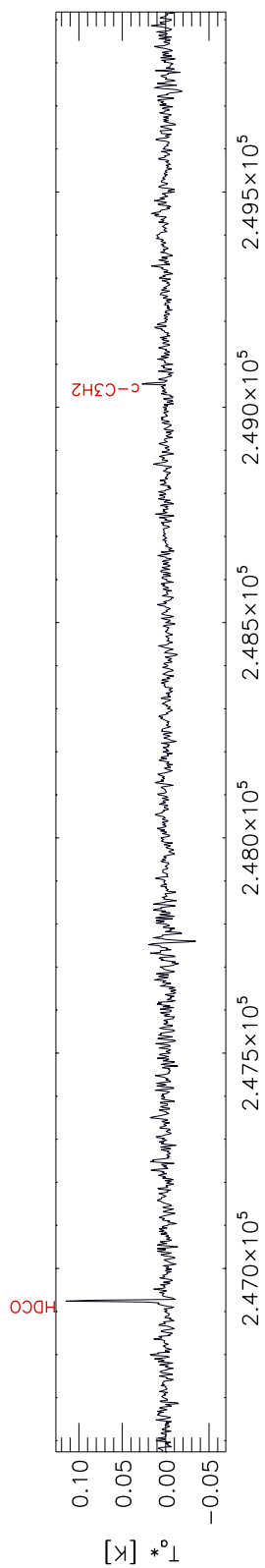
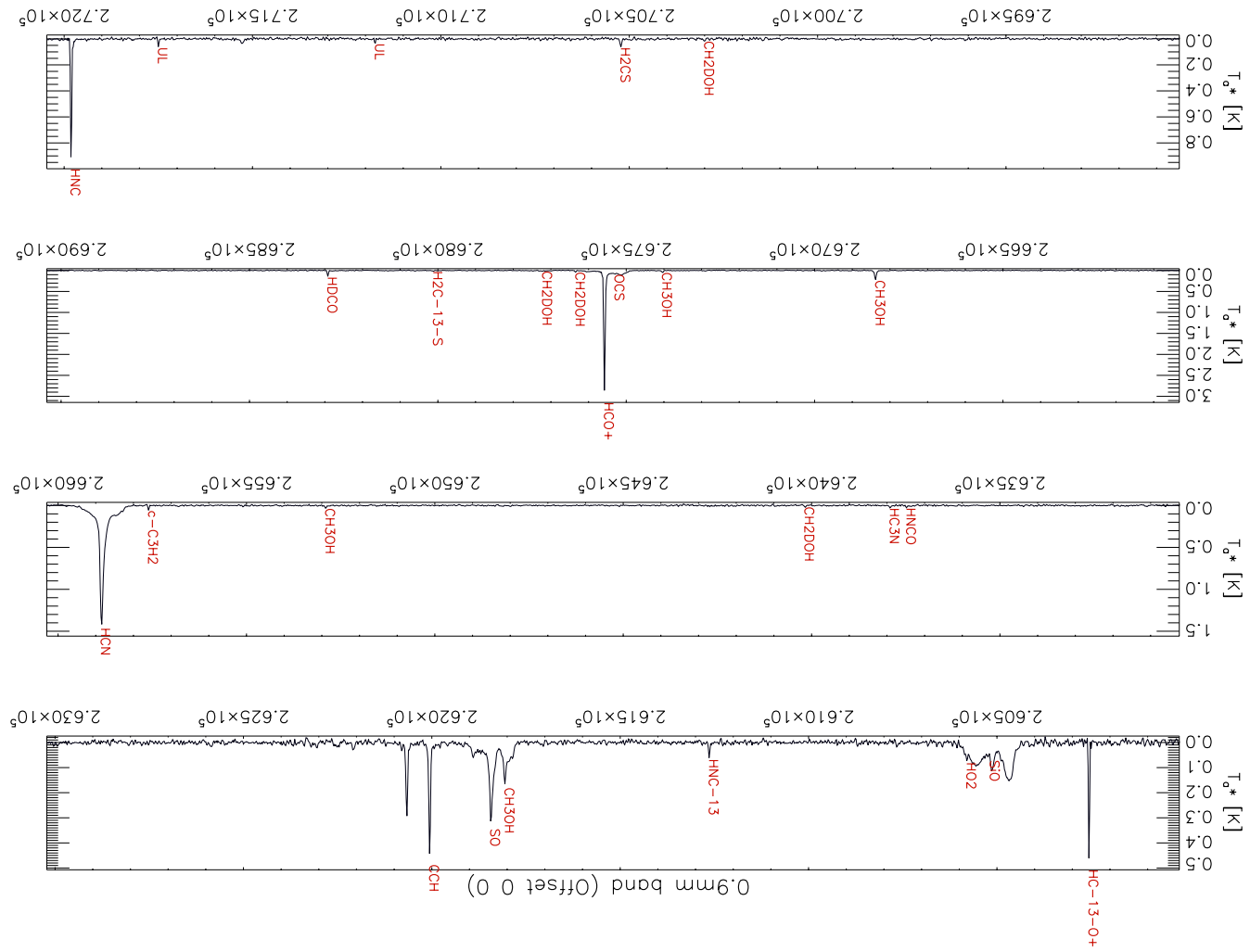
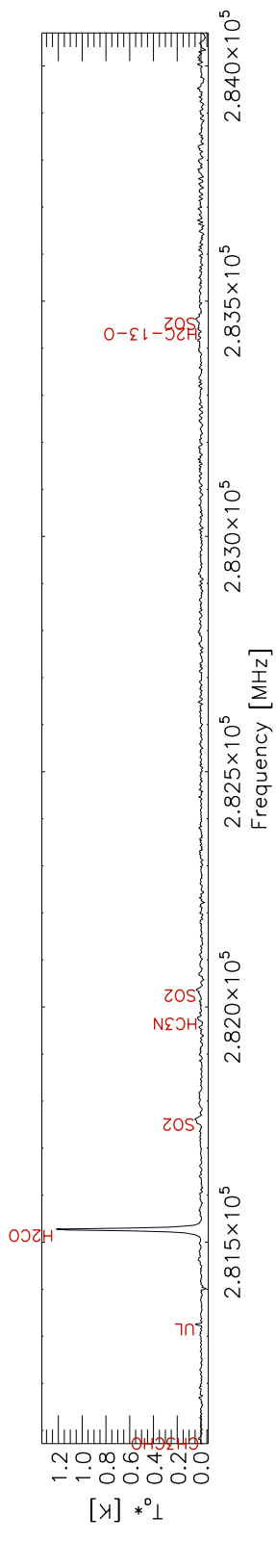
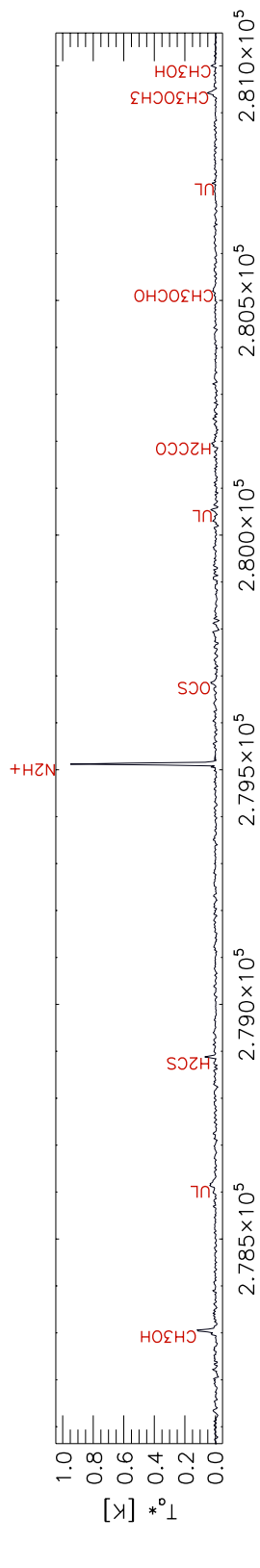
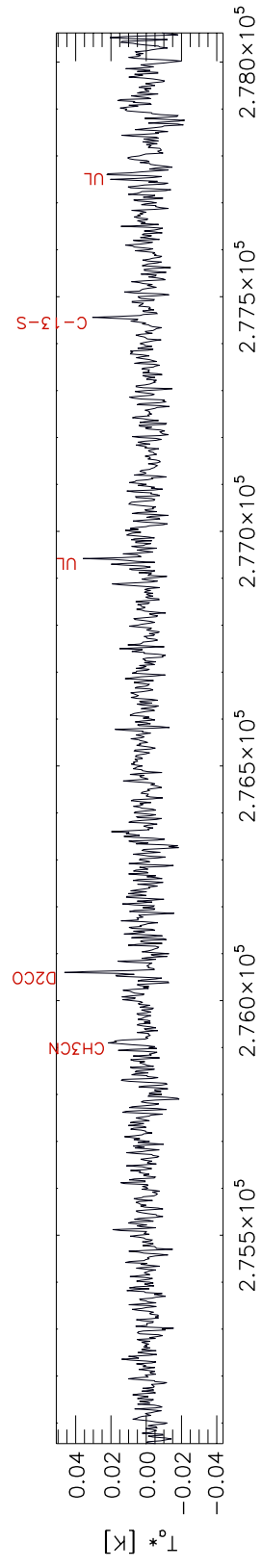
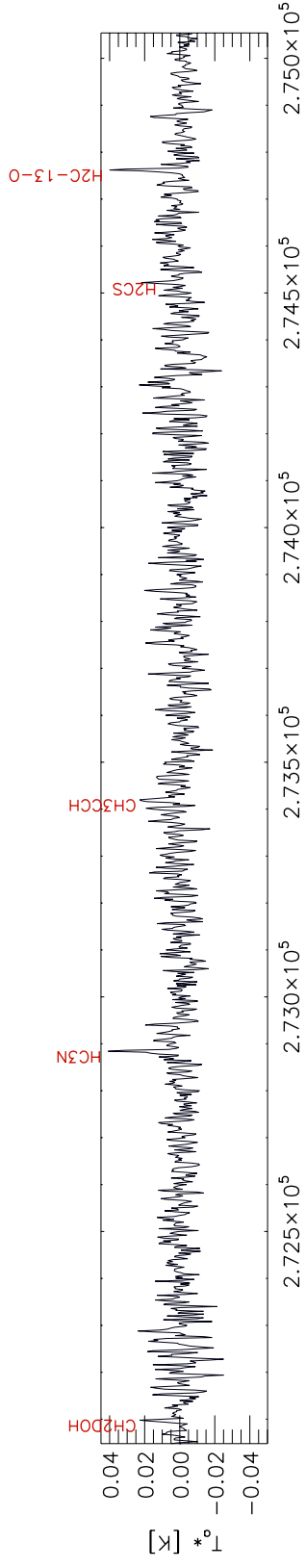
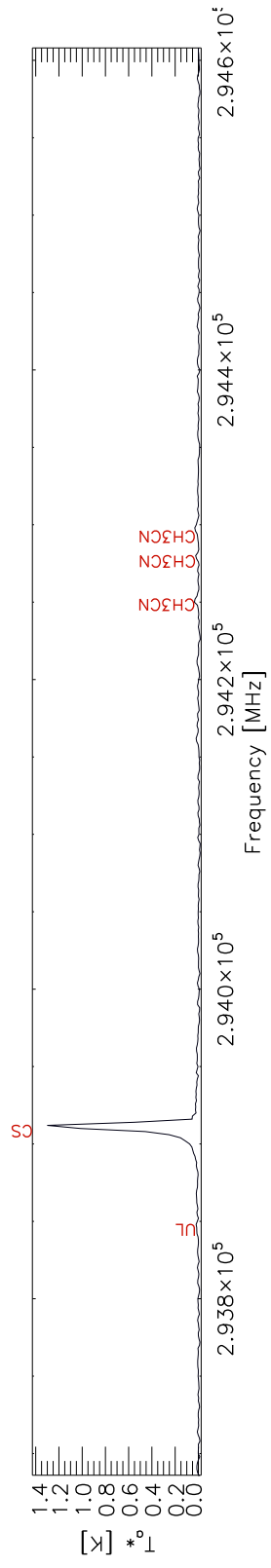
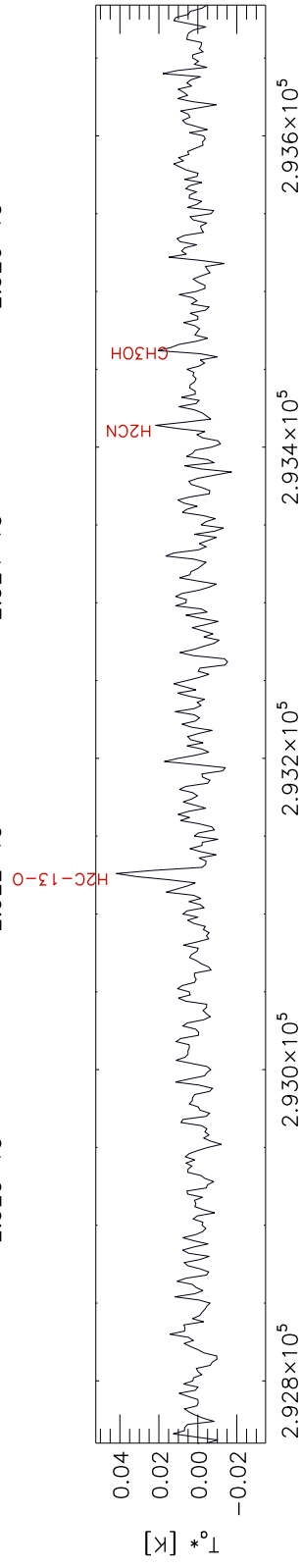
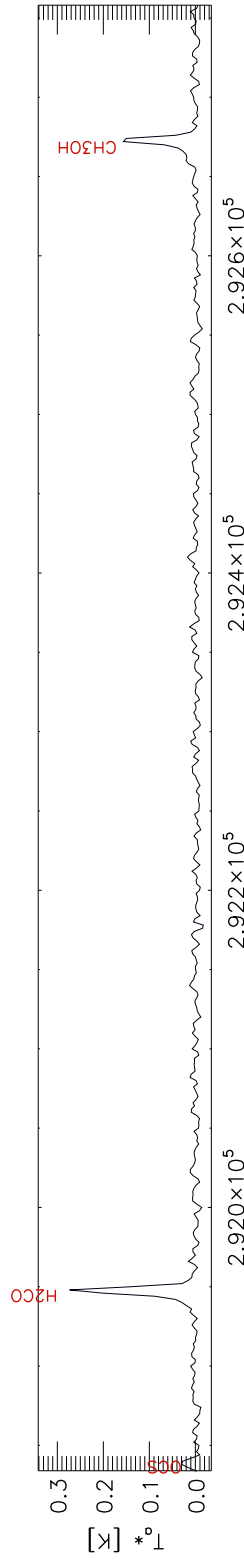
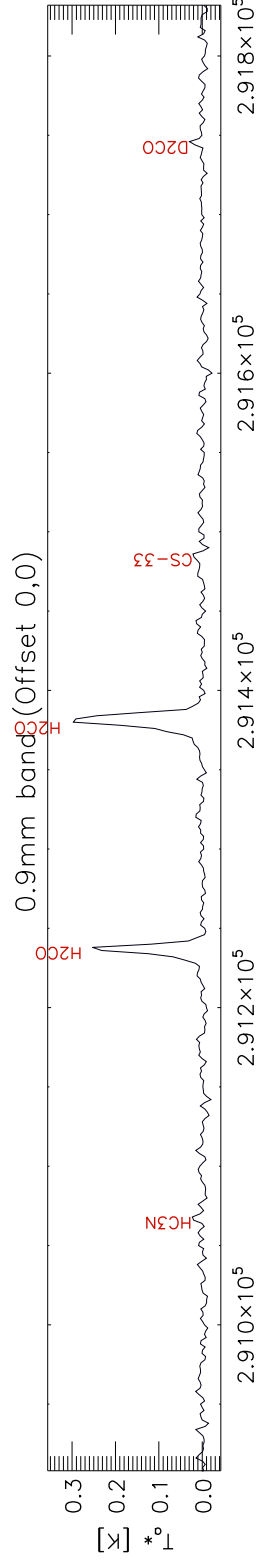


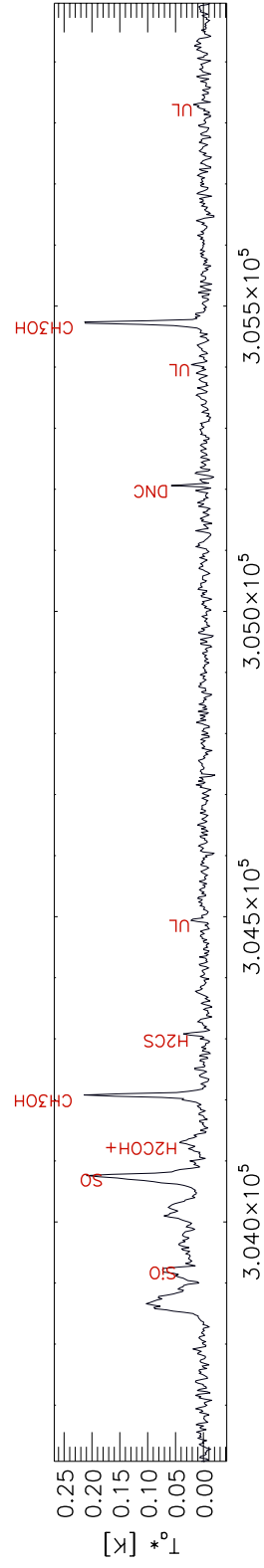
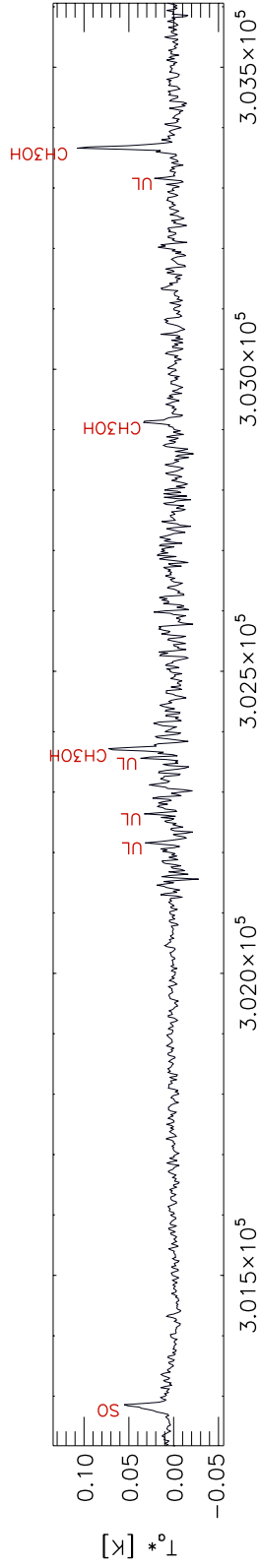
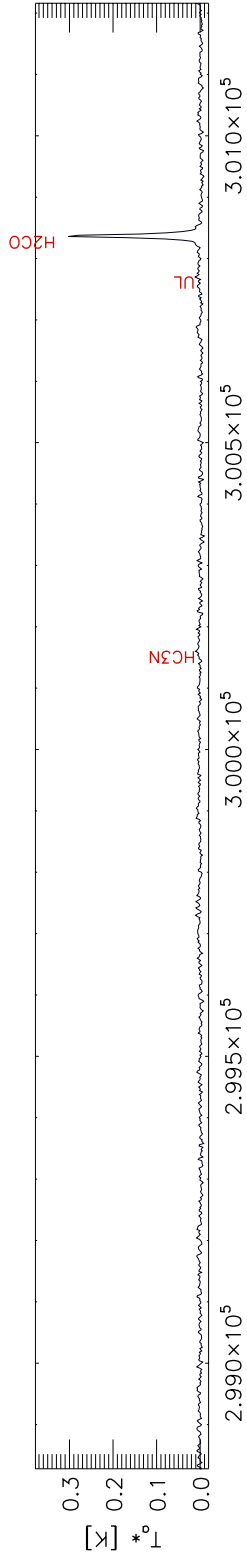
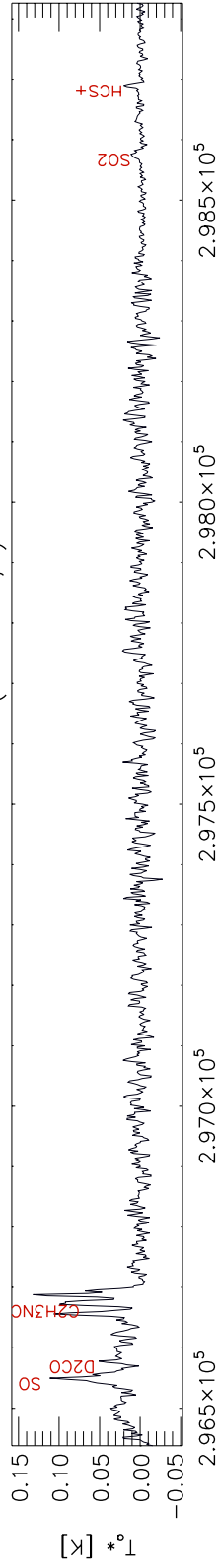
Figure 4.22: 0.9 mm band from 260-305 GHz. Signals are in antenna temperature (K).

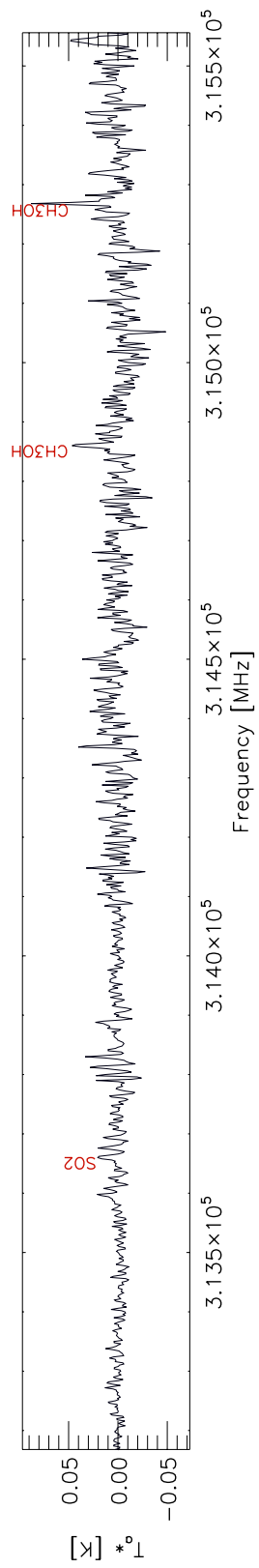
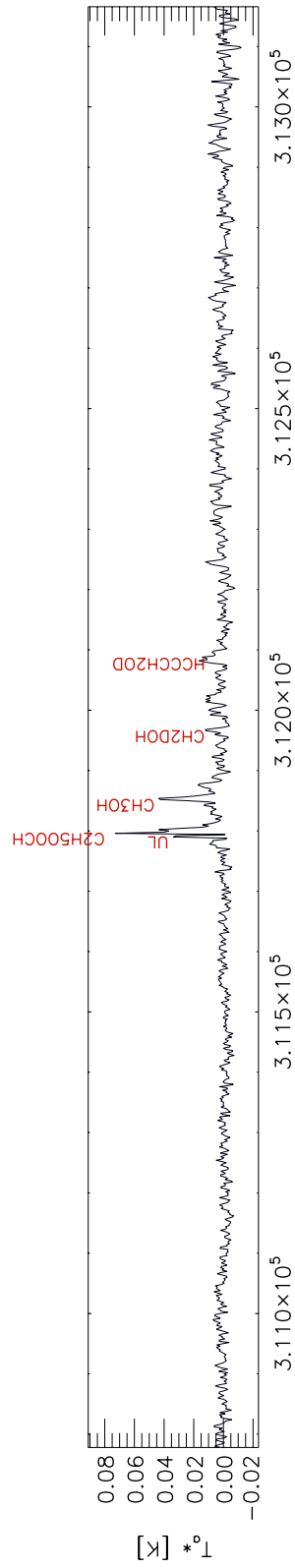
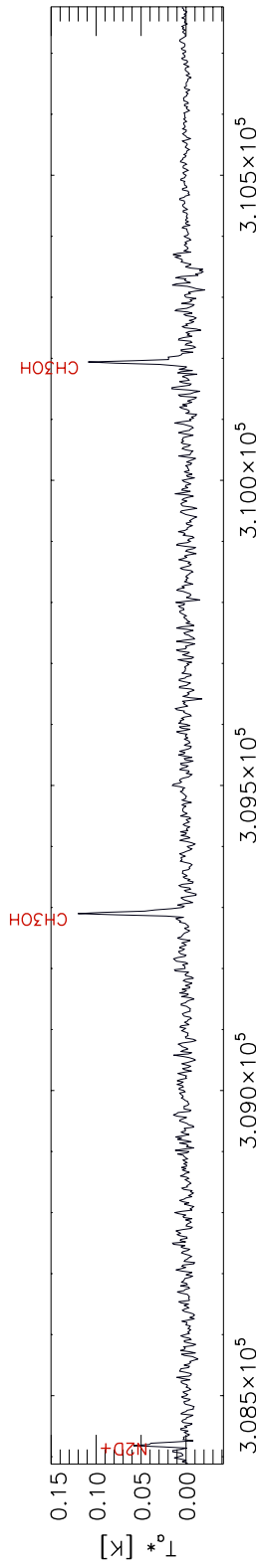
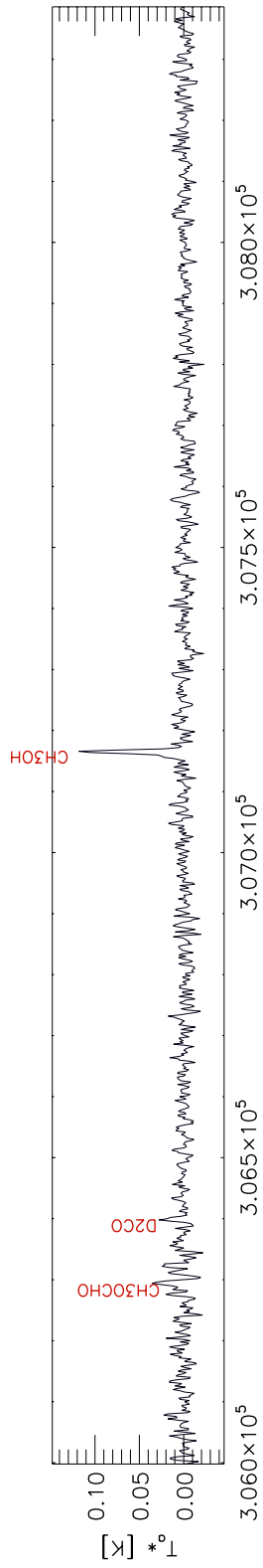






0.9mm band (Offset 0,0)





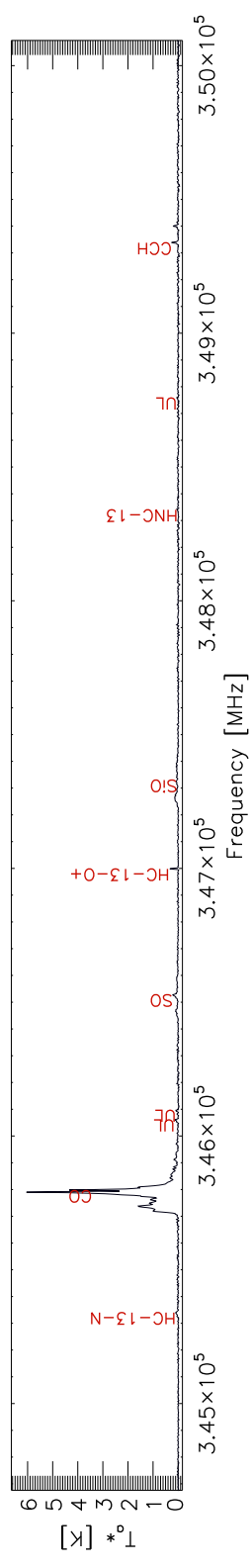
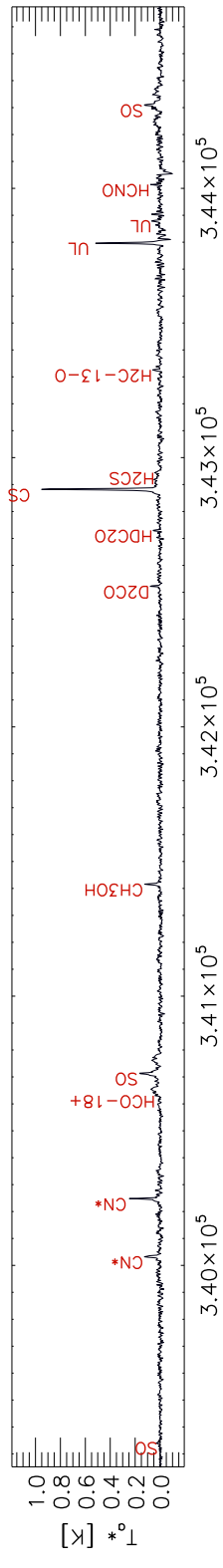
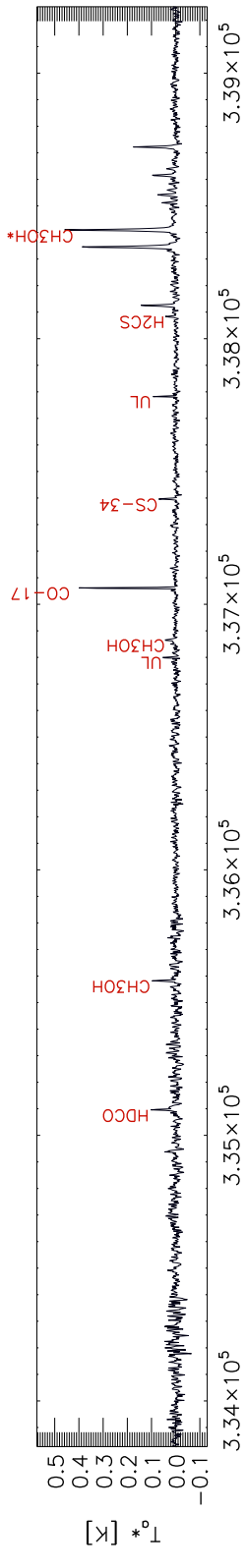
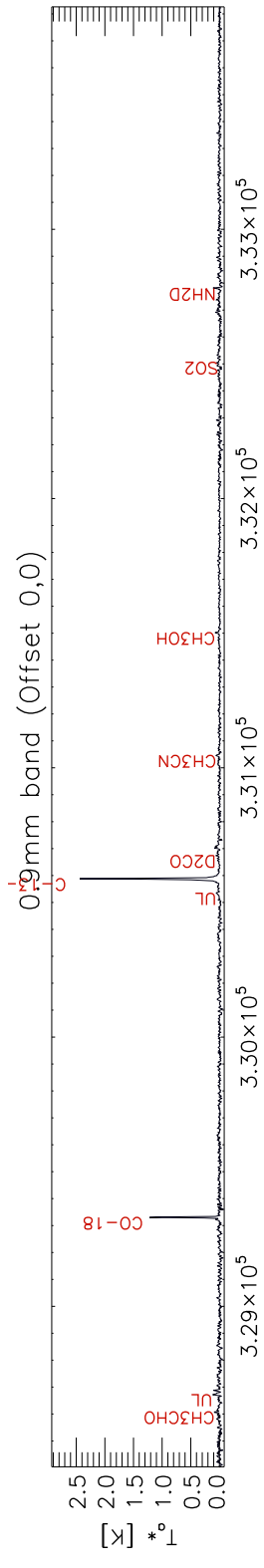
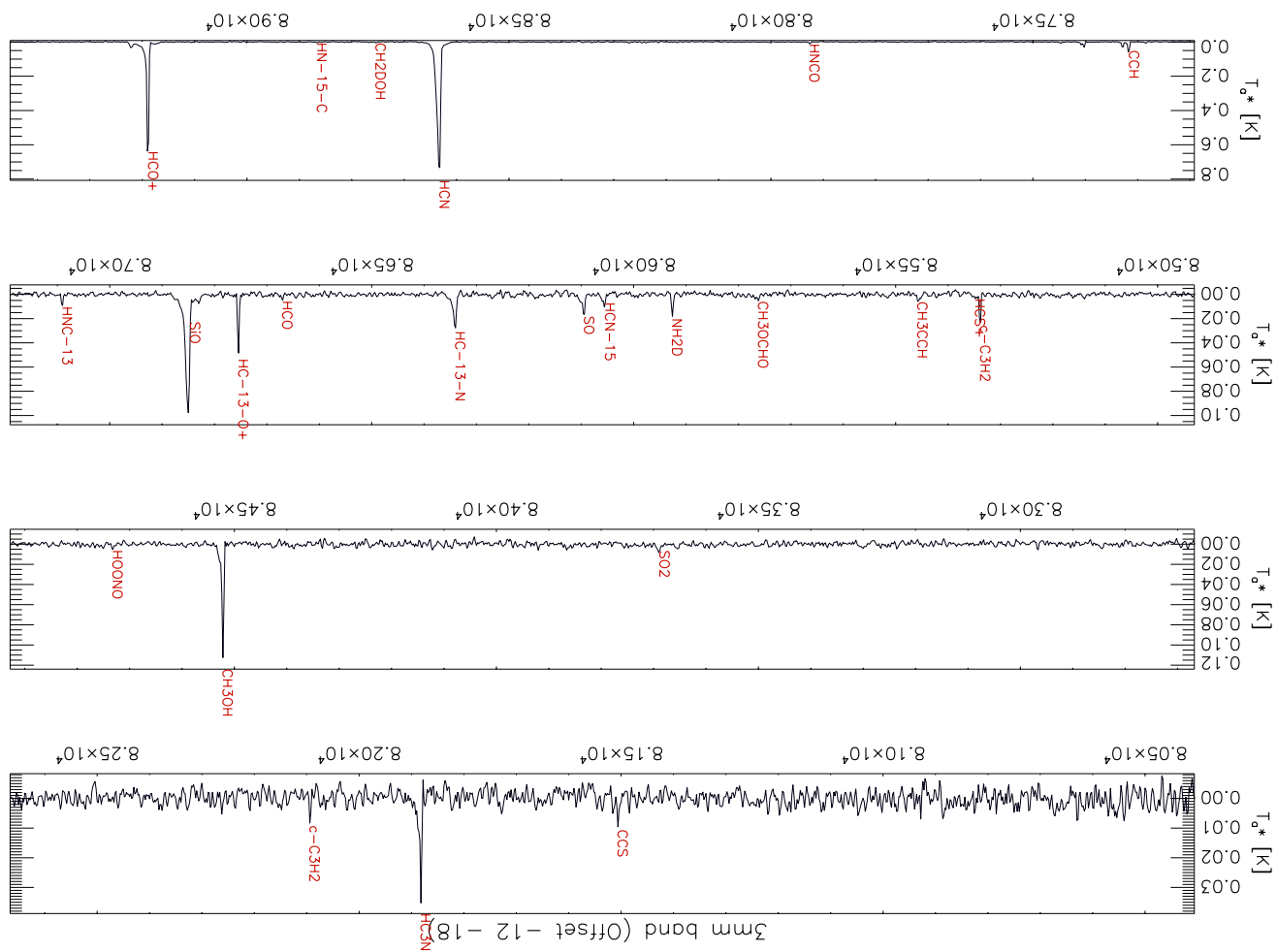
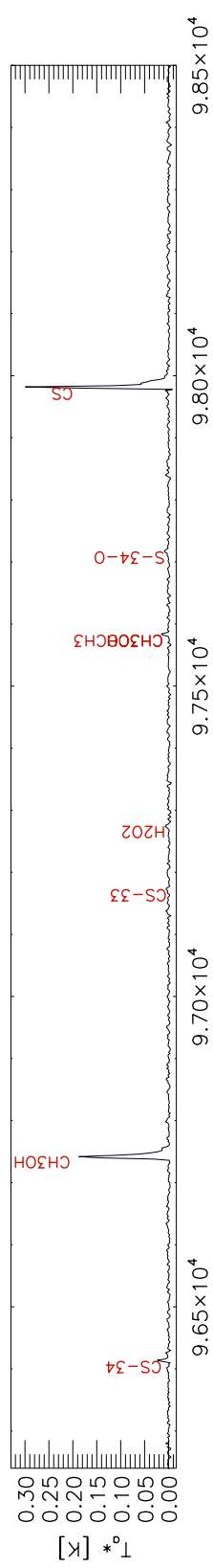
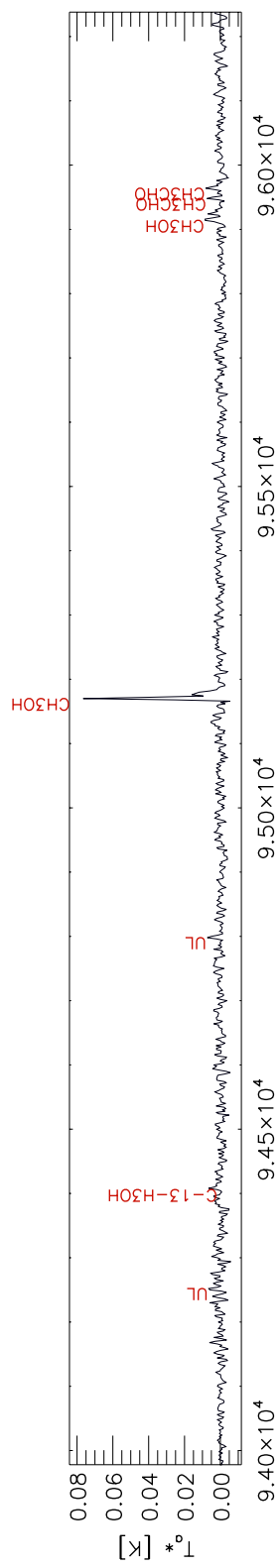
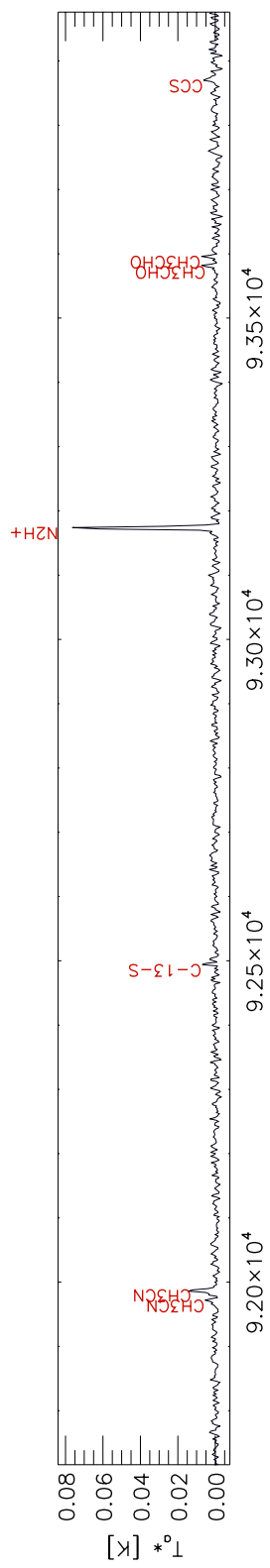
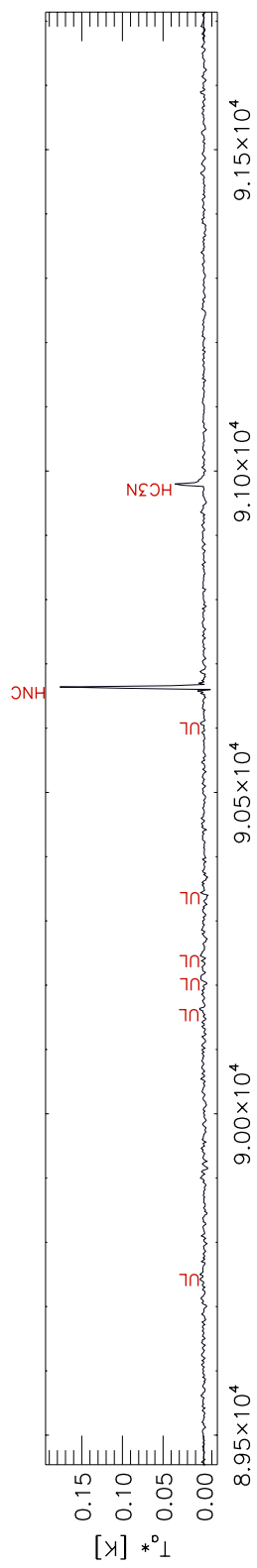
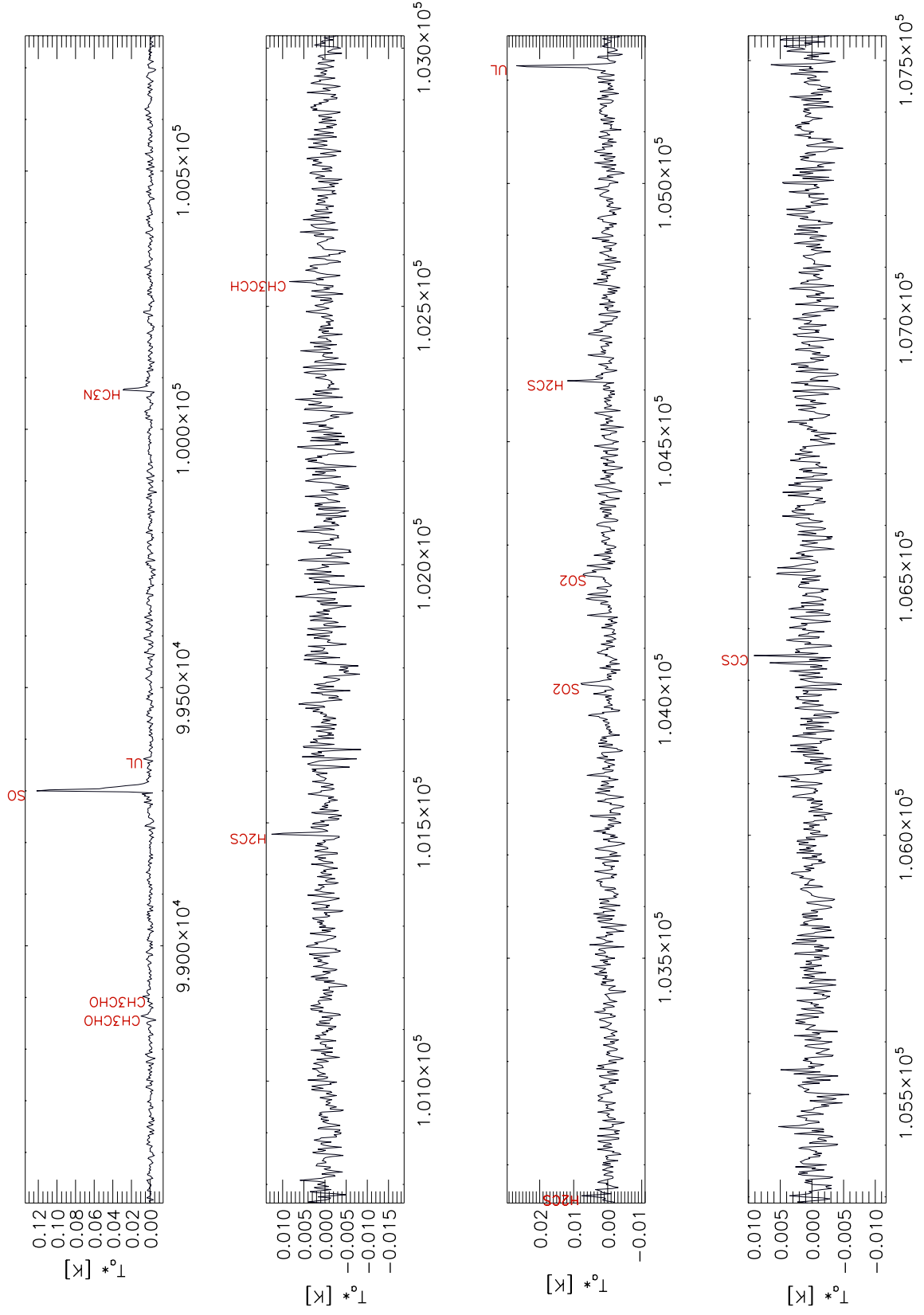


Figure 4.23: 3 mm band from 80-116 GHz. Signals are in antenna temperature (K).







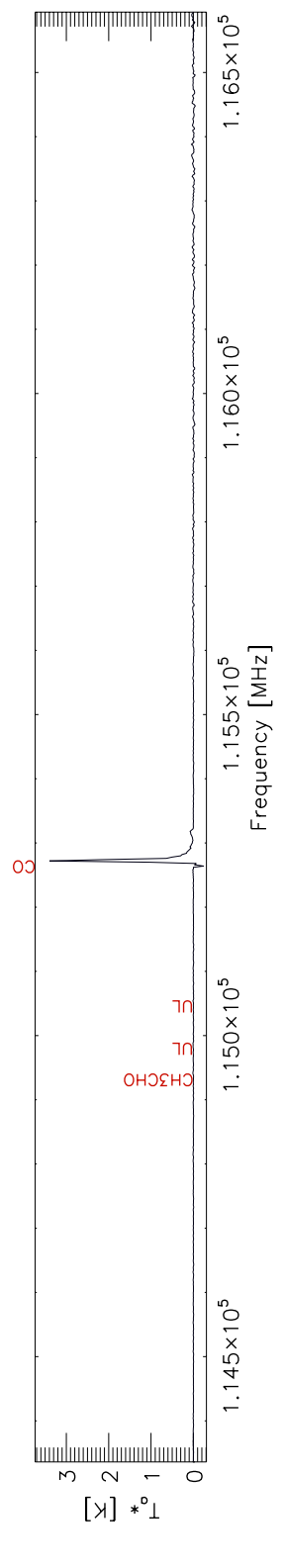
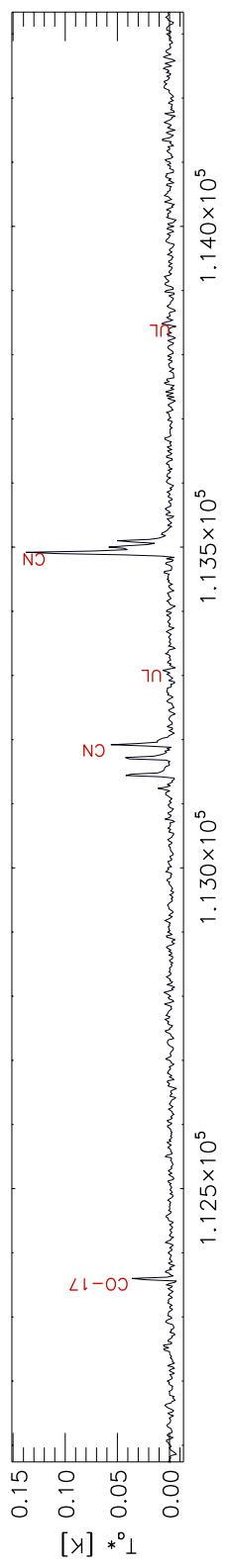
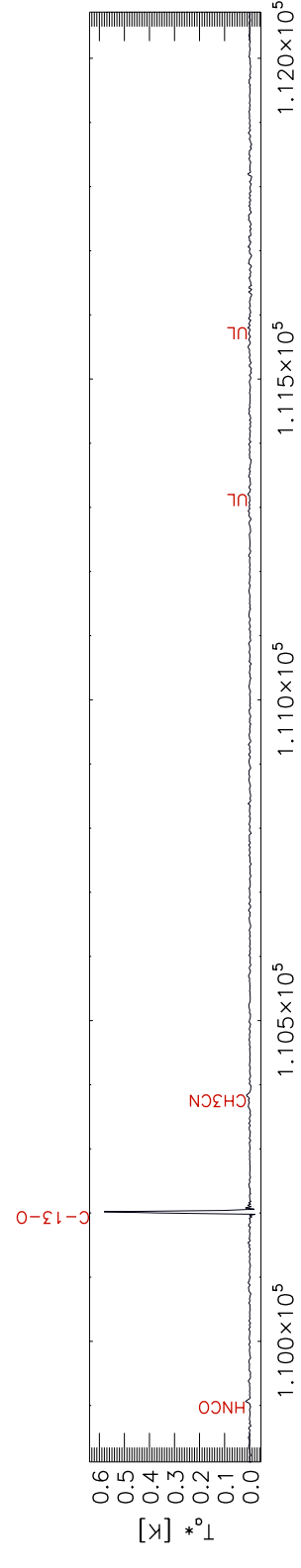
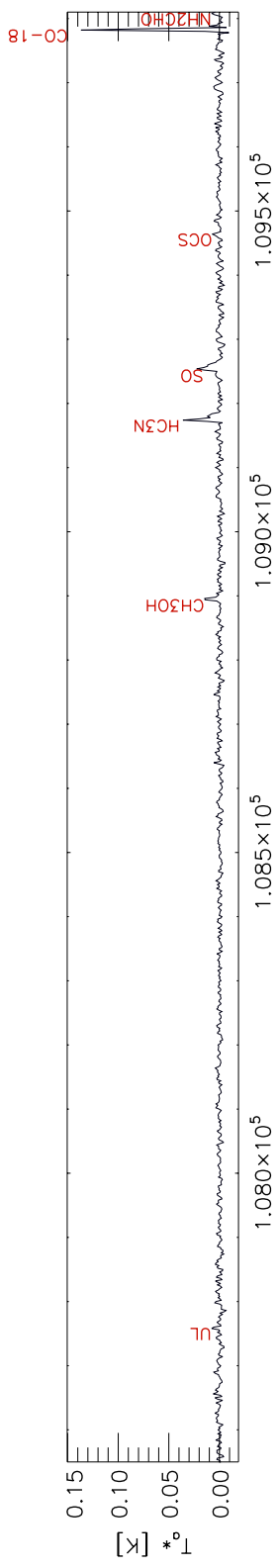
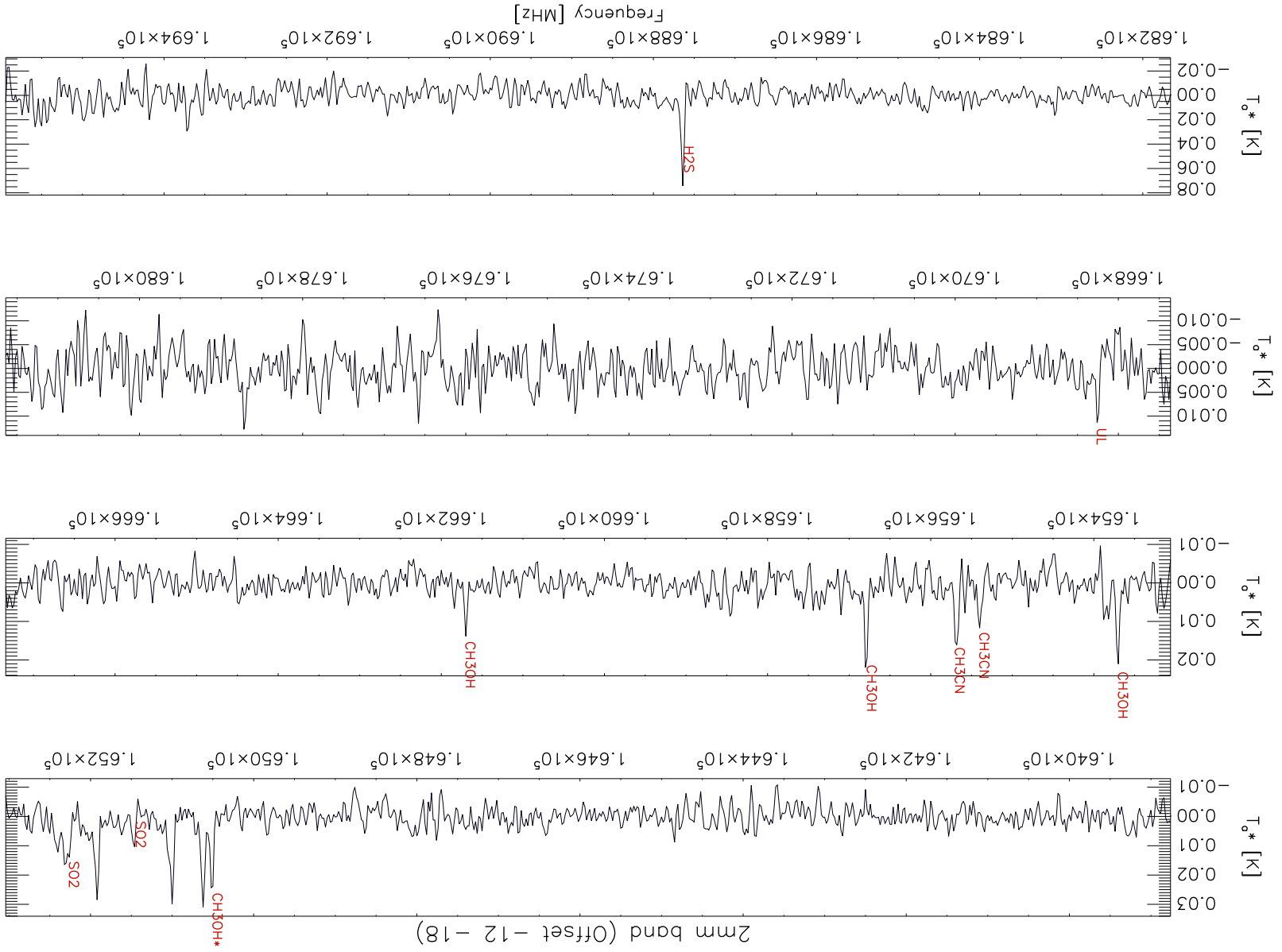
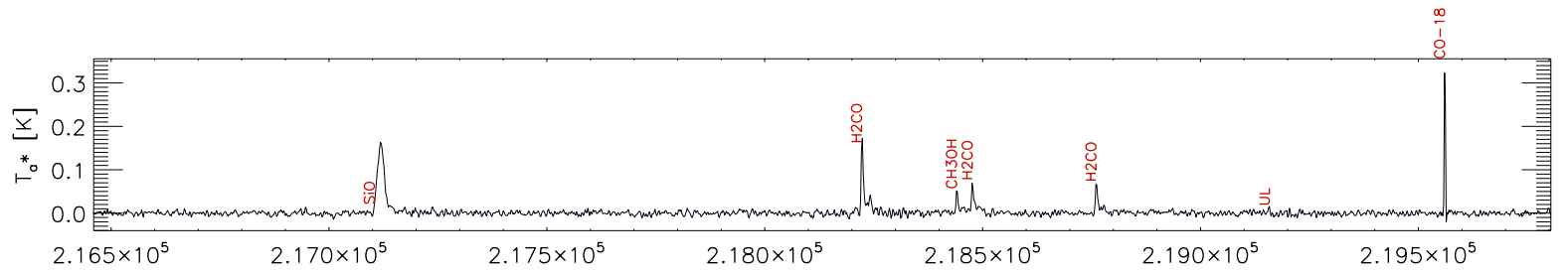
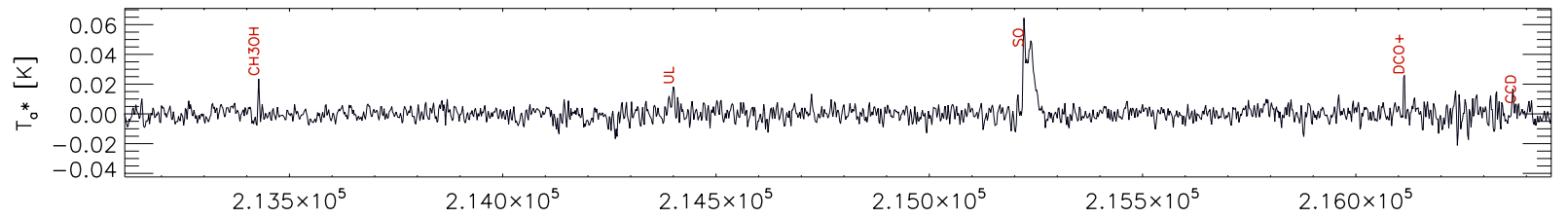
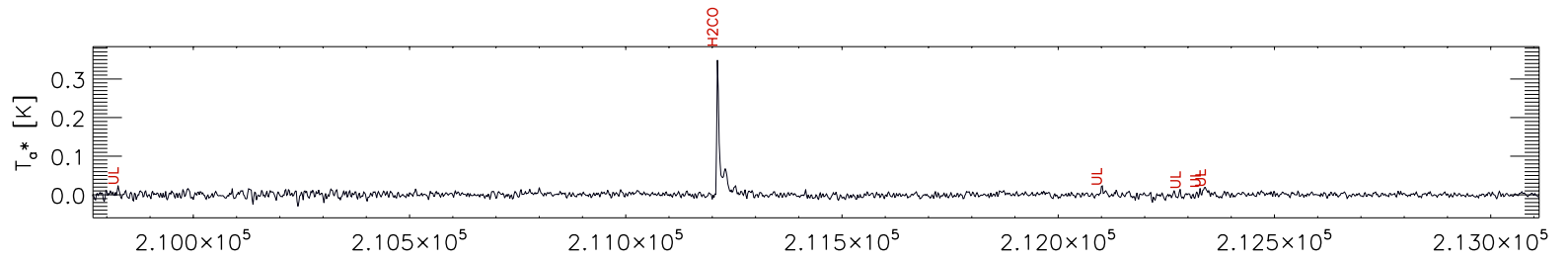
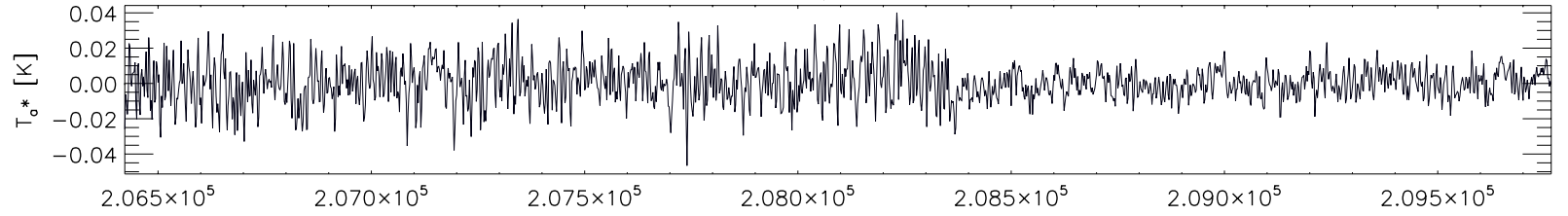
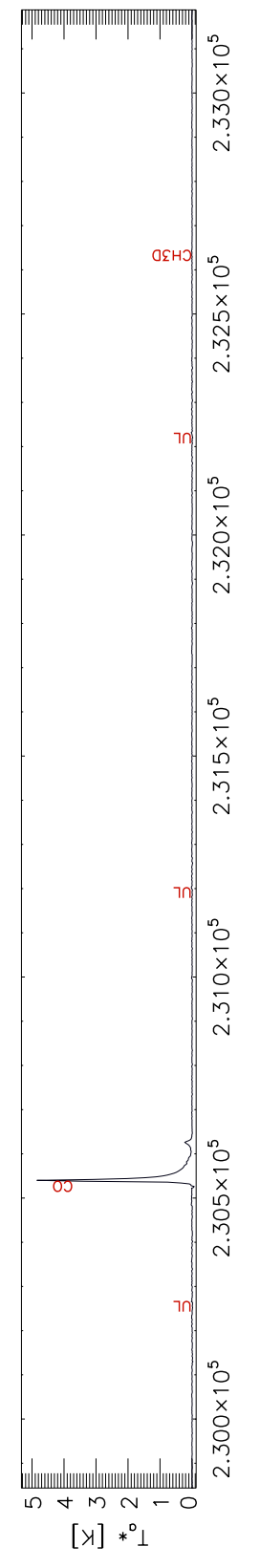
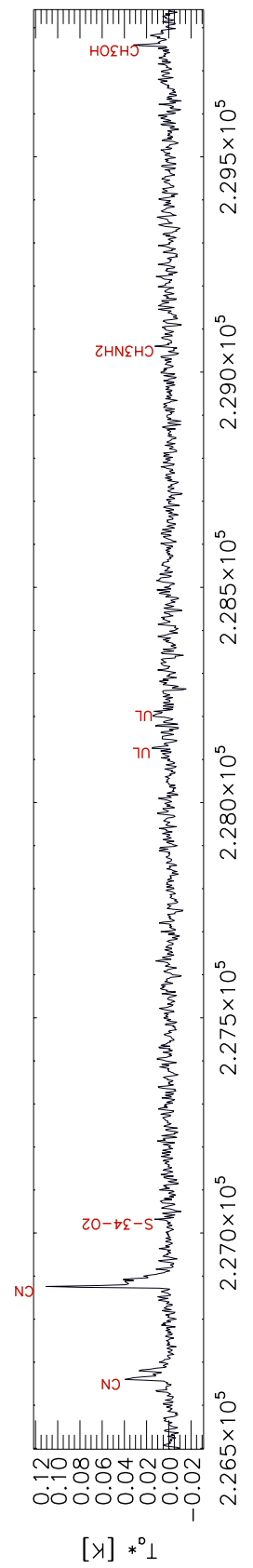
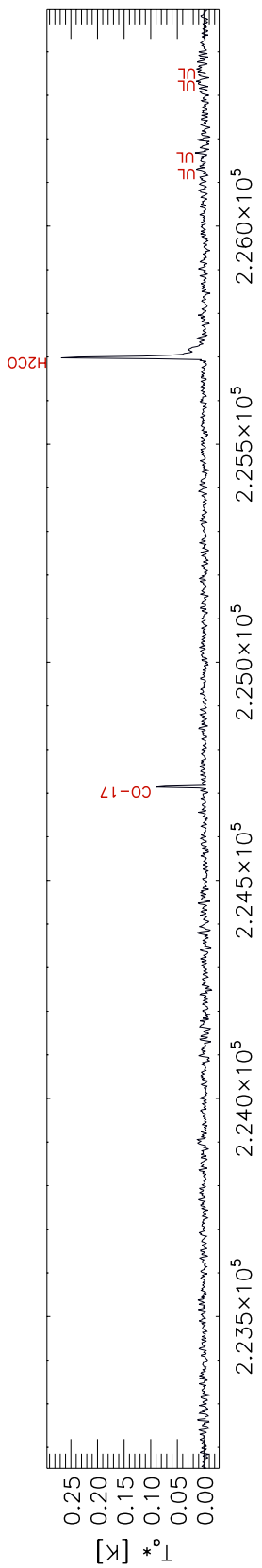
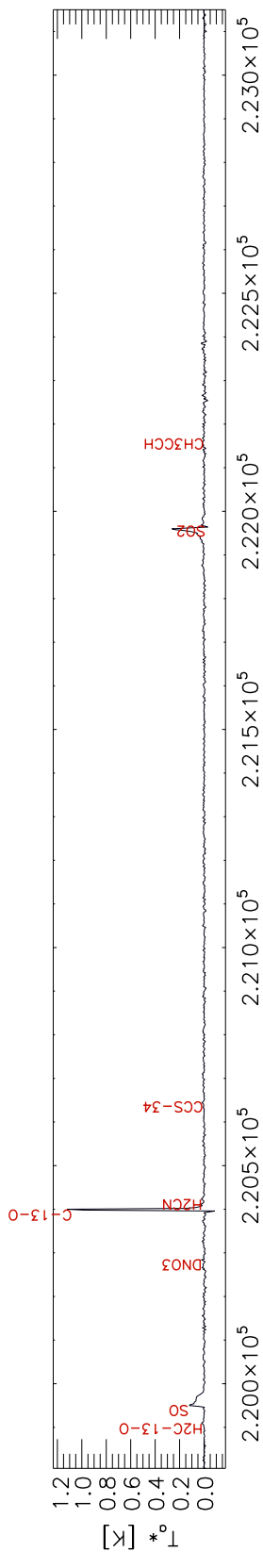


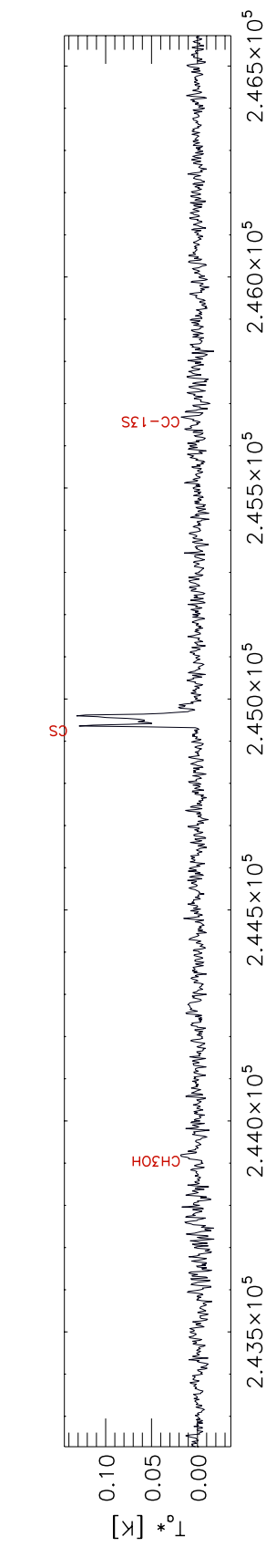
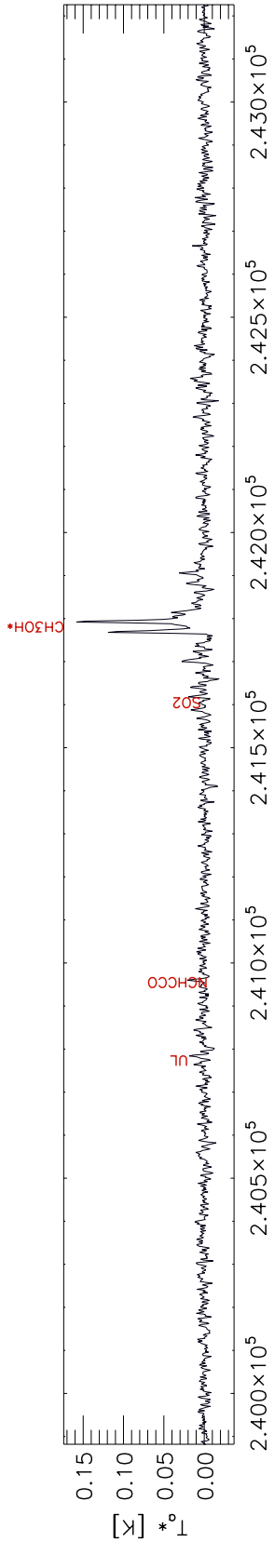
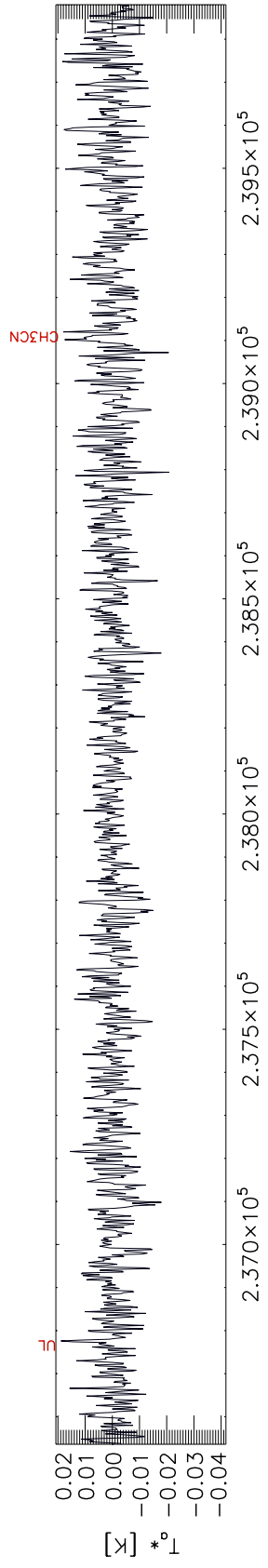
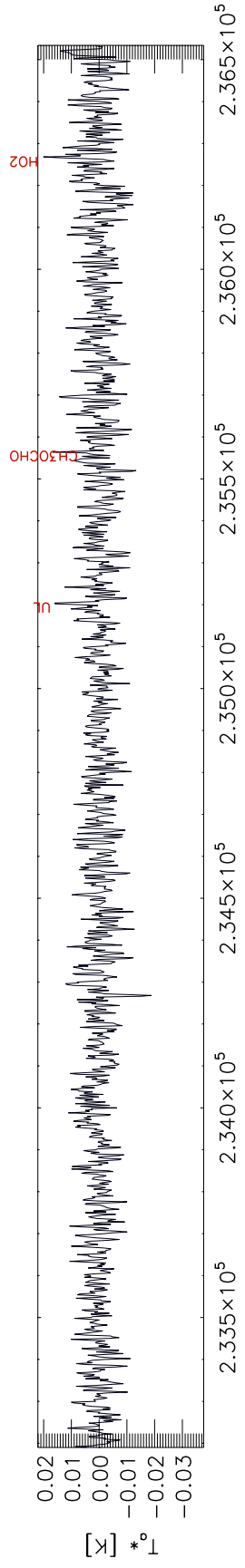
Figure 4.24: 2 mm band from 164-170 GHz. Signals are in antenna temperature (K).

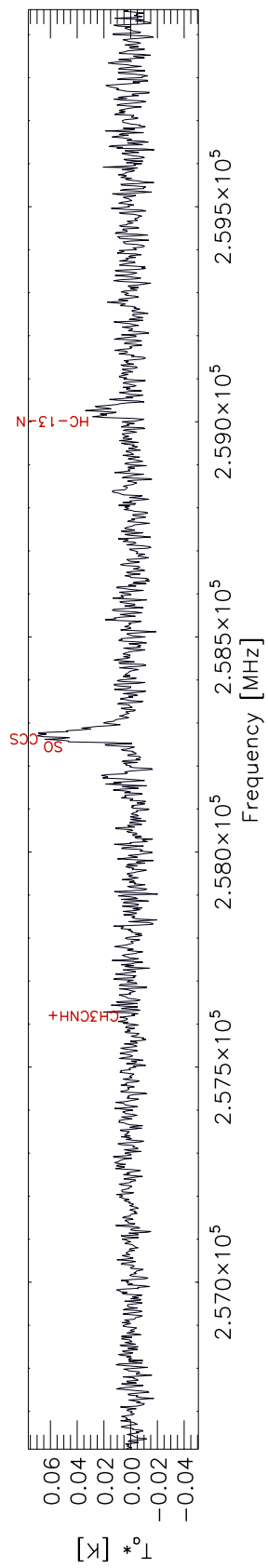
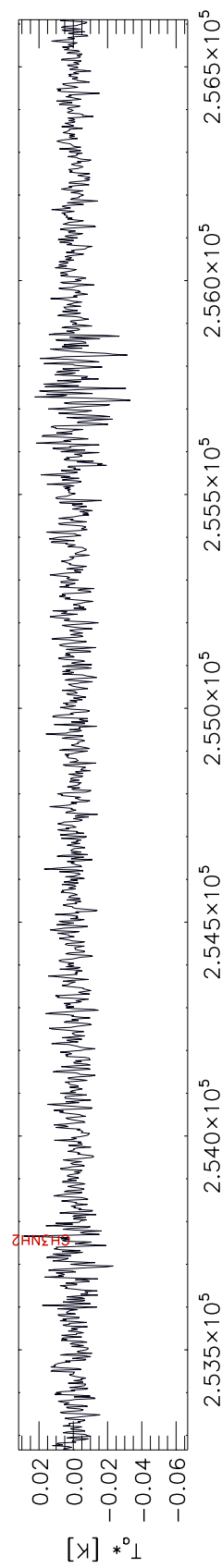
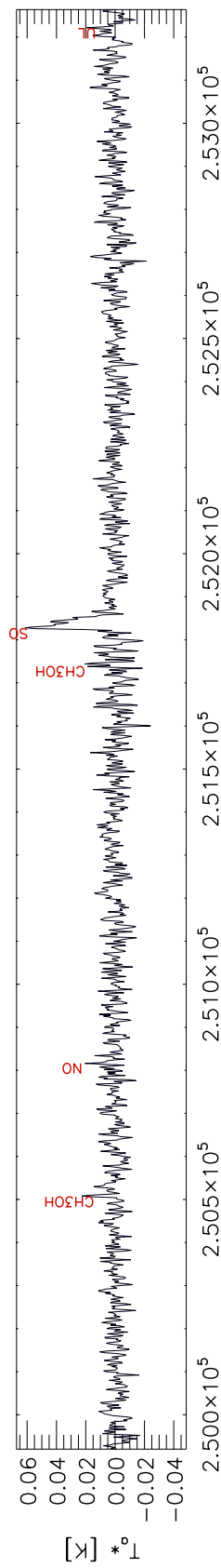
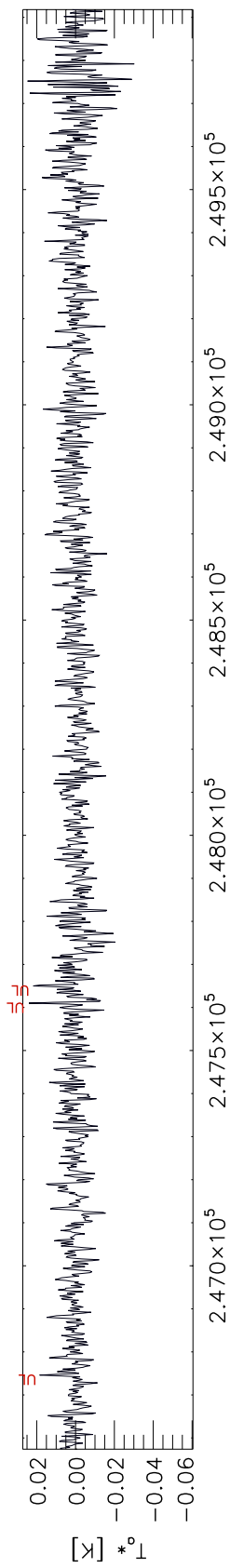


1.3mm band (Offset -12 -18)

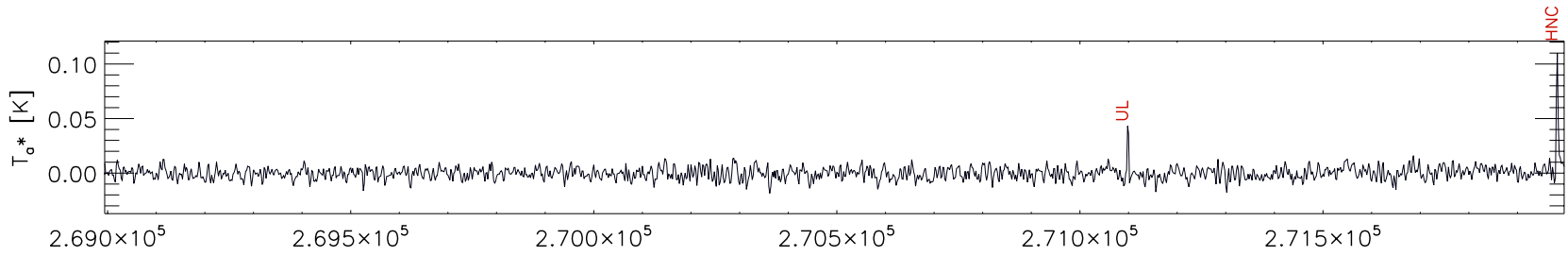
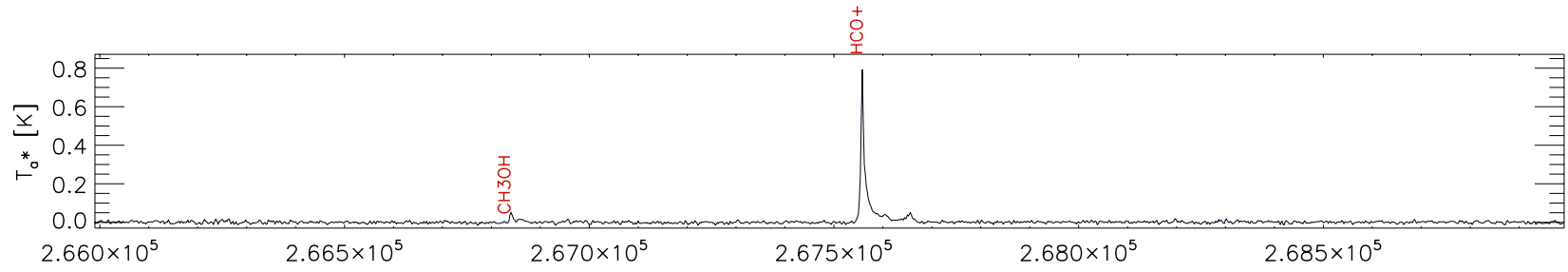
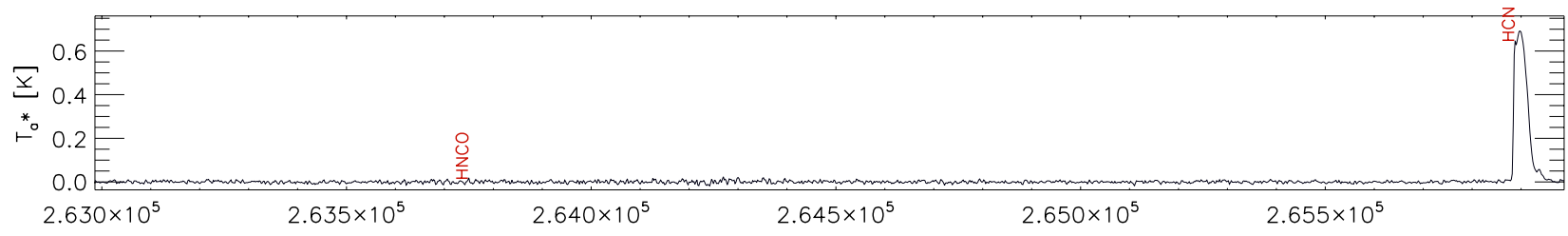
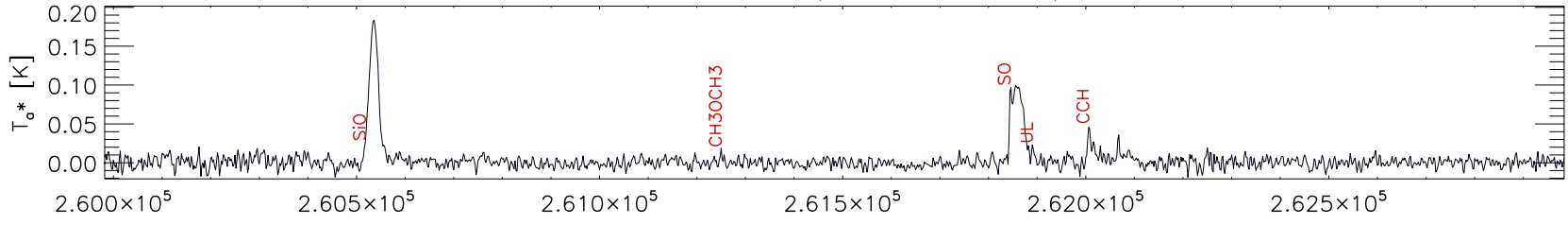


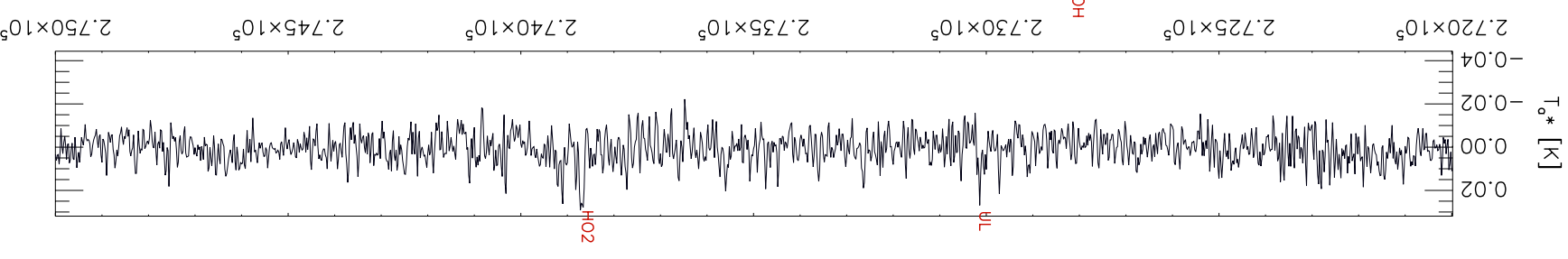
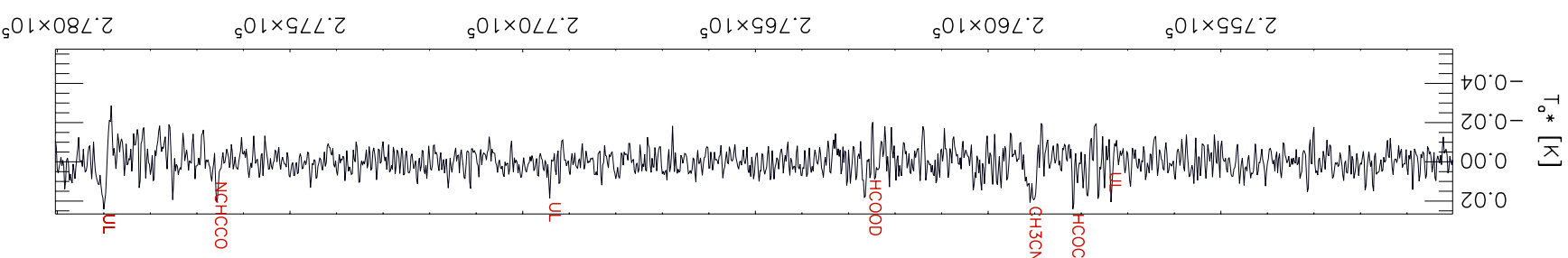
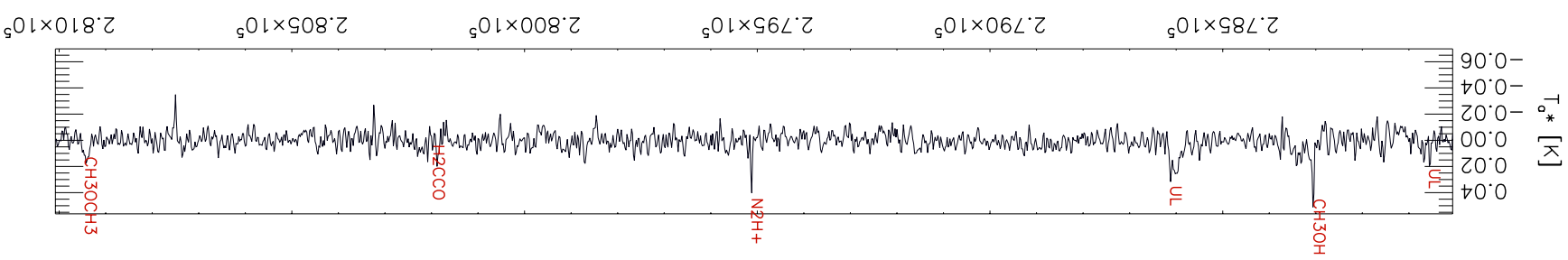
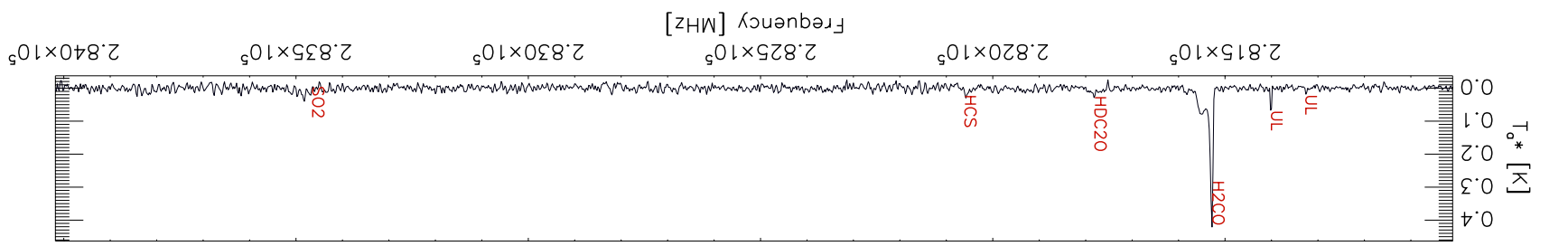




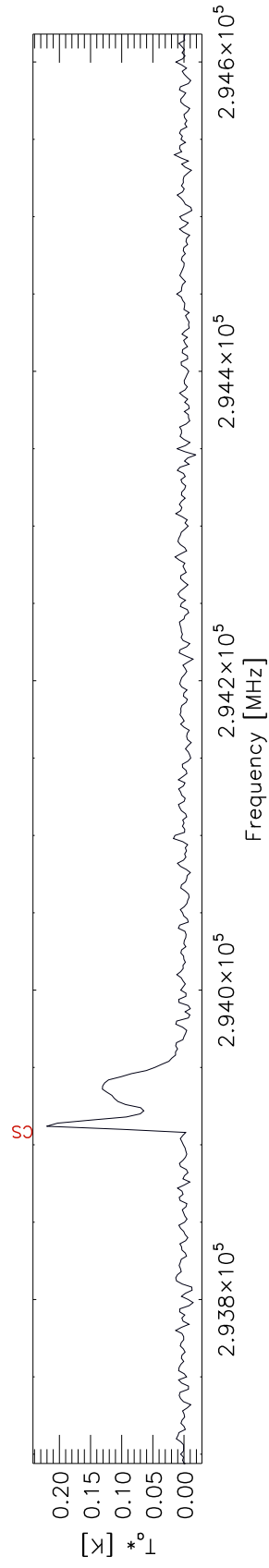
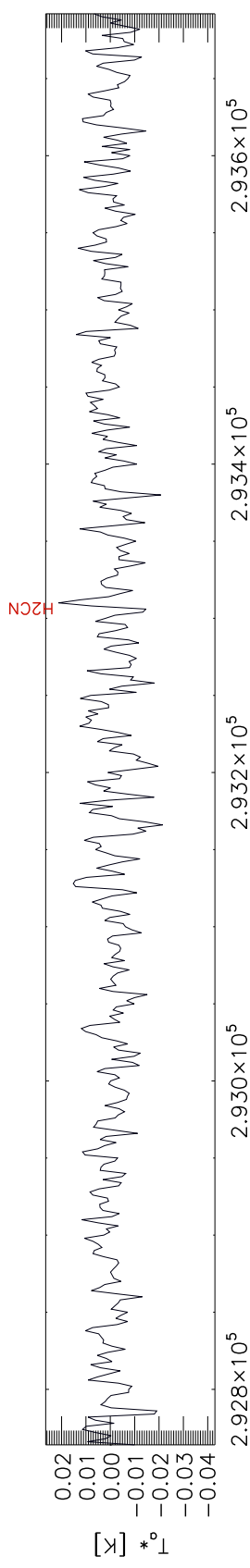
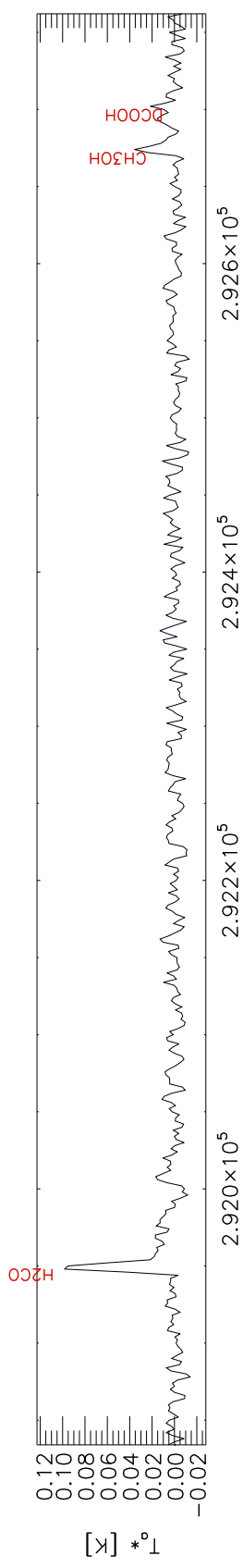
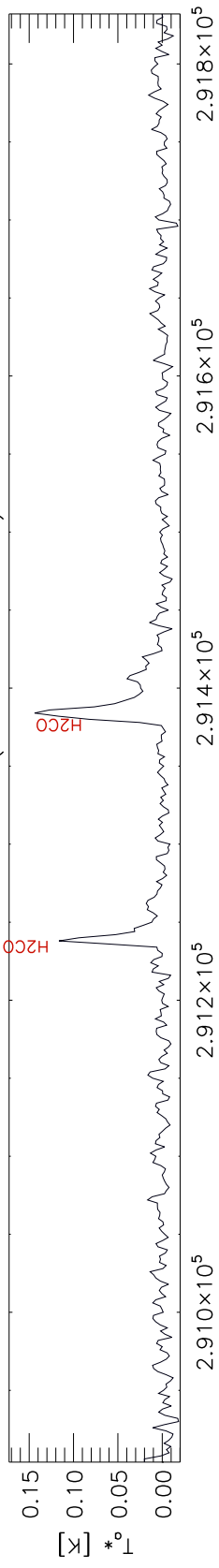


0.9mm band (Offset -12 -18)

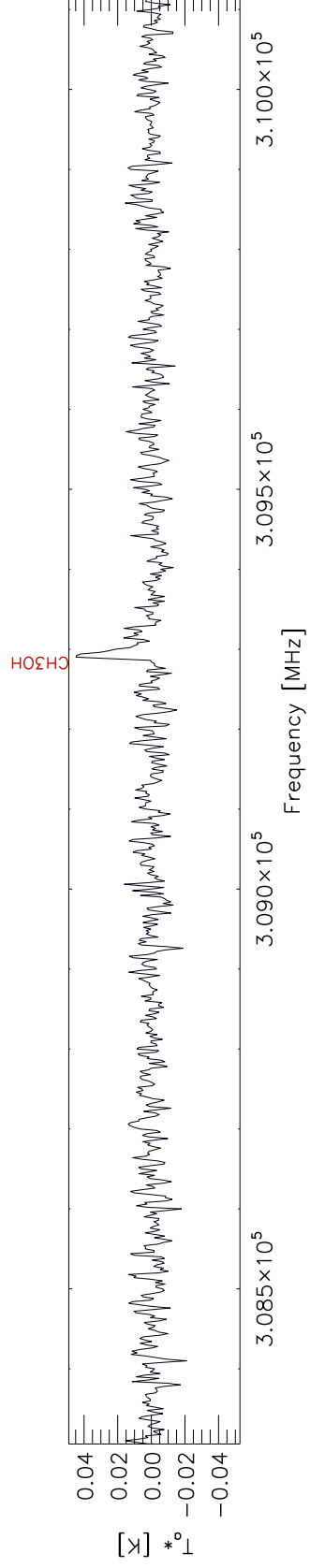
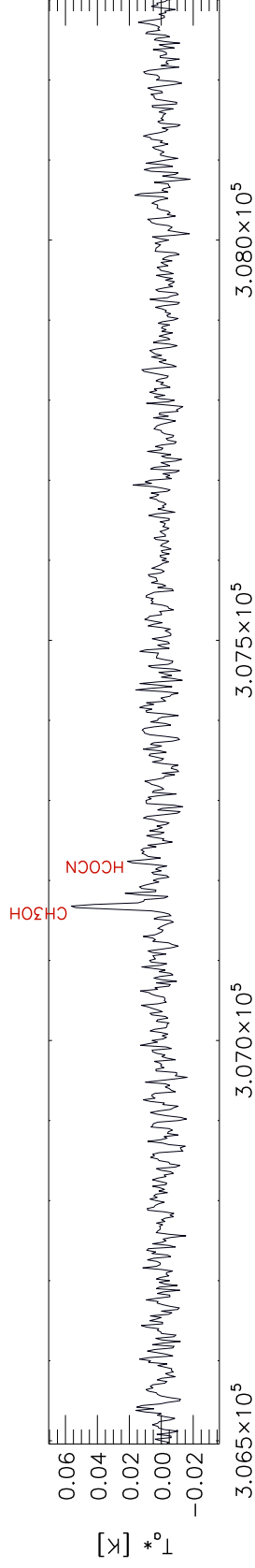
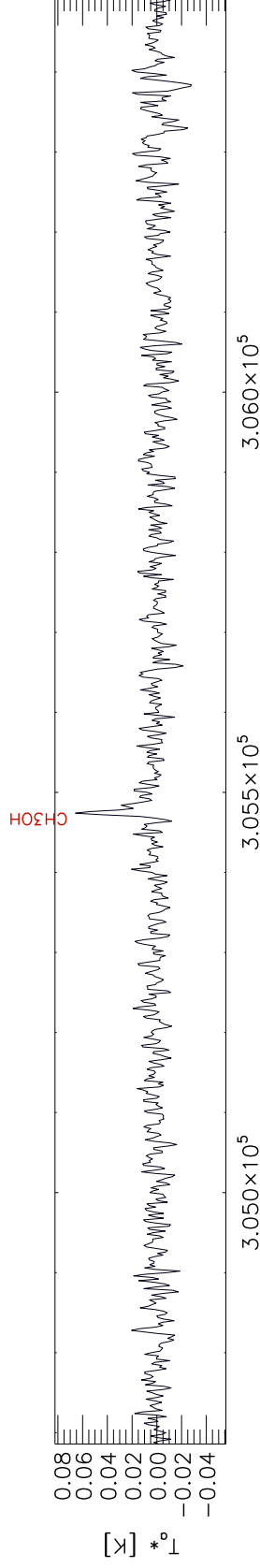
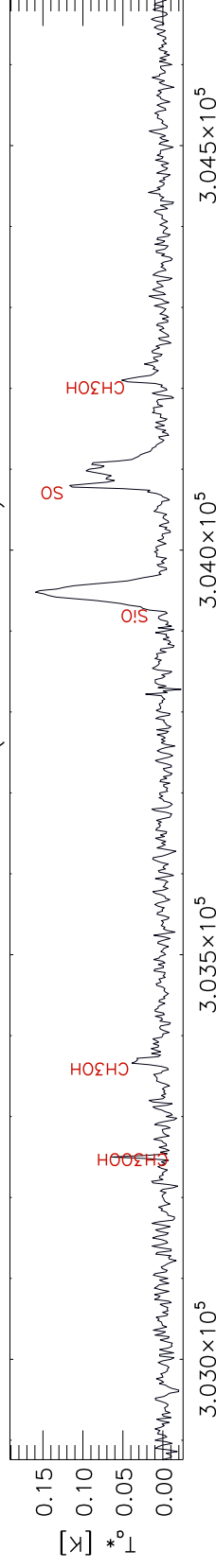




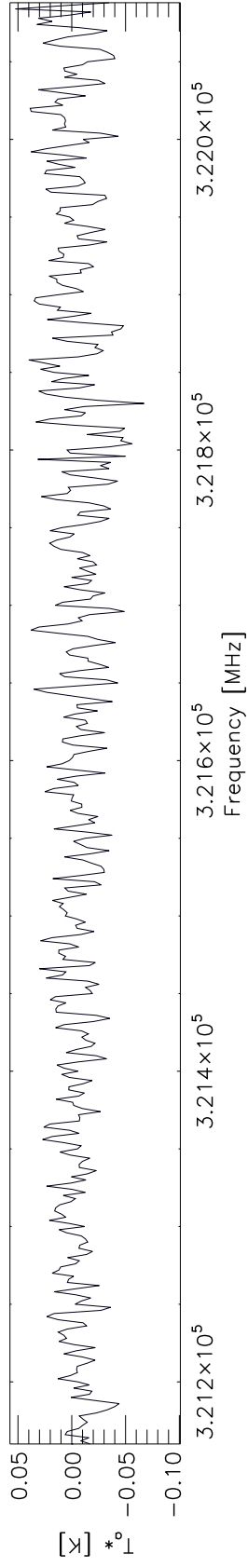
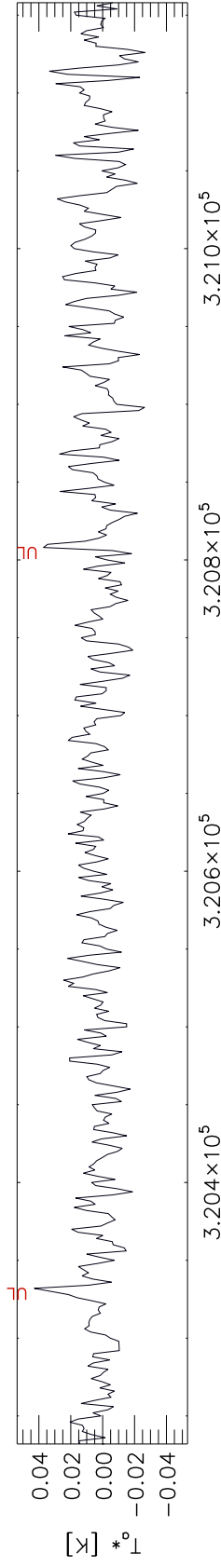
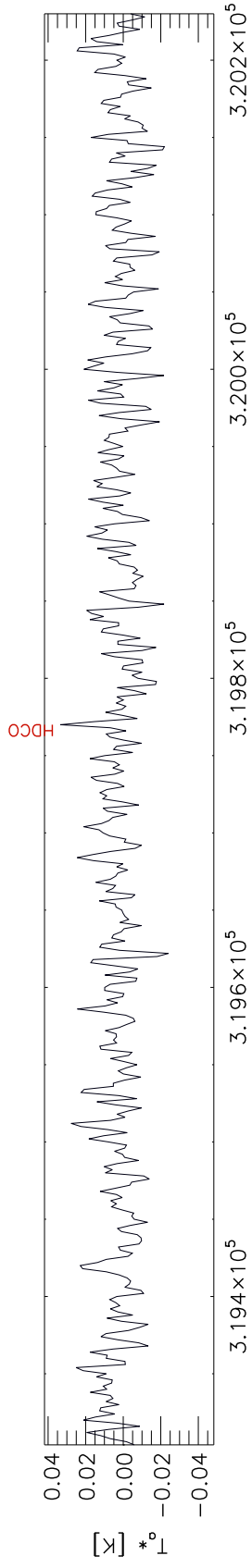
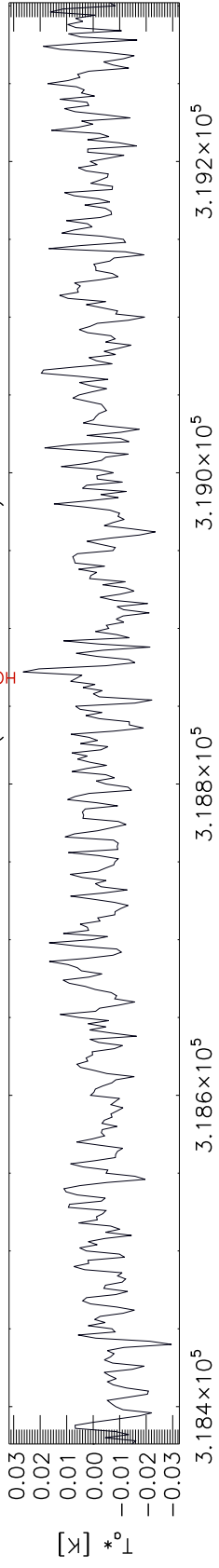
0.9mm band (Offset -12 -18)



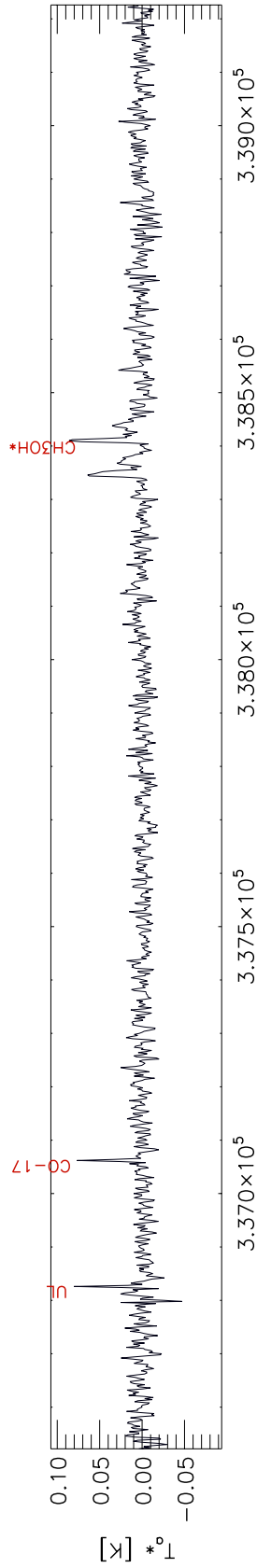
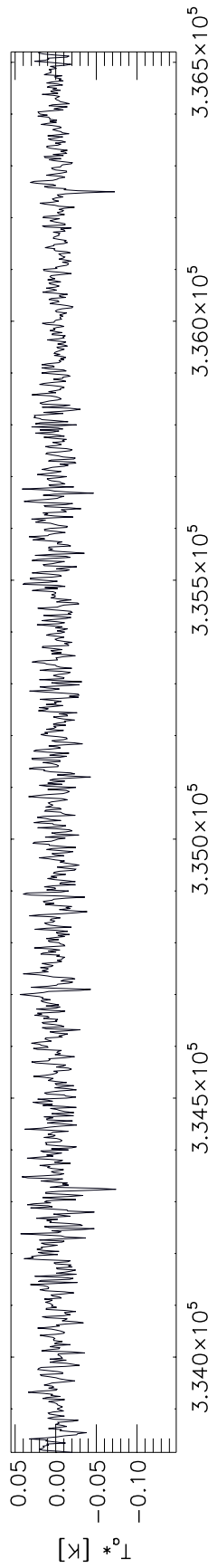
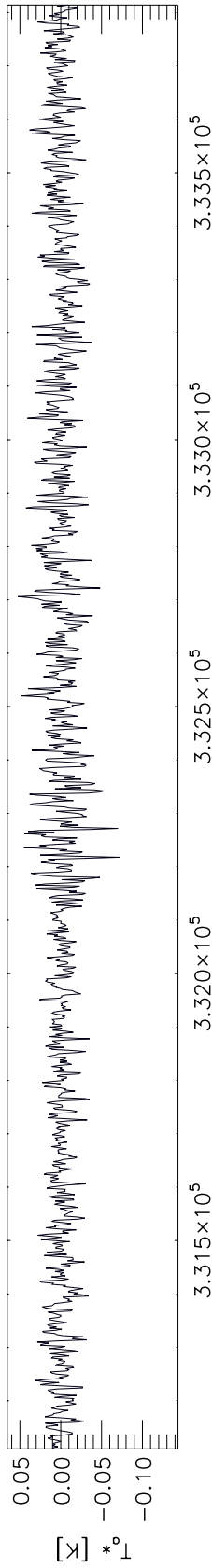
0.9mm band (Offset -12 -18)



0.9mm band (Offset -12 -18)



0.9mm band (Offset -12 -18)



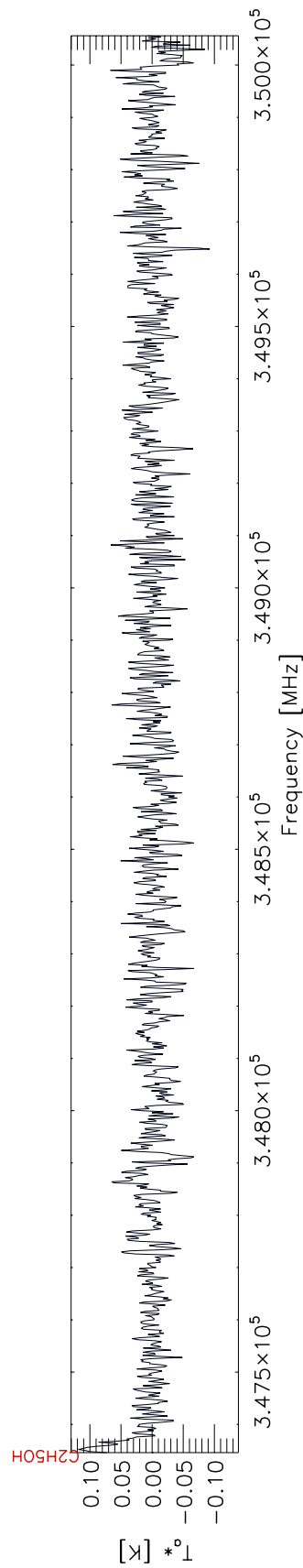
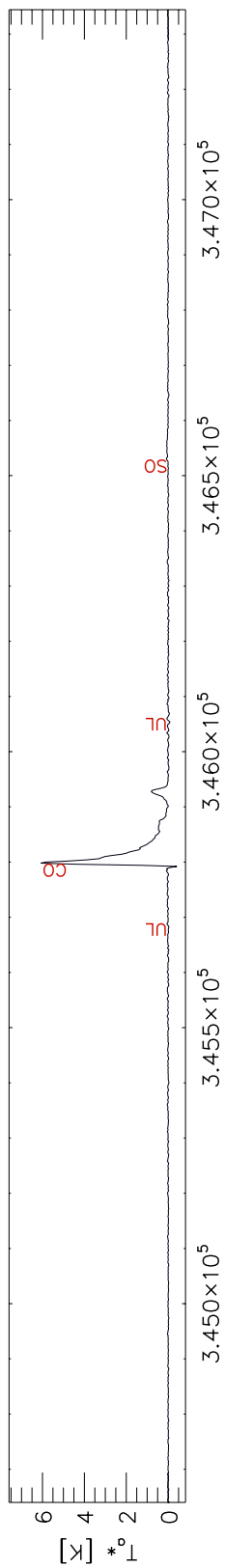
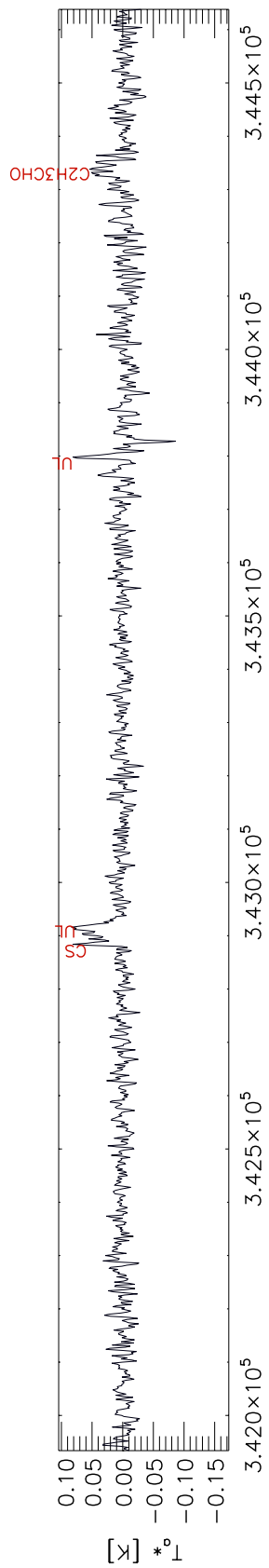
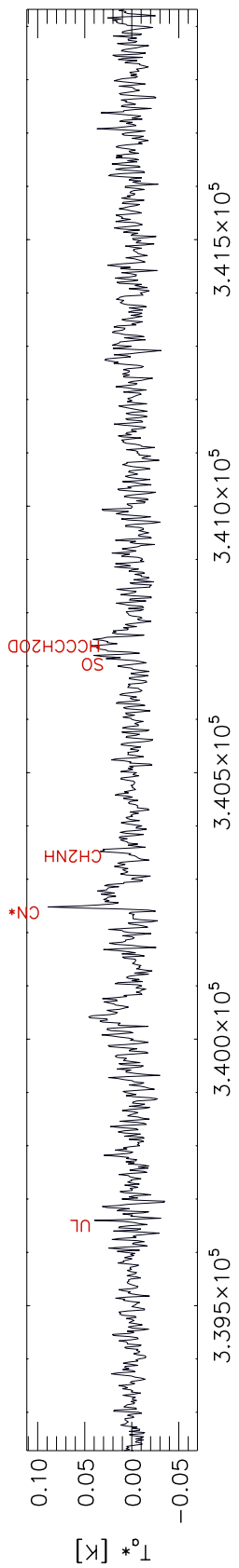


Table 4.11: Overview of the Cep E spectral survey, 0,0 offset

	Molecule	Mol. transition	Frequency	Eup(K)	Tpeak	rms	$\int_{-90}^{-30} T_a dV$	$\int_{-30}^{10} T_a dV$	$\int_{30}^{80} T_a dV$
1	CC-13S	6 7 7-5 6 7	81156,078	15,3	0,013	0,003	$\leq 0,061$	$0,139 \pm 0,025$	$\leq 0,055$
2	CCS	6 7 - 5 6	81505,170	15,4	0,014	0,003	$\leq 0,061$	$0,167 \pm 0,025$	$\leq 0,055$
3	HC3N	9-8	81881,468	19,6	0,073	0,003	$\leq 0,060$	$0,972 \pm 0,025$	$\leq 0,055$
4	c-C3H2	2 0 2 0- 1 1 1 0	82093,559	6,4	0,014	0,003	$\leq 0,060$	$0,153 \pm 0,025$	$\leq 0,055$
5	SO2	817-808	83688,093	36,7	0,013	0,003	$\leq 0,060$	$0,268 \pm 0,024$	$\leq 0,055$
6	UL		83759,029		0,010	0,003	$\leq 0,060$	$0,192 \pm 0,024$	$\leq 0,055$
7	CH3OH	5-1 0- 4 0 0	84521,172	40,4	0,163	0,001	$0,191 \pm 0,015$	$2,419 \pm 0,012$	$0,038 \pm 0,014$
8	c-C3H2	3 2 2 - 3 1 3	84727,688	16,1	0,005	0,001	$0,127 \pm 0,015$	$0,093 \pm 0,012$	$\leq 0,028$
9	HOONO	7 0 7 7-6 1 6 7	84732,073	17,4	-	-	--	--	--
10	OCS	7-6	85139,121	16,3	0,007	0,001	$0,083 \pm 0,015$	$0,087 \pm 0,012$	$\leq 0,028$
11	HCO-18+	1-0	85162,157	4,1	0,009	0,001	$\leq 0,030$	$0,108 \pm 0,012$	$\leq 0,028$
12	HCS+	2-1	85347,890	6,1	0,005	0,001	$\leq 0,030$	$0,098 \pm 0,012$	$0,045 \pm 0,014$
13	c-C3H2	2 1 2 0-1 0 1 0	85338,893	6,4	0,051	0,001	$0,066 \pm 0,015$	$0,699 \pm 0,012$	$\leq 0,028$
14	CH3CCH	5 0-4 0	85457,272	12,3	0,016	0,001	$\leq 0,030$	$0,223 \pm 0,012$	$\leq 0,028$
15	CH3CCH	5 1- 4 1	85455,667	19,5	0,016	0,001	$\leq 0,030$	$0,207 \pm 0,012$	$\leq 0,028$
16	C4H	910 9- 8 9 8	85634,004	20,5	0,005	0,001	$\leq 0,030$	$0,046 \pm 0,012$	$\leq 0,028$
17	C4H	91010- 8 9 9	85634,015	20,5	0,005	0,001	$\leq 0,030$	$0,046 \pm 0,012$	$\leq 0,028$
18	NH2OH	5 0 5- 4 1 3	85755,730	36,3	0,005	0,001	$0,071 \pm 0,015$	$0,123 \pm 0,012$	$0,061 \leq 0,028$
19	CH3OCHO	21 516 2-21 417 2	85761,876	155,8	0,005	0,001	--	--	--
20	NH2D	1 1 1 0- 1 0 1 1	85926,278	20,7	0,075	0,001	$\leq 0,030$	$0,915 \pm 0,012$	$\leq 0,028$
21	HCN-15	1-0	86054,961	4,1	0,016	0,001	$0,139 \pm 0,012$	$0,283 \pm 0,010$	$\leq 0,022$
22	SO	22-11	86093,950	19,3	0,039	0,001	$0,050 \pm 0,012$	$0,658 \pm 0,010$	$0,167 \pm 0,011$
23	HC-13-N	1-0	86339,922	4,1	0,062	0,001	$0,074 \pm 0,012$	$1,079 \pm 0,010$	$\leq 0,022$
24	UL		86517,959		0,004	0,001	$0,034 \pm 0,012$	$0,091 \pm 0,010$	$\leq 0,022$
25	HCO	1 0 1 2 2-0 0 0 1 1	86670,760	4,2	0,004	0,001	$\leq 0,024$	$0,060 \pm 0,010$	$\leq 0,022$
26	HCO	1 0 1 2 1-0 0 0 1 0	86708,360	4,2	0,005	0,001	$\leq 0,024$	$0,065 \pm 0,010$	$0,032 \pm 0,011$
27	HC-13-O+	(1-0)	86753,950	4,2	0,100	0,001	$\leq 0,024$	$1,183 \pm 0,010$	$0,037 \pm 0,011$
28	SiO	2-1	86846,960	6,3	0,071	0,001	$1,240 \pm 0,012$	$2,410 \pm 0,010$	$1,509 \pm 0,011$
29	HNC-13	1-0	87090,850	4,2	0,022	0,001	$\leq 0,024$	$0,300 \pm 0,010$	$\leq 0,022$
30	CCH	1 2 2- 0 1 1	87316,925	4,2	0,096	0,001	$0,803 \pm 0,012$	$1,369 \pm 0,010$	$0,023 \pm 0,011$
31	UL		87757,990		0,007	0,001	$\leq 0,024$	$0,095 \pm 0,010$	$\leq 0,022$
32	HNCO	4 0 4- 3 0 3	87925,237	10,5	0,019	0,001	$0,081 \pm 0,012$	$0,253 \pm 0,010$	$\leq 0,022$
33	UL		88177,958		-	-	--	--	--
34	UL		88214,019		-	-	--	--	--
35	UL		88237,850		-	-	--	--	--
36	UL		88246,003		-	-	--	--	--
37	UL		88271,926		0,007	0,001	$\leq 0,028$	$0,115 \pm 0,011$	$0,042 \pm 0,013$
38	UL		88551,156		0,005	0,001	$\leq 0,028$	$0,073 \pm 0,011$	$\leq 0,025$
39	CH2DOH	3 1 2 0-3 0 3 0	88754,512	17,1	0,005	0,001	$\leq 0,028$	$0,061 \pm 0,011$	$\leq 0,025$
40	HCN	(1-0)	88632,146	4,3	0,862	0,001	$2,508 \pm 0,014$	$18,698 \pm 0,011$	$1,711 \pm 0,013$
41	UL		88754,053		0,005	0,001	$\leq 0,028$	$0,064 \pm 0,011$	$\leq 0,025$
42	HN-15-C	1-0	88865,715	4,3	0,006	0,001	$\leq 0,028$	$0,063 \pm 0,011$	$0,029 \pm 0,013$
43	HCO+	1-0	89188,525	4,3	0,755	0,001	$0,838 \pm 0,014$	$11,638 \pm 0,011$	$3,284 \pm 0,013$
44	CH2DOH	2 0 2 0-1 0 1 0	89407,817	6,4	0,005	0,001	$\leq 0,028$	$0,012 \pm 0,011$	$\leq 0,025$

45	UL		89741,918	-	-	--	--	--	
46	UL		89750,033	-	-	--	--	--	
47	UL		90162,350	-	-	--	--	--	
48	UL		90210,262	-	-	--	--	--	
49	UL		90245,783	-	-	--	--	--	
50	UL		90344,085	-	-	--	--	--	
51	UL		90356,544	0,004	0,001	≤ 0,022	0,084 ± 0,009	≤ 0,020	
52	UL		90607,602	-	-	--	--	--	
53	HNC	1-0	90663,593	4,4	0,339	0,001	0,074 ± 0,011	3,869 ± 0,009	≤ 0,020
54	CCS	7 7-6 6	90686,381	26,1	0,007	0,001	≤ 0,022	0,042 ± 0,009	≤ 0,020
55	HC3N	10-9	90979,023	24	0,070	0,001	≤ 0,022	1,064 ± 0,009	≤ 0,020
56	CH3CN	50-40	91987,088	13,2	0,021	0,001	≤ 0,022	0,379 ± 0,009	0,073 ± 0,010
57	CH3CN	51-41	91985,314	20,4	0,021	0,001	≤ 0,022	0,345 ± 0,009	0,082 ± 0,010
58	CH3CN	5 2- 4 2	91979,994	41,9	0,006	0,001	0,205 ± 0,011	0,198 ± 0,009	0,028 ± 0,010
59	CH3CN	5 3- 4 3	91971,130	77,6	0,005	0,001	0,379 ± 0,022	0,078 ± 0,009	≤ 0,010
60	C-13-S	2-1	92494,308	6,7	0,017	0,001	≤ 0,026	0,224 ± 0,011	≤ 0,024
61	UL		92551,920		0,003	0,001	≤ 0,026	0,049 ± 0,011	≤ 0,024
62	UL		92872,121		0,004	0,001	≤ 0,026	0,043 ± 0,011	≤ 0,024
63	N2H+	1-0	93173,392	4,5	0,250	0,001	0,061 ± 0,013	3,819 ± 0,011	0,027 ± 0,012
64	CH3CHO	5 1 5 0- 4 1 4 0	93580,859	15,7	0,009	0,001	≤ 0,026	0,128 ± 0,011	≤ 0,024
65	CH3CHO	5 1 5 1- 4 1 4 1	93595,276	15,8	0,011	0,001	0,030 ± 0,013	0,168 ± 0,011	≤ 0,024
66	CCS	7 8 - 6 7	93870,107	19,9	0,019	0,001	≤ 0,026	0,193 ± 0,011	0,056 ± 0,012
67	UL		94252,060		-	-	--	--	--
68	C-13-H3OH	2 -1 2 0-1 -1 1 0	94405,163	12,4	0,008	0,002	≤ 0,041	0,123 ± 0,017	≤ 0,037
69	UL		94797,961		-	-	--	--	--
70	CH3OH	8 0 8 +0-7 1 7 +0	95169,463	83,5	0,096	0,002	0,144 ± 0,020	1,226 ± 0,017	0,079 ± 0,019
71	CH3OH	2 1 + 0-1 1 + 0	95914,310	21,4	0,021	0,002	≤ 0,041	0,294 ± 0,017	≤ 0,037
72	CH3CHO	5 0 5 2-4 0 4 2	95947,340	13,9	0,013	0,002	0,175 ± 0,020	0,131 ± 0,017	≤ 0,037
73	CH3CHO	5 0 5 0-4 0 4 0	95963,380	13,8	0,018	0,002	≤ 0,041	0,176 ± 0,017	≤ 0,037
74	CS-34	2 0-1 0	96412,950	6,9	0,045	0,002	≤ 0,031	0,597 ± 0,013	≤ 0,028
75	CH3CHO	5 2 3 0-4 2 2 0	96632,627	23	0,007	0,002	≤ 0,031	0,067 ± 0,013	≤ 0,028
76	CH3OH	2 0 + 0-1 0 + 0	96741,371	7	0,324	0,002	0,533 ± 0,015	6,196 ± 0,013	0,076 ± 0,014
77	CS-33	2-1	97172,064	7	0,009	0,002	≤ 0,031	0,095 ± 0,013	≤ 0,028
78	H2O2	10 010 3-10 110 0	97274,010	151,9	-	-	--	--	--
79	OCS	8-7	97301,209	21	0,007	0,002	≤ 0,031	0,083 ± 0,013	≤ 0,028
80	CH3OH	2 1 1 -0-1 1 0 -0	97582,804	21,6	0,027	0,002	≤ 0,031	0,343 ± 0,013	≤ 0,028
81	CH3COCH3	4 3 2 0-3 0 3 1	97582,337	8,2	0,027	0,002	≤ 0,031	0,343 ± 0,013	≤ 0,028
82	S-34-O	23-12	97715,317	9,1	0,014	0,002	≤ 0,031	0,261 ± 0,013	≤ 0,028
83	CS	2-1	97980,953	7,1	0,547	0,002	0,466 ± 0,015	7,794 ± 0,013	0,175 ± 0,014
84	CH3CHO	5 1 4 2 - 4 1 3 2	98863,328	16,6	0,017	0,002	≤ 0,031	0,152 ± 0,013	≤ 0,029
85	CH3CHO	5 1 4 0- 4 1 3 0	98900,948	16,5	0,012	0,002	≤ 0,031	0,102 ± 0,013	≤ 0,029
86	SO	23-12	99299,870	9,2	0,295	0,002	0,494 ± 0,016	4,444 ± 0,013	0,625 ± 0,014
87	UL		99362,029		-	-	--	--	--
88	H2CCN	5 1 5 6-4 1 4 5	99689,294	27,5	0,009	0,002	≤ 0,031	0,058 ± 0,013	≤ 0,029
89	UL		99730,008		0,008	0,002	≤ 0,031	0,092 ± 0,013	≤ 0,029
90	UL		99794,010		0,008	0,002	≤ 0,031	0,013 ± 0,013	0,051 ± 0,014
91	CCS	8 7-7 6	99866,521	28,1	0,008	0,002	≤ 0,031	0,004 ± 0,013	0,079 ± 0,014

92	HC3N	11-10	100076,392	28,8	0,089	0,002	0,103 ± 0,016	1,043 ± 0,013	≤ 0,030
93	H2CS	3 1 3- 2 1 2	101477,810	22,9	0,032	0,002	≤ 0,033	0,384 ± 0,013	≤ 0,030
94	UL		101603,079		0,011	0,002	≤ 0,033	0,123 ± 0,013	≤ 0,030
95	H2CCO	5 1 4-4 1 3	101981,429	27,7	0,012	0,002	0,083 ± 0,016	0,060 ± 0,013	≤ 0,030
96	CH3CCH	6 1-5 1	102546,024	24,4	0,022	0,002	≤ 0,036	0,256 ± 0,015	≤ 0,033
97	CH3CCH	6 0-5 0	102547,984	17,2	0,022	0,002	≤ 0,036	0,256 ± 0,015	≤ 0,033
98	H2CS	3 2 2-2 2 1	103039,990	62,6	0,022	0,002	0,052 ± 0,018	0,207 ± 0,015	≤ 0,033
99	H2CS	3 0 3-2 0 2	103040,220	9,9	0,022	0,002	0,053 ± 0,018	0,209 ± 0,015	≤ 0,033
100	SO2	313-202	104029,418	7,7	0,018	0,002	0,035 ± 0,016	0,372 ± 0,013	0,058 ± 0,015
101	SO2	10 19-10 010	104239,295	54,7	0,014	0,002	≤ 0,033	0,247 ± 0,013	0,045 ± 0,015
102	H2CS	3 1 2 - 2 1 1	104617,040	23,2	0,027	0,002	≤ 0,033	0,285 ± 0,013	≤ 0,030
103	UL		105228,889		0,030	0,002	0,184 ± 0,016	0,613 ± 0,013	0,030 ± 0,015
104	CCS	8 9-7 8	106347,726	25	0,017	0,002	0,071 ± 0,016	0,160 ± 0,013	0,059 ± 0,014
105	UL		106518,955		0,011	0,002	≤ 0,031	0,152 ± 0,013	≤ 0,028
106	UL		107423,933		0,008	0,002	≤ 0,031	0,071 ± 0,013	≤ 0,028
107	UL		107758,094		0,008	0,002	0,040 ± 0,015	0,143 ± 0,013	≤ 0,028
108	UL		108649,952		0,007	0,002	0,043 ± 0,014	0,118 ± 0,011	≤ 0,025
109	CH3OH	0+000-1-110	108893,963	13,1	0,037	0,002	0,031 ± 0,014	0,428 ± 0,011	≤ 0,025
110	HC3N	12-11	109173,634	34,1	0,099	0,002	0,075 ± 0,014	1,048 ± 0,011	0,058 ± 0,013
111	SO	32-21	109252,220	21,1	0,058	0,002	0,176 ± 0,014	0,918 ± 0,011	0,245 ± 0,013
112	OCS	9-8	109463,063	26,3	0,014	0,002	≤ 0,028	0,115 ± 0,011	≤ 0,025
113	CO-18	(1-0)	109781,915	5,3	0,237	0,002	≤ 0,028	2,006 ± 0,011	≤ 0,025
114	NH2CHO	17 21517-16 31416	109808,1846	170,9	-	-	--	--	--
115	HNCO	5 0 5- 4 0 4	109905,749	15,8	0,028	0,002	0,062 ± 0,014	0,313 ± 0,011	≤ 0,025
116	NH2D	1111-1010	110153,594	21,3	0,044	0,002	≤ 0,045	0,391 ± 0,018	≤ 0,041
117	C-13-O	1-0	110201,404	5,3	0,795	0,002	0,058 ± 0,022	8,051 ± 0,018	0,061 ± 0,020
118	CH3CN	6 3-5 3	110364,354	82,9	0,010	0,002	0,592 ± 0,022	0,154 ± 0,018	≤ 0,041
119	CH3CN	6 2-5 2	110374,989	47,1	0,010	0,002	0,315 ± 0,022	0,306 ± 0,018	≤ 0,041
120	CH3CN	6 1-5 1	110381,372	25,7	0,013	0,002	≤ 0,045	0,560 ± 0,018	0,101 ± 0,020
121	CH3CN	6 0- 5 0	110383,500	18,5	0,032	0,002	≤ 0,045	0,509 ± 0,018	0,133 ± 0,020
122	D2CO	2 1 2- 1 1 1	110837,830	13,4	0,013	0,002	≤ 0,045	0,095 ± 0,018	≤ 0,041
123	CH3OH	7 2 5 +0-8 1 8 +0	111289,550	102,7	0,008	0,002	≤ 0,036	0,098 ± 0,015	0,054 ± 0,017
124	UL		111319,895		-	-	--	--	--
125	UL		111580,396		-	-	--	--	--
126	CH3CHO	6 1 6 0-5 1 5 0	112248,728	21,1	0,014	0,002	≤ 0,036	0,319 ± 0,015	≤ 0,033
127	CH3CHO	6 1 6 1-5 1 5 1	112254,524	21,2	0,017	0,002	≤ 0,036	0,381 ± 0,015	≤ 0,033
128	CO-17	1-0	112359,894	5,4	0,064	0,002	0,177 ± 0,018	0,661 ± 0,015	0,087 ± 0,016
129	CN*	1 0 1 2 - 0 0 1 2	113191,325	5,4	0,099	0,002	0,153 ± 0,018	1,186 ± 0,015	1,095 ± 0,016
130	UL		113307,4863		-	-	--	--	--
131	CCS	9 8-8 7	113410,186	33,6	0,009	0,002	≤ 0,036	0,100 ± 0,015	≤ 0,033
132	CN*	1023-0012	113490,985	5,4	0,201	0,002	1,931 ± 0,018	3,789 ± 0,015	0,212 ± 0,016
133	CH3OCHO	9 3 6 2-8 3 5 2	113743,107	32,9	0,006	0,002	≤ 0,036	0,045 ± 0,015	≤ 0,033
134	UL		113845,5879		-	-	--	--	--
135	CH3CHO	6 0 6 2-5 0 5 2	114940,190	19,5	0,026	0,003	0,112 ± 0,027	0,178 ± 0,022	≤ 0,049
136	CH3CHO	6 0 6 0-5 0 5 0	114959,911	19,4	0,020	0,003	0,119 ± 0,027	0,088 ± 0,022	≤ 0,049
137	UL		114988,051		0,011	0,003	0,057 ± 0,027	0,145 ± 0,022	≤ 0,049
138	UL		115054,9023		-	-	--	--	--

139	UL		115155,014		0,012	0,003	0,065 ± 0,027	0,162 ± 0,022	≤ 0,049
140	CO	1-0	115271,202	5,5	3,152	0,003	4,326 ± 0,027	52,610 ± 0,022	6,472 ± 0,025
141	UL		164736,027		0,015	0,003	≤ 0,048	0,069 ± 0,039	≤ 0,044
142	CH3OH*	1 1 0-1 0 0	165050,175	23,4	0,065	0,003	0,467 ± 0,024	0,848 ± 0,020	≤ 0,044
143	SO2	5 2 4-5 1 5	165144,651	23,6	0,026	0,003	0,119 ± 0,024	0,366 ± 0,020	≤ 0,044
144	SO2	7 1 7-6 0 6	165225,452	27,1	0,056	0,003	0,237 ± 0,024	0,956 ± 0,020	≤ 0,044
145	CH3CN	9 0-8 0	165569,082	39,7	0,037	0,003	0,056 ± 0,024	0,566 ± 0,020	0,137 ± 0,022
146	CH3CN	9 1-8 1	165565,891	46,9	0,035	0,003	0,043 ± 0,024	0,644 ± 0,020	0,140 ± 0,022
147	CH3CN	9 2-8 2	165556,322	68,4	0,017	0,003	0,291 ± 0,024	0,389 ± 0,020	≤ 0,044
148	CH3CN	9 3-8 3	165540,377	104,1	0,020	0,003	0,696 ± 0,024	0,169 ± 0,020	0,112 ± 0,022
149	CH3OH	6 +1 5 0 - 6 +0 6 0	165678,770	69,9	0,050	0,003	≤ 0,048	0,502 ± 0,020	≤ 0,044
150	D2CO	3 1 3-2 1 2	166102,750	21,3	0,035	0,003	≤ 0,047	0,287 ± 0,019	≤ 0,043
151	CH3OH	7 1 0-7 0 0	166169,098	86,1	0,041	0,003	≤ 0,047	0,389 ± 0,019	≤ 0,043
152	CCS	1312-1211	166662,354	61,8	0,013	0,003	0,088 ± 0,024	0,127 ± 0,019	≤ 0,043
153	UL		166825,948		-	-	-	-	-
154	CH3OH	8 1 0-8 0 0	166898,566	104,6	0,026	0,003	≤ 0,047	0,298 ± 0,019	≤ 0,043
155	H2C-13-S	5 1 4-4 1 3	167543,379	37,3	0,013	0,003	≤ 0,047	0,234 ± 0,019	≤ 0,043
156	CH3OCH3	4 2 2 0-3 1 3 0	167746,603	14,7	0,014	0,003	≤ 0,047	0,170 ± 0,019	≤ 0,043
157	H2S-34	1 1 0-1 0 1	167910,516	27,8	0,017	0,003	0,161 ± 0,024	0,127 ± 0,019	0,045 ± 0,022
158	CH3OH	9 +1 8 0-9 +0 9 0	167931,130	125,5	0,022	0,003	≤ 0,047	0,172 ± 0,019	≤ 0,043
159	CH3CHO	9 1 9 0-8 1 8 0	168093,480	42,7	0,020	0,006	≤ 0,091	0,220 ± 0,037	≤ 0,083
160	CH3OH	4 1 0-3 2 0	168577,831	44,3	0,019	0,006	≤ 0,091	0,084 ± 0,037	≤ 0,083
161	H2S	1 1 0-1 0 1	168762,762	27,9	0,254	0,006	≤ 0,091	2,637 ± 0,037	0,176 ± 0,041
162	H2CS	5 1 5-4 1 4	169113,529	37,5	0,059	0,006	0,083 ± 0,045	0,356 ± 0,037	≤ 0,083
163	SO2	3 2 2-2 1 1	208700,336	15,3	0,018	0,006	≤ 0,082	0,286 ± 0,033	0,129 ± 0,037
164	H2CS	615-514	209200,620	48,3	0,046	0,006	0,642 ± 0,041	0,434 ± 0,033	≤ 0,074
165	HC3N	23-22	209230,234	120,6	0,059	0,006	≤ 0,081	0,537 ± 0,033	≤ 0,037
166	UL		209825,717		-	-	-	-	-
167	HCCCH2OD	10 110 1-9 2 8 0	210801,080	33,8	0,032	0,005	≤ 0,061	0,267 ± 0,025	≤ 0,056
168	S-34-O	5 5-4 4	211013,673	43,6	0,020	0,005	0,114 ± 0,031	0,156 ± 0,025	≤ 0,056
169	H2CO	313-212	211212,225	32,1	0,966	0,005	0,117 ± 0,031	9,086 ± 0,025	0,324 ± 0,028
170	UL		212100,404		0,055	0,005	≤ 0,062	0,345 ± 0,025	≤ 0,056
171	UL		212282,018		-	-	-	-	-
172	UL		212328,018		-	-	-	-	-
173	UL		212339,680		-	-	-	-	-
174	H2C-13-O	303-202	212811,184	20,4	0,021	0,005	≤ 0,062	0,156 ± 0,025	≤ 0,056
175	CH3OH	1+100-0000	213427,118	23,4	0,041	0,005	≤ 0,062	0,338 ± 0,025	≤ 0,056
176	UL		214346,852		0,029	0,005	0,152 ± 0,034	0,332 ± 0,027	≤ 0,061
177	UL		214400,130		-	-	-	-	-
178	SO	55-44	215220,653	44,1	0,205	0,005	0,928 ± 0,034	3,001 ± 0,027	1,503 ± 0,031
179	S-34-O	5 6-4 5	215839,436	34,4	0,017	0,005	0,208 ± 0,033	0,224 ± 0,027	≤ 0,061
180	DCO+	3-2	216112,582	20,7	0,332	0,005	≤ 0,061	1,643 ± 0,025	≤ 0,055
181	c-C3H2	3 3 0 0-2 2 1 0	216278,756	19,5	0,059	0,005	≤ 0,061	0,332 ± 0,025	≤ 0,055
182	CCD	3 4 4-2 3 4	216373,320	20,8	0,035	0,005	0,064 ± 0,030	0,157 ± 0,025	≤ 0,055
183	H2S	2 2 0-2 1 1	216709,389	15,6	0,030	0,005	≤ 0,061	0,094 ± 0,025	≤ 0,055
184	CH3OH	5140-4220	216945,521	55,9	0,039	0,005	0,168 ± 0,030	0,403 ± 0,025	≤ 0,055
185	SiO	5-4	217104,980	31,3	0,129	0,005	3,917 ± 0,030	3,178 ± 0,025	4,340 ± 0,028

186	DCN	3 0 0-2 0 0	217238,538	20,9	0,145	0,005	0,132 ± 0,030	0,859 ± 0,025	≤ 0,055
187	UL		217624,000		0,016	0,005	≤ 0,060	0,081 ± 0,025	0,074 ± 0,028
188	c-C3H2	6 060-5 150	217822,148	38,6	0,103	0,005	≤ 0,060	0,607 ± 0,025	≤ 0,055
189	c-C3H2	5 140-4 230	217940,046	35,4	0,062	0,005	0,208 ± 0,030	0,441 ± 0,025	≤ 0,055
190	c-C3H2	5 2 4-4 1 3	218160,456	35,4	0,022	0,004	0,554 ± 0,028	0,379 ± 0,023	≤ 0,051
191	H2CO	303-202	218221,989	21	0,983	0,004	0,260 ± 0,028	8,213 ± 0,023	0,406 ± 0,025
192	CH2DOH	5 2 4 1-5 1 5 1	218316,390	58,8	0,016	0,004	0,306 ± 0,028	0,555 ± 0,023	0,129 ± 0,025
193	HC3N	24-23	218324,723	131	0,049	0,004	0,221 ± 0,028	0,569 ± 0,023	≤ 0,051
194	CH3OH	4+220-3+120	218440,050	45,5	0,240	0,004	2,326 ± 0,028	1,986 ± 0,023	≤ 0,051
195	H2CO	322-221	218476,071	68,1	0,250	0,004	0,137 ± 0,028	2,245 ± 0,023	≤ 0,025
196	H2CO	321-220	218759,966	68,1	0,250	0,004	≤ 0,055	2,121 ± 0,023	≤ 0,051
197	OCS	18-17	218903,356	99,8	0,026	0,004	0,069 ± 0,028	0,182 ± 0,023	≤ 0,051
198	UL		219158,057		-	-	--	--	--
199	CO-18	(2-1)	219560,033	15,8	0,813	0,004	≤ 0,055	4,106 ± 0,023	≤ 0,051
200	UL		219760,578		0,016	0,004	0,329 ± 0,028	0,054 ± 0,023	≤ 0,050
201	HNCO	10 010-9 0 9	219798,274	58	0,041	0,004	≤ 0,055	0,316 ± 0,023	0,102 ± 0,025
202	H2C-13-O	3 1 2-2 1 1	219908,525	32,9	0,122	0,004	6,843 ± 0,028	2,850 ± 0,023	≤ 0,050
203	SO	56-45	219949,442	35	0,392	0,004	1,487 ± 0,028	6,151 ± 0,023	2,694 ± 0,025
204	CH2DOH	5 1 5 0-4 1 4 0	220071,805	35,8	0,020	0,004	0,050 ± 0,028	0,302 ± 0,023	0,105 ± 0,025
205	CH3OH	8+080-7+160	220078,490	96,6	0,034	0,004	0,085 ± 0,028	0,279 ± 0,023	≤ 0,052
206	UL		220170,164		0,027	0,004	0,131 ± 0,028	0,278 ± 0,023	≤ 0,052
207	UL		220245,841		0,018	0,004	0,126 ± 0,028	0,153 ± 0,023	≤ 0,052
208	DNO3	11 5 6-12 211	220284,876	65,9	-	-	--	--	--
209	C-13-O	2-1	220398,677	15,9	2,192	0,004	0,175 ± 0,028	13,405 ± 0,023	0,585 ± 0,026
210	H2CN	3 2 211 4-2 2 111 3	220421,216	68,6	-	-	--	--	--
211	CCS-34	2423-2323	220645,462	187,1	-	-	--	--	--
212	CH3CN	12 3-13 3	220709,016	133,3	0,019	0,004	≤ 0,057	0,213 ± 0,023	0,077 ± 0,026
213	CH3CN	12 1-13 1	220743,011	76,1	0,026	0,004	≤ 0,057	0,348 ± 0,023	0,198 ± 0,026
214	CH3CN	12 0-13 0	220747,261	68,9	0,026	0,004	≤ 0,057	0,316 ± 0,023	≤ 0,052
215	D2CO	4 1 4-3 1 3	221191,665	32	0,043	0,004	≤ 0,057	0,273 ± 0,023	≤ 0,052
216	SO2	11 111-10 010	221965,210	60,4	0,199	0,004	1,763 ± 0,028	3,268 ± 0,023	0,402 ± 0,026
217	CH3CCH	13 1-12 1	222162,729	81,9	0,018	0,004	≤ 0,056	0,119 ± 0,023	≤ 0,052
218	CH3CCH	13 0-12 0	222166,970	74,7	0,018	0,004	≤ 0,056	0,119 ± 0,023	≤ 0,052
219	UL		222214,277		0,031	0,004	≤ 0,049	0,125 ± 0,020	≤ 0,045
220	UL		222559,945		0,021	0,004	≤ 0,049	0,043 ± 0,020	≤ 0,045
221	CH2DOH	5 2 4 2-4 2 3 2	223117,442	67,7	0,012	0,004	≤ 0,049	0,078 ± 0,020	0,052 ± 0,022
222	CH2DOH	5 0 5 0-4 0 4 0	223196,401	32,2	0,022	0,004	≤ 0,049	0,187 ± 0,020	≤ 0,045
223	UL		224327,855		0,018	0,004	≤ 0,052	0,169 ± 0,021	0,092 ± 0,024
224	CO-17	2-1	224714,385	16,2	0,265	0,004	≤ 0,052	1,008 ± 0,021	≤ 0,048
225	H2CO	312-211	225697,775	33,4	0,958	0,004	≤ 0,052	8,038 ± 0,021	0,175 ± 0,024
226	UL		226130,046		-	-	--	--	--
227	UL		226167,548		-	-	--	--	--
228	UL		226332,328		-	-	--	--	--
229	UL		226359,603		-	-	--	--	--
230	CN	2 0 2 3-1 0 1 2	226659,575	16,3	0,140	0,004	0,530 ± 0,026	1,358 ± 0,021	0,111 ± 0,024
231	CN	2 0 3 2-1 0 2 1	226875,897	16,3	0,303	0,005	0,103 ± 0,031	3,135 ± 0,025	0,168 ± 0,028
232	S-34-O2	12 3 9-12 210	227031,881	93,1	-	-	--	--	--

233	c-C3H2	4 320-3 210	227169,127	29,1	0,037	0,005	≤ 0,062	0,131 ± 0,025	≤ 0,057
234	HC3N	25-24	227418,905	141,9	0,033	0,005	≤ 0,062	0,110 ± 0,025	≤ 0,057
235	UL		228126,378		-	-	--	--	--
236	UL		228138,033		0,023	0,005	≤ 0,064	0,070 ± 0,026	≤ 0,059
237	UL		228201,706		-	-	--	--	--
238	UL		228212,097		-	-	--	--	--
239	DNC	3-2	228910,481	22	0,130	0,005	≤ 0,064	0,605 ± 0,026	≤ 0,059
240	CH3NH2	3 3 7-4 2 7	229059,714	48,2	-	-	--	--	--
241	CH3OH	8-100-7070	229758,756	89,1	0,137	0,005	≤ 0,064	1,089 ± 0,026	≤ 0,059
242	UL		230265,783		-	-	--	--	--
243	CO	2-1	230538,000	16,6	4,430	0,007	11,611 ± 0,042	104,220 ± 0,034	27,068 ± 0,038
244	OCS	19-18	231060,983	110,9	0,023	0,007	≤ 0,083	0,142 ± 0,034	≤ 0,076
245	UL		231202,187		-	-	--	--	--
246	C-13-S	5-4	231220,996	33,3	0,032	0,007	≤ 0,083	0,183 ± 0,034	≤ 0,076
247	CH3OH	10 2-0-9 3-0	231281,110	165,3	0,021	0,007	≤ 0,083	0,089 ± 0,034	≤ 0,076
248	N2D+	3-2	231321,828	22,2	0,070	0,007	≤ 0,083	0,360 ± 0,034	≤ 0,076
249	D2CO	404-303	231410,272	27,9	0,096	0,007	0,086 ± 0,041	0,244 ± 0,034	≤ 0,076
250	UL		232230,842		-	-	--	--	--
251	UL		232345,986		0,020	0,005	≤ 0,062	0,130 ± 0,025	≤ 0,057
252	CH3D		232644,301	11,2	-	-	--	--	--
253	D2CO	423-322	233650,441	49,6	0,034	0,005	≤ 0,062	0,176 ± 0,025	0,074 ± 0,028
254	UL		234226,959		0,016	0,005	≤ 0,058	0,044 ± 0,024	≤ 0,053
255	CH3OH	4 2 - 0-5 1 - 0	234683,370	60,9	0,021	0,005	≤ 0,058	0,155 ± 0,024	≤ 0,053
256	SO2	422-313	235151,720	19	0,029	0,005	≤ 0,058	0,375 ± 0,024	0,101 ± 0,027
257	UL		235203,274		-	-	--	--	--
258	CH3OCHO	19 614 1-18 612 2	235566,262	136,7	0,017	0,005	≤ 0,058	0,663 ± 0,024	≤ 0,053
259	CC-13S	4 3 4 - 1 2 3	235996,797	12,9	0,017	0,005	0,082 ± 0,029	0,134 ± 0,024	0,137 ± 0,026
259	D2CO	422-321	236102,086	49,8	0,036	0,005	≤ 0,057	0,074 ± 0,023	0,062 ± 0,028
260	SO2	16 115-15 214	236216,685	130,7	0,017	0,005	0,320 ± 0,029	0,113 ± 0,023	≤ 0,052
261	UL		236237,642		0,020	0,005	0,073 ± 0,029	0,313 ± 0,023	≤ 0,052
262	HO2	4 1 4 5 5-5 0 5 6 5	236267,795	58,2	-	-	--	--	--
263	HC3N	26 - 25	236512,777	153,2	0,031	0,005	≤ 0,057	0,170 ± 0,023	≤ 0,052
264	H2CS	7 1 7-6 1 6	236726,770	58,6	0,050	0,005	≤ 0,057	0,391 ± 0,023	≤ 0,052
265	UL		236776,017		-	-	--	--	--
266	UL		237235,994		0,018	0,005	≤ 0,057	0,057 ± 0,023	≤ 0,052
267	CH3CN	13 3-12 3	239096,497	144,6	0,025	0,004	≤ 0,055	0,109 ± 0,022	≤ 0,050
268	CH3CN	13 2 -12 2	239119,504	109	0,013	0,004	0,079 ± 0,027	0,194 ± 0,022	0,071 ± 0,025
269	CH3CN	13 1-12 1	239133,313	87,5	0,023	0,004	≤ 0,055	0,288 ± 0,022	≤ 0,050
270	CH3CN	13 0-12 0	239137,916	80,3	0,024	0,004	≤ 0,055	0,208 ± 0,022	≤ 0,050
271	CH3CCH	14 1 -13 1	239247,727	93,3	0,028	0,004	≤ 0,055	0,251 ± 0,022	0,090 ± 0,025
272	CH3CCH	14 0- 13 0	239252,297	86,1	0,017	0,004	≤ 0,055	0,219 ± 0,022	0,060 ± 0,025
273	CH3OH	5 1 + 0-4 1 + 0	239746,219	49,1	0,097	0,004	≤ 0,055	0,730 ± 0,022	≤ 0,050
274	H2CCO	12 112-11 111	240185,794	88	0,027	0,004	0,078 ± 0,023	0,089 ± 0,019	≤ 0,043
275	CH3OH	5 3 0- 6 2 0	240241,490	82,5	0,016	0,004	0,303 ± 0,023	0,080 ± 0,019	≤ 0,043
276	H2CS	7 0 7-6 0 6	240266,320	46,1	0,035	0,004	≤ 0,047	0,309 ± 0,019	≤ 0,043
277	H2CS	7 2 6-6 2 5	240381,750	98,9	0,016	0,004	0,087 ± 0,023	0,173 ± 0,019	≤ 0,043
278	H2CS	7 3 5 - 6 3 4	240392,362	164,5	0,017	0,004	0,092 ± 0,023	0,222 ± 0,019	≤ 0,043

279	H2CS	7 3 4-6 3 3	240393,032	164,5	0,017	0,004	0,089 ± 0,023	0,228 ± 0,019	≤ 0,043
280	H2CS	7 2 5-6 2 4	240548,229	98,9	0,015	0,004	≤ 0,023	0,061 ± 0,019	≤ 0,043
281	CH2DOH	7 0 7 0-6 1 6 0	240643,977	60	0,014	0,004	≤ 0,047	0,154 ± 0,019	≤ 0,043
282	UL		240783,987		-	-	--	--	--
283	NCHCCO	28 524-28 425	240965,908	137,1	0,020	0,004	≤ 0,023	0,456 ± 0,019	≤ 0,021
284	CS-34	5-4	241016,194	34,7	0,114	0,004	≤ 0,047	0,741 ± 0,019	0,506 ± 0,021
285	UL		241180,123		0,016	0,004	0,052 ± 0,023	0,141 ± 0,019	≤ 0,043
286	HDO	2 1 1-2 1 2	241561,550	95,2	0,016	0,004	0,325 ± 0,023	0,074 ± 0,019	≤ 0,043
287	SO2	5 2 4-4 1 3	241615,798	23,6	0,036	0,004	≤ 0,047	0,357 ± 0,019	0,070 ± 0,021
288	UL		241638,010	0,017		0,004	≤ 0,047	0,099 ± 0,019	≤ 0,043
289	CH3OH*	505+0-404+0	241791,431	34,8	0,646	0,004	1,115 ± 0,023	5,854 ± 0,019	0,292 ± 0,021
290	HNCO	11 110-12 012	242639,704	113,2	0,015	0,004	≤ 0,046	0,117 ± 0,019	≤ 0,042
291	OCS	20-19	243218,040	122,6	0,025	0,005	0,134 ± 0,029	0,229 ± 0,024	≤ 0,053
292	CH2DCCH	15 114 -14 113	243637,154	99	0,018	0,005	≤ 0,058	0,173 ± 0,024	≤ 0,053
293	CH3OH	514-0-413-0	243915,826	49,7	0,110	0,005	≤ 0,058	0,814 ± 0,024	≤ 0,053
294	H2CS	7 1 6- 6 1 5	244048,504	60	0,040	0,006	≤ 0,068	0,222 ± 0,028	≤ 0,062
295	c-C3H2	3 2 1 0-2 1 2 0	244222,133	18,2	0,033	0,006	≤ 0,068	0,348 ± 0,028	≤ 0,062
296	DNO3	8 4 4-7 2 5	244251,878	36,9	0,032	0,006	0,167 ± 0,034	0,446 ± 0,028	≤ 0,062
297	SO2	14 014 -13 113	244254,218	93,9	0,025	0,006	0,167 ± 0,034	0,446 ± 0,028	≤ 0,062
298	CS	5-4	244935,557	35,3	0,932	0,006	2,230 ± 0,034	7,447 ± 0,028	0,233 ± 0,031
299	D2CO	413-312	245532,752	34,9	0,032	0,006	0,154 ± 0,034	0,060 ± 0,028	≤ 0,062
300	HC3N	27-26	245606,320	165	0,023	0,006	≤ 0,068	0,075 ± 0,028	≤ 0,062
301	CC-13S	192020-181920	245667,6478	120,9	-	-	--	--	--
302	SOO-18	8 3 5-8 2 6	246119,374	52,9	0,019	0,006	≤ 0,067	0,104 ± 0,028	≤ 0,062
303	UL		246746,002		-	-	--	--	--
304	HDCO	4 1 4-3 1 3	246924,600	37,6	0,115	0,006	0,075 ± 0,034	0,525 ± 0,027	≤ 0,061
305	UL		247610,234		-	-	--	--	--
306	UL		247650,048		-	-	--	--	--
307	c-C3H2	5 2 3 0-4 3 2 0	249054,368	41	0,026	0,005	≤ 0,058	0,199 ± 0,024	≤ 0,053
308	NO	3 1 3 4 - 2-1 2 3	250436,848	19,2	0,025	0,004	0,137 ± 0,024	0,351 ± 0,020	≤ 0,044
309	NO	3 1 3 3 - 2-1 2 2	250440,659	19,2	0,025	0,004	0,137 ± 0,024	0,351 ± 0,020	≤ 0,044
310	NO	3 1 3 2- 2-1 2 1	250448,530	19,2	0,014	0,004	0,412 ± 0,024	0,372 ± 0,020	≤ 0,044
311	CH3OH	11 0 11 +0-10 1 10 +0	250506,980	153,1	0,049	0,004	≤ 0,048	0,399 ± 0,020	0,358 ± 0,022
312	CH3COCH3	1410 5 0-13 9 4 0	250634,375	87,7	0,016	0,004	≤ 0,048	0,069 ± 0,020	≤ 0,044
313	NO	3-1 3 4-2 1 2 3	250796,176	19,3	0,020	0,004	0,141 ± 0,024	0,177 ± 0,020	0,075 ± 0,022
314	NO	3-1 3 3-2 1 2 2	250815,594	19,3	0,030	0,004	≤ 0,048	0,146 ± 0,020	0,170 ± 0,022
315	NO	3-1 3 2-2 1 2 1	250816,954	19,3	0,030	0,004	≤ 0,048	0,146 ± 0,020	0,170 ± 0,022
316	SO2	13 113-12 012	251199,675	82,2	0,048	0,004	0,301 ± 0,024	0,810 ± 0,020	0,356 ± 0,022
317	SO2	8 3 5 - 8 2 6	251210,586	55,2	0,023	0,004	0,266 ± 0,024	0,697 ± 0,020	≤ 0,044
318	c-C3H2	7 0 7 0-6 1 6 0	251314,337	50,7	0,064	0,004	≤ 0,048	0,261 ± 0,020	0,167 ± 0,022
319	c-C3H2	6 2 5 0-5 1 4 0	251527,302	47,5	0,030	0,004	≤ 0,048	0,305 ± 0,020	≤ 0,044
320	CH3OH	6 3 3 -0-6 2 4 +0	251738,520	98,5	0,040	0,004	≤ 0,048	0,175 ± 0,020	≤ 0,044
321	CH3OH*	5 3 - 0-5 2 + 0	251811,956	84,6	0,075	0,004	1,634 ± 0,024	3,020 ± 0,020	0,924 ± 0,022
322	SO	6 5-5 4	251825,770	50,7	0,207	0,004	1,476 ± 0,024	3,105 ± 0,020	1,491 ± 0,022
323	CH3OH	8 3 6 +0 - 8 2 7 -0	251984,702	133,5	0,035	0,004	≤ 0,048	0,171 ± 0,020	0,532 ± 0,022
324	CH3OH	9 3 7 +0- 9 2 8 -0	252090,380	154,4	0,030	0,004	0,074 ± 0,024	0,214 ± 0,020	≤ 0,044
325	CH3OH	10 3 8 +0-10 2 9 -0	252252,850	177,6	0,027	0,004	0,072 ± 0,024	0,111 ± 0,020	≤ 0,044

326	CH3OH	11 3 9 +0 -11 2 10 -0	252485,649	203,2	0,018	0,004	≤ 0,048	0,114 ± 0,020	≤ 0,044
327	UL		253220,923		0,017	0,005	≤ 0,057	0,076 ± 0,023	≤ 0,052
328	UL		253756,141		0,024	0,005	0,077 ± 0,028	0,201 ± 0,023	≤ 0,052
329	CH3NH2	6 2 7-6 1 7	253768,519	60,6	-	-	--	--	--
330	CH3OH	200-1-10	254015,377	20,1	0,100	0,004	≤ 0,053	0,824 ± 0,022	0,055 ± 0,024
331	SO2	6 3 3 - 6 2 4	254280,536	41,4	0,026	0,004	0,109 ± 0,027	0,351 ± 0,022	0,120 0,049
332	UL		254421,899		0,016	0,004	0,042 ± 0,027	0,065 ± 0,022	≤ 0,049
333	UL		254564,747		0,053	0,004	≤ 0,053	0,378 ± 0,022	≤ 0,049
334	HC3N	28-27	254699,500	177,3	0,032	0,004	0,092 ± 0,027	0,359 ± 0,022	≤ 0,049
335	c-C3H2	5 3 3 0-4 2 2 0	254987,640	41,1	0,019	0,004	≤ 0,053	0,119 ± 0,022	≤ 0,049
336	OCS	21-20	255374,461	134,8	0,028	0,004	≤ 0,053	0,106 ± 0,022	≤ 0,049
337	HCO-18+	3-2	255480,039	24,5	0,058	0,004	≤ 0,053	0,149 ± 0,022	≤ 0,049
338	SO2	4 3 1-4 2 2	255553,303	31,3	0,023	0,004	≤ 0,053	0,173 ± 0,022	≤ 0,049
339	CH2DOH	3 2 2 0-3 1 3 0	255647,816	29	0,020	0,004	0,408 ± 0,027	0,125 ± 0,022	≤ 0,049
340	HDCO	404-303	256585,430	30,8	0,167	0,007	≤ 0,080	0,804 ± 0,032	≤ 0,073
341	CH2DOH	4 1 4 0-3 0 3 0	256731,552	25,2	0,023	0,007	≤ 0,080	0,081 ± 0,032	≤ 0,073
342	CH3CN	14 0-13 0	257527,383	92,8	0,025	0,007	≤ 0,079	0,283 ± 0,032	≤ 0,073
343	CH3CN	14 1 - 13 1	257522,427	99,9	0,022	0,007	≤ 0,079	0,332 ± 0,032	≤ 0,073
344	CH3CN	14 3 - 13 3	257482,792	157,1	0,020	0,007	0,326 ± 0,040	≤ 0,065	≤ 0,073
345	CH3CNH+	15 3-14 3	257630,157	163,2	-	-	--	--	--
346	HDCO	4 2 3-3 2 2	257748,760	62,8	0,071	0,007	≤ 0,079	0,265 ± 0,032	≤ 0,072
347	CH2DOH	4 2 3 1-3 1 3 2	257895,673	48	0,024	0,008	≤ 0,095	0,208 ± 0,039	≤ 0,086
348	HCN-15	3-2	258157,100	24,8	0,045	0,008	≤ 0,094	0,210 ± 0,039	0,115 ± 0,043
349	SO	6 6-5 5	258255,813	56,6	0,182	0,008	0,999 ± 0,047	2,322 ± 0,039	1,187 ± 0,043
350	CCS	2019-1918	258274,287	135,4	-	-	--	--	--
351	UL		258564,045		0,027	0,008	≤ 0,094	0,207 ± 0,039	≤ 0,086
352	HC-13-N	3-2	259011,798	24,9	0,117	0,008	0,417 ± 0,047	1,001 ± 0,039	0,316 ± 0,043
353	HOONO	16 41316-15 31216	259025,703	102,1	-	-	--	--	--
354	HDCO	422-321	259034,916	62,9	0,044	0,008	≤ 0,094	0,478 ± 0,039	0,188 ± 0,043
355	HC-13-O+	3-2	260255,339	25	0,458	0,007	≤ 0,084	1,858 ± 0,034	0,120 ± 0,038
356	SiO	6-5	260518,020	43,8	0,110	0,007	4,334 ± 0,042	2,597 ± 0,034	4,661 ± 0,038
357	HO2	4 0 4 5 4- 3 0 3 4 4	260579,539	31,3	0,073	0,007	≤ 0,084	2,104 ± 0,034	≤ 0,076
358	CH3OCH3	15 510 0-15 411 0	261250,655	144,4	-	-	--	--	--
359	HNC-13	3-2	261263,481	25,1	0,061	0,007	≤ 0,083	0,341 ± 0,034	0,097 ± 0,038
360	CH3OH	2 1 0-1 0 0	261805,675	28	0,165	0,007	5,744 ± 0,042	2,985 ± 0,034	≤ 0,076
361	SO	6 7-5 6	261843,684	47,6	0,313	0,007	1,801 ± 0,042	5,031 ± 0,034	2,590 ± 0,038
362	UL		261890,195		-	-	--	--	--
363	CCH	3 4 3-2 3 2	262006,403	25,1	0,442	0,006	2,186 ± 0,033	3,178 ± 0,027	0,150 ± 0,030
364	HNCO	12 0 12-11 0 11	263748,625	82,4	0,027	0,006	≤ 0,066	0,209 ± 0,027	≤ 0,061
365	HC3N	29-28	263791,922	190,1	0,028	0,006	≤ 0,066	0,192 ± 0,027	≤ 0,061
366	CH2DOH	6 1 6 0-5 1 5 0	264017,721	48,5	0,022	0,005	≤ 0,054	0,075 ± 0,022	≤ 0,050
367	CH3OH	6 +1 5 0 - 5 +2 3 0	265289,650	69,9	0,033	0,005	≤ 0,054	0,246 ± 0,022	≤ 0,049
368	c-C3H2	4 4 1 0-3 3 0 0	265759,438	32,2	0,057	0,005	≤ 0,054	0,188 ± 0,022	≤ 0,049
369	HCN	(3-2)	265886,180	25,5	1,417	0,005	3,550 ± 0,027	22,495 ± 0,022	2,952 ± 0,025
370	CH3OH	5+230-4+130	266838,130	57,1	0,218	0,005	≤ 0,057	1,529 ± 0,023	≤ 0,052
371	CH3OH	9 0 0- 8 1 0	267403,471	117,5	0,045	0,005	0,060 ± 0,029	0,347 ± 0,023	0,089 ± 0,026
372	OCS	22-21	267530,219	147,7	0,084	0,005	≤ 0,057	3,269 ± 0,023	≤ 0,052

373	HCO+	(3-2)	267557,930	25,7	2,856	0,005	0,983 ± 0,029	17,361 ± 0,023	2,522 ± 0,026
374	CH2DOH	6 0 6 0-5 0 5 0	267634,613	45	0,038	0,005	≤ 0,054	0,270 ± 0,022	≤ 0,049
375	CH2DOH	6 0 6 2-5 0 5 2	267722,687	63,4	0,016	0,005	0,205 ± 0,027	0,295 ± 0,022	≤ 0,049
376	H2C-13-S	8 1 7 - 7 1 6	268012,418	71,1	0,018	0,005	≤ 0,054	0,163 ± 0,022	≤ 0,049
377	HDCO	4 1 3-3 1 2	268292,020	40,2	0,140	0,005	≤ 0,054	0,712 ± 0,022	≤ 0,049
378	CH2DOH	7 2 6 0-7 1 7 0	270299,931	76,2	0,017	0,005	≤ 0,054	0,072 ± 0,022	≤ 0,049
379	H2CS	8 1 8 -7 1 7	270521,931	71,6	0,061	0,005	≤ 0,062	0,364 ± 0,025	0,129 ± 0,028
380	UL		271097,896		-	-	--	--	--
381	UL		271174,916		0,034	0,005	0,035 ± 0,031	0,178 ± 0,025	≤ 0,057
382	SO2	7 2 6-6 1 5	271529,015	35,5	0,036	0,005	0,096 ± 0,031	0,425 ± 0,025	≤ 0,057
383	UL		271749,994		0,061	0,005	0,119 ± 0,031	0,135 ± 0,025	≤ 0,057
384	HNC	3-2	271981,142	26,1	0,908	0,005	0,220 ± 0,031	4,379 ± 0,025	0,132 ± 0,028
385	CH2DOH	6 1 5 0-5 1 4 0	272098,059	49,8	0,023	0,005	≤ 0,062	0,149 ± 0,025	0,096 ± 0,028
386	HC3N	30-29	272884,734	203	0,041	0,007	0,239 ± 0,040	0,402 ± 0,033	0,046 ± 0,037
387	UL		273014,105		-	-	--	--	--
388	CH3CCH	16 0-15 0	273419,921	111,5	0,023	0,007	0,153 ± 0,040	0,307 ± 0,033	0,119 ± 0,037
389	HO2	4 1 4 4 3-3 1 3 4 4	273867,541	59	-	-	--	--	--
390	H2CS	8 0 8-7 0 7	274520,870	59,3	0,022	0,007	0,111 ± 0,038	0,153 ± 0,031	≤ 0,069
391	H2C-13-O	4 1 4-3 1 3	274762,112	44,8	0,040	0,007	≤ 0,075	0,221 ± 0,031	≤ 0,069
392	UL		275737,129		-	-	--	--	--
393	HCOCH2OH	15 511 0-14 410 0	275818,070	82,2	-	-	--	--	--
394	CH3CN	15 1 - 14 1	275910,263	113,2	0,021	0,007	≤ 0,075	0,219 ± 0,031	0,153 ± 0,034
395	D2CO	5 1 5-4 1 4	276060,243	45,2	0,046	0,006	≤ 0,071	0,277 ± 0,029	0,231 ± 0,032
396	HCOOD	4 3 2-4 2 3	276253,448	34,3	-	-	--	--	--
397	UL		276941,911		0,036	0,006	0,205 ± 0,035	0,320 ± 0,029	0,013 ± 0,032
398	C-13-S	6-5	277455,481	46,6	0,031	0,006	≤ 0,071	0,168 ± 0,029	0,074 ± 0,032
399	NCHCO	25 223-24 124	277660,410	90	-	-	--	--	--
400	UL		277761,123		0,023	0,006	≤ 0,071	0,106 ± 0,029	≤ 0,065
401	UL		277899,926		-	-	--	--	--
402	UL		277900,063		-	-	--	--	--
403	UL		278056,137		-	-	--	0,052 -	--
404	CH3OH	9-10- 8 00	278304,512	110	0,119	0,006	0,146 ± 0,036	0,838 ± 0,029	0,093 ± 0,032
405	UL		278612,614		0,032	0,006	≤ 0,071	0,591 ± 0,029	≤ 0,065
406	H2CS	8 1 7-7 1 6	278886,400	73,4	0,070	0,006	0,231 ± 0,035	0,401 ± 0,029	0,098 ± 0,032
407	N2H+	3-2	279511,735	26,8	0,949	0,006	≤ 0,071	4,287 ± 0,029	≤ 0,065
408	OCS	23-22	279685,318	161,1	0,030	0,006	≤ 0,071	0,196 ± 0,029	0,124 ± 0,032
409	UL		280051,835		0,032	0,006	≤ 0,067	0,082 ± 0,027	≤ 0,061
410	H2CCO	14 114 - 13 113	280195,983	113,9	0,024	0,006	≤ 0,066	0,136 ± 0,027	≤ 0,061
411	CH3OCHO	26 026 2-25 125 1	280522,834	184,7	0,019	0,006	≤ 0,067	0,211 ± 0,027	≤ 0,061
412	UL		280748,864		0,023	0,006	0,129 ± 0,034	0,091 ± 0,027	≤ 0,061
413	CH3OCH3	4 4 0 0-3 3 1 0	280943,497	31,6	0,055	0,006	≤ 0,067	0,450 ± 0,027	≤ 0,061
414	CH3OH	11 2 + 0-10 3 + 0	281000,109	190,9	0,028	0,006	≤ 0,067	0,159 ± 0,027	≤ 0,061
415	CH3CHO	15 015 2-14 014 2	281083,430	109,2	0,022	0,006	≤ 0,067	0,060 ± 0,027	≤ 0,061
416	UL		281325,531		0,047	0,006	≤ 0,067	0,118 ± 0,027	≤ 0,061
417	UL		281400,000		-	-	--	--	--
418	H2CO	4 1 4-3 1 3	281526,929	45,6	0,421	0,006	0,178 ± 0,033	10,066 ± 0,027	0,389 ± 0,030
419	SO2	15 115-14 014	281762,600	107,5	0,050	0,006	0,325 ± 0,033	0,644 ± 0,027	0,134 ± 0,030

420	HDCCO	15 015-14 014	281780,467	108,3	-	-	--	--	--
421	HC3N	31-30	281976,777	216,7	0,028	0,008	0,436 ± 0,045	0,198 ± 0,037	≤ 0,083
422	SO2	6 2 4- 5 1 5	282036,566	29,2	0,039	0,009	≤ 0,106	0,348 ± 0,043	0,236 ± 0,048
423	HCS	7 0 7 7 6-6 0 6 6 6	282060,214	54,2	-	-	--	--	--
424	H2C-13-O	4 0 4 - 3 0 3	283441,876	34,1	0,027	0,009	0,639 ± 0,053	0,677 ± 0,043	0,253 ± 0,048
425	SO2	16 016-15 115	283464,768	121	0,043	0,009	0,427 ± 0,053	0,687 ± 0,043	0,508 ± 0,048
426	HC3N	32-31	291068,427	230,5	0,023	0,006	≤ 0,069	0,095 ± 0,028	≤ 0,063
427	H2CO	4 2 3-3 2 2	291237,780	82,1	0,253	0,006	≤ 0,069	1,891 ± 0,028	≤ 0,063
428	H2CO	4 3 2-3 3 1	291380,488	140,9	0,297	0,006	≤ 0,069	3,194 ± 0,028	0,134 ± 0,032
429	CS-33	6-5	291485,935	49	0,021	0,006	≤ 0,069	0,167 ± 0,028	≤ 0,063
430	D2CO	5 2 4-4 2 3	291745,750	63,6	0,029	0,006	≤ 0,069	0,102 ± 0,028	≤ 0,063
431	OCS	24-23	291839,653	175,1	0,029	0,006	≤ 0,069	0,076 ± 0,028	≤ 0,063
432	H2CO	4 2 2-3 2 1	291948,068	82,1	0,273	0,006	≤ 0,069	1,818 ± 0,028	0,067 ± 0,032
433	CH3OH	6 1 5 -0-5 1 4 -0	292672,890	63,7	0,156	0,006	≤ 0,069	1,152 ± 0,028	≤ 0,063
434	DCOOH	6 2 4-5 1 5	292699,937	31,4	-	-	--	--	--
435	H2C-13-O	4 1 3-3 1 2	293126,515	47	0,042	0,006	≤ 0,069	0,264 ± 0,028	0,065 ± 0,032
436	H2CN	4 2 3 3 6-3 2 2 0 6	293310,628	82,8	-	-	--	--	--
437	H2CN	4 2 323 2-3 2 220 2	293414,564	82,8	0,022	0,006	≤ 0,035	0,075 ± 0,028	≤ 0,063
438	CH3OH	3 2 + 0-4 1 + 0	293464,055	51,6	0,021	0,006	≤ 0,069	0,090 ± 0,028	≤ 0,063
439	UL		293847,895		0,020	0,006	≤ 0,069	0,326 ± 0,028	≤ 0,063
440	CS	6-5	293912,244	49,4	1,298	0,006	0,362 ± 0,035	8,806 ± 0,028	0,395 ± 0,032
441	CH3CN	16 5-15 5	294161,001	298,8	0,019	0,006	≤ 0,069	0,049 ± 0,028	≤ 0,063
442	CH3CN	16 3-15 3	294251,461	184,4	0,035	0,006	0,358 ± 0,035	0,136 ± 0,028	0,098 ± 0,032
443	CH3CN	16 2-15 2	294279,750	148,8	0,023	0,006	≤ 0,069	0,218 ± 0,028	≤ 0,063
444	CH3CN	16 1-15 1	294296,728	127,3	0,030	0,006	≤ 0,069	0,303 ± 0,028	0,103 ± 0,032
445	SO	7 6- 6 5	296550,045	64,9	0,110	0,008	1,463 ± 0,042	1,792 ± 0,034	1,122 ± 0,038
446	D2CO	5 2 3-4 2 2	296577,045	64	0,049	0,008	1,345 ± 0,042	1,096 ± 0,034	≤ 0,076
447	UL		296655,885		0,105	0,008	1,677 ± 0,042	1,658 ± 0,034	≤ 0,076
448	C2H3NC	30 130-29 129	296670,402	223,9	0,098	0,008	0,646 ± 0,042	2,514 ± 0,034	≤ 0,076
449	UL		296688,330		0,131	0,008	≤ 0,083	2,187 ± 0,034	≤ 0,076
450	SO2	9 2 8-8 1 7	298576,307	51	0,012	0,003	≤ 0,033	0,071 ± 0,014	≤ 0,030
451	HCS+	7-6	298690,453	57,3	0,021	0,003	≤ 0,033	0,137 ± 0,014	≤ 0,030
452	HC3N	33-32	300159,647	245,1	0,011	0,003	0,074 ± 0,018	0,128 ± 0,015	0,071 ± 0,017
453	UL		300769,821		0,012	0,003	2,506 ± 0,018	0,153 ± 0,015	≤ 0,033
454	H2CO	4 1 3-3 1 2	300836,635	47,9	0,303	0,003	≤ 0,036	2,477 ± 0,015	0,186 ± 0,017
455	SO	7 7-6 6	301286,124	71	0,055	0,003	0,359 ± 0,018	0,813 ± 0,015	0,248 ± 0,017
456	UL		302215,818		0,030	0,007	≤ 0,081	0,058 ± 0,033	≤ 0,074
457	UL		302263,870		0,031	0,007	0,277 ± 0,040	0,312 ± 0,033	≤ 0,074
458	UL		302356,170		0,036	0,007	0,295 ± 0,040	0,597 ± 0,033	0,364 ± 0,037
459	CH3OH	3 0 0-2-1 0	302369,773	27,1	0,071	0,007	0,322 ± 0,040	0,694 ± 0,033	0,340 ± 0,037
460	CH3OH	12 0 + 0-11 1 + 0	302912,979	180,9	0,034	0,007	≤ 0,081	0,167 ± 0,033	≤ 0,074
461	CH3OOH	13 310 5-14 212 2	303253,454	121,7	-	-	--	--	--
462	UL		303315,871		0,022	0,006	≤ 0,062	0,051 ± 0,025	≤ 0,056
463	CH3OH	1 1 0 0-1 0 1 + 0	303366,890	16,9	0,108	0,006	≤ 0,062	0,839 ± 0,025	0,082 ± 0,028
464	Is a line?		303823,162		-	-	--	--	--
465	SiO	7-6	303926,960	58,3	0,073	0,006	1,909 ± 0,034	1,606 ± 0,028	2,668 ± 0,031
466	SO	7 8-6 7	304077,844	62,1	0,208	0,006	0,808 ± 0,034	3,044 ± 0,028	2,154 ± 0,031

467	H2COH+	5 1 5 - 4 1 4	304129,931	51,8	0,041	0,006	1,381 ± 0,034	0,713 ± 0,028	3,251 ± 0,031
468	CH3OH	2 1 1 -0-2 0 2 +0	304208,350	21,6	0,211	0,006	≤ 0,068	1,630 ± 0,028	0,668 ± 0,031
469	H2CS	9 1 9 - 8 1 8	304305,975	86,2	0,038	0,006	≤ 0,068	0,055 ± 0,028	≤ 0,062
470	UL		304494,064		0,023	0,006	≤ 0,068	0,060 ± 0,028	≤ 0,062
471	DNC	4-3	305206,219	36,6	0,059	0,006	≤ 0,068	0,066 ± 0,028	≤ 0,062
472	UL		305404,007		0,023	0,006	1,583 ± 0,034	0,096 ± 0,028	≤ 0,062
473	CH3OH	3 1 2 -0-3 0 3 +0	305473,520	28,6	0,214	0,006	≤ 0,068	1,611 ± 0,028	0,111 ± 0,031
474	UL		305830,093		0,019	0,006	≤ 0,068	0,069 ± 0,028	≤ 0,062
475	CH3OCHO	11 3 9 0-10 110 0	306292,438	45	0,035	0,007	0,224 ± 0,036	0,326 ± 0,029	≤ 0,066
476	D2CO	5 1 4-4 1 3	306398,012	49,6	0,027	0,007	0,128 ± 0,036	0,084 ± 0,029	≤ 0,066
477	CH3OH	4 1 3 -0-4 0 4 +0	307165,940	38	0,119	0,007	0,067 ± 0,036	0,981 ± 0,029	≤ 0,066
478	HCOCN	14 213-13 112	307224,324	60,7	-	-	--	--	--
479	HDCO	5 1 5-4 1 4	308418,200	52,4	0,058	0,005	≤ 0,056	0,469 ± 0,023	≤ 0,051
480	N2D+	4-3	308422,222	37	0,04	0,005	≤ 0,056	0,429 ± 0,023	≤ 0,051
481	CH3OH	5 1 4 -0-5 0 5 +0	309290,400	49,7	0,120	0,005	≤ 0,056	0,872 ± 0,023	0,215 ± 0,026
482	CH3OH	3 +1 2 0 - 2 +0 2 0	310193,000	35	0,108	0,006	≤ 0,062	0,707 ± 0,025	≤ 0,057
483	UL		311790,935		0,035	0,004	≤ 0,046	0,697 ± 0,019	≤ 0,042
484	C2H5OOCH	30 426 0-29 227 0	311796,665	134,7	0,074	0,004	0,721 ± 0,023	0,721 ± 0,019	≤ 0,042
485	CH3OH	6 1 5 -0-6 0 6 +0	311852,640	63,7	0,045	0,004	0,224 ± 0,023	0,562 ± 0,019	≤ 0,042
486	CH2DOH	7 0 7 0-6 0 6 0	311966,026	60	0,012	0,004	0,260 ± 0,023	0,048 ± 0,019	0,231 ± 0,021
487	HCCCH2OD	19 614 1-20 516 0	312086,283	133,6	0,015	0,004	≤ 0,046	0,190 ± 0,019	0,259 ± 0,021
488	SO2	17 117-16 016	313660,850	136,1	0,021	0,004	≤ 0,046	0,222 ± 0,019	0,187 ± 0,021
489	CH3OH	7 1 - 0-7 0 + 0	314859,528	80,1	0,046	0,013	0,102 ± 0,071	0,463 ± 0,058	≤ 0,130
490	CH3OH	6 2 0-5 1 0	315266,861	71	0,088	0,013	≤ 0,143	0,646 ± 0,058	≤ 0,130
491	HC-13-OOH	7 3 4-7 2 5	318872,427	58	-	-	--	--	--
492	HDCO	5 0 5-4 0 4	319769,680	46,2	-	-	--	--	--
493	UL		320332,025		-	-	--	--	--
494	UL		320808,830		-	-	--	--	--
495	CH3CHO	10 4 6 0-10 3 7 0	328607,492	87,1	0,086	0,019	1,045 ± 0,100	0,851 ± 0,082	≤ 0,183
496	UL		328671,883		0,117	0,019	0,638 ± 0,100	1,106 ± 0,082	1,043 ± 0,091
497	UL		328688,066		0,101	0,019	0,406 ± 0,100	1,143 ± 0,082	0,814 ± 0,091
498	CO-18	3-2	329330,545	31,6	1,223	0,019	≤ 0,200	5,077 ± 0,082	0,101 ± 0,091
499	HONO	14 312 0- 13 311 0	330281,232	153,8	-	-	--	--	--
500	UL		330309,980		-	-	--	--	--
501	CH3OCHO	10 8 2 0-9 7 3 0	330323,938	74,9	-	-	--	--	--
502	C2H3CN	11 3 8 010 - 10 2 9 010	330373,191	49,5	-	-	--	--	--
503	UL		330534,379		0,055	0,014	13,187 ± 0,071	0,674 ± 0,058	≤ 0,130
504	C-13-O	3-2	330587,960	31,7	2,441	0,014	0,706 ± 0,071	12,836 ± 0,058	0,191 ± 0,065
505	D2CO	6 1 6-5 1 5	330674,796	61,1	0,063	0,014	1,171 ± 0,071	0,926 ± 0,058	≤ 0,130
506	UL		330689,887		-	0,014	0,504 ± 0,071	1,286 ± 0,058	≤ 0,130
507	UL		330706,789		0,087	0,014	0,326 ± 0,071	1,200 ± 0,058	≤ 0,130
508	CH3CN	18 2-17 2	331046,096	179,5	0,059	0,014	≤ 0,142	0,444 ± 0,058	≤ 0,130
509	CH3OH	11 1 - 0-11 0 + 0	331502,319	169	0,077	0,014	≤ 0,142	0,510 ± 0,058	≤ 0,130
510	SO2	4 3 1-3 2 2	332505,242	31,3	0,051	0,014	0,484 ± 0,071	0,413 ± 0,058	≤ 0,129
511	NH2D	1 0 1 1 0-0 0 0 1 1	332780,945	16,6	0,112	0,017	≤ 0,175	0,270 ± 0,072	0,676 ± 0,080
512	HDCO	5 1 4-4 1 3	335096,739	56,2	0,103	0,015	≤ 0,155	0,749 ± 0,063	≤ 0,141
513	CH3OH	7 1 + 0 - 6 1 + 0	335582,017	79	0,098	0,015	≤ 0,155	0,443 ± 0,063	≤ 0,141

514	UL		336799,688		0,053	0,008	≤ 0,081	0,244 ± 0,033	≤ 0,074
515	UL		336826,194		-	-	--	--	--
516	CH3OH	12 1 - 0-12 0 + 0	336865,149	197,1	0,043	0,008	0,087 ± 0,041	0,434 ± 0,033	≤ 0,074
517	CO-17	3-2	337061,130	32,4	0,400	0,008	0,152 ± 0,041	1,572 ± 0,033	≤ 0,074
518	CS-34	7-6	337396,690	64,8	0,070	0,008	≤ 0,081	0,091 ± 0,033	0,081 ± 0,037
519	UL		337782,039		0,094	0,008	≤ 0,081	0,168 ± 0,033	≤ 0,074
520	H2CS	10 110-9 1 9	338083,195	102,4	0,043	0,008	0,807 ± 0,041	0,232 ± 0,034	≤ 0,075
521	CH3OH*	7 0 + 0-6 0 + 0	338408,698	65	0,460	0,008	0,520 ± 0,041	3,498 ± 0,034	3,117 ± 0,038
522	SO	3 3-2 3	339341,459	25,5	0,031	0,008	≤ 0,082	0,165 ± 0,034	≤ 0,075
523	UL		339660,008		-	-	--	--	--
524	CN*	3 0 3 4 - 2 0 2 3	340031,549	32,7	0,127	0,011	≤ 0,111	1,155 ± 0,045	0,533 ± 0,050
525	CN*	3 0 4 4-2 0 3 3	340247,770	32,7	0,250	0,011	0,092 ± 0,055	1,673 ± 0,045	0,335 ± 0,050
526	CH2NH	3 1 3 3-2 0 2 3	340353,0513	25,5	-	-	--	--	--
527	HCO-18+	4-3	340630,692	40,9	0,038	0,011	≤ 0,111	0,970 ± 0,045	≤ 0,101
528	SO	8 7-7 6	340714,155	81,2	0,165	0,011	1,497 ± 0,055	2,296 ± 0,045	1,601 ± 0,050
529	DNO3	14 7 8-14 411	340733,410	103	-	-	--	--	--
530	HCCCH2OD	10 3 7 1-10 2 9 0	340747,655	44,3	-	-	--	--	--
531	CH3OH	7 1 - 0 - 6 1 - 0	341415,615	80,1	0,127	0,011	≤ 0,110	0,770 ± 0,045	0,162 ± 0,050
532	D2CO	6 0 6 - 5 0 5	342522,445	58,1	0,079	0,011	0,399 ± 0,058	0,400 ± 0,047	≤ 0,106
533	HDCCO	18 117 - 17 116	342729,742	165,2	0,055	0,011	0,380 ± 0,058	0,321 ± 0,047	≤ 0,106
534	CS	7-6	342882,850	65,8	0,951	0,011	1,142 ± 0,058	6,186 ± 0,047	0,470 ± 0,053
535	UL		342918,742		0,047	0,011	0,341 ± 0,058	1,192 ± 0,047	≤ 0,106
536	H2CS	10 010- 9 0 9	342944,369	90,6	0,041	0,011	0,195 ± 0,058	0,608 ± 0,047	≤ 0,106
537	H2C-13-O	5 1 5 - 4 1 4	343325,713	61,3	0,060	0,011	0,302 ± 0,058	0,321 ± 0,047	0,125 ± 0,053
538	UL		343796,109		0,519	0,011	0,226 ± 0,058	2,212 ± 0,047	≤ 0,106
539	UL		343879,078		0,066	0,011	0,298 ± 0,058	0,481 ± 0,047	≤ 0,106
540	UL		343904,063		0,069	0,011	≤ 0,116	0,258 ± 0,047	≤ 0,106
541	HCNO	15-14	344014,004	132,1	0,078	0,016	≤ 0,167	0,301 ± 0,068	≤ 0,152
542	SO	8 8-7 7	344310,612	87,5	0,125	0,016	1,029 ± 0,083	1,874 ± 0,068	1,282 ± 0,076
543	C2H3CHO	15 313 0-14 212 0	344340,801	69,8	-	-	--	--	--
544	SO2	13 212- 12 111	345338,538	93	0,098	0,016	0,334 ± 0,083	1,144 ± 0,068	≤ 0,152
545	HC-13-N	4-3	345339,769	41,4	0,098	0,016	0,332 ± 0,083	1,158 ± 0,068	≤ 0,152
546	UL		345688,051		-	-	--	--	--
547	CO	3-2	345795,990	33,2	6,049	0,016	15,563 ± 0,083	99,158 ± 0,068	34,524 ± 0,076
548	UL		345912,164		0,168	0,016	1,660 ± 0,083	3,046 ± 0,068	≤ 0,152
549	UL		345970,453		0,080	0,016	1,318 ± 0,083	0,953 ± 0,068	≤ 0,152
550	UL		346060,031		0,135	0,015	≤ 0,156	1,032 ± 0,064	≤ 0,143
551	UL		346096,195		0,090	0,015	≤ 0,156	0,300 ± 0,064	≤ 0,143
552	SO	8 9-7 8	346528,481	78,8	0,210	0,015	1,917 ± 0,078	3,127 ± 0,064	2,026 ± 0,071
553	C2H3NC	14 312-14 113	346540,163	71,7	-	-	--	--	--
554	HC-13-O+	4-3	346998,336	41,6	0,326	0,015	≤ 0,156	1,083 ± 0,064	0,206 ± 0,071
555	SiO	8-7	347330,579	75	0,080	0,015	2,585 ± 0,078	1,794 ± 0,064	3,906 ± 0,071
556	HNC-13	4-3	348340,270	41,8	0,055	0,015	2,032 ± 0,078	1,749 ± 0,064	4,167 ± 0,071
557	C2H5OH	14 312 2-13 211 2	347350,929	99,7	-	-	--	--	--
558	UL		348758,961		0,053	0,015	≤ 0,156	0,146 ± 0,064	≤ 0,142
559	CCH	4 5 5-3 4 4	349337,706	41,9	0,254	0,015	1,394 ± 0,078	1,269 ± 0,063	≤ 0,142

Table 4.12: Overview of the Cep E spectral survey, -12, -18 offset

	Molecule	Mol. transition	Frequency	Eup(K)	Tpeak	rms	$\int_{-150}^{-100} T_a dV$	$\int_{-90}^{-30} T_a dV$	$\int_{-30}^{10} T_a dV$
1	CC-13S	6 7 7-5 6 7	81156,078	15,3	-	-	--	--	--
2	CCS	6 7 - 5 6	81505,170	15,4	0,010	0,003	$0,050 \pm 0,025$	$\leq 0,054$	$0,141 \pm 0,022$
3	HC3N	9-8	81881,468	19,6	0,035	0,003	$\leq 0,049$	$0,205 \pm 0,027$	$0,499 \pm 0,022$
4	c-C3H2	2 0 2 0- 1 1 1 0	82093,559	6,4	0,008	0,002	$\leq 0,037$	$\leq 0,040$	$0,050 \pm 0,016$
5	SO2	817-808	83688,093	36,7	0,008	0,002	$0,050 \pm 0,018$	$0,064 \pm 0,020$	$0,178 \pm 0,016$
6	UL		83759,029		-	-	--	--	--
7	CH3OH	5-1 0- 4 0 0	84521,172	40,4	0,112	0,001	$\leq 0,025$	$0,337 \pm 0,014$	$1,656 \pm 0,011$
8	c-C3H2	3 2 2 - 3 1 3	84727,688	16,1	-	-	--	--	--
9	HOONO	7 0 7 7-6 1 6 7	84732,073	17,4	0,006	0,001	$0,053 \pm 0,012$	$0,046 \pm 0,014$	$0,088 \pm 0,011$
10	OCS	7-6	85139,121	16,3	-	-	--	--	--
11	HCO-18+	1-0	85162,157	4,1	-	-	--	--	--
12	HCS+	2-1	85347,890	6,1	0,33	0,001	$\leq 0,025$	$\leq 0,027$	$0,092 \pm 0,011$
13	c-C3H2	2 1 2 0-1 0 1 0	85338,893	6,4	0,023	0,001	$\leq 0,025$	$0,066 \pm 0,014$	$0,315 \pm 0,011$
14	CH3CCH	5 0-4 0	85457,272	12,3	0,006	0,001	$\leq 0,025$	$\leq 0,027$	$0,136 \pm 0,011$
15	CH3CCH	5 1- 4 1	85455,667	19,5	0,006	0,001	$\leq 0,025$	$\leq 0,027$	$0,131 \pm 0,011$
16	C4H	910 9- 8 9 8	85634,004	20,5	-	-	--	--	--
17	C4H	91010- 8 9 9	85634,015	20,5	-	-	--	--	--
18	NH2OH	5 0 5- 4 1 3	85755,730	36,3	-	-	--	--	--
19	CH3OCHO	21 516 2-21 417 2	85761,876	155,8	0,005	0,001	$0,028 \pm 0,012$	$0,078 \pm 0,013$	$0,094 \pm 0,011$
20	NH2D	1 1 1 0- 1 0 1 1	85926,278	20,7	0,018	0,001	$\leq 0,025$	$\leq 0,027$	$0,237 \pm 0,011$
21	HCN-15	1-0	86054,961	4,1	0,010	0,001	$\leq 0,023$	$0,051 \pm 0,013$	$0,189 \pm 0,011$
22	SO	22-11	86093,950	19,3	0,016	0,001	$\leq 0,023$	$0,145 \pm 0,013$	$0,316 \pm 0,011$
23	HC-13-N	1-0	86339,922	4,1	0,028	0,001	$\leq 0,023$	$0,205 \pm 0,013$	$0,585 \pm 0,010$
24	UL		86517,959		-	-	--	--	--
25	HCO	1 0 1 2 2-0 0 0 1 1	86670,760	4,2	0,005	0,001	$0,072 \pm 0,012$	$\leq 0,026$	$0,066 \pm 0,010$
26	HCO	1 0 1 2 1-0 0 0 1 0	86708,360	4,2	-	-	--	--	--
27	HC-13-O+	(1-0)	86753,950	4,2	0,049	0,001	$\leq 0,023$	$0,038 \pm 0,013$	$0,608 \pm 0,010$
28	SiO	2-1	86846,960	6,3	0,098	0,001	$0,084 \pm 0,012$	$1,551 \pm 0,013$	$1,850 \pm 0,010$
29	HNC-13	1-0	87090,850	4,2	0,009	0,001	$\leq 0,023$	$\leq 0,026$	$0,126 \pm 0,010$
30	CCH	1 2 2- 0 1 1	87316,925	4,2	0,060	0,001	$\leq 0,023$	$0,533 \pm 0,013$	$0,845 \pm 0,010$
31	UL		87757,990		-	-	--	--	--
32	HNCO	4 0 4- 3 0 3	87925,237	10,5	0,011	0,001	$\leq 0,023$	$0,043 \pm 0,013$	$0,137 \pm 0,010$
33	UL		88177,958		0,004	0,001	$\leq 0,024$	$\leq 0,027$	$0,028 \pm 0,011$
34	UL		88214,019		0,005	0,001	$\leq 0,024$	$\leq 0,027$	$0,027 \pm 0,011$
35	UL		88237,850		0,005	0,001	$\leq 0,024$	$0,062 \pm 0,013$	$0,064 \pm 0,011$
36	UL		88246,003		0,006	0,001	$\leq 0,024$	$\leq 0,027$	$0,074 \pm 0,011$
37	UL		88271,926		0,007	0,001	$\leq 0,024$	$\leq 0,027$	$0,102 \pm 0,011$
38	UL		88551,156		-	-	--	--	--
39	CH2DOH	3 1 2 0-3 0 3 0	88754,512	17,1	0,006	0,001	$\leq 0,024$	$0,058 \pm 0,027$	$0,060 \pm 0,011$
40	HCN	(1-0)	88632,146	4,3	0,735	0,001	$0,173 \pm 0,012$	$5,820 \pm 0,013$	$16,883 \pm 0,011$
41	UL		88754,053		0,006	0,001	$\leq 0,024$	$0,059 \pm 0,013$	$0,060 \pm 0,011$
42	HN-15-C	1-0	88865,715	4,3	0,005	0,001	$0,043 \pm 0,012$	$\leq 0,027$	$0,071 \pm 0,011$
43	HCO+	1-0	89188,525	4,3	0,639	0,001	$0,842 \pm 0,012$	$2,013 \pm 0,013$	$10,273 \pm 0,011$
44	CH2DOH	2 0 2 0-1 0 1 0	89407,817	6,4	-	-	--	--	--

45	UL		89741,918		0,004	0,001	≤ 0,024	0,081 ± 0,013	0,078 ± 0,011
46	UL		89750,033		0,004	0,001	≤ 0,024	≤ 0,026	0,085 ± 0,011
47	UL		90162,350		0,005	0,001	≤ 0,019	≤ 0,021	0,070 ± 0,009
48	UL		90210,262		0,004	0,001	0,076 ± 0,010	≤ 0,021	0,081 ± 0,009
49	UL		90245,783		0,004	0,001	≤ 0,019	≤ 0,021	0,056 ± 0,009
50	UL		90344,085		0,004	0,001	≤ 0,019	≤ 0,021	0,020 ± 0,009
51	UL		90356,544		-	-	--	--	--
52	UL		90607,602		0,004	0,001	≤ 0,019	≤ 0,021	0,040 ± 0,009
53	HNC	1-0	90663,593	4,4	0,180	0,001	≤ 0,019	0,034 ± 0,011	2,063 ± 0,009
54	CCS	7 7-6 6	90686,381	26,1	-	-	--	--	--
55	HC3N	10-9	90979,023	24	0,036	0,001	≤ 0,019	0,060 ± 0,011	0,520 ± 0,009
56	CH3CN	50-40	91987,088	13,2	0,015	0,001	≤ 0,019	≤ 0,021	0,276 ± 0,009
57	CH3CN	51-41	91985,314	20,4	0,015	0,001	≤ 0,019	≤ 0,021	0,262 ± 0,009
58	CH3CN	5 2- 4 2	91979,994	41,9	-	-	--	--	--
59	CH3CN	5 3- 4 3	91971,130	77,6	0,005	0,001	≤ 0,019	0,280 ± 0,021	0,087 ± 0,009
60	C-13-S	2-1	92494,308	6,7	0,007	0,001	0,021 ± 0,010	≤ 0,022	0,063 ± 0,009
61	UL		92551,920		-	-	--	--	--
62	UL		92872,121		-	-	--	--	--
63	N2H+	1-0	93173,392	4,5	0,077	0,001	≤ 0,020	≤ 0,022	1,165 ± 0,009
64	CH3CHO	5 1 5 0- 4 1 4 0	93580,859	15,7	0,007	0,001	≤ 0,020	0,100 ± 0,011	0,100 ± 0,009
65	CH3CHO	5 1 5 1- 4 1 4 1	93595,276	15,8	0,007	0,001	≤ 0,020	≤ 0,022	0,088 ± 0,009
66	CCS	7 8 - 6 7	93870,107	19,9	0,006	0,001	≤ 0,020	≤ 0,022	0,114 ± 0,009
67	UL		94252,060		0,006	0,002	≤ 0,034	0,129 ± 0,019	0,074 ± 0,015
68	C-13-H3OH	2 -1 2 0-1 -1 1 0	94405,163	12,4	0,007	0,002	≤ 0,034	0,052 ± 0,019	0,070 ± 0,015
69	UL		94797,961		0,007	0,002	≤ 0,034	≤ 0,037	0,086 ± 0,015
70	CH3OH	8 0 8 +0-7 1 7 +0	95169,463	83,5	0,077	0,002	≤ 0,034	0,257 ± 0,018	0,945 ± 0,015
71	CH3OH	2 1 + 0-1 1 + 0	95914,310	21,4	0,010	0,002	≤ 0,034	0,102 ± 0,018	0,155 ± 0,015
72	CH3CHO	5 0 5 2-4 0 4 2	95947,340	13,9	0,008	0,002	≤ 0,034	0,137 ± 0,018	0,062 ± 0,015
73	CH3CHO	5 0 5 0-4 0 4 0	95963,380	13,8	0,008	0,002	≤ 0,034	≤ 0,037	0,123 ± 0,015
74	CS-34	2 0-1 0	96412,950	6,9	0,028	0,002	≤ 0,027	0,067 ± 0,015	0,261 ± 0,012
75	CH3CHO	5 2 3 0-4 2 2 0	96632,627	23	-	-	--	--	--
76	CH3OH	2 0 + 0-1 0 + 0	96741,371	7	0,214	0,002	≤ 0,027	0,560 ± 0,015	3,387 ± 0,012
77	CS-33	2-1	97172,064	7	0,005	0,002	≤ 0,027	≤ 0,030	0,082 ± 0,012
78	H2O2	10 010 3-10 110 0	97274,010	151,9	0,007	0,002	0,030 ± 0,014	≤ 0,030	0,081 ± 0,012
79	OCS	8-7	97301,209	21	-	-	--	--	--
80	CH3OH	2 1 1 -0-1 1 0 -0	97582,804	21,6	0,017	0,002	≤ 0,027	≤ 0,030	0,181 ± 0,012
81	CH3COCH3	4 3 2 0-3 0 3 1	97582,337	8,2	0,017	0,002	≤ 0,027	≤ 0,030	0,181 ± 0,012
82	S-34-O	23-12	97715,317	9,1	0,009	0,002	0,034 ± 0,014	≤ 0,030	0,183 ± 0,012
83	CS	2-1	97980,953	7,1	0,322	0,002	0,039 ± 0,014	1,121 ± 0,015	4,024 ± 0,012
84	CH3CHO	5 1 4 2 - 4 1 3 2	98863,328	16,6	0,009	0,002	0,135 ± 0,014	≤ 0,031	0,123 ± 0,013
85	CH3CHO	5 1 4 0- 4 1 3 0	98900,948	16,5	0,010	0,002	≤ 0,029	0,080 ± 0,016	0,113 ± 0,013
86	SO	23-12	99299,870	9,2	0,135	0,002	0,059 ± 0,014	0,693 ± 0,016	2,068 ± 0,013
87	UL		99362,029		0,007	0,002	≤ 0,029	≤ 0,031	0,042 ± 0,013
88	H2CCN	5 1 5 6-4 1 4 5	99689,294	27,5	-	-	--	--	--
89	UL		99730,008		-	-	--	--	--
90	UL		99794,010		-	-	--	--	--
91	CCS	8 7-7 6	99866,521	28,1	-	-	--	--	--

92	HC3N	11-10	100076,392	28,8	0,029	0,002	≤ 0,038	0,159 ± 0,021	0,441 ± 0,017
93	H2CS	3 1 3- 2 1 2	101477,810	22,9	0,013	0,002	≤ 0,038	0,070 ± 0,021	0,120 ± 0,017
94	UL		101603,079		-	-	--	--	--
95	H2CCO	5 1 4-4 1 3	101981,429	27,7	-	-	--	--	--
96	CH3CCH	6 1-5 1	102546,024	24,4	0,008	0,002	≤ 0,038	0,054 ± 0,021	0,118 ± 0,017
97	CH3CCH	6 0-5 0	102547,984	17,2	0,008	0,002	≤ 0,038	0,054 ± 0,021	0,118 ± 0,017
98	H2CS	3 2 2-2 2 1	103039,990	62,6	0,008	0,002	≤ 0,038	≤ 0,041	0,094 ± 0,017
99	H2CS	3 0 3-2 0 2	103040,220	9,9	0,008	0,002	≤ 0,038	≤ 0,041	0,095 ± 0,017
100	SO2	313-202	104029,418	7,7	0,008	0,002	≤ 0,030	≤ 0,033	0,144 ± 0,013
101	SO2	10 19-10 010	104239,295	54,7	0,007	0,002	0,032 ± 0,015	0,145 ± 0,016	0,156 ± 0,013
102	H2CS	3 1 2 - 2 1 1	104617,040	23,2	0,012	0,002	≤ 0,030	0,045 ± 0,016	0,131 ± 0,013
103	UL		105228,889		0,027	0,002	≤ 0,030	≤ 0,033	0,368 ± 0,013
104	CCS	8 9-7 8	106347,726	25	0,009	0,002	≤ 0,032	≤ 0,035	0,062 ± 0,014
105	UL		106518,955		-	-	--	--	--
106	UL		107423,933		-	-	--	--	--
107	UL		107758,094		0,008	0,002	≤ 0,032	≤ 0,035	0,071 ± 0,014
108	UL		108649,952		-	-	--	--	--
109	CH3OH	0+000-1-110	108893,963	13,1	0,015	0,002	≤ 0,030	≤ 0,033	0,198 ± 0,013
110	HC3N	12-11	109173,634	34,1	0,036	0,002	≤ 0,030	0,111 ± 0,016	0,462 ± 0,013
111	SO	32-21	109252,220	21,1	0,022	0,002	≤ 0,030	0,083 ± 0,016	0,416 ± 0,013
112	OCS	9-8	109463,063	26,3	0,007	0,002	≤ 0,030	0,044 ± 0,016	0,074 ± 0,013
113	CO-18	(1-0)	109781,915	5,3	0,137	0,002	≤ 0,030	0,065 ± 0,016	1,234 ± 0,013
114	NH2CHO	17 21517-16 31416	109808,1846	170,9	0,008	0,002	0,066 ± 0,015	≤ 0,033	0,091 ± 0,013
115	HNCO	5 0 5- 4 0 4	109905,749	15,8	0,016	0,002	≤ 0,030	≤ 0,033	0,145 ± 0,013
116	NH2D	1111-1010	110153,594	21,3	-	-	--	--	--
117	C-13-O	1-0	110201,404	5,3	0,582	0,002	≤ 0,037	≤ 0,041	5,481 ± 0,017
118	CH3CN	6 3-5 3	110364,354	82,9	-	-	--	--	--
119	CH3CN	6 2-5 2	110374,989	47,1	-	-	--	--	--
120	CH3CN	6 1-5 1	110381,372	25,7	0,012	0,002	≤ 0,037	≤ 0,041	0,217 ± 0,017
121	CH3CN	6 0- 5 0	110383,500	18,5	0,012	0,002	≤ 0,037	≤ 0,041	0,188 ± 0,017
122	D2CO	2 1 2- 1 1 1	110837,830	13,4	-	-	--	--	--
123	CH3OH	7 2 5 +0-8 1 8 +0	111289,550	102,7	-	-	--	--	--
124	UL		111319,895		0,007	0,002	≤ 0,034	≤ 0,038	0,050 ± 0,015
125	UL		111580,396		0,007	0,002	≤ 0,034	≤ 0,038	0,053 ± 0,015
126	CH3CHO	6 1 6 0-5 1 5 0	112248,728	21,1	-	-	--	--	--
127	CH3CHO	6 1 6 1-5 1 5 1	112254,524	21,2	-	-	--	--	--
128	CO-17	1-0	112359,894	5,4	0,036	0,002	≤ 0,034	≤ 0,037	0,247 ± 0,015
129	CN*	1 0 1 2 - 0 0 1 2	113191,325	5,4	0,056	0,002	≤ 0,034	0,052 ± 0,019	0,682 ± 0,015
130	UL		113307,4863		0,007	0,002	≤ 0,034	≤ 0,037	0,052 ± 0,015
131	CCS	9 8-8 7	113410,186	33,6	-	-	--	--	--
132	CN*	1023-0012	113490,985	5,4	0,137	0,002	≤ 0,034	1,514 ± 0,019	2,280 ± 0,015
133	CH3OCHO	9 3 6 2-8 3 5 2	113743,107	32,9	-	-	--	--	--
134	UL		113845,5879		0,008	0,002	≤ 0,034	≤ 0,037	0,034 ± 0,015
135	CH3CHO	6 0 6 2-5 0 5 2	114940,190	19,5	0,012	0,003	0,130 ± 0,026	0,086 ± 0,028	0,093 ± 0,023
136	CH3CHO	6 0 6 0-5 0 5 0	114959,911	19,4	-	-	--	--	--
137	UL		114988,051		0,010	0,003	≤ 0,051	≤ 0,056	0,120 ± 0,023
138	UL		115054,9023		0,010	0,003	0,122 ± 0,026	≤ 0,056	≤ 0,046

139	UL		115155,014		-	-	--	--	--
140	CO	1-0	115271,202	5,5	3,401	0,003	$1,923 \pm 0,025$	$7,656 \pm 0,028$	$38,192 \pm 0,023$
141	UL		164736,027		-	-	--	--	--
142	CH3OH*	1 1 0-1 0 0	165050,175	23,4	0,024	0,003	$\leq 0,045$	$0,250 \pm 0,025$	$0,334 \pm 0,020$
143	SO2	5 2 4-5 1 5	165144,651	23,6	0,010	0,003	$\leq 0,045$	$0,144 \pm 0,025$	$0,055 \pm 0,020$
144	SO2	7 1 7-6 0 6	165225,452	27,1	0,014	0,003	$\leq 0,045$	$0,154 \pm 0,025$	$0,265 \pm 0,020$
145	CH3CN	9 0-8 0	165569,082	39,7	0,016	0,003	$\leq 0,045$	$0,053 \pm 0,025$	$0,184 \pm 0,020$
146	CH3CN	9 1-8 1	165565,891	46,9	0,010	0,003	$\leq 0,045$	$0,045 \pm 0,025$	$0,180 \pm 0,020$
147	CH3CN	9 2-8 2	165556,322	68,4	-	-	--	--	--
148	CH3CN	9 3-8 3	165540,377	104,1	0,010	0,003	$\leq 0,040$	$0,199 \pm 0,022$	$0,087 \pm 0,018$
149	CH3OH	6 +1 5 0-6 +0 6 0	165678,770	69,9	0,022	0,003	$0,130 \pm 0,020$	$0,075 \pm 0,022$	$0,244 \pm 0,018$
150	D2CO	3 1 3-2 1 2	166102,750	21,3	-	-	--	--	--
151	CH3OH	7 1 0-7 0 0	166169,098	86,1	0,014	0,003	$\leq 0,045$	$\leq 0,049$	$0,127 \pm 0,020$
152	CCS	1312-1211	166662,354	61,8	-	-	--	--	--
153	UL		166825,948		0,011	0,003	$\leq 0,045$	$0,070 \pm 0,025$	$0,064 \pm 0,020$
154	CH3OH	8 1 0-8 0 0	166898,566	104,6	-	-	--	--	--
155	H2C-13-S	5 1 4-4 1 3	167543,379	37,3	-	-	--	--	--
156	CH3OCH3	4 2 2 0-3 1 3 0	167746,603	14,7	-	-	--	--	--
157	H2S-34	1 1 0-1 0 1	167910,516	27,8	-	-	--	--	--
158	CH3OH	9 +1 8 0-9 +0 9 0	167931,130	125,5	-	-	--	--	--
159	CH3CHO	9 1 9 0-8 1 8 0	168093,480	42,7	-	-	--	--	--
160	CH3OH	4 1 0-3 2 0	168577,831	44,3	-	-	--	--	--
161	H2S	1 1 0-1 0 1	168762,762	27,9	0,074	0,005	$0,287 \pm 0,037$	$0,272 \pm 0,040$	$0,574 \pm 0,033$
162	H2CS	5 1 5-4 1 4	169113,529	37,5	-	-	--	--	--
163	SO2	3 2 2-2 1 1	208700,336	15,3	-	-	--	--	--
164	H2CS	615-514	209200,620	48,3	-	-	--	--	--
165	HC3N	23-22	209230,234	120,6	0,023	0,007	$\leq 0,085$	$\leq 0,093$	$0,128 \pm 0,038$
166	UL		209825,717		0,024	0,007	$\leq 0,085$	$\leq 0,093$	$0,140 \pm 0,038$
167	HCCCH2OD	10 110 1-9 2 8 0	210801,080	33,8	-	-	--	--	--
168	S-34-O	5 5-4 4	211013,673	43,6	-	-	--	--	--
169	H2CO	313-212	211212,225	32,1	0,350	0,006	$0,099 \pm 0,034$	$1,305 \pm 0,037$	$3,166 \pm 0,030$
170	UL		212100,404		0,023	0,004	$\leq 0,048$	$\leq 0,053$	$0,245 \pm 0,022$
171	UL		212282,018		0,015	0,004	$\leq 0,048$	$0,097 \pm 0,027$	$0,017 \pm 0,022$
172	UL		212328,018		0,017	0,004	$\leq 0,048$	$0,063 \pm 0,027$	$0,207 \pm 0,022$
173	UL		212339,680		0,019	0,004	$\leq 0,048$	$\leq 0,053$	$0,345 \pm 0,022$
174	H2C-13-O	303-202	212811,184	20,4	-	-	--	--	--
175	CH3OH	1+100-0000	213427,118	23,4	0,023	0,004	$\leq 0,048$	$\leq 0,053$	$0,066 \pm 0,022$
176	UL		214346,852		-	-	--	--	--
177	UL		214400,130		0,018	0,004	$\leq 0,048$	$\leq 0,053$	$0,279 \pm 0,022$
178	SO	55-44	215220,653	44,1	0,064	0,004	$\leq 0,049$	$0,874 \pm 0,027$	$0,980 \pm 0,022$
179	S-34-O	5 6-4 5	215839,436	34,4	-	-	--	--	--
180	DCO+	3-2	216112,582	20,7	0,026	0,005	$\leq 0,055$	$0,122 \pm 0,030$	$0,137 \pm 0,024$
181	c-C3H2	3 3 0 0-2 2 1 0	216278,756	19,5	-	-	--	--	--
182	CCD	3 4 4-2 3 4	216373,320	20,8	0,017	0,005	$\leq 0,055$	$\leq 0,060$	$0,100 \pm 0,024$
183	H2S	2 2 0-2 1 1	216709,389	15,6	-	-	--	--	--
184	CH3OH	5140-4220	216945,521	55,9	-	-	--	--	--
185	SiO	5-4	217104,980	31,3	0,163	0,005	$0,146 \pm 0,027$	$2,403 \pm 0,030$	$2,018 \pm 0,024$

186	DCN	3 0 0- 2 0 0	217238,538	20,9	-	-	--	--	--
187	UL		217624,000		-	-	--	--	--
188	c-C3H2	6 060-5 150	217822,148	38,6	-	-	--	--	--
189	c-C3H2	5 140- 4 230	217940,046	35,4	-	-	--	--	--
190	c-C3H2	5 2 4 - 4 1 3	218160,456	35,4	-	-	--	--	--
191	H2CO	303-202	218221,989	21	0,172	0,004	≤ 0,050	0,607 ± 0,028	1,643 ± 0,022
192	CH2DOH	5 2 4 1-5 1 5 1	218316,390	58,8	-	-	--	--	--
193	HC3N	24-23	218324,723	131	-	-	--	--	--
194	CH3OH	4+220-3+120	218440,050	45,5	0,051	0,004	≤ 0,050	1,056 ± 0,028	0,472 ± 0,022
195	H2CO	322-221	218476,071	68,1	0,069	0,004	≤ 0,050	0,197 ± 0,028	0,806 ± 0,022
196	H2CO	321-220	218759,966	68,1	0,066	0,004	≤ 0,050	0,241 ± 0,027	0,640 ± 0,022
197	OCS	18-17	218903,356	99,8	-	-	--	--	--
198	UL		219158,057		0,016	0,004	≤ 0,050	≤ 0,055	≤ 0,045
199	CO-18	(2-1)	219560,033	15,8	0,323	0,004	≤ 0,050	≤ 0,055	1,557 ± 0,022
200	UL		219760,578		-	-	--	--	--
201	HNCO	10 010 - 9 0 9	219798,274	58	-	-	--	--	--
202	H2C-13-O	3 1 2-2 1 1	219908,525	32,9	0,019	0,004	≤ 0,050	2,089 ± 0,027	0,169 ± 0,022
203	SO	56-45	219949,442	35	0,118	0,004	≤ 0,050	1,095 ± 0,027	1,808 ± 0,022
204	CH2DOH	5 1 5 0-4 1 4 0	220071,805	35,8	-	-	--	--	--
205	CH3OH	8+080 - 7+160	220078,490	96,6	-	-	--	--	--
206	UL		220170,164		-	-	--	--	--
207	UL		220245,841		-	-	--	--	--
208	DNO3	11 5 6-12 211	220284,876	65,9	0,019	0,005	≤ 0,062	0,076 ± 0,034	0,101 ± 0,028
209	C-13-O	2-1	220398,677	15,9	1,121	0,005	≤ 0,062	0,234 ± 0,034	6,146 ± 0,028
210	H2CN	3 2 211 4-2 2 111 3	220421,216	68,6	0,021	0,005	≤ 0,062	0,072 ± 0,034	0,422 ± 0,028
211	CCS-34	2423-2323	220645,462	187,1	0,016	0,005	0,090 ± 0,031	0,237 ± 0,034	0,136 ± 0,028
212	CH3CN	12 3 - 13 3	220709,016	133,3	-	-	--	--	--
213	CH3CN	12 1-13 1	220743,011	76,1	-	-	--	--	--
214	CH3CN	12 0 -13 0	220747,261	68,9	-	-	--	--	--
215	D2CO	4 1 4 - 3 1 3	221191,665	32	-	-	--	--	--
216	SO2	11 111-10 010	221965,210	60,4	0,263	0,005	≤ 0,061	0,162 ± 0,034	2,786 ± 0,027
217	CH3CCH	13 1 - 12 1	222162,729	81,9	0,012	0,004	≤ 0,050	≤ 0,055	0,227 ± 0,022
218	CH3CCH	13 0 - 12 0	222166,970	74,7	0,012	0,004	≤ 0,050	≤ 0,055	0,227 ± 0,022
219	UL		222214,277		-	-	--	--	--
220	UL		222559,945		-	-	--	--	--
221	CH2DOH	5 2 4 2-4 2 3 2	223117,442	67,7	-	-	--	--	--
222	CH2DOH	5 0 5 0-4 0 4 0	223196,401	32,2	-	-	--	--	--
223	UL		224327,855		-	-	--	--	--
224	CO-17	2-1	224714,385	16,2	0,091	0,004	≤ 0,047	0,113 ± 0,026	0,440 ± 0,021
225	H2CO	312-211	225697,775	33,4	0,268	0,004	≤ 0,047	0,564 ± 0,026	2,364 ± 0,021
226	UL		226130,046		0,014	0,004	≤ 0,047	0,074 ± 0,026	0,083 ± 0,021
227	UL		226167,548		0,017	0,004	≤ 0,047	≤ 0,051	0,080 ± 0,021
228	UL		226332,328		0,014	0,004	≤ 0,047	0,256 ± 0,026	0,169 ± 0,021
229	UL		226359,603		0,014	0,004	≤ 0,047	0,123 ± 0,026	0,208 ± 0,021
230	CN	2 0 2 3 - 1 0 1 2	226659,575	16,3	0,040	0,004	≤ 0,047	0,375 ± 0,026	0,531 ± 0,021
231	CN	2 0 3 2- 1 0 2 1	226875,897	16,3	0,111	0,004	0,058 ± 0,025	0,528 ± 0,027	1,295 ± 0,022
232	S-34-O2	12 3 9-12 210	227031,881	93,1	0,013	0,004	≤ 0,050	≤ 0,054	0,038 ± 0,022

233	c-C3H2	4 320-3 210	227169,127	29,1	-	-	--	--	--
234	HC3N	25-24	227418,905	141,9	-	-	--	--	--
235	UL		228126,378		0,015	0,004	≤ 0,050	≤ 0,054	0,155 ± 0,022
236	UL		228138,033		-	-	--	--	--
237	UL		228201,706		0,015	0,004	≤ 0,050	0,072 ± 0,027	0,218 ± 0,022
238	UL		228212,097		0,013	0,004	≤ 0,050	≤ 0,054	0,221 ± 0,022
239	DNC	3-2	228910,481	22	-	-	--	--	--
240	CH3NH2	3 3 7-4 2 7	229059,714	48,2	0,013	0,004	≤ 0,050	≤ 0,054	0,027 ≤ 0,044
241	CH3OH	8-100-7070	229758,756	89,1	0,032	0,004	≤ 0,050	0,212 ± 0,027	0,346 ± 0,022
242	UL		230265,783		0,020	0,004	0,114 ± 0,025	≤ 0,055	≤ 0,045
243	CO	2-1	230538,000	16,6	4,842	0,006	3,608 ± 0,035	15,193 ± 0,038	48,662 ± 0,031
244	OCS	19-18	231060,983	110,9	-	-	--	--	--
245	UL		231202,187		0,020	0,006	≤ 0,034	≤ 0,075	0,066 ± 0,030
246	C-13-S	5-4	231220,996	33,3	-	-	--	--	--
247	CH3OH	10 2-0-9 3-0	231281,110	165,3	-	-	--	--	--
248	N2D+	3-2	231321,828	22,2	-	-	--	--	--
249	D2CO	404-303	231410,272	27,9	-	-	--	--	--
250	UL		232230,842		0,022	0,006	≤ 0,068	≤ 0,075	0,042 ≤ 0,061
251	UL		232345,986		-	-	--	--	--
252	CH3D		232644,301	11,2	0,014	0,004	≤ 0,049	≤ 0,053	0,101 ± 0,022
253	D2CO	423-322	233650,441	49,6	-	-	--	--	--
254	UL		234226,959		-	-	--	--	--
255	CH3OH	4 2 - 0-5 1 - 0	234683,370	60,9	-	-	--	--	--
256	SO2	422-313	235151,720	19	-	-	--	--	--
257	UL		235203,274		0,016	0,005	≤ 0,053	≤ 0,058	0,143 ± 0,024
258	CH3OCHO	19 614 1-18 612 2	235566,262	136,7	0,017	0,005	0,083 ± 0,027	≤ 0,058	0,104 ± 0,024
259	CC-13S	4 3 4 - 1 2 3	235996,797	12,9	-	-	--	--	--
259	D2CO	422-321	236102,086	49,8	-	-	--	--	--
260	SO2	16 115-15 214	236216,685	130,7	-	-	--	--	--
261	UL		236237,642		-	-	--	--	--
262	HO2	4 1 4 5 5-5 0 5 6 5	236267,795	58,2	0,020	0,005	≤ 0,053	0,103 ± 0,029	0,149 ± 0,024
263	HC3N	26 - 25	236512,777	153,2	-	-	--	--	--
264	H2CS	7 1 7-6 1 6	236726,770	58,6	-	-	--	--	--
265	UL		236776,017		0,019	0,005	≤ 0,061	≤ 0,067	0,145 ± 0,027
266	UL		237235,994		-	-	--	--	--
267	CH3CN	13 3-12 3	239096,497	144,6	-	-	--	--	--
268	CH3CN	13 2 -12 2	239119,504	109	0,018	0,005	≤ 0,061	≤ 0,067	0,185 ± 0,027
269	CH3CN	13 1-12 1	239133,313	87,5	-	-	--	--	--
270	CH3CN	13 0-12 0	239137,916	80,3	-	-	--	--	--
271	CH3CCH	14 1 -13 1	239247,727	93,3	-	-	--	--	--
272	CH3CCH	14 0- 13 0	239252,297	86,1	-	-	--	--	--
273	CH3OH	5 1 + 0-4 1 + 0	239746,219	49,1	-	-	--	--	--
274	H2CCO	12 112-11 111	240185,794	88	-	-	--	--	--
275	CH3OH	5 3 0- 6 2 0	240241,490	82,5	-	-	--	--	--
276	H2CS	7 0 7-6 0 6	240266,320	46,1	-	-	--	--	--
277	H2CS	7 2 6-6 2 5	240381,750	98,9	-	-	--	--	--
278	H2CS	7 3 5 - 6 3 4	240392,362	164,5	-	-	--	--	--

279	H2CS	7 3 4-6 3 3	240393,032	164,5	-	-	--	--	--
280	H2CS	7 2 5-6 2 4	240548,229	98,9	-	-	--	--	--
281	CH2DOH	7 0 7 0-6 1 6 0	240643,977	60	-	-	--	--	--
282	UL		240783,987		0,018	0,004	$0,073 \pm 0,024$	$0,108 \pm 0,026$	$0,074 \pm 0,021$
283	NCHCCO	28 524-28 425	240965,908	137,1	0,021	0,004	$\leq 0,048$	$0,139 \pm 0,026$	$0,124 \pm 0,021$
284	CS-34	5-4	241016,194	34,7	-	-	--	--	--
285	UL		241180,123		-	-	--	--	--
286	HDO	2 1 1-2 1 2	241561,550	95,2	-	-	--	--	--
287	SO2	5 2 4-4 1 3	241615,798	23,6	0,020	0,004	$\leq 0,048$	$\leq 0,052$	$0,137 \pm 0,021$
288	UL		241638,010	0,017	0,017	0,004	$\leq 0,048$	$\leq 0,052$	$0,154 \pm 0,021$
289	CH3OH*	505+0-404+0	241791,431	34,8	0,158	0,004	$0,256 \pm 0,024$	$0,793 \pm 0,026$	$2,179 \pm 0,021$
290	HNCO	11 110-12 012	242639,704	113,2	-	-	--	--	--
291	OCS	20-19	243218,040	122,6	-	-	--	--	--
292	CH2DCCH	15 114 -14 113	243637,154	99	-	-	--	--	--
293	CH3OH	514-0-413-0	243915,826	49,7	0,018	0,005	$\leq 0,057$	$\leq 0,062$	$0,236 \pm 0,025$
294	H2CS	7 1 6- 6 1 5	244048,504	60	-	-	--	--	--
295	c-C3H2	3 2 1 0-2 1 2 0	244222,133	18,2	-	-	--	--	--
296	DNO3	8 4 4-7 2 5	244251,878	36,9	-	-	--	--	--
297	SO2	14 014 -13 113	244254,218	93,9	-	-	--	--	--
298	CS	5-4	244935,557	35,3	0,129	0,005	$0,114 \pm 0,027$	$2,100 \pm 0,030$	$1,635 \pm 0,024$
299	D2CO	413-312	245532,752	34,9	-	-	--	--	--
300	HC3N	27-26	245606,320	165	-	-	--	--	--
301	CC-13S	192020-181920	245667,6478	120,9	0,019	0,005	$\leq 0,056$	$\leq 0,062$	$0,157 \pm 0,025$
302	SOO-18	8 3 5-8 2 6	246119,374	52,9	-	-	--	--	--
303	UL		246746,002		0,019	0,005	$\leq 0,056$	$\leq 0,062$	$0,114 \pm 0,025$
304	HDCO	4 1 4-3 1 3	246924,600	37,6	-	-	--	--	--
305	UL		247610,234		0,024	0,005	$\leq 0,056$	$\leq 0,061$	$0,091 \pm 0,025$
306	UL		247650,048		0,022	0,005	$\leq 0,056$	$0,085 \pm 0,031$	$0,208 \pm 0,025$
307	c-C3H2	5 2 3 0-4 3 2 0	249054,368	41	-	-	--	--	--
308	NO	3 1 3 4 - 2-1 2 3	250436,848	19,2	-	-	--	--	--
309	NO	3 1 3 3 - 2-1 2 2	250440,659	19,2	-	-	--	--	--
310	NO	3 1 3 2- 2-1 2 1	250448,530	19,2	-	-	--	--	--
311	CH3OH	11 0 11 +0-10 1 10 +0	250506,980	153,1	0,023	0,006	$\leq 0,063$	$0,099 \pm 0,034$	$0,145 \pm 0,028$
312	CH3COCH3	1410 5 0-13 9 4 0	250634,375	87,7	-	-	--	--	--
313	NO	3-1 3 4-2 1 2 3	250796,176	19,3	-	-	--	--	--
314	NO	3-1 3 3-2 1 2 2	250815,594	19,3	0,021	0,006	$\leq 0,063$	$\leq 0,069$	$0,156 \pm 0,028$
315	NO	3-1 3 2-2 1 2 1	250816,954	19,3	0,021	0,006	$\leq 0,063$	$\leq 0,069$	$0,156 \pm 0,028$
316	SO2	13 113-12 012	251199,675	82,2	-	-	--	--	--
317	SO2	8 3 5 - 8 2 6	251210,586	55,2	-	-	--	--	--
318	c-C3H2	7 0 7 0-6 1 6 0	251314,337	50,7	-	-	--	--	--
319	c-C3H2	6 2 5 0-5 1 4 0	251527,302	47,5	-	-	--	--	--
320	CH3OH	6 3 3 -0-6 2 4 +0	251738,520	98,5	0,019	0,006	$\leq 0,031$	$\leq 0,069$	$0,067 \pm 0,028$
321	CH3OH*	5 3 - 0-5 2 + 0	251811,956	84,6	-	-	--	--	--
322	SO	6 5-5 4	251825,770	50,7	0,061	0,006	$0,194 \pm 0,031$	$0,666 \pm 0,034$	$0,993 \pm 0,028$
323	CH3OH	8 3 6 +0 - 8 2 7 -0	251984,702	133,5	-	-	--	--	--
324	CH3OH	9 3 7 +0- 9 2 8 -0	252090,380	154,4	-	-	--	--	--
325	CH3OH	10 3 8 +0-10 2 9 -0	252252,850	177,6	-	-	--	--	--

326	CH3OH	11 3 9 +0 -11 2 10 -0	252485,649	203,2	-	-	--	--	--
327	UL		253220,923		0,019	0,006	≤ 0,063	≤ 0,069	0,231 ± 0,028
328	UL		253756,141		-	-	--	--	--
329	CH3NH2	6 2 7-6 1 7	253768,519	60,6	0,029	0,006	≤ 0,062	≤ 0,068	0,093 ± 0,028
330	CH3OH	200-1-10	254015,377	20,1	-	-	--	--	--
331	SO2	6 3 3 - 6 2 4	254280,536	41,4	-	-	--	--	--
332	UL		254421,899		-	-	--	--	--
333	UL		254564,747		-	-	--	--	--
334	HC3N	28-27	254699,500	177,3	-	-	--	--	--
335	c-C3H2	5 3 3 0-4 2 2 0	254987,640	41,1	-	-	--	--	--
336	OCS	21-20	255374,461	134,8	-	-	--	--	--
337	HCO-18+	3-2	255480,039	24,5	-	-	--	--	--
338	SO2	4 3 1-4 2 2	255553,303	31,3	-	-	--	--	--
339	CH2DOH	3 2 2 0-3 1 3 0	255647,816	29	-	-	--	--	--
340	HDCO	404-303	256585,430	30,8	-	-	--	--	--
341	CH2DOH	4 1 4 0-3 0 3 0	256731,552	25,2	-	-	--	--	--
342	CH3CN	14 0-13 0	257527,383	92,8	-	-	--	--	--
343	CH3CN	14 1 - 13 1	257522,427	99,9	-	-	--	--	--
344	CH3CN	14 3 - 13 3	257482,792	157,1	-	-	--	--	--
345	CH3CNH+	15 3-14 3	257630,157	163,2	0,021	0,006	≤ 0,059	≤ 0,065	0,121 ± 0,027
346	HDCO	4 2 3-3 2 2	257748,760	62,8	-	-	--	--	--
347	CH2DOH	4 2 3 1-3 1 3 2	257895,673	48	-	-	--	--	--
348	HCN-15	3-2	258157,100	24,8	-	-	--	--	--
349	SO	6 6-5 5	258255,813	56,6	0,047	0,007	≤ 0,071	1,429 ± 0,039	1,257 ± 0,032
350	CCS	2019-1918	258274,287	135,4	0,070	0,007	≤ 0,071	0,574 ± 0,039	2,025 ± 0,032
351	UL		258564,045		-	-	--	--	--
352	HC-13-N	3-2	259011,798	24,9	0,028	0,007	0,101 ± 0,036	0,347 ± 0,039	0,448 ± 0,032
353	HOONO	16 41316-15 31216	259025,703	102,1	0,034	0,007	0,121 ± 0,036	≤ 0,078	0,774 ± 0,032
354	HDCO	422-321	259034,916	62,9	0,027	0,007	≤ 0,071	≤ 0,078	0,578 ± 0,032
355	HC-13-O+	3-2	260255,339	25	-	-	--	--	--
356	SiO	6-5	260518,020	43,8	0,183	0,006	0,085 ± 0,034	2,743 ± 0,037	2,116 ± 0,030
357	HO2	4 0 4 5 4- 3 0 3 4 4	260579,539	31,3	-	-	--	--	--
358	CH3OCH3	15 510 0-15 411 0	261250,655	144,4	0,019	0,006	≤ 0,067	≤ 0,074	0,087 ± 0,030
359	HNC-13	3-2	261263,481	25,1	-	-	--	--	--
360	CH3OH	2 1 0-1 0 0	261805,675	28	-	-	--	--	--
361	SO	6 7-5 6	261843,684	47,6	0,098	0,006	0,071 ± 0,034	1,760 ± 0,037	1,914 ± 0,030
362	UL		261890,195		0,023	0,006	≤ 0,067	≤ 0,073	0,627 ± 0,030
363	CCH	3 4 3-2 3 2	262006,403	25,1	0,046	0,005	0,140 ± 0,029	0,506 ± 0,032	0,575 ± 0,026
364	HNCO	12 0 12-11 0 11	263748,625	82,4	0,019	0,005	≤ 0,058	0,094 ± 0,032	0,061 ± 0,026
365	HC3N	29-28	263791,922	190,1	-	-	--	--	--
366	CH2DOH	6 1 6 0-5 1 5 0	264017,721	48,5	-	-	--	--	--
367	CH3OH	6 +1 5 0 - 5 +2 3 0	265289,650	69,9	-	-	--	--	--
368	c-C3H2	4 4 1 0-3 3 0 0	265759,438	32,2	-	-	--	--	--
369	HCN	(3-2)	265886,180	25,5	0,648	0,005	0,120 ± 0,026	10,330 ± 0,029	14,207 ± 0,023
370	CH3OH	5+230-4+130	266838,130	57,1	0,051	0,005	0,062 ± 0,026	0,206 ± 0,028	0,463 ± 0,023
371	CH3OH	9 0 0- 8 1 0	267403,471	117,5	-	-	--	--	--
372	OCS	22-21	267530,219	147,7	-	-	--	--	--

373	HCO+	(3-2)	267557,930	25,7	0,792	0,005	0,883 ± 0,026	2,011 ± 0,028	7,945 ± 0,023
374	CH2DOH	6 0 6 0-5 0 5 0	267634,613	45	-	-	--	--	--
375	CH2DOH	6 0 6 2-5 0 5 2	267722,687	63,4	-	-	--	--	--
376	H2C-13-S	8 1 7 - 7 1 6	268012,418	71,1	-	-	--	--	--
377	HDCCO	4 1 3-3 1 2	268292,020	40,2	-	-	--	--	--
378	CH2DOH	7 2 6 0-7 1 7 0	270299,931	76,2	-	-	--	--	--
379	H2CS	8 1 8 -7 1 7	270521,931	71,6	-	-	--	--	--
380	UL		271097,896		0,043	0,006	≤ 0,058	≤ 0,063	0,065 ± 0,026
381	UL		271174,916		-	-	--	--	--
382	SO2	7 2 6-6 1 5	271529,015	35,5	-	-	--	--	--
383	UL		271749,994		-	-	--	--	--
384	HNC	3-2	271981,142	26,1	0,034	0,006	0,120 ± 0,029	0,133 ± 0,032	0,670 ± 0,026
385	CH2DOH	6 1 5 0-5 1 4 0	272098,059	49,8	-	-	--	--	--
386	HC3N	30-29	272884,734	203	-	-	--	--	--
387	UL		273014,105		0,025	0,006	≤ 0,068	≤ 0,074	0,143 ± 0,030
388	CH3CCH	16 0-15 0	273419,921	111,5	-	-	--	--	--
389	HO2	4 1 4 4 3-3 1 3 4 4	273867,541	59	0,029	0,006	0,073 ± 0,034	0,265 ± 0,037	0,395 ± 0,030
390	H2CS	8 0 8-7 0 7	274520,870	59,3	-	-	--	--	--
391	H2C-13-O	4 1 4-3 1 3	274762,112	44,8	-	-	--	--	--
392	UL		275737,129		0,020	0,006	≤ 0,062	≤ 0,034	0,062 ± 0,028
393	HCOCH2OH	15 511 0-14 410 0	275818,070	82,2	0,024	0,006	≤ 0,062	≤ 0,068	0,057 ± 0,028
394	CH3CN	15 1 - 14 1	275910,263	113,2	0,020	0,006	≤ 0,062	≤ 0,068	0,382 ± 0,028
395	D2CO	5 1 5-4 1 4	276060,243	45,2	-	-	--	--	--
396	HCOOD	4 3 2-4 2 3	276253,448	34,3	0,018	0,006	≤ 0,059	≤ 0,065	0,136 ± 0,027
397	UL		276941,911		0,019	0,006	≤ 0,059	0,101 ± 0,032	0,107 ± 0,027
398	C-13-S	6-5	277455,481	46,6	-	-	--	--	--
399	NCHCCO	25 223-24 124	277660,410	90	0,021	0,006	≤ 0,059	≤ 0,065	0,193 ± 0,026
400	UL		277761,123		-	-	--	--	--
401	UL		277899,926		0,024	0,006	≤ 0,059	≤ 0,065	0,316 ± 0,026
402	UL		277900,063		0,024	0,006	≤ 0,059	≤ 0,065	0,316 ± 0,026
403	UL		278056,137		0,020	0,006	≤ 0,059	≤ 0,065	0,176 ± 0,026
404	CH3OH	9-10- 8 00	278304,512	110	0,051	0,006	≤ 0,059	0,317 ± 0,032	0,399 ± 0,026
405	UL		278612,614		0,032	0,006	≤ 0,059	0,039 ± 0,032	0,541 ± 0,026
406	H2CS	8 1 7-7 1 6	278886,400	73,4	-	-	--	--	--
407	N2H+	3-2	279511,735	26,8	0,040	0,006	≤ 0,059	≤ 0,065	0,122 ± 0,026
408	OCS	23-22	279685,318	161,1	-	-	--	--	--
409	UL		280051,835		-	-	--	--	--
410	H2CCO	14 114 - 13 113	280195,983	113,9	0,020	0,006	≤ 0,063	0,224 ± 0,035	0,077 ± 0,028
411	CH3OCHO	26 026 2-25 125 1	280522,834	184,7	-	-	--	--	--
412	UL		280748,864		-	-	--	--	--
413	CH3OCH3	4 4 0 0-3 3 1 0	280943,497	31,6	0,017	0,005	≤ 0,056	≤ 0,061	0,224 ± 0,025
414	CH3OH	11 2 + 0-10 3 + 0	281000,109	190,9	-	-	--	--	--
415	CH3CHO	15 015 2-14 014 2	281083,430	109,2	-	-	--	--	--
416	UL		281325,531		0,019	0,005	≤ 0,056	≤ 0,061	0,069 ± 0,025
417	UL		281400,000		0,067	0,006	≤ 0,063	≤ 0,069	0,336 ± 0,028
418	H2CO	4 1 4-3 1 3	281526,929	45,6	0,421	0,006	0,110 ± 0,031	1,474 ± 0,034	3,726 ± 0,028
419	SO2	15 115-14 014	281762,600	107,5	-	-	--	--	--

420	HDCCO	15 015-14 014	281780,467	108,3	0,029	0,006	≤ 0,063	≤ 0,069	0,478 ± 0,028
421	HC3N	31-30	281976,777	216,7	-	-	--	--	--
422	SO2	6 2 4- 5 1 5	282036,566	29,2	-	-	--	--	--
423	HCS	7 0 7 7 6-6 0 6 6 6	282060,214	54,2	0,031	0,008	≤ 0,087	≤ 0,095	0,245 ± 0,039
424	H2C-13-O	4 0 4 - 3 0 3	283441,876	34,1	-	-	--	--	--
425	SO2	16 016-15 115	283464,768	121	0,040	0,008	≤ 0,087	0,466 ± 0,048	0,230 ± 0,039
426	HC3N	32-31	291068,427	230,5	-	-	--	--	--
427	H2CO	4 2 3-3 2 2	291237,780	82,1	0,116	0,006	≤ 0,057	0,185 ± 0,031	1,027 ± 0,025
428	H2CO	4 3 2-3 3 1	291380,488	140,9	0,144	0,006	≤ 0,057	0,654 ± 0,031	1,564 ± 0,025
429	CS-33	6-5	291485,935	49	-	-	--	--	--
430	D2CO	5 2 4-4 2 3	291745,750	63,6	-	-	--	--	--
431	OCS	24-23	291839,653	175,1	-	-	--	--	--
432	H2CO	4 2 2-3 2 1	291948,068	82,1	0,098	0,006	≤ 0,057	0,313 ± 0,031	0,853 ± 0,025
433	CH3OH	6 1 5 -0-5 1 4 -0	292672,890	63,7	0,036	0,006	≤ 0,057	0,134 ± 0,031	0,193 ± 0,025
434	DCOOH	6 2 4-5 1 5	292699,937	31,4	0,022	0,006	≤ 0,057	≤ 0,062	0,219 ± 0,025
435	H2C-13-O	4 1 3-3 1 2	293126,515	47	-	-	--	--	--
436	H2CN	4 2 3 3 6-3 2 2 0 6	293310,628	82,8	0,021	0,006	≤ 0,064	≤ 0,070	0,071 ≤ 0,057
437	H2CN	4 2 323 2-3 2 220 2	293414,564	82,8	-	-	--	--	--
438	CH3OH	3 2 + 0-4 1 + 0	293464,055	51,6	-	-	--	--	--
439	UL		293847,895		-	-	--	--	--
440	CS	6-5	293912,244	49,4	0,220	0,006	≤ 0,064	2,401 ± 0,035	2,605 ± 0,029
441	CH3CN	16 5-15 5	294161,001	298,8	-	-	--	--	--
442	CH3CN	16 3-15 3	294251,461	184,4	-	-	--	--	--
443	CH3CN	16 2-15 2	294279,750	148,8	-	-	--	--	--
444	CH3CN	16 1-15 1	294296,728	127,3	-	-	--	--	--
445	SO	7 6- 6 5	296550,045	64,9	-	-	--	--	--
446	D2CO	5 2 3-4 2 2	296577,045	64	-	-	--	--	--
447	UL		296655,885		-	-	--	--	--
448	C2H3NC	30 130-29 129	296670,402	223,9	-	-	--	--	--
449	UL		296688,330		-	-	--	--	--
450	SO2	9 2 8-8 1 7	298576,307	51	-	-	--	--	--
451	HCS+	7-6	298690,453	57,3	-	-	--	--	--
452	HC3N	33-32	300159,647	245,1	-	-	--	--	--
453	UL		300769,821		-	-	--	--	--
454	H2CO	4 1 3-3 1 2	300836,635	47,9	-	-	--	--	--
455	SO	7 7-6 6	301286,124	71	-	-	--	--	--
456	UL		302215,818		-	-	--	--	--
457	UL		302263,870		-	-	--	--	--
458	UL		302356,170		-	-	--	--	--
459	CH3OH	3 0 0-2-1 0	302369,773	27,1	-	-	--	--	--
460	CH3OH	12 0 + 0-11 1 + 0	302912,979	180,9	-	-	--	--	--
461	CH3OOH	13 310 5-14 212 2	303253,454	121,7	0,065	0,006	≤ 0,056	≤ 0,062	0,181 ± 0,025
462	UL		303315,871		-	-	--	--	--
463	CH3OH	1 1 0 -0-1 0 1 +0	303366,890	16,9	0,039	0,007	0,110 ± 0,033	0,160 ± 0,036	0,454 ± 0,030
464	Is a line?		303823,162		0,022	0,007	≤ 0,066	≤ 0,072	≤ 0,059
465	SiO	7-6	303926,960	58,3	0,159	0,007	≤ 0,066	2,104 ± 0,036	1,554 ± 0,029
466	SO	7 8-6 7	304077,844	62,1	0,116	0,007	0,530 ± 0,033	1,568 ± 0,036	1,801 ± 0,029

467	H ₂ COH+	5 1 5 - 4 1 4	304129,931	51,8	-	-	--	--	--
468	CH ₃ OH	2 1 1 -0-2 0 2 +0	304208,350	21,6	0,051	0,007	0,154 ± 0,033	0,205 ± 0,036	0,471 ± 0,029
469	H ₂ CS	9 1 9 - 8 1 8	304305,975	86,2	-	-	--	--	--
470	UL		304494,064		-	-	--	--	--
471	DNC	4-3	305206,219	36,6	-	-	--	--	--
472	UL		305404,007		-	-	--	--	--
473	CH ₃ OH	3 1 2 -0-3 0 3 +0	305473,520	28,6	0,066	0,008	≤ 0,075	0,287 ± 0,041	0,672 ± 0,033
474	UL		305830,093		-	-	--	--	--
475	CH ₃ OCHO	11 3 9 0-10 110 0	306292,438	45	-	-	--	--	--
476	D ₂ CO	5 1 4-4 1 3	306398,012	49,6	-	-	--	--	--
477	CH ₃ OH	4 1 3 -0-4 0 4 +0	307165,940	38	0,056	0,006	≤ 0,060	0,378 ± 0,033	0,455 ± 0,027
478	HCOCN	14 213-13 112	307224,324	60,7	0,021	0,006	≤ 0,060	0,080 ± 0,033	0,258 ± 0,027
479	HD ₂ CO	5 1 5-4 1 4	308418,200	52,4	-	-	--	--	--
480	N ₂ D+	4-3	308422,222	37	-	-	--	--	--
481	CH ₃ OH	5 1 4 -0-5 0 5 +0	309290,400	49,7	0,045	0,006	≤ 0,056	0,136 ± 0,031	0,481 ± 0,025
482	CH ₃ OH	3 +1 2 0 - 2 +0 2 0	310193,000	35	-	-	--	--	--
483	UL		311790,935		-	-	--	--	--
484	C ₂ H ₅ O ₂ CH	30 426 0-29 227 0	311796,665	134,7	-	-	--	--	--
485	CH ₃ OH	6 1 5 -0-6 0 6 +0	311852,640	63,7	-	-	--	--	--
486	CH ₂ DOH	7 0 7 0-6 0 6 0	311966,026	60	-	-	--	--	--
487	HCCCH ₂ OD	19 614 1-20 516 0	312086,283	133,6	-	-	--	--	--
488	SO ₂	17 117-16 016	313660,850	136,1	-	-	--	--	--
489	CH ₃ OH	7 1 - 0-7 0 + 0	314859,528	80,1	-	-	--	--	--
490	CH ₃ OH	6 2 0-5 1 0	315266,861	71	-	-	--	--	--
491	HC-13-O ₂ H	7 3 4-7 2 5	318872,427	58	0,028	0,009	≤ 0,084	≤ 0,092	≤ 0,075
492	HD ₂ CO	5 0 5-4 0 4	319769,680	46,2	0,030	0,009	0,146 ± 0,042	≤ 0,092	0,168 ± 0,037
493	UL		320332,025		0,043	0,012	≤ 0,118	0,101 ± 0,065	0,374 ± 0,053
494	UL		320808,830		0,037	0,012	≤ 0,118	0,271 ± 0,065	≤ 0,105
495	CH ₃ CHO	10 4 6 0-10 3 7 0	328607,492	87,1	-	-	--	--	--
496	UL		328671,883		-	-	--	--	--
497	UL		328688,066		0,078	0,021	≤ 0,196	0,228 ± 0,107	0,256 ± 0,088
498	CO-18	3-2	329330,545	31,6	0,189	0,021	≤ 0,196	≤ 0,215	0,642 ± 0,088
499	HONO	14 312 0- 13 311 0	330281,232	153,8	0,049	0,013	≤ 0,121	0,276 ± 0,066	0,140 ± 0,054
500	UL		330309,980		0,049	0,013	≤ 0,121	0,190 ± 0,066	0,141 ± 0,054
501	CH ₃ OCHO	10 8 2 0-9 7 3 0	330323,938	74,9	0,041	0,013	≤ 0,121	0,368 ± 0,066	≤ 0,109
502	C ₂ H ₃ CN	11 3 8 010 - 10 2 9 010	330373,191	49,5	0,043	0,013	≤ 0,121	≤ 0,133	0,231 ± 0,054
503	UL		330534,379		-	-	--	--	--
504	C-13-O	3-2	330587,960	31,7	1,024	0,013	1,166 ± 0,061	0,732 ± 0,066	4,565 ± 0,054
505	D ₂ CO	6 1 6-5 1 5	330674,796	61,1	-	0,013	--	--	--
506	UL		330689,887		0,121	0,013	0,152 ± 0,061	≤ 0,133	1,768 ± 0,054
507	UL		330706,789		0,093	0,013	0,210 ± 0,061	≤ 0,133	1,164 ± 0,054
508	CH ₃ CN	18 2-17 2	331046,096	179,5	-	-	--	--	--
509	CH ₃ OH	11 1 - 0-11 0 + 0	331502,319	169	-	-	--	--	--
510	SO ₂	4 3 1-3 2 2	332505,242	31,3	-	-	--	--	--
511	NH ₂ D	1 0 1 1 0-0 0 0 1 1	332780,945	16,6	-	-	--	--	--
512	HD ₂ CO	5 1 4-4 1 3	335096,739	56,2	-	-	--	--	--
513	CH ₃ OH	7 1 + 0 - 6 1 + 0	335582,017	79	-	-	--	--	--

514	UL		336799,688	-	-	--	--	--	--
515	UL		336826,194	0,076	0,009	≤ 0,082	≤ 0,090	0,218 ± 0,037	--
516	CH3OH	12 1 - 0-12 0 + 0	336865,149	197,1	-	-	--	--	--
517	CO-17	3-2	337061,130	32,4	0,077	0,009	≤ 0,082	≤ 0,090	0,292 ± 0,037
518	CS-34	7-6	337396,690	64,8	-	-	--	--	--
519	UL		337782,039	-	-	--	--	--	--
520	H2CS	10 110-9 1 9	338083,195	102,4	-	-	--	--	--
521	CH3OH*	7 0 + 0-6 0 + 0	338408,698	65	0,086	0,009	≤ 0,085	0,462 ± 0,047	0,697 ± 0,038
522	SO	3 3-2 3	339341,459	25,5	-	-	--	--	--
523	UL		339660,008	-	0,042	0,011	≤ 0,099	≤ 0,108	≤ 0,088
524	CN*	3 0 3 4 - 2 0 2 3	340031,549	32,7	-	-	--	--	--
525	CN*	3 0 4 4-2 0 3 3	340247,770	32,7	0,089	0,011	0,216 ± 0,049	0,603 ± 0,054	0,667 ± 0,044
526	CH2NH	3 1 3 3-2 0 2 3	340353,0513	25,5	0,036	0,011	0,107 ± 0,049	≤ 0,108	0,182 ± 0,044
527	HCO-18+	4-3	340630,692	40,9	-	-	--	--	--
528	SO	8 7-7 6	340714,155	81,2	0,041	0,011	≤ 0,099	0,546 ± 0,054	0,431 ± 0,044
529	DNO3	14 7 8-14 411	340733,410	103	0,037	0,011	≤ 0,099	≤ 0,108	0,967 ± 0,044
530	HCCCH2OD	10 3 7 1-10 2 9 0	340747,655	44,3	0,041	0,011	≤ 0,099	≤ 0,108	0,856 ± 0,044
531	CH3OH	7 1 - 0 - 6 1 - 0	341415,615	80,1	-	-	--	--	--
532	D2CO	6 0 6 - 5 0 5	342522,445	58,1	-	-	--	--	--
533	HDCCO	18 117 - 17 116	342729,742	165,2	-	-	--	--	--
534	CS	7-6	342882,850	65,8	0,082	0,011	0,283 ± 0,051	1,280 ± 0,056	1,048 ± 0,045
535	UL		342918,742	-	0,084	0,011	≤ 0,101	0,336 ± 0,056	1,625 ± 0,045
536	H2CS	10 010- 9 0 9	342944,369	90,6	-	-	--	--	--
537	H2C-13-O	5 1 5 - 4 1 4	343325,713	61,3	-	-	--	--	--
538	UL		343796,109	-	0,081	0,011	≤ 0,101	≤ 0,111	0,381 ± 0,045
539	UL		343879,078	-	-	-	--	--	--
540	UL		343904,063	-	-	-	--	--	--
541	HCNO	15-14	344014,004	132,1	-	-	--	--	--
542	SO	8 8-7 7	344310,612	87,5	-	-	--	--	--
543	C2H3CHO	15 313 0-14 212 0	344340,801	69,8	0,054	0,016	≤ 0,150	≤ 0,165	≤ 0,134
544	SO2	13 212- 12 111	345338,538	93	-	-	--	--	--
545	HC-13-N	4-3	345339,769	41,4	-	-	--	--	--
546	UL		345688,051	-	0,057	0,016	≤ 0,150	1,203 ± 0,082	0,164 ± 0,067
547	CO	3-2	345795,990	33,2	6,073	0,016	10,445 ± 0,075	39,563 ± 0,082	75,136 ± 0,067
548	UL		345912,164	-	-	-	--	--	--
549	UL		345970,453	-	-	-	--	--	--
550	UL		346060,031	-	0,061	0,016	≤ 0,146	0,251 ± 0,080	≤ 0,131
551	UL		346096,195	-	-	-	--	--	--
552	SO	8 9-7 8	346528,481	78,8	0,084	0,016	0,187 ± 0,073	1,388 ± 0,080	1,131 ± 0,065
553	C2H3NC	14 312-14 113	346540,163	71,7	0,066	0,016	0,153 ± 0,073	0,794 ± 0,080	1,741 ± 0,065
554	HC-13-O+	4-3	346998,336	41,6	-	-	--	--	--
555	SiO	8-7	347330,579	75	-	-	--	--	--
556	HNC-13	4-3	348340,270	41,8	-	-	--	--	--
557	C2H5OH	14 312 2-13 211 2	347350,929	99,7	0,118	0,016	≤ 0,146	≤ 0,160	≤ 0,131
558	UL		348758,961	-	-	-	--	--	--
559	CCH	4 5 5-3 4 4	349337,706	41,9	-	-	--	--	--

Chapter 5

The jet of Cep E

5.1 The jet molecular tracers

Over all the unbiased spectral survey some species present line profiles with a broad wing component that starts at the ambient cloud velocity ($V_{LSR} = -10.9 \text{ km s}^{-1}$) and extends towards the red in the case of the offset position (0, 0) and towards the blue in south position (-12, -18). This wing component decreases gradually in intensity until it merges at high velocities in the spectrum as a separate secondary peak of intensity.

For example, Figures 5.1 and 5.2 show the CO 1 - 0 to 4 - 3 and SiO 2 - 1 to 8 - 7 spectra towards the central position and the south outflow lobe. The observed profiles have emission up to high velocities ($\sim 100 \text{ km s}^{-1}$ from the rest velocity). As we already mention in chapter 4, from the line profiles it can be distinguish clearly two kinematical components, in addition to the ambient velocity one: i) wing emission, observed especially in the CO lines, prominent at velocities lower than $\sim 40 \text{ km s}^{-1}$ from the rest velocity; ii) high velocity emission, particularly bright in the SiO lines compared to the ambient and wing emission, at velocities larger than $\sim 40 \text{ km s}^{-1}$ from the rest velocity. This emission is relatively weak and broad between ~ -80 and $\sim -20 \text{ km s}^{-1}$ and much more intense and evident in the velocity range $30 - 80 \text{ km s}^{-1}$. Note that the contribution of the CO wing emission at velocities $\geq 30 \text{ km s}^{-1}$ decreases with increasing J: at J=4 there is almost no trace of CO wing

emission. Analogously, for the southern lobe (offset $-12''$, $-18''$), the gas forms a broad wing of relatively slow gas that start at the ambient cloud velocity and decrease smoothly towards the negative velocities up to find a secondary intensity peak centered about -125 km s^{-1} . Similar (wing and high velocity) components have been observed in several sources and are usually considered as due to the entrained gas and the high velocity jet respectively [Bachiller et al., 2001]; [Jørgensen et al., 2007]; [Santiago-García et al., 2009]; [Hirano et al., 2010].

For the analysis, we separate the wing emission in moderate velocity (MV) and high velocity (HV) components towards the central position and in extremely high velocity (EHV) component for the south position. Adopted velocity ranges are listed in Table 5.1 and illustrated in Fig 4.9. Note that in the table, the MV and HV components are label 'north' because the gas emission from these components traces the north ejection of material. Similarly, the EHV component is labeled 'south'.

At the central position we could detected CO, SiO, HCO⁺, HCN and SO emission coming from the North-MV and North-HV components (see Figs 5.1 to 5.5). On the contrary, only CO, HCO⁺ and HCN have been detected in the South-EHV component. Table 5.1 summarizes the situation.

At the central position, the SiO present the brightest emission from the North MV and HV components with peak intensities about 0.35 K from J transitions between 2 and 8 (See Figure 5.2). Our observations show that in both positions the HCO⁺ emission has a line profile similar to the CO line profile, with intensities in the North-HV component around 0.15 K. On the contrary, at the offset position (-12 , -18) SiO does not shows clearly the presence of a jet, but only a prominent wing component.

Table 5.1: Velocity components.

Velocity Component	Velocity range (km s^{-1})	Position ($''$, $''$)	Physical component	Detected species
North-MV	30 to 45	0,0	north cavity	CO, SiO, HCO ⁺ , HCN, SO
North-HV	50 to 80	0,0	north jet	CO, SiO, HCO ⁺ , HCN, SO
South-EHV	-150 to -100	-12,-18	south jet	CO, HCO ⁺ , HCN

Other molecules like SO presents important emission also around 0.2 K for the North-HV peak emission at central position (See figure 5.5).

As discussed by other authors (e.g. [Tafalla et al., 2010]), even a single velocity component may mask more than one physical component and only high resolution observations can help to fully disentangle the different physical components in the line of sight. To this end, the CO high spatial resolution channel map, obtained with the IRAM Plateau de Bure Interferometer (Lefloch et al. in preparation) and shown in Fig. 4.1, is of great help in understanding the origin and nature of the emission observed with the single-dish reported in the present work. (See section 4.2 to see a description of the maps.)

Table 5.2 lists the detected lines for each species and their integrated emission in the North-MV, North-HV and South-EHV velocity interval components

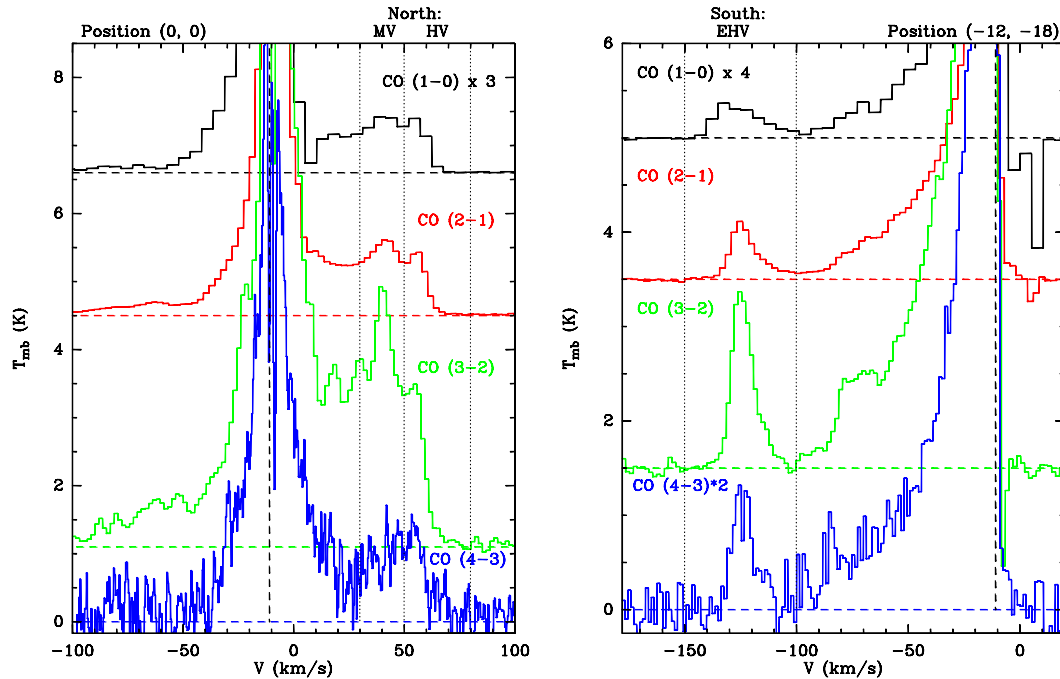


Figure 5.1: Spectra of the CO emission lines observed toward both positions. At the *left* (0,0) position, and at the *right* the (-12,-18) position. In both panels the spectra of lowest transition were observed with IRAM-30m telescope and transition CO (4 -3) were observed with CSO for the (0,0) offset and with JCMT for the offset (-12,-18). Intensities are in units of antenna temperature (K). A vertical offset is added to each emission line to help the comparison. The vertical *dotted lines* show the velocity range where appear the EHV component associated with the jet. (See the text).

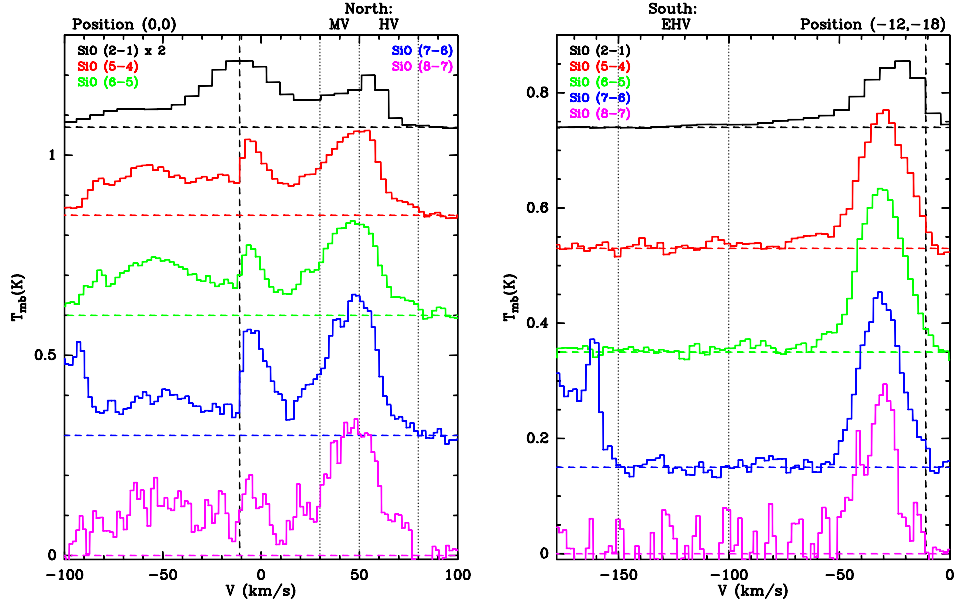


Figure 5.2: SiO jet emission from both; the source and bowshock positions. A vertical offset is added to each emission line to help the comparison. The vertical *dotted lines* show the velocity range components.

respectively. Note that the table lists also the J=12–11 and 13–12 transitions observed towards the south jet by [Gómez-Ruiz et al., 2012]. On the contrary, the table does not report the SO transition at 261.843 GHz because of the presence of one methanol line in the North-MV interval.

Finally, the profiles of selected lines in the 201–267 GHz interval, zoomed around the North-MV, North-HV and South-EHV velocity intervals, are shown in Fig. 5.6. Towards the central position, CO and HCO⁺ have very similar spectra profile with (little) contribution from the wings, while SiO and SO profiles are rather dominated by the North-MV and North-HV components. HCN, on the contrary, presents a very important contribution from the wing component. In the case of SiO, the lines in the North-MV and North-HV components are even brighter than those from the ambient velocity. Clearly, SiO is the best tracer of the North-MV and North-HV components. Surprising enough, however, SiO is very weak in the South-EHV component towards the south jet.

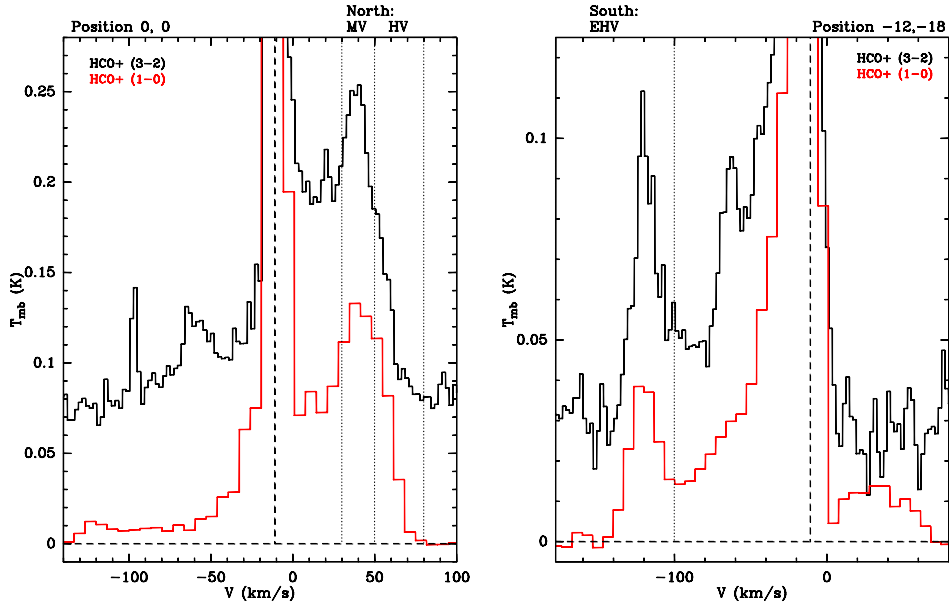


Figure 5.3: HCO⁺ jet emission from both; the source and bowshock positions. A vertical offset is added to each emission line to help the comparison. The vertical *dotted lines* show the velocity range components.

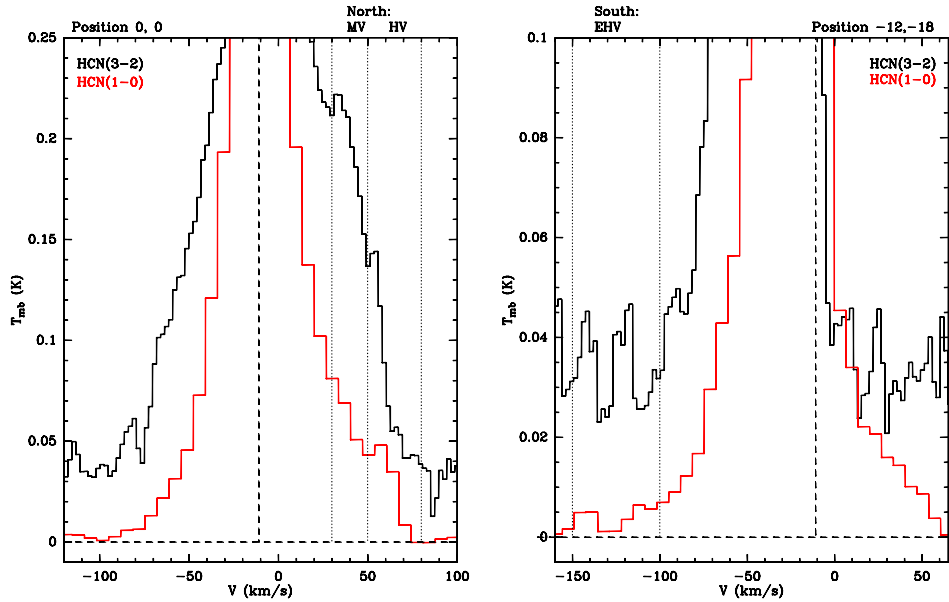


Figure 5.4: HCN jet emission from both; the source and bowshock positions. A vertical offset is added to each emission line to help the comparison. The vertical *dotted lines* show the velocity range components.

Table 5.2: Integrated flux intensities between 30 to 45 km s⁻¹(MV component) and 50 to 80 km s⁻¹(HV component) towards the central position, and between -100 to -150 km s⁻¹towards the south outflow lobe (EHV component).

Frequency (MHz)	Trans.	E_{up} (K)	HPBW (arcsec)	North jet		South jet
				$\int_{30}^{45} T_{mb}dV$ (K km s ⁻¹)	$\int_{50}^{80} T_{mb}dV$ (K km s ⁻¹)	$\int_{-100}^{-150} T_{mb}dV$ (K km s ⁻¹)
CO						
115271.2	1-0	5.5	21.1	3.7 ± 0.4	2.9 ± 0.3	2.3 ± 0.3
230537.9	2-1	16.6	10.6	21.8±4.4	15.1±3.0	9.5 ± 1.9
345795.9	3-2	33.2	7.0	46.4±13.9	24.6±7.4	24.4± 7.3
461040.8	4-3	55.4	20.0	13.7±4.3	16.2±5.1	20.35± 7.0
1381995.1	12-11	431.3	21.7	–	–	6.0± 1.0
1496922.9	13-12	503.1	20	–	–	4.8± 1.0
¹³ CO						
220398.7	2-1	15.9	11.0	0.5± 0.1	0.4 ± 0.1	≤ 0.2
330589.0	3-2	31.7	7.4	1.0± 0.3	≤ 0.6	≤ 0.25
SiO						
86847.0	2-1	6.3	28.0	0.6 ± 0.1	0.9±0.1	≤ 0.1
217105.0	5-4	31.3	11.2	2.5± 0.5	2.9±0.6	≤ 0.3
260518.0	6-5	43.8	9.3	2.9±0.6	3.1±0.6	≤ 0.4
303927.0	7-6	58.4	8.0	3.8±1.1	4.0±1.2	≤ 0.3
347330.6	8-7	75.1	7.0	3.7±1.1	4.2±1.3	≤ 1.0
HCO ⁺						
89188.5	1-0	4.3	27.3	1.9± 0.2	1.4±0.2	1.0 ± 0.1
267557.9	3-2	25.7	9.1	2.5± 0.5	1.1±0.3	1.4 ± 0.3
HCN						
88632.1	1-0	4.3	27.4	1.0± 0.1	0.8±0.1	0.20 ± 0.04
265886.1	3-2	25.5	9.1	2.6± 0.5	1.3±0.3	≤ 0.25
SO						
86093.9	2 ₂ -1 ₁	19.3	28.3	0.07± 0.01	0.10±0.02	≤ 0.1
99299.9	2 ₃ -1 ₂	9.2	24.5	0.30± 0.05	0.40±0.07	≤ 0.1
109252.2	3 ₂ -2 ₁	21.1	22.3	0.10± 0.03	0.15±0.05	≤ 0.1
215220.6	5 ₅ -4 ₄	44.1	11.3	0.8± 0.2	1.1±0.2	≤ 0.2
219949.4	5 ₆ -4 ₅	35	11.1	1.8± 0.4	1.4±0.3	≤ 0.25
251825.8	6 ₅ -5 ₄	50.7	9.7	1.2± 0.2	1.0±0.2	≤ 0.4
258255.8	6 ₆ -5 ₅	56.6	9.4	1.0± 0.2	1.0±0.3	≤ 0.4
304077.8	7 ₈ -6 ₇	62.1	8.0	1.7± 0.5	1.7±0.5	≤ 1.0
340714.1	8 ₇ -7 ₆	81.2	7.1	1.6± 0.5	1.1±0.4	≤ 0.9
346528.5	8 ₉ -7 ₈	78.8	7.0	2.1± 0.7	1.3±0.5	≤ 1.5

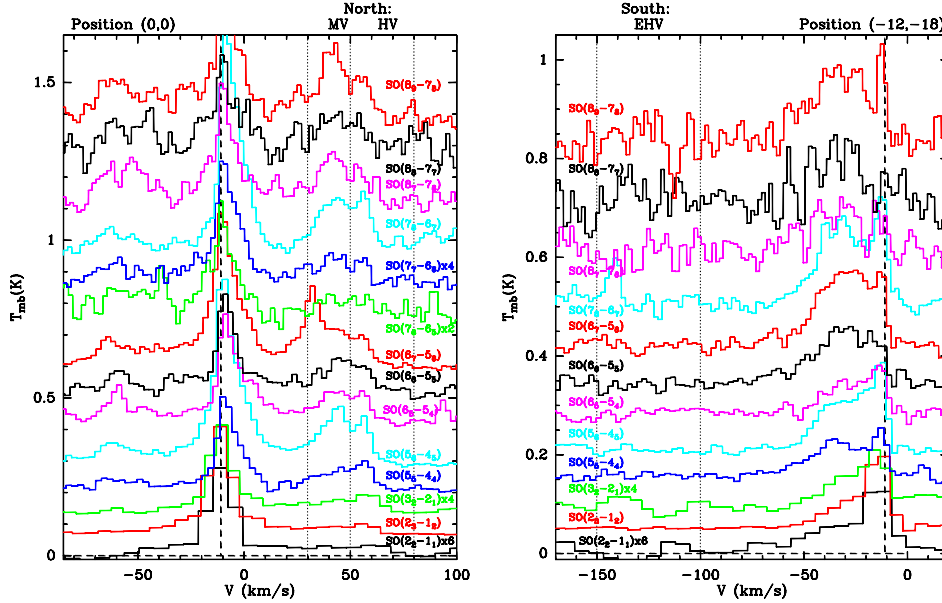


Figure 5.5: SO jet emission from both; the source and bowshock positions. A vertical offset is added to each emission line to help the comparison. The vertical *dotted lines* show the velocity range components.

5.2 Derivation of the column density

5.2.1 Rotational diagrams

We start with a first level of analysis, by means of a rotational diagram analysis, performed using the CASSIS package (Centre d'Analyse Scientifique de Spectres Infrarouges et Submillimétriques; <http://cassis.cesr.fr>). For this analysis, the line emission was integrated between 30 and 80 km s^{-1} (North MV+HV component) for each line. The analysis gives as result the column densities ranging from 6.6×10^{12} for the HCN to $1.2 \pm 0.1 \times 10^{16}$ for the CO. The rotational temperatures cover a range between 10 to 30 K (See table 5.3). The analysis was carried out taking into account a beam dilution correction for a source size of $\sim 3'' \times 3''$.

In figures 5.7 and 5.8 are shown the rotational diagrams for the molecules that present emission from the jet.

Figure 5.6: (*left*) CO, SiO, HCN, HCO⁺ and SO spectra at (0,0) offset with detected jet emission at high velocities. *Vertical dash line* marks the ambient cloud velocity ($\sim -10.9 \text{ km s}^{-1}$), and *vertical dotted lines* mark the velocities at 30, 50 and 80 km s^{-1} . In the range 30 to 45 km s^{-1} we have the moderate velocity component of the north jet (North-MV), and between 50 to 80 km s^{-1} we have the high velocity component (North-HV). (*right*) The same molecular transitions at (-12,-18) offset. Unlike the spectra on the left, only CO and HCO⁺ spectra show clearly detected jet emission at South-EHV. *Vertical dotted lines* mark the velocity limits between -100 and -150 km s^{-1} .

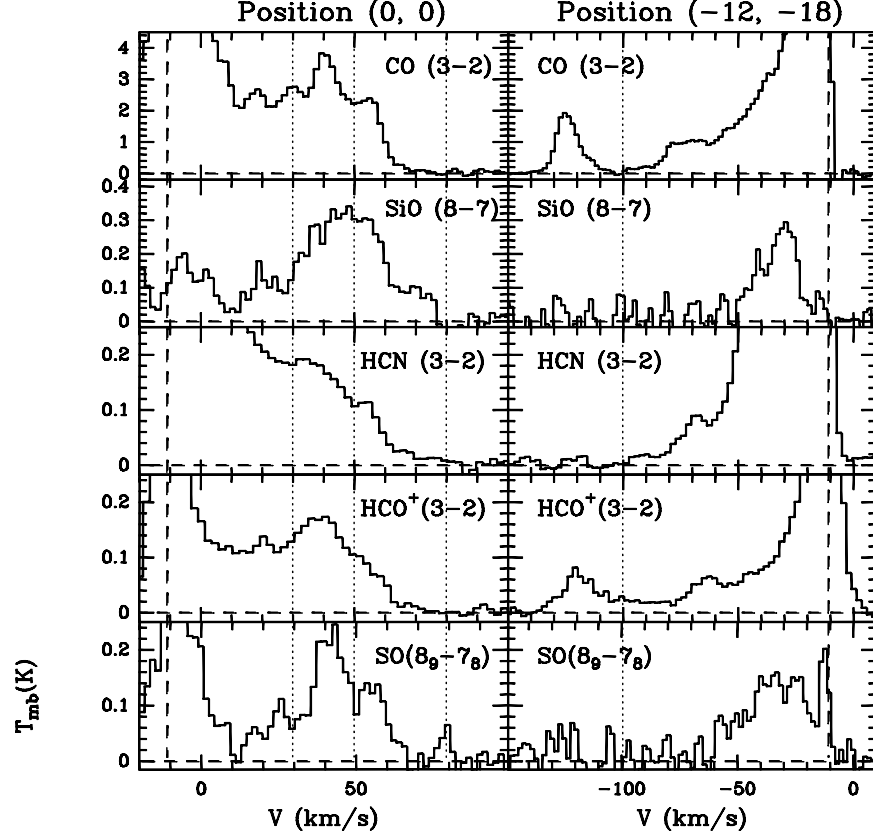


Table 5.3: Molecular column densities and rotational temperatures derived by interpreting the emission between 30 to 80 km s^{-1} (MV and HV components together). The abundances are expressed with respect to H₂ and CO-normalized, i.e. $X_{4}^{\text{CO}} = N/N_{\text{CO}} \times 10^4$. The beam dilution correction was performed considering a source size of $3'' \times 3''$.

Molecule	N (cm^{-2})	T _{ex} (K)	X ₄ ^{CO}
CO	$1.2 \pm 0.1 \times 10^{16}$	17_{-1}^{+2}	1×10^4
SiO	$1.1_{-0.3}^{+0.4} \times 10^{13}$	16_{-2}^{+3}	9.2_{-3}^{+4}
SO	$3.1_{-0.4}^{+0.5} \times 10^{13}$	27_{-1}^{+2}	25.8_{-5}^{+6}
HCO ⁺	9.6×10^{12}	10 ± 4	8
HCN	6.6×10^{12}	10 ± 3	5.5

Figure 5.7: Rotational diagrams of CO and SiO molecules. The *squares* are the data and the red line are the fit. In some cases the error bar is smaller than the symbol. The resulting column density and rotational temperature are listed in table 5.3.

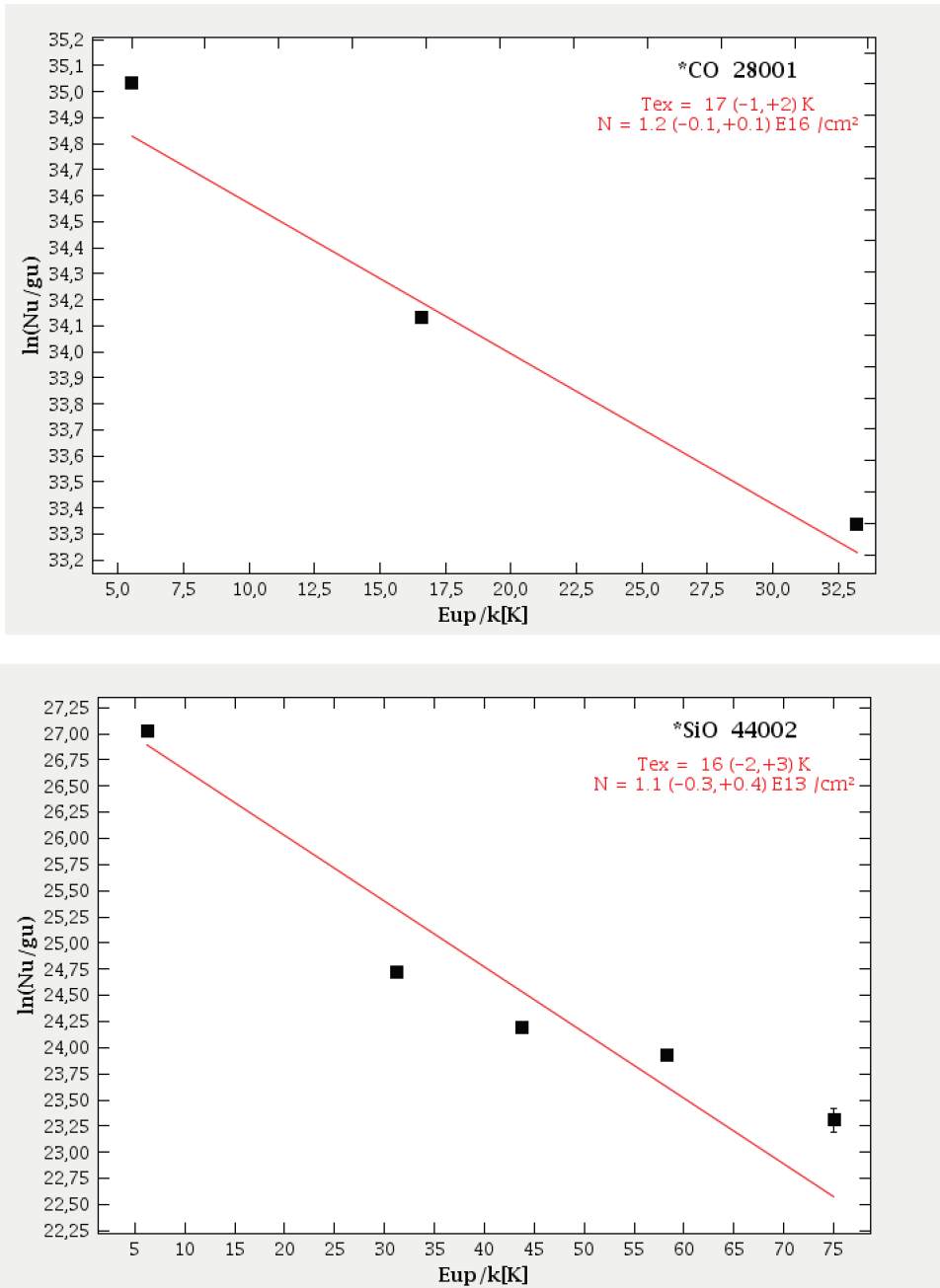


Figure 5.8: Rotational diagrams of SO, HCO⁺ and HCN molecules. The *squares* are the data and the red line are the fit. In some cases the error bar is smaller than the symbol. The resulting column density and rotational temperature are listed in table 5.3.

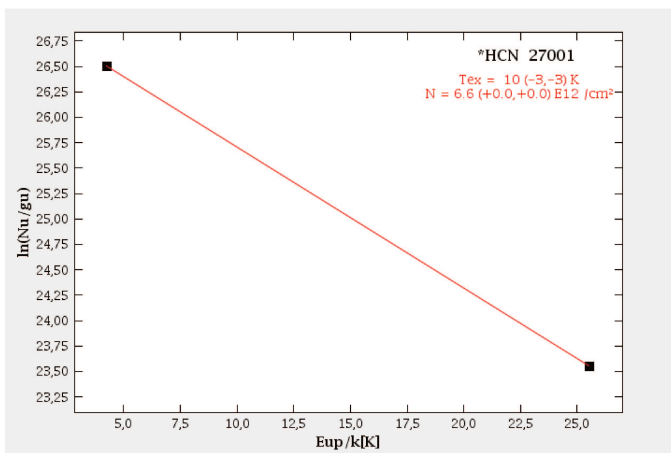
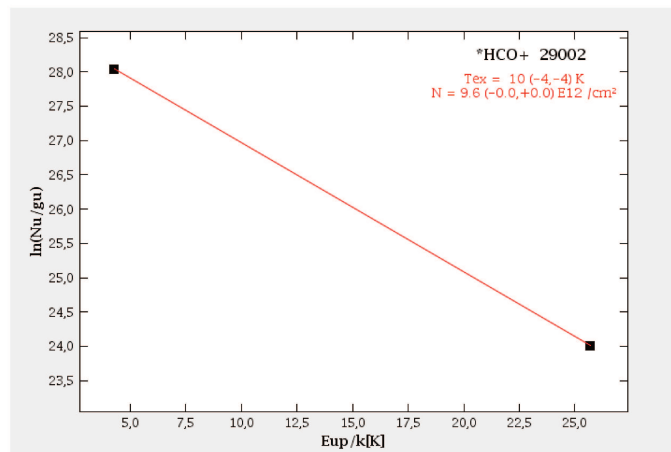
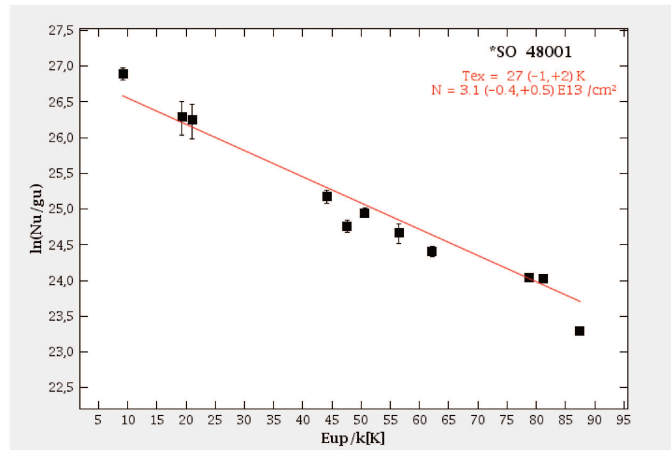


Table 5.4: Temperature, density and sizes of the velocity components of Tab. 5.1.

	Comp.	T (K)	n (cm^{-3})	size (arcsec)
North-MV	I	~ 20	$\sim 3 \times 10^5$	5
	II	100–200	$2\text{--}4 \times 10^6$	4
North-HV	I	~ 30	$\sim 3 \times 10^5$	4
	II	100–200	$2\text{--}4 \times 10^6$	3
South-EHV	I	50–80	1×10^5	2
	II	300–400	2×10^6	2

5.2.2 Non-LTE LVG analysis

Once we had a general idea about the column densities and rotational temperatures, we carried out a detail analysis using the non-LTE Large Velocity-Gradient code described in [Ceccarelli et al., 2003]. The code was adapted to take into account the emission from a jet for the analysis of the North-HV and South-EHV components, whereas it uses a standard circular gaussian source for the analysis of the North-MV component. Specifically, the filling factor in the case of an infinite jet with a transversal size j_a observed with a telescope beam HPBW is j_a/HPBW . The collisional coefficients are taken from Yang et al. (2010) for CO, Turner et al. (1992) for SiO, Flower (1999) for HCO^+ , Dumouchel et al. (2010) for HCN and Green (1994) for SO.

We obtained a grid of models, where we varied the gas density and temperature, the species column density and the sizes of the source and jet, covering a large parameter space. We then best fitted the observations against the model predictions.

The results of the fits in the North-MV, North-HV and South-EHV components are reported in Tabs. 5.4 and 5.5. In the next sections, we will discuss in detail how they have been obtained and the results.

Table 5.5: Column densities and abundances. Note: the abundances are computed assuming a CO abundance with respect to the H₂ of 10⁻⁴.

Species	Comp.	N _x (cm ⁻²)	N _x /N _{CO}	N _x /N _{H2} ^a
North-MV component				
CO	I	5×10 ¹⁶	1.0	1×10 ⁻⁴
	II	1×10 ¹⁷	1.0	1×10 ⁻⁴
SiO	I	3×10 ¹³	6×10 ⁻⁴	6×10 ⁻⁸
	II	2×10 ¹³	2×10 ⁻⁴	2×10 ⁻⁸
SO	I	1×10 ¹⁴	2×10 ⁻³	2×10 ⁻⁷
	II	1×10 ¹⁴	1×10 ⁻³	1×10 ⁻⁷
HCN	I	5×10 ¹³	1×10 ⁻³	1×10 ⁻⁷
	II	3×10 ¹²	3×10 ⁻⁵	3×10 ⁻⁹
North-HV component				
CO	I	1.5×10 ¹⁶	1.0	1×10 ⁻⁴
	II	2×10 ¹⁶	1.0	1×10 ⁻⁴
SiO	I	8×10 ¹²	5×10 ⁻⁴	5×10 ⁻⁸
	II	1×10 ¹³	5×10 ⁻⁴	5×10 ⁻⁸
SO	I	2×10 ¹³	3×10 ⁻³	1×10 ⁻⁷
	II	4.5×10 ¹³	2×10 ⁻³	2×10 ⁻⁷
HCN	I	6×10 ¹²	4×10 ⁻⁴	4×10 ⁻⁸
	II	2×10 ¹²	1×10 ⁻⁴	1×10 ⁻⁸
South-EHV component				
CO	I	4×10 ¹⁶	1.0	1×10 ⁻⁴
	II	2×10 ¹⁶	1.0	1×10 ⁻⁴
HCO ⁺	I	1×10 ¹³	3×10 ⁻⁴	3×10 ⁻⁸
	II	≤ 2 × 10 ¹²	≤ 1 × 10 ⁻⁴	≤ 1 × 10 ⁻⁸
HCN	I	6×10 ¹²	2×10 ⁻⁴	2×10 ⁻⁸
	II	≤ 5 × 10 ¹¹	≤ 2 × 10 ⁻⁵	≤ 2 × 10 ⁻⁹

5.2.3 North-MV component

To find the best fit solution, we adopted the following strategy for the North-MV component: 1) we first tried to best fit the observed SiO lines¹ with a single physical component; 2) the fit was not good enough and, therefore, we best fitted the SiO data with two physical components, where we fitted simultaneously the

¹We used the SiO rather than the CO lines because the SiO lines are sensitive to higher densities than the CO lines can probe. Consequently, a fit with the CO lines would miss the high density gas probed by the high J SiO lines.

SiO and SO lines, to limit the degeneracy in the parameter space; 3) we then fit the other species by using the same two physical components derived in step 2.

As shown in Fig. 5.9, one single component does not fit all the observed SiO lines. In practice, while the J=5 to 8 lines are well fitted by a gas with a density of $2 - 4 \times 10^6 \text{ cm}^{-3}$ and temperature 100–200 K, the 2-1 line requires the presence of colder and less dense gas. This second component is well constrained when considering together the SiO and SO emission. With this further constraint, the gas of the second component has a density ($3 \times 10^5 \text{ cm}^{-3}$) and a temperature ~ 20 K. The warm component covers about $4''$ while the cold one is slightly more extended, $5''$. These two components fit fairly well also the CO and HCN emission. Conversely, the HCO^+ emission cannot be fitted by neither of the two components, as it requires a less dense gas, of less than $\sim 5 \times 10^4 \text{ cm}^{-3}$. Looking at the HCO^+ spectra (Fig. 5.6), it is likely that this is because the HCO^+ North-MV line is largely contaminated by the entrained gas component. In the following, unfortunately, we will not consider any further, therefore, the HCO^+ case.

The warm and dense component has a size of $4''$ in good agreement with the dimensions of the cavity shown by the map of Fig. 4.1. We conclude that this physical component, the one marked II in the Tab. 5.5, describes the physical and chemical conditions in the cavity created at the base of the north jet. On the contrary, the component I probably describes the physical and chemical conditions of the entrained gas at large scale.

From a chemical point of view, we remark the following. First, both the SiO/CO and SO/CO abundance ratios are similar, within a factor 3, in the component II, associated with the cavity, and in the component I, associated with the entrained gas. In both components, SO is about five times more abundant than SiO. On the contrary, the HCN/CO ratio is very different in the two components, with the warm and dense component about about a factor 30 lower.

5.2.4 North-HV component

We followed a procedure similar to that used for the North-MV component. Also in this case, two physical components are required to fit the SiO, SO, CO and HCN lines (Tab. 5.4). In fact, the two physical components are approximatively

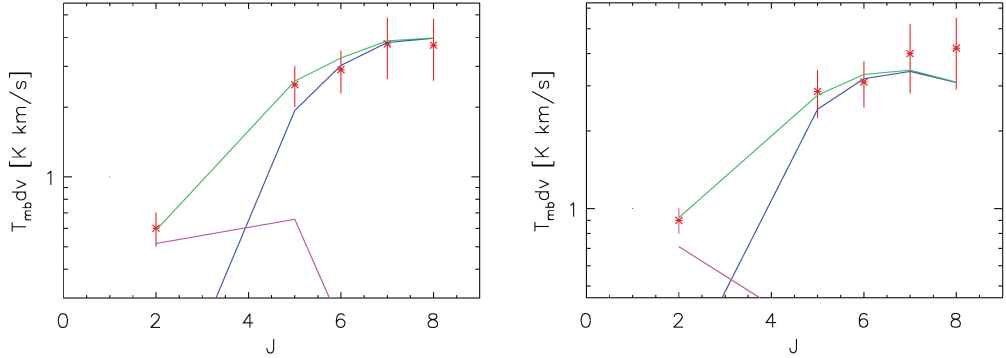


Figure 5.9: Observed (red points) and best fit model predictions (green line) of the SiO lines in the North-MV (*left*) and North-HV (*right*) components (Tab. 5.1). The blue lines show the warm and dense components (marked as Component II in Tab. 5.4) while the magenta lines at the left bottom corners show the less dense and colder components (marked as Component I in Tab. 5.4).

the same than those in the North-MV velocity component. The warm component covers about $3''$ while the cold is slightly more extended $4''$. Similarly, the HCO^+ lines requires a different, less dense gas.

The physical component marked II in the Tab. 5.5, describes the physical and chemical conditions of the north jet. On the contrary, the component I probably describes the physical and chemical conditions of the entrained gas close to the central object.

From a chemical point of view, we remark that the SO/CO abundance ratio is a factor 2 larger than SiO/CO and HCN/CO ratios in the component I associated with the entrained gas. Contrary, the SO/CO abundance ratio is a factor 4 larger than SiO/CO ratio, and 20 times larger than HCN/CO ratio in the component II associated with the jet.

It is important to note that the SiO/CO , SO/CO and HCN/CO abundance ratios show an enhancement of 2.5, 2 and 3 respectively in the warm component between the MV and HV components.

5.2.5 South-EHV component

In this velocity component, we only detected CO , HCO^+ and HCN . The analysis of all lines, including the CO high J lines observed with SOFIA by Gomez-Ruiz et al. (2012), show that, also in this case, two components are required to fit

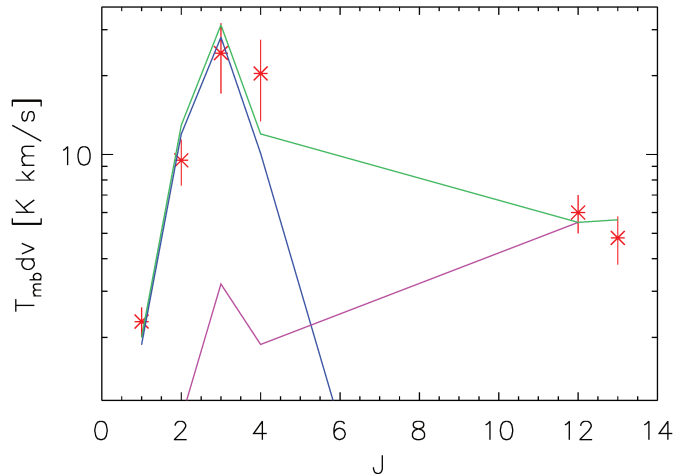


Figure 5.10: Observed (red points) and best fit model predictions (green line) of the SiO lines in the South-EHV component observed towards the south lobe (Tab. 5.1). The magenta line shows the warm and dense component (marked as Component II in Tab. 5.4) while the blue line shows the less dense and colder component (marked as Component I in Tab. 5.4).

all the lines, a warm and dense plus a colder and less dense physical component. The HCO^+ lines provide severe constraints on the colder component, which has a density of $1 \times 10^5 \text{ cm}^{-3}$ and a temperature larger than $\sim 50 \text{ K}$. The CO lines provide then a severe constraint to the second component, which has a temperature 300–400 K and a density of $\sim 2 \times 10^6 \text{ cm}^{-3}$. Both components are fitted with a jet whose transversal size is $2''$.

Note that the larger number of CO lines combined with the HCO^+ lines allows us to better constrain the warm and dense component seen by Gomez-Ruiz et al. (2012). Restricting the analysis to the CO lines only, in fact, leads to (slightly) misleading results. Our best fit to all the CO lines is shown in Fig. 5.10 against the observations.

From a chemical point of view, the largest difference is seen in the HCN, which is lower than about a factor 10 in the warm and dense component with respect to the cold component.

Table 5.6: List of the abundance with respect to CO of the species present in L1157-B1, CepE, L1448, I04166. The abundances are expressed with respect to H₂ and CO-normalized, i.e, $X^{\text{CO}}_4 = N/N_{\text{CO}} \times 10^4$.

	Cep E	L1157-B1 ^a	L1448 ^b	I04166 ^c
SiO	5	10	11	12.5
SO	22.5	21	19	23
CH ₃ OH		191	28	20
HCO ⁺	3	1.5	0.88	0.9
HCN	1	26.4	2.1	0.88
H ₂ CO		14.5	0.40	<1.4

^aTaken from [Tafalla et al., 2010] and calculated from [Bachiller and Perez Gutierrez, 1997].

^{b, c}Taken from [Tafalla et al., 2010] at EHV regime.

5.3 Discussion

5.3.1 Comparison with other outflow sources

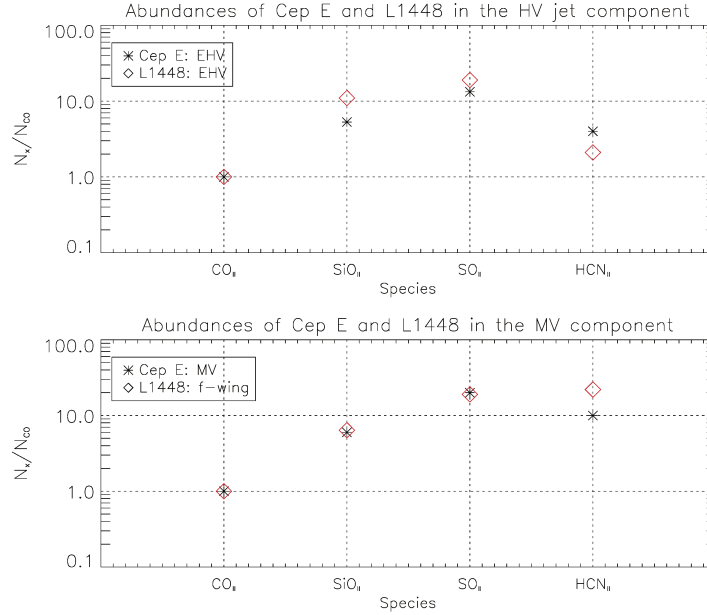
In this section, we compare the molecular composition obtained with the previous analysis with the composition observed towards low-mass protostars.

Some examples of outflows line spectral surveys driven by a low-mass protostar have been carried out selecting some specific frequency line transitions e.g. [Bachiller, 1996], [Bachiller and Perez Gutierrez, 1997], [Bachiller et al., 2001] towards L1157-BI, [Jiménez-Serra et al., 2004] towards L1448 and [Tafalla et al., 2010] towards both, L1448 and I04166. Mainly in CO, SiO, SO, H₂O and CH₃OH molecular lines.

As we already mentioned, the L1157 outflow is the prototype of the so-called chemically active outflows driven by a Class 0 protostar. [Bachiller et al., 2001] observed this object with IRAM-30m telescope and report 18 molecular transition detected towards the blue lobe. In later works [Codella et al., 2010] detected a total of 27 emission lines in their survey towards B1 as part of the Herschel key program CHESS (Chemical HERSchel Surveys of Star forming regions). [Tafalla et al., 2010] observed towards two YSO's, L1448 and I04166 in 33 frequencies corresponding to CO, ¹³CO, SiO, SO, CH₃OH, HC₃N, CS, HCO⁺, HCN, H₂CO, SO₂, H₂S, SiS and HNC also with IRAM-30m (See Table 5.6).

In Table 5.6 we present the abundance values of Cep E in the HV regime

Figure 5.11: Comparison between the normalized CO abundances found by [Tafalla et al., 2010] (*red diamonds*) towards L1448 and our values from the LVG analysis (*stars*) for the HV I (*top*) and MV I regime (*bottom*).

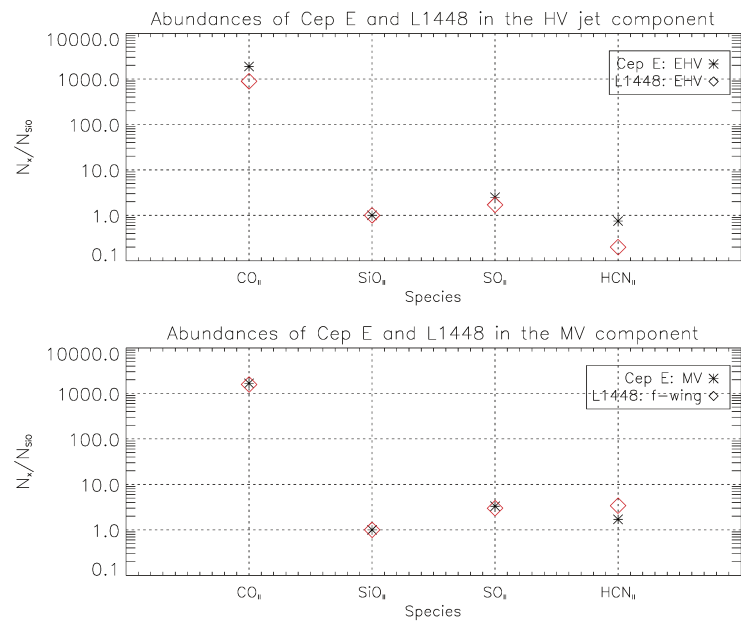


(warm component) together with the abundances of other three low-mass sources: L1157-B1 in the f-wing component [Bachiller and Perez Gutierrez, 1997], L1448 and I04166 in the EHV component [Tafalla et al., 2010]. In an effort to compare our results with previous studies, we present Figures 5.11 and 5.12. These figures show the relative abundances respect to CO and SiO found by [Tafalla et al., 2010] towards L1448 protostellar object and the abundances found in the present work towards Cep E North MV and HV components.

The velocity ranges of the f-wing (20 to 55 km s⁻¹) and the EHV (55 to 85 km s⁻¹) components defined in Tafalla's paper correspond to our MV and HV velocity ranges. The red diamonds correspond to abundances calculated towards L1448 and the black stars correspond to component I and II of Cep E north lobe. There is a good agreement between the abundance values for the component I and the values reported by [Tafalla et al., 2010].

In the next chapter we present the summary and the conclusions of this multi-line analysis.

Figure 5.12: Comparison between the normalized SiO abundances found by [Tafalla et al., 2010] (red diamonds) towards L1448 and our values from the LVG analysis (stars) for the HV I (top) and MV I regime (bottom).



Conclusions and perspectives

My thesis I was founded on the study of the young IM Cep E protostar. This is mainly because this kind of objects are crucial for understanding the overall star forming process as they constitute the link between low- and high-mass range (e.g., [Fuente et al., 2012]; [Crimier et al., 2010]).

Recent studies have started to shed light on the first phases of intermediate mass star formation. [Crimier et al., 2010] determined the physical structure (density-temperature radial profiles) of the protostellar envelopes of five Class 0 IM protostars, among them Cep E-mm source. Later, [Alonso-Albi et al., 2010] carried out a physical and chemical study of Crimier et al. sample of protostars determining the CO depletion and the N_2H^+ deuteration. But there is not an unbiased study toward any of this kind of IM young stellar objects.

Cep E-mm is the only Class 0 IM protostar so far studied systematically over the entire mm bands. This type of study provides an excellent template upon which to base interpretations of other IM young protostars. The wealth of data obtained on this source allowed us to derive the physical conditions and chemical abundances of different species, both in the envelope and in the outflowing material.

Summary

The unbiased spectral survey results can be summarized as follows.

We have presented an unbiased spectral survey of the 3, 1, and 0.9mm bands accessible from the ground towards the IM Class 0 source Cep E. We used the IRAM-30 m telescope, performing about 80 h of observations at two offset

positions: (0",0") and (-12", -18").

More than 500 lines with $S/N \geq 3$ and upper energy levels lower than 250K have been identified by comparing the observed spectra with the JPL and CDMS catalogs. They correspond to 60 chemically distinct species.

From a chemical point of view, the Cep E-mm source present in general a chemical richness both in the envelope and in the outflowing material. In the envelope, we could observe strong deuteration as well as richness in complex molecules, typical of hot core chemistry.

The analysis of the line profiles of this large set of identified species allow us to recognize that emission predominantly originates from three kinematical components: the ambient gas at $\sim -10.9 \text{ km s}^{-1}$, the entrained gas at $(-90 \rightarrow -12)$ and $(-9 \rightarrow +30)$ and the jet, mostly detected at -125 km s^{-1} (south jet) in the $(-12,-18)$ position and at $+50 \text{ km s}^{-1}$ (north jet) in the $(0,0)$ position (see chapter 4).

The line profiles that exhibit emission from the jet component are CO, SiO, SO, HCN and HCO^+ toward the position $(0,0)$ and CO, HCN and HCO^+ toward the position $(-12,-18)$ (see chapter 5).

To derive reliable estimates of the corresponding chemical abundances from the jet component, we carried out a non-LTE radiative transfer modeling. The results of this analysis is summarized in Tables 5.4 and 5.5.

Perspectives

The work presented in this thesis, is one of the first steps toward a more complete description of the formation process of intermediate-mass stars. Evidently, we are far from fully understand the star formation process of this type of IM objects. The contribution of the present work gives some clues that should continue to be explored.

For example, the chemical richness revealed in this source can be compared with other low- and high mass sources, helping to understand similarities and differences between the different mass ranges.

Despite the difficulties in estimating the abundances, that often suffer large uncertainties due to the poorly known physical conditions, geometry, and sizes, this is of paramount importance for understanding the interplay between gas phase and grain surface chemistry in protostellar envelopes, and eventually the chemical evolution from hot cores/corinos to protoplanetary disks.

Appendix A

Population Diagram

The population diagram is a technique to estimate the cloud physical conditions from the molecular line emission; like the column densities of the observed species and the temperature in the region covered by the telescope beam.

It is based on the relation between the observed emission line intensities and the column densities of such emitting molecules. An optically thin transition produces an antenna temperature that is proportional to the column density in the upper level of the transition being observed. If besides, all transitions are thermalized, it is possible to convert that particular column density in the total column density of the specie.

The term *population or rotation diagram* refer more precisely to a plot of the column density per statistical weight of a number of molecular energy levels, as a function of their energy above the ground state. See figure 2.9. The traditional use of this type of diagram has been to assume that the emission is optically thin and that LTE applies.

In the case of local thermodynamic equilibrium (LTE) in the gas, this will just be a Boltzmann distribution, so a plot of the natural logarithm of N_u/g_u versus E_u/k will yield a straight line with a slope of $1/T$, where g_u is the statistical weight of the level u and E_u is the energy above the ground state. The temperature inferred is often called the *rotational temperature* (T_{rot}). The temperature obtained would be expected to be equal to the kinetic temperature (T_{kin}) if all levels were thermalized [Goldsmith and Langer, 1999].

In a spectral survey, it may have sufficient number of transitions to check the

self consistency of the assumptions of optical thinness and thermalization. An either, an analysis of the excitation is possible.

However, this method presents many uncertainties associated with the assumption of complete thermalization and thin line emission.

The column density in the upper state transition of an observed molecule can be expressed in function of the integer intensity of the line by

$$N_u = \frac{8\pi\nu_{ul}^2}{hc^3A_{ul}} \left(1 - \frac{J_\nu(T_{bg})}{J_\nu(T_{ex})}\right)^{-1} \frac{\tau}{1 - e^{-\tau}} \int T_B dv \quad (\text{A.1})$$

where ν_{ul} is the transition frequency between the upper and lower level, and A_{ul} is the Einstein coefficient of spontaneous emission; the transition probability between the two levels, T_{bg} (2,7 K) is the cosmic background radiation, T_{ex} is the excitation temperature of the transition, τ is the optical depth of the transition, T_B is the observed line bright temperature and $J_\nu(T)$ is the source function, defined as

$$J_\nu(T) = \frac{h\nu}{k} \left(e^{\frac{h\nu}{kT}} - 1\right)^{-1} \quad (\text{A.2})$$

Assuming that the emission is optically thin ($\tau \ll 1$) and that the emission comes from a region of the spectra where apply the Rayleigh-Jeand approximation ($h\nu \gg kT$) and that the background radiation is negligible ($T_{bg} \ll T_{ex}$), the equation A.1 can be reduced as

$$N_u = \frac{8\pi\nu_{ul}^2}{hc^3A_{ul}} W = \gamma_u W \quad (\text{A.3})$$

where, it is written for short $W = \int T_B dv$ and all the constants replaced by γ_u .

If the emission is not optically thin, an optical depth correction factor can be defined as

$$C_\tau = \frac{\tau}{1 - e^{-\tau}} \quad (\text{A.4})$$

so that gives the follow relations

$$N_u = \gamma_u W C_\tau = N_u^{thin} C_\tau \quad (\text{A.5})$$

In the case of arbitrary excitation, a different temperature may characterize the population of each level relative to that of the ground state or relative to that of any other level. The excitation temperature T_{ex} is defined by the relative populations or column densities of any two levels i and j of statistical weights g_i and g_j and energies E_i and E_j relative to an arbitrary common reference, through

$$\frac{N_i}{N_j} = \frac{g_i}{g_j} \exp[-(E_i - E_j)/kT_{ex}] \quad (\text{A.6})$$

For a molecule in local thermal equilibrium (LTE), all excitation temperatures are the same, then the population function of the upper lever is given by Boltzmann

$$N_u = \frac{N}{Z} g_u e^{-E_u/kT} \quad (\text{A.7})$$

where N is the total column density of the species in question, and Z is the partition fuction, given by

$$Z = \sum_{\text{All levels}} N_i \quad (\text{A.8})$$

We can rewrite this equation to obtain

$$\ln \frac{N_u}{g_u} = -\frac{1}{T} \frac{E_u}{k} + \ln N - \ln Z \quad (\text{A.9})$$

Obviously, the eq.A.9 is a equation of a line with slope $-1/T$ and a y-intercept of $\ln N - \ln Z$.

$$y = a x + b \quad (\text{A.10})$$

When the optical depth is not small then, using the correction factor in the eq.A.9 gives

$$\ln \frac{\gamma_u W}{g_u} = -\frac{1}{T} \frac{E_u}{k} + \ln N - \ln Z - \ln C_\tau \quad (\text{A.11})$$

here it still assuming populations of all levels are in LTE at temperature T .

Appendix B

LVG or Sobolev approximation

To derive the physical properties of a molecular cloud from line observations, one has to know or assume the molecular excitation conditions. The Sobolev approximation neglecting nonlocal radiative interactions is often used for a simple estimate. It is based on the existence of large velocity gradients throughout the cloud. [Ossenkopf \[1997\]](#).

It is assumed that the line widths are due to the existence of large velocity gradients throughout the cloud, so that the variation of the velocity between points relatively close is bigger than the local velocity dispersion. In other words, a line is Doppler shifted across its own width on a short length. Whenever one can assume that all other physical quantities remain constant at this scale, the radiative transfer integral can be solved locally for each point.

The statistical equilibrium equations describe the variation of the population of level i with energy E_i due to both collisional and radiative transitions.

$$\frac{dn_i}{dt} = - \sum_{j \neq i} R_{ij} n_i + \sum_{j \neq i} R_{ji} n_j - \sum_{j \neq i} C'_{ij} n_i + \sum_{j \neq i} C'_{ji} n_j \quad (\text{B.1})$$

where, R_{ij} is the probability of radiative transition from i to j level. Both, R_{ij} and R_{ji} can be written in terms of Einstein coefficients.

$$R_{ij} = A_{ij} + 4\pi \bar{J} B_{ij} \quad (E_i > E_j) \quad (\text{B.2})$$

$$R_{ji} = 4\pi \bar{J} B_{ji} \quad (E_i > E_j) \quad (\text{B.3})$$

where, \bar{J} is the mean intensity for all angle and frequency.

$$\bar{J} = \int J_\nu \Phi(\nu) d\nu; \quad J_\nu = \frac{1}{4\pi} \int I_\nu(\theta, \phi) d\omega \quad (\text{B.4})$$

where $\Phi(\nu)$ is the line profile.

The C'_{ij} are the collisional transition probability. $C'_{ij} = n\gamma_{ij}$ and $C'_{ji} = n\gamma_{ji}$ where γ_{ij} and γ_{ji} are the excitation and de-excitation collisional coefficients; and n is the number density of the collisors, these can be H_2 , H or He . The collisional coefficients depend on the temperature of the gas, the density of collisors, geometric cross section of the collision and the velocity of the particles.

The calculation of the collisional coefficients, is a very complicated task, which requires the most advanced knowledge of quantum molecular physics coupled with the most advanced numerical techniques and; as far possible, very difficult laboratory experiments. For this reason, at present, we know the collisional coefficients of a relatively small number of molecules: CO , H_2 , and approximated estimates for H_2O , H_2CO , CN , HCN , etc. with a degree of accuracy that can be poor.

For a stationary situation, $dn_i/dt=0, \forall i$. Thus, there is a equation system that allow, in principle, to compute the population of the levels. However, in eq.B.2 to eq.B.4 appear the \bar{J} in each point under consideration and that depends in turn of the population levels. Thus, the solutions of this equation system can be complicated. This can be avoid using the Sobolev approximation. Then, the equation system is split into many independent equations.

It is assuming that the velocity field is such that there is no radiative interaction between distant points, so that a photon emitted by a molecule that is not absorbed locally by another molecule in the near zone may escape of the cloud. The points in the same velocity zones have similar physical conditions and therefore the same excitation conditions.

In the radiative interaction limit, the value of the mean intensity at any point in the cloud when, one integers over the line profile depends only on the local value of source function and of the probability that a photon emitted in that point can escape from the cloud without interact. Sobolev's approach therefore implies a localized radiative transfer, ie, a single point interact radiatively with their surroundings so that J does not depend on what happens outside of that

surroundings, is a local function.

References

- Alonso-Albi, T. and Fuente, A.: 2011, in G. Alecian, K. Belkacem, R. Samadi, and D. Valls-Gabaud (eds.), *SF2A-2011: Proceedings of the Annual meeting of the French Society of Astronomy and Astrophysics*, pp 413–418 [19](#)
- Alonso-Albi, T., Fuente, A., Bachiller, R., Neri, R., Planesas, P., Testi, L., Berné, O., and Joblin, C.: 2009, *A&A* **497**, 117 [21](#)
- Alonso-Albi, T., Fuente, A., Crimier, N., Caselli, P., Ceccarelli, C., Johnstone, D., Planesas, P., Rizzo, J. R., Wyrowski, F., Tafalla, M., Lefloch, B., Maret, S., and Dominik, C.: 2010, *A&A* **518**, A52+ [xi](#), [73](#), [74](#), [75](#), [110](#), [118](#), [195](#)
- André, P., Men'shchikov, A., Bontemps, S., Könyves, V., Motte, F., Schneider, N., Didelon, P., Minier, V., Saraceno, P., Ward-Thompson, D., di Francesco, J., White, G., Molinari, S., Testi, L., Abergel, A., Griffin, M., Henning, T., Royer, P., Merín, B., Vavrek, R., Attard, M., Arzoumanian, D., Wilson, C. D., Ade, P., Aussel, H., Baluteau, J.-P., Benedettini, M., Bernard, J.-P., Blommaert, J. A. D. L., Cambrésy, L., Cox, P., di Giorgio, A., Hargrave, P., Hennemann, M., Huang, M., Kirk, J., Krause, O., Launhardt, R., Leeks, S., Le Penneç, J., Li, J. Z., Martin, P. G., Maury, A., Olofsson, G., Omont, A., Peretto, N., Pezzuto, S., Prusti, T., Roussel, H., Russeil, D., Sauvage, M., Sibthorpe, B., Sicilia-Aguilar, A., Spinoglio, L., Waelkens, C., Woodcraft, A., and Zavagno, A.: 2010, *A&A* **518**, L102 [vii](#), [12](#)
- André, P., Men'shchikov, A., Könyves, V., and Arzoumanian, D.: 2011, in M. Röllig, R. Simon, V. Ossenkopf, and J. Stutzki (eds.), *EAS Publications Series*, Vol. 52 of *EAS Publications Series*, pp 167–172 [12](#)

- Andre, P., Ward-Thompson, D., and Barsony, M.: 1993, *ApJ* **406**, 122 [9](#), [16](#)
- Andre, P., Ward-Thompson, D., and Barsony, M.: 2000, *Protostars and Planets IV* pp 59–+ [10](#), [16](#)
- Anglada, G.: 1995, in S. Lizano & J. M. Torrelles (ed.), *Revista Mexicana de Astronomia y Astrofisica Conference Series*, Vol. 1 of *Revista Mexicana de Astronomia y Astrofisica*, vol. 27, pp 67–+ [25](#)
- Arce, H. G., Santiago-García, J., Jørgensen, J. K., Tafalla, M., and Bachiller, R.: 2008, *ApJL* **681**, L21 [27](#)
- Arce, H. G., Shepherd, D., Gueth, F., Lee, C.-F., Bachiller, R., Rosen, A., and Beuther, H.: 2007, *Protostars and Planets V* pp 245–260 [ix](#), [22](#), [35](#)
- Armstrong, J. T.: 1989, in G. Winnewisser and J. T. Armstrong (eds.), *The Physics and Chemistry of Interstellar Molecular Clouds - mm and Sub-mm Observations in Astrophysics*, Vol. 331 of *Lecture Notes in Physics*, Berlin Springer Verlag, pp 143–151 [22](#)
- Ayala, S., Noriega-Crespo, A., Garnavich, P. M., Curiel, S., Raga, A. C., Böhm, K.-H., and Raymond, J.: 2000, *AJ* **120**, 909 [xiii](#), [81](#), [82](#), [83](#), [86](#)
- Bachiller, R.: 1996, *ARA&A* **34**, 111 [2](#), [88](#), [192](#)
- Bachiller, R. and Perez Gutierrez, M.: 1997, *ApJL* **487**, L93+ [viii](#), [28](#), [192](#), [193](#)
- Bachiller, R., Pérez Gutiérrez, M., Kumar, M. S. N., and Tafalla, M.: 2001, *A&A* **372**, 899 [2](#), [26](#), [28](#), [88](#), [99](#), [178](#), [192](#)
- Bacmann, A., Lefloch, B., Ceccarelli, C., Castets, A., Steinacker, J., and Loinard, L.: 2002, *A&A* **389**, L6 [11](#)
- Bacmann, A., Lefloch, B., Ceccarelli, C., Steinacker, J., Castets, A., and Loinard, L.: 2003, *ApJL* **585**, L55 [118](#)
- Ballesteros-Paredes, J., Klessen, R. S., Mac Low, M.-M., and Vazquez-Semadeni, E.: 2007, *Protostars and Planets V* pp 63–80 [12](#), [13](#)

- Beltrán, M. T., Estalella, R., Girart, J. M., Ho, P. T. P., and Anglada, G.: 2008, *A&A* **481**, 93 [21](#)
- Beltrán, M. T., Girart, J. M., Estalella, R., Ho, P. T. P., and Palau, A.: 2002, *ApJ* **573**, 246 [21](#)
- Benson, P. J. and Myers, P. C.: 1989, *ApJS* **71**, 89 [11](#)
- Bergin, E. A., Phillips, T. G., Comito, C., Crockett, N. R., Lis, D. C., Schilke, P., Wang, S., Bell, T. A., Blake, G. A., Bumble, B., Caux, E., Cabrit, S., Ceccarelli, C., Cernicharo, J., Daniel, F., de Graauw, T., Dubernet, M.-L., Emprechtinger, M., Encrenaz, P., Falgarone, E., Gerin, M., Giesen, T. F., Goicoechea, J. R., Goldsmith, P. F., Gupta, H., Hartogh, P., Helmich, F. P., Herbst, E., Joblin, C., Johnstone, D., Kawamura, J. H., Langer, W. D., Latter, W. B., Lord, S. D., Maret, S., Martin, P. G., Melnick, G. J., Menten, K. M., Morris, P., Müller, H. S. P., Murphy, J. A., Neufeld, D. A., Ossenkopf, V., Pagani, L., Pearson, J. C., Péroult, M., Plume, R., Roelfsema, P., Qin, S.-L., Salez, M., Schlemmer, S., Stutzki, J., Tielens, A. G. G. M., Trappe, N., van der Tak, F. F. S., Vastel, C., Yorke, H. W., Yu, S., and Zmuidzinas, J.: 2010, *A&A* **521**, L20 [2](#)
- Beuther, H., Churchwell, E. B., McKee, C. F., and Tan, J. C.: 2007, *Protostars and Planets V* pp 165–180 [20](#)
- Beuther, H., Linz, H., Henning, T., Bik, A., Wyrowski, F., Schuller, F., Schilke, P., Thorwirth, S., and Kim, K.-T.: 2011, *A&A* **531**, A26 [19](#)
- Beuther, H. and Steinacker, J.: 2007, *ApJL* **656**, L85 [6](#)
- Blaauw, A.: 1964, *ARA&A* **2**, 213 [67](#)
- Blaauw, A., Hiltner, W. A., and Johnson, H. L.: 1959, *ApJ* **130**, 69 [67](#), [69](#), [83](#)
- Blake, G. A., van Dishoeck, E. F., Jansen, D. J., Groesbeck, T. D., and Mundy, L. G.: 1994, *ApJ* **428**, 680 [2](#)

- Bonnell, I. A.: 2002, in P. Crowther (ed.), *Hot Star Workshop III: The Earliest Phases of Massive Star Birth*, Vol. 267 of *Astronomical Society of the Pacific Conference Series*, pp 193–+ [20](#)
- Bontemps, S., André, P., Könyves, V., Men'shchikov, A., Schneider, N., Maury, A., Peretto, N., Arzoumanian, D., Attard, M., Motte, F., Minier, V., Didelon, P., Saraceno, P., Abergel, A., Baluteau, J.-P., Bernard, J.-P., Cambrésy, L., Cox, P., di Francesco, J., di Giorgio, A. M., Griffin, M., Hargrave, P., Huang, M., Kirk, J., Li, J., Martin, P., Merín, B., Molinari, S., Olofsson, G., Pezzuto, S., Prusti, T., Roussel, H., Russeil, D., Sauvage, M., Sibthorpe, B., Spinoglio, L., Testi, L., Vavrek, R., Ward-Thompson, D., White, G., Wilson, C., Woodcraft, A., and Zavagno, A.: 2010, *A&A* **518**, L85 [vii](#), [11](#), [12](#)
- Bontemps, S., Andre, P., Terebey, S., and Cabrit, S.: 1996, *A&A* **311**, 858 [17](#), [29](#), [33](#)
- Bottinelli, S., Ceccarelli, C., Lefloch, B., Williams, J. P., Castets, A., Caux, E., Cazaux, S., Maret, S., Parise, B., and Tielens, A. G. G. M.: 2004, *ApJ* **615**, 354 [16](#)
- Bottinelli, S., Ceccarelli, C., Williams, J. P., and Lefloch, B.: 2007, *A&A* **463**, 601 [16](#), [21](#)
- Buckle, J. V. and Fuller, G. A.: 2003, *A&A* **399**, 567 [28](#)
- Cabrit, S., Edwards, S., Strom, S. E., and Strom, K. M.: 1990, *ApJ* **354**, 687 [31](#)
- Canto, J. and Raga, A. C.: 1991, *ApJ* **372**, 646 [ix](#), [34](#), [35](#)
- Caratti o Garatti, A., Giannini, T., Nisini, B., and Lorenzetti, D.: 2006, *A&A* **449**, 1077 [25](#)
- Caselli, P.: 2011, in *IAU Symposium*, Vol. 280 of *IAU Symposium*, pp 19–32 [7](#), [11](#)
- Caselli, P., Walmsley, C. M., Tafalla, M., Dore, L., and Myers, P. C.: 1999, *ApJL* **523**, L165 [11](#)

- Caselli, P., Walmsley, C. M., Zucconi, A., Tafalla, M., Dore, L., and Myers, P. C.: 2002, *ApJ* **565**, 344 [74](#)
- Caux, E., Kahane, C., Castets, A., Coutens, A., Ceccarelli, C., Bacmann, A., Bisschop, S., Bottinelli, S., Comito, C., Helmich, F. P., Lefloch, B., Parise, B., Schilke, P., Tielens, A. G. G. M., van Dishoeck, E., Vastel, C., Wakelam, V., and Walters, A.: 2011, *A&A* **532**, A23+ [2](#), [88](#), [108](#)
- Cazaux, S., Tielens, A. G. G. M., Ceccarelli, C., Castets, A., Wakelam, V., Caux, E., Parise, B., and Teyssier, D.: 2003, *ApJL* **593**, L51 [27](#)
- Ceccarelli, C.: 2007, in *Molecules in Space and Laboratory* [108](#)
- Ceccarelli, C., Caselli, P., Herbst, E., Tielens, A. G. G. M., and Caux, E.: 2007, *Protostars and Planets V* pp 47–62 [11](#)
- Ceccarelli, C., Castets, A., Caux, E., Hollenbach, D., Loinard, L., Molinari, S., and Tielens, A. G. G. M.: 2000, *A&A* **355**, 1129 [16](#)
- Ceccarelli, C. and CHESS Consortium: 2010, in *38th COSPAR Scientific Assembly*, Vol. 38 of *COSPAR Meeting*, p. 2476 [2](#), [88](#)
- Ceccarelli, C., Maret, S., Tielens, A. G. G. M., Castets, A., and Caux, E.: 2003, *A&A* **410**, 587 [187](#)
- Cernicharo, J., Bachiller, R., and Gonzalez-Alfonso, E.: 1996, *A&A* **305**, L5 [27](#)
- Chandler, C. J., Barsony, M., and Moore, T. J. T.: 1998, *MNRAS* **299**, 789 [16](#)
- Chandrasekhar, S. and Fermi, E.: 1953, *ApJ* **118**, 116 [13](#)
- Chini, R., Ward-Thompson, D., Kirk, J. M., Nielbock, M., Reipurth, B., and Sievers, A.: 2001, *A&A* **369**, 155 [xii](#), [70](#), [79](#), [80](#)
- Codella, C., Ceccarelli, C., Lefloch, B., Fontani, F., Busquet, G., Caselli, P., Kahane, C., Lis, D., Taquet, V., Vasta, M., Viti, S., and Wiesenfeld, L.: 2012, *ApJL* **757**, L9 [2](#), [110](#), [118](#)

- Codella, C., Lefloch, B., Ceccarelli, C., Cernicharo, J., Caux, E., Lorenzani, A., Viti, S., Hily-Blant, P., Parise, B., Maret, S., Nisini, B., Caselli, P., Cabrit, S., Pagani, L., Benedettini, M., Boogert, A., Gueth, F., Melnick, G., Neufeld, D., Pacheco, S., Salez, M., Schuster, K., Bacmann, A., Baudry, A., Bell, T., Bergin, E. A., Blake, G., Bottinelli, S., Castets, A., Comito, C., Coutens, A., Crimier, N., Dominik, C., Demyk, K., Encrenaz, P., Falgarone, E., Fuente, A., Gerin, M., Goldsmith, P., Helmich, F., Hennebelle, P., Henning, T., Herbst, E., Jacq, T., Kahane, C., Kama, M., Klotz, A., Langer, W., Lis, D., Lord, S., Pearson, J., Phillips, T., Saraceno, P., Schilke, P., Tielens, X., van der Tak, F., van der Wiel, M., Vastel, C., Wakelam, V., Walters, A., Wyrowski, F., Yorke, H., Borys, C., Delorme, Y., Kramer, C., Larsson, B., Mehdi, I., Ossenkopf, V., and Stutzki, J.: 2010, *A&A* **518**, L112 [192](#)
- Codella, C., Lorenzani, A., Gallego, A. T., Cesaroni, R., and Moscadelli, L.: 2004, *A&A* **417**, 615 [18](#)
- Commercon, B., Launhardt, R., Dullemond, C. P., and Henning, T.: 2012, *ArXiv e-prints* [11](#)
- Crapsi, A., Caselli, P., Walmsley, C. M., Myers, P. C., Tafalla, M., Lee, C. W., and Bourke, T. L.: 2005, *ApJ* **619**, 379 [118](#)
- Crimier, N., Ceccarelli, C., Alonso-Albi, T., Fuente, A., Caselli, P., Johnstone, D., Kahane, C., Lefloch, B., Maret, S., Plume, R., Rizzo, J. R., Tafalla, M., van Dishoeck, E., and Wyrowski, F.: 2010, *A&A* **516**, A102+ [x](#), [xi](#), [xix](#), [2](#), [69](#), [70](#), [71](#), [72](#), [83](#), [105](#), [195](#)
- Crutcher, R. M., Wandelt, B., Heiles, C., Falgarone, E., and Troland, T. H.: 2010, *ApJ* **725**, 466 [8](#)
- Davis, C. J., Eisloffel, J., and Ray, T. P.: 1994, *ApJL* **426**, L93 [81](#)
- Davis, C. J. and Smith, M. D.: 1996, *A&A* **310**, 961 [82](#)
- Devine, D., Reipurth, B., and Bally, J.: 1997, in B. Reipurth & C. Bertout (ed.), *Herbig-Haro Flows and the Birth of Stars*, Vol. 182 of *IAU Symposium*, pp 91P–+ [80](#)

- di Francesco, J., Evans, II, N. J., Caselli, P., Myers, P. C., Shirley, Y., Aikawa, Y., and Tafalla, M.: 2007, *Protostars and Planets V* pp 17–32 [7](#), [11](#)
- Dib, S., Kim, J., Vázquez-Semadeni, E., Burkert, A., and Shadmehri, M.: 2007, *ApJ* **661**, 262 [11](#)
- Dobashi, K., Uehara, H., Kandori, R., Sakurai, T., Kaiden, M., Umemoto, T., and Sato, F.: 2005, *PASJ* **57**, 1 [x](#), [68](#)
- Downes, D.: 1989, in I. Appenzeller, H. J. Habing, and P. Lena (eds.), *Evolution of Galaxies: Astronomical Observations*, Vol. 333 of *Lecture Notes in Physics*, Berlin Springer Verlag, p. 351 [55](#)
- Draine, B. T.: 1980, *ApJ* **241**, 1021 [36](#)
- Draine, B. T. and McKee, C. F.: 1993, *ARA&A* **31**, 373 [39](#)
- Efremov, Y. N. and Elmegreen, B. G.: 1998, *MNRAS* **299**, 588 [10](#)
- Eisloffel, J., Smith, M. D., and Davis, C. J.: 2000, *A&A* **359**, 1147 [25](#)
- Eisloffel, J., Smith, M. D., Davis, C. J., and Ray, T. P.: 1996, *AJ* **112**, 2086 [xi](#), [xii](#), [72](#), [76](#), [77](#), [79](#), [80](#), [82](#), [83](#), [86](#)
- Emprechtinger, M., Caselli, P., Volgenau, N. H., Stutzki, J., and Wiedner, M. C.: 2009, *A&A* **493**, 89 [110](#), [118](#)
- Evans, II, N. J., Dunham, M. M., Jørgensen, J. K., Enoch, M. L., Merín, B., van Dishoeck, E. F., Alcalá, J. M., Myers, P. C., Stapelfeldt, K. R., Huard, T. L., Allen, L. E., Harvey, P. M., van Kempen, T., Blake, G. A., Koerner, D. W., Mundy, L. G., Padgett, D. L., and Sargent, A. I.: 2009, *ApJS* **181**, 321 [16](#)
- Falgarone, E. and Puget, J. L.: 1986, *A&A* **162**, 235 [7](#)
- Falgarone, E., Troland, T. H., Crutcher, R. M., and Paubert, G.: 2008, *A&A* **487**, 247 [8](#)
- Feigelson, E. D. and Montmerle, T.: 1999, *ARA&A* **37**, 363 [vii](#), [17](#)

- Ferreira, J., Pelletier, G., and Appl, S.: 1997, in B. Reipurth and C. Bertout (eds.), *Herbig-Haro Flows and the Birth of Stars*, Vol. 182 of *IAU Symposium*, p. 112P [88](#)
- Few, R. W. and Cohen, R. J.: 1983, *MNRAS* **203**, 853 [67](#)
- Fiege, J. D. and Henriksen, R. N.: 1996a, *MNRAS* **281**, 1038 [34](#)
- Fiege, J. D. and Henriksen, R. N.: 1996b, *MNRAS* **281**, 1055 [ix](#), [34](#), [35](#)
- Froebrich, D.: 2005, *ApJS* **156**, 169 [3](#)
- Froebrich, D., Scholz, A., Eislöffel, J., and Murphy, G. C.: 2005, *A&A* **432**, 575 [18](#)
- Froebrich, D., Smith, M. D., and Eislöffel, J.: 2003a, *ApSS* **287**, 217 [83](#), [84](#)
- Froebrich, D., Smith, M. D., Hodapp, K.-W., and Eislöffel, J.: 2003b, *MNRAS* **346**, 163 [69](#), [70](#), [71](#), [83](#)
- Fuente, A., Alonso-Albi, T., Bachiller, R., Natta, A., Testi, L., Neri, R., and Planesas, P.: 2006, *ApJL* **649**, L119 [21](#)
- Fuente, A., Caselli, P., McCoey, C., Cernicharo, J., Johnstone, D., Fich, M., van Kempen, T., van Dishoeck, E., Yıldız, U., Visser, R., Kristensen, L., Alonso-Albi, T., Herpin, F., and Tisi, S.: 2012, *A&A* **540**, A75 [1](#), [195](#)
- Fuente, A., Ceccarelli, C., Neri, R., Alonso-Albi, T., Caselli, P., Johnstone, D., van Dishoeck, E. F., and Wyrowski, F.: 2007, *A&A* **468**, L37 [2](#)
- Fukui, Y.: 1989, in B. Reipurth (ed.), *European Southern Observatory Conference and Workshop Proceedings*, Vol. 33 of *European Southern Observatory Conference and Workshop Proceedings*, pp 95–117 [83](#)
- Fukui, Y., Sugitani, K., Takaba, H., Iwata, T., Mizuno, A., Ogawa, H., and Kawabata, K.: 1986, *ApJL* **311**, L85 [22](#)
- Giannini, T., Nisini, B., and Lorenzetti, D.: 2001, in G. L. Pilbratt, J. Cernicharo, A. M. Heras, T. Prusti, and R. Harris (eds.), *The Promise of the Herschel Space Observatory*, Vol. 460 of *ESA Special Publication*, p. 409 [27](#), [83](#)

- Goldreich, P. and Kwan, J.: 1974, *ApJ* **189**, 441 [7](#)
- Goldsmith, P. F. and Langer, W. D.: 1999, *ApJ* **517**, 209 [105](#), [199](#)
- Gómez-Ruiz, A. I., Gusdorf, A., Leurini, S., Codella, C., Güsten, R., Wyrowski, F., Requena-Torres, M. A., Risacher, C., and Wampfler, S. F.: 2012, *A&A* **542**, L9 [180](#)
- Gondhalekar, P. M. and Wilson, R.: 1975, *A&A* **38**, 329 [1](#)
- Gueth, F. and Guilloteau, S.: 1999, *A&A* **343**, 571 [viii](#), [23](#)
- Guillet, V., Jones, A. P., and Pineau Des Forêts, G.: 2009, *A&A* **497**, 145 [27](#), [38](#)
- Guillet, V., Pineau Des Forêts, G., and Jones, A. P.: 2011, *A&A* **527**, A123 [39](#)
- Gusdorf, A., Cabrit, S., Flower, D. R., and Pineau Des Forêts, G.: 2008, *A&A* **482**, 809 [39](#)
- Habing, H. J.: 1968, *BAIN* **19**, 421 [1](#)
- Hartigan, P., Raymond, J., and Pierson, R.: 2004, *ApJL* **614**, L69 [38](#)
- Herbst, E. and van Dishoeck, E. F.: 2009, *ARA&A* **47**, 427 [2](#), [88](#), [108](#)
- Hirano, N., Ho, P. P. T., Liu, S.-Y., Shang, H., Lee, C.-F., and Bourke, T. L.: 2010, *ApJ* **717**, 58 [99](#), [178](#)
- Hodapp, K.-W.: 1994, *ApJS* **94**, 615 [xi](#), [76](#)
- Hogerheijde, M. R., van Dishoeck, E. F., Salverda, J. M., and Blake, G. A.: 1999, *ApJ* **513**, 350 [2](#)
- Hollenbach, D. and McKee, C. F.: 1979, *ApJS* **41**, 555 [39](#)
- Hollenbach, D. and McKee, C. F.: 1989, *ApJ* **342**, 306 [ix](#), [36](#), [37](#)
- Hollenbach, D. J., Ceccarelli, C., Neufeld, D. A., and Tielens, A. G. G. M.: 1995, in M. R. Haas, J. A. Davidson, and E. F. Erickson (eds.), *From Gas to Stars to Dust*, Vol. 73 of *Astronomical Society of the Pacific Conference Series*, pp 243–250 [15](#)

- Jiménez-Serra, I., Caselli, P., Martín-Pintado, J., and Hartquist, T. W.: 2008, *A&A* **482**, 549 [39](#)
- Jiménez-Serra, I., Martín-Pintado, J., Rodríguez-Franco, A., and Marcelino, N.: 2004, *ApJL* **603**, L49 [2](#), [88](#), [192](#)
- Jordi, C., Trullols, E., and Galadi-Enriquez, D.: 1996, *A&A* **312**, 499 [67](#)
- Jørgensen, J. K., Bourke, T. L., Myers, P. C., Di Francesco, J., van Dishoeck, E. F., Lee, C.-F., Ohashi, N., Schöier, F. L., Takakuwa, S., Wilner, D. J., and Zhang, Q.: 2007, *ApJ* **659**, 479 [99](#), [178](#)
- Jørgensen, J. K., Schöier, F. L., and van Dishoeck, E. F.: 2002, *A&A* **389**, 908 [16](#)
- Jørgensen, J. K., Schöier, F. L., and van Dishoeck, E. F.: 2004, *A&A* **416**, 603 [11](#)
- Kauffmann, J. and Pillai, T.: 2010, *ApJL* **723**, L7 [6](#)
- Kaufman, M. J. and Neufeld, D. A.: 1996, *ApJ* **456**, 611 [24](#), [27](#), [39](#)
- Kim, H.-D., Cho, S.-H., Chung, H.-S., Kim, H.-R., Roh, D.-G., Kim, H.-G., Minh, Y. C., and Minn, Y.-K.: 2000, *ApJS* **131**, 483 [2](#), [88](#)
- Kim, S.-J., Kim, H.-D., Lee, Y., Minh, Y. C., Balasubramanyam, R., Burton, M. G., Millar, T. J., and Lee, D.-W.: 2006, *ApJS* **162**, 161 [2](#), [88](#)
- Klessen, R.: 2001, *ArXiv Astrophysics e-prints* [12](#)
- Konigl, A. and Pudritz, R. E.: 2000, *Protostars and Planets IV* pp 759–+ [32](#)
- Könyves, V., André, P., Men'shchikov, A., Schneider, N., Arzoumanian, D., Bontemps, S., Attard, M., Motte, F., Didelon, P., Maury, A., Abergel, A., Ali, B., Baluteau, J.-P., Bernard, J.-P., Cambrésy, L., Cox, P., di Francesco, J., di Giorgio, A. M., Griffin, M. J., Hargrave, P., Huang, M., Kirk, J., Li, J. Z., Martin, P., Minier, V., Molinari, S., Olofsson, G., Pezzuto, S., Russeil, D., Roussel, H., Saraceno, P., Sauvage, M., Sibthorpe, B., Spinoglio, L., Testi, L.,

- Ward-Thompson, D., White, G., Wilson, C. D., Woodcraft, A., and Zavagno, A.: 2010, *A&A* **518**, L106 [vii](#), [11](#), [12](#)
- Kramer, C., Stutzki, J., Rohrig, R., and Corneliusen, U.: 1998, *A&A* **329**, 249 [13](#)
- Kraus, J. D.: 1950, *Radio Astronomy*, McGraw-Hill [44](#)
- Krumholz, M. R., Klein, R. I., and McKee, C. F.: 2005a, in R. Cesaroni, M. Felli, E. Churchwell, & M. Walmsley (ed.), *Massive Star Birth: A Crossroads of Astrophysics*, Vol. 227 of *IAU Symposium*, pp 231–236 [20](#)
- Krumholz, M. R., McKee, C. F., and Klein, R. I.: 2005b, *ApJL* **618**, L33 [20](#)
- Kun, M., Kiss, Z. T., and Balog, Z.: 2008, *Star Forming Regions in Cepheus*, p. 136 [x](#), [68](#)
- Kwan, J. and Scoville, N.: 1976, *ApJL* **210**, L39 [9](#)
- Lada, C. J.: 1985, *ARA&A* **23**, 267 [18](#)
- Lada, C. J.: 1987, in M. Peimbert & J. Jugaku (ed.), *Star Forming Regions*, Vol. 115 of *IAU Symposium*, pp 1–17 [16](#), [17](#)
- Lada, C. J. and Wilking, B. A.: 1984, *ApJ* **287**, 610 [9](#)
- Ladd, E. F. and Hodapp, K.-W.: 1997, *ApJ* **474**, 749 [viii](#), [xii](#), [25](#), [72](#), [79](#), [80](#), [85](#), [86](#)
- Ladd, E. F. and Howe, J. E.: 1997, in B. Reipurth & C. Bertout (ed.), *Herbig-Haro Flows and the Birth of Stars*, Vol. 182 of *IAU Symposium*, pp 144P–+ [71](#)
- Larson, R. B.: 1969, *MNRAS* **145**, 271 [15](#)
- Larson, R. B.: 1981, *MNRAS* **194**, 809 [8](#), [13](#)
- Lee, C.-F., Ho, P. T. P., Palau, A., Hirano, N., Bourke, T. L., Shang, H., and Zhang, Q.: 2007, *ApJ* **670**, 1188 [viii](#), [23](#)

- Lefloch, B., Cabrit, S., Busquet, G., Codella, C., Ceccarelli, C., Cernicharo, J., Pardo, J. R., Benedettini, M., Lis, D. C., and Nisini, B.: 2012, *ArXiv e-prints* [2](#)
- Lefloch, B., Cernicharo, J., Pacheco, S., and Ceccarelli, C.: 2011, *A&A* **527**, L3 [2](#), [3](#), [69](#), [78](#), [83](#)
- Lefloch, B., Cernicharo, J., Reipurth, B., Pardo, J. R., and Neri, R.: 2007, *ApJ* **658**, 498 [22](#)
- Lefloch, B., Eisloffel, J., and Lazareff, B.: 1996, *A&A* **313**, L17 [xii](#), [69](#), [70](#), [71](#), [76](#), [77](#), [78](#), [83](#), [99](#)
- Lery, T., Henriksen, R. N., Fiege, J. D., Ray, T. P., Frank, A., and Bacciotti, F.: 2002, *A&A* **387**, 187 [34](#)
- Lombardi, M. and Alves, J.: 2001, *A&A* **377**, 1023 [x](#), [68](#)
- Machida, M. N., Inutsuka, S.-i., and Matsumoto, T.: 2008, *ApJ* **676**, 1088 [88](#)
- Maret, S., Bergin, E. A., Neufeld, D. A., Green, J. D., Watson, D. M., Harwit, M. O., Kristensen, L. E., Melnick, G. J., Sonnentrucker, P., Tolls, V., Werner, M. W., Willacy, K., and Yuan, Y.: 2009, *ApJ* **698**, 1244 [24](#)
- Maret, S., Hily-Blant, P., Pety, J., Bardeau, S., and Reynier, E.: 2011, *A&A* **526**, A47 [100](#)
- Margulès, L., Motiyenko, R., Demyk, K., Tercero, B., Cernicharo, J., Sheng, M., Weidmann, M., Gripp, J., Mäder, H., and Demaison, J.: 2009, *A&A* **493**, 565 [2](#)
- Margulis, M. and Lada, C. J.: 1985, *ApJ* **299**, 925 [22](#)
- Matzner, C. D. and McKee, C. F.: 1999, *ApJL* **526**, L109 [33](#)
- McCaughrean, M. J., Rayner, J. T., and Zinnecker, H.: 1994, *ApJL* **436**, L189 [viii](#), [23](#), [82](#)
- McKee, C. F. and Ostriker, E. C.: 2007, *ARA&A* **45**, 565 [12](#)

- McKee, C. F. and Tan, J. C.: 2003, *ApJ* **585**, 850 [20](#)
- McKee, C. F. and Zweibel, E. G.: 1995, *ApJ* **440**, 686 [7](#)
- Men'shchikov, A., André, P., Didelon, P., Könyves, V., Schneider, N., Motte, F., Bontemps, S., Arzoumanian, D., Attard, M., Abergel, A., Baluteau, J.-P., Bernard, J.-P., Cambrésy, L., Cox, P., di Francesco, J., di Giorgio, A. M., Griffin, M., Hargrave, P., Huang, M., Kirk, J., Li, J. Z., Martin, P., Minier, V., Miville-Deschênes, M.-A., Molinari, S., Olofsson, G., Pezzuto, S., Roussel, H., Russeil, D., Saraceno, P., Sauvage, M., Sibthorpe, B., Spinoglio, L., Testi, L., Ward-Thompson, D., White, G., Wilson, C. D., Woodcraft, A., and Zavagno, A.: 2010, *A&A* **518**, L103 [11](#)
- Moro-Martín, A., Noriega-Crespo, A., Molinari, S., Testi, L., Cernicharo, J., and Sargent, A.: 2001, *ApJ* **555**, 146 [xi](#), [69](#), [71](#), [72](#), [73](#), [83](#)
- Motte, F., Andre, P., and Neri, R.: 1998, *A&A* **336**, 150 [11](#)
- Mouschovias, T. C.: 1976, *ApJ* **207**, 141 [7](#)
- Mouschovias, T. C.: 1987, in G. E. Morfill and M. Scholer (eds.), *NATO ASIC Proc. 210: Physical Processes in Interstellar Clouds*, pp 491–552 [13](#)
- Mouschovias, T. C. and Psaltis, D.: 1995, *ApJL* **444**, L105 [8](#)
- Mundt, R. and Ray, T. P.: 1994, in P. S. The, M. R. Perez, & E. P. J. van den Heuvel (ed.), *The Nature and Evolutionary Status of Herbig Ae/Be Stars*, Vol. 62 of *Astronomical Society of the Pacific Conference Series*, pp 237–+ [32](#)
- Myers, P. C.: 1985, in G. Serra (ed.), *Lecture Notes in Physics, Berlin Springer Verlag*, Vol. 237 of *Lecture Notes in Physics, Berlin Springer Verlag*, pp 87–94 [7](#)
- Neri, R., Fuente, A., Ceccarelli, C., Caselli, P., Johnstone, D., van Dishoeck, E. F., Wyrowski, F., Tafalla, M., Lefloch, B., and Plume, R.: 2007, *A&A* **468**, L33 [2](#)

- Nisini, B., Benedettini, M., Giannini, T., Caux, E., di Giorgio, A. M., Liseau, R., Lorenzetti, D., Molinari, S., Saraceno, P., Smith, H. A., Spinoglio, L., and White, G. J.: 1999, *A&A* **350**, 529 [27](#)
- Nisini, B., Codella, C., Giannini, T., Santiago Garcia, J., Richer, J. S., Bachiller, R., and Tafalla, M.: 2007, *A&A* **462**, 163 [38](#)
- Noriega-Crespo, A. and Garnavich, P. M.: 1997, in A. M. Heras, K. Leech, N. R. Trams, & M. Perry (ed.), *The first ISO workshop on Analytical Spectroscopy*, Vol. 419 of *ESA Special Publication*, pp 287–+ [80](#)
- Noriega-Crespo, A. and Garnavich, P. M.: 2001, *AJ* **122**, 3317 [81](#), [83](#)
- Noriega-Crespo, A., Moro-Martin, A., Carey, S., Morris, P. W., Padgett, D. L., Latter, W. B., and Muzerolle, J.: 2004, *ApJS* **154**, 402 [69](#), [71](#), [82](#)
- Noriega-Crespo, A., Moro-Martin, A., Carey, S., Morris, P. W., Padgett, D. L., Latter, W. B., and Muzerolle, J.: 2005, in A. Wilson (ed.), *ESA Special Publication*, Vol. 577 of *ESA Special Publication*, pp 453–454 [70](#)
- Ossenkopf, V.: 1997, *New Astronomy* **2**, 365 [203](#)
- Ostriker, E. C.: 2009, in *The Evolving ISM in the Milky Way and Nearby Galaxies* [14](#)
- Padoan, P., Juvela, M., Goodman, A. A., and Nordlund, Å.: 2001, *ApJ* **553**, 227 [12](#), [13](#)
- Parise, B., Ceccarelli, C., Tielens, A. G. G. M., Castets, A., Caux, E., Lefloch, B., and Maret, S.: 2006, *A&A* **453**, 949 [110](#), [118](#)
- Penzias, A. A. and Burrus, C. A.: 1973, *ARA&A* **11**, 51 [54](#)
- Plume, R., Fuller, G. A., Helmich, F., van der Tak, F. F. S., Roberts, H., Bowey, J., Buckle, J., Butner, H., Caux, E., Ceccarelli, C., van Dishoeck, E. F., Friberg, P., Gibb, A. G., Hatchell, J., Hogerheijde, M. R., Matthews, H., Millar, T. J., Mitchell, G., Moore, T. J. T., Ossenkopf, V., Rawlings, J. M. C., Richer, J., Roellig, M., Schilke, P., Spaans, M., Tielens, A. G. G. M., Thompson, M. A.,

- Viti, S., Weferling, B., White, G. J., Wouterloot, J., Yates, J., and Zhu, M.: 2007, *PASP* **119**, 102 [2](#), [88](#)
- Plume, R., Jaffe, D. T., Evans, II, N. J., Martin-Pintado, J., and Gomez-Gonzalez, J.: 1997, *ApJ* **476**, 730 [20](#)
- Pudritz, R. E., Ouyed, R., Fendt, C., and Brandenburg, A.: 2007, *Protostars and Planets V* pp 277–294 [31](#)
- Qiu, K., Zhang, Q., Megeath, S. T., Gutermuth, R. A., Beuther, H., Shepherd, D. S., Sridharan, T. K., Testi, L., and De Pree, C. G.: 2008, *ApJ* **685**, 1005 [19](#)
- Raga, A. and Cabrit, S.: 1993, *A&A* **278**, 267 [ix](#), [33](#), [35](#)
- Raga, A. C., Noriega-Crespo, A., Reipurth, B., Garnavich, P. M., Heathcote, S., Böhm, K. H., and Curiel, S.: 2002, *ApJL* **565**, L29 [23](#)
- Reipurth, B.: 2000, *VizieR Online Data Catalog* **5104**, 0 [30](#)
- Reipurth, B. and Bally, J.: 2001, *ARA&A* **39**, 403 [22](#)
- Reipurth, B., Yu, K. C., Heathcote, S., Bally, J., and Rodríguez, L. F.: 2000, *AJ* **120**, 1449 [24](#)
- Roberts, H., Herbst, E., and Millar, T. J.: 2003, *ApJL* **591**, L41 [74](#)
- Rybicki, G. and Lightman, A. P.: 1979, *Radiative Processes in Astrophysics*, WILEY-VCH Verlag GmbH 62Co. KGaA, Weinheim [45](#)
- Sadavoy, S. I., di Francesco, J., André, P., Pezzuto, S., Bernard, J.-P., Bontemps, S., Bressert, E., Chitsazzadeh, S., Fallscheer, C., Hennemann, M., Hill, T., Martin, P., Motte, F., Nguyen Luong, Q., Peretto, N., Reid, M., Schneider, N., Testi, L., White, G. J., and Wilson, C.: 2012, *A&A* **540**, A10 [11](#)
- Sakai, N., Sakai, T., Hirota, T., and Yamamoto, S.: 2008, *ApJ* **672**, 371 [2](#), [88](#)
- Santiago-García, J., Tafalla, M., Johnstone, D., and Bachiller, R.: 2009, *A&A* **495**, 169 [99](#), [178](#)

- Saraceno, P., Andre, P., Ceccarelli, C., Griffin, M., and Molinari, S.: 1996, *A&A* **309**, 827 [17](#), [18](#), [29](#)
- Sargent, A. I.: 1977, *ApJ* **218**, 736 [67](#), [83](#), [100](#)
- Schöier, F. L., Jørgensen, J. K., van Dishoeck, E. F., and Blake, G. A.: 2002, *A&A* **390**, 1001 [16](#)
- Schreyer, K., Henning, T., van der Tak, F. F. S., Boonman, A. M. S., and van Dishoeck, E. F.: 2002, *A&A* **394**, 561 [2](#)
- Schulz, N. S.: 2005, *From Dust To Stars Studies of the Formation and Early Evolution of Stars*, Prawis [vii](#), [ix](#), [11](#), [32](#)
- Schütz, O., Meeus, G., and Sterzik, M. F.: 2005, *A&A* **431**, 175 [1](#)
- Shang, H., Allen, A., Li, Z.-Y., Liu, C.-F., Chou, M.-Y., and Anderson, J.: 2006, *ApJ* **649**, 845 [34](#), [88](#)
- Shang, H., Glassgold, A. E., Shu, F. H., and Lizano, S.: 2002, *ApJ* **564**, 853 [31](#)
- Shepherd, D.: 2003, in J. M. De Buizer and N. S. van der Bliëk (eds.), *Galactic Star Formation Across the Stellar Mass Spectrum*, Vol. 287 of *Astronomical Society of the Pacific Conference Series*, pp 333–344 [18](#)
- Shu, F. H.: 1977, *ApJ* **214**, 488 [7](#), [71](#)
- Shu, F. H., Adams, F. C., and Lizano, S.: 1987, *ARA&A* **25**, 23 [13](#), [20](#)
- Shu, F. H., Ruden, S. P., Lada, C. J., and Lizano, S.: 1991, *ApJL* **370**, L31 [ix](#), [33](#), [35](#)
- Smith, M. D., Froebrich, D., and Eislöffel, J.: 2003, *ApJ* **592**, 245 [xiii](#), [82](#), [83](#), [84](#), [85](#), [86](#)
- Sugimura, M., Yamaguchi, T., Sakai, T., Umemoto, T., Sakai, N., Takano, S., Aikawa, Y., Hirano, N., Liu, S.-Y., Millar, T. J., Nomura, H., Su, Y.-N., Takakuwa, S., and Yamamoto, S.: 2011, *PASJ* **63**, 459 [88](#), [110](#)

- Suttner, G., Smith, M. D., Yorke, H. W., and Zinnecker, H.: 1997, *A&A* **318**, 595 [81](#), [82](#)
- Tafalla, M. and Bachiller, R.: 2011, in *IAU Symposium*, Vol. 280 of *IAU Symposium*, pp 88–102 [viii](#), [26](#)
- Tafalla, M., Myers, P. C., Caselli, P., and Walmsley, C. M.: 2004, *ApSS* **292**, 347 [11](#)
- Tafalla, M., Myers, P. C., Caselli, P., Walmsley, C. M., and Comito, C.: 2002, *ApJ* **569**, 815 [11](#)
- Tafalla, M., Santiago-García, J., Hacar, A., and Bachiller, R.: 2010, *A&A* **522**, A91 [xviii](#), [23](#), [179](#), [192](#), [193](#), [194](#)
- Tassis, K. and Mouschovias, T. C.: 2004, *ApJ* **616**, 283 [14](#)
- Tercero, B., Cernicharo, J., Pardo, J. R., and Goicoechea, J. R.: 2010, *A&A* **517**, A96 [88](#)
- Tercero, B., Margulès, L., Carvajal, M., Motiyenko, R. A., Huet, T. R., Alekseev, E. A., Kleiner, I., Guillemin, J. C., Møllendal, H., and Cernicharo, J.: 2012, *A&A* **538**, A119 [2](#), [88](#)
- Tercero, B., Vincent, L., Cernicharo, J., Viti, S., and Marcelino, N.: 2011, *A&A* **528**, A26 [2](#), [88](#)
- Thompson, M. A. and MacDonald, G. H.: 1999, *AApS* **135**, 531 [2](#), [88](#)
- Thompson, M. A. and Macdonald, G. H.: 2003, *A&A* **407**, 237 [2](#), [88](#)
- Thorwirth, S., Walsh, A. J., Wyrowski, F., Schilke, P., Beuther, H., Hunter, T. R., Comito, C., Leurini, S., Tieftrunk, A. R., Burton, M. G., and Menten, K. M.: 2007, in *Molecules in Space and Laboratory* [2](#), [88](#)
- Troland, T. H. and Crutcher, R. M.: 2008, *ApJ* **680**, 457 [8](#)
- van Dishoeck, E. F., Blake, G. A., Jansen, D. J., and Groesbeck, T. D.: 1995, *ApJ* **447**, 760 [2](#), [118](#)

- Velusamy, T., Langer, W. D., Kumar, M. S. N., and Grave, J. M. C.: 2011, *ApJ* **741**, 60 [xi](#), [72](#), [73](#)
- Verschuur, G.: 1987, *The Invisible Universe Revealed, The Story of Radio Astronomy*, Springer-Verlag [43](#)
- von Hoerner, S.: 1967, *Journal of the Structural Division ASCE, Vol. 93, p. 461-485, NRAO Reprint B90* **93**, 461 [60](#)
- Wakelam, V., Ceccarelli, C., Castets, A., Lefloch, B., Loinard, L., Faure, A., Schneider, N., and Benayoun, J.-J.: 2005, *A&A* **437**, 149 [28](#)
- Ward-Thompson, D., Kirk, J. M., André, P., Saraceno, P., Didelon, P., Könyves, V., Schneider, N., Abergel, A., Baluteau, J.-P., Bernard, J.-P., Bontemps, S., Cambrésy, L., Cox, P., di Francesco, J., di Giorgio, A. M., Griffin, M., Hargrave, P., Huang, M., Li, J. Z., Martin, P., Men'shchikov, A., Minier, V., Molinari, S., Motte, F., Olofsson, G., Pezzuto, S., Russeil, D., Sauvage, M., Sibthorpe, B., Spinoglio, L., Testi, L., White, G., Wilson, C., Woodcraft, A., and Zavagno, A.: 2010, *A&A* **518**, L92 [11](#)
- Ward-Thompson, D., Scott, P. F., Hills, R. E., and Andre, P.: 1994, *MNRAS* **268**, 276 [11](#)
- Whelan, E. T., Bacciotti, F., Ray, T., and Dougados, C.: 2011, in G. E. Romero, R. A. Sunyaev, and T. Belloni (eds.), *IAU Symposium*, Vol. 275 of *IAU Symposium*, pp 396–399 [18](#)
- Wilson, T.L. and Rohlfs, K. and Huttemeister, S.: 1987, *Tools of Radio Astronomy*, Springer-Verlag [47](#), [48](#)
- Wolfire, M. G. and Cassinelli, J. P.: 1987, *ApJ* **319**, 850 [20](#)
- Wouterloot, J. G. A. and Walmsley, C. M.: 1986, *A&A* **168**, 237 [69](#)
- Wouterloot, J. G. A., Walmsley, C. M., and Henkel, C.: 1988, *A&A* **203**, 367 [67](#)
- Xie, T.: 1997, *ApJL* **475**, L139 [8](#)
- Yu, Z.-Y., Nagahama, T., and Fukui, Y.: 1996, *ApJ* **471**, 867 [67](#)

- Zhang, Q., Hunter, T. R., Sridharan, T. K., and Ho, P. T. P.: 2001, in *American Astronomical Society Meeting Abstracts*, Vol. 33 of *Bulletin of the American Astronomical Society*, p. 134.13 [18](#)
- Zinnecker, H., McCaughrean, M. J., and Rayner, J.: 1996, in S. Beckwith, J. Staude, A. Quetz, and A. Natta (eds.), *Disks and Outflows Around Young Stars*, Vol. 465 of *Lecture Notes in Physics*, Berlin Springer Verlag [82](#)
- Zuckerman, B. and Palmer, P.: 1974, *ARA&A* **12**, 279 [7](#)